Simulations of source recovery and completeness in galaxy surveys at high redshift

---

Submitted in Total Fulfillment

of the Requirements of the Degree of

Doctor of Philosophy

School of Physics

The University of Melbourne

Victoria, Australia

Daniela Patricia Carrasco Núñez

October 2018

Abstract

The search for and characterisation of galaxies at high-redshift is a very active topic in Astrophysics. Thanks to advances in observations from space, the redshift frontier is approaching the epoch of formation of first generation objects. Thus, these samples of galaxies can give us insight into the processes that govern galaxy formation and evolution. One of the key observables used to characterise galaxy populations throughout the cosmic history is their luminosity function (number of galaxies per unit luminosity per unit volume), which requires knowledge and characterisation of the completeness and selection functions of a survey, in addition to the catalogue of discovered objects. In this thesis, we present a search for high-redshift galaxies (redshift $z \gtrsim 6$) in two in the Hubble Space Telescope surveys, the Brightest of Reionizing Galaxies Survey (BoRG), and the Reionization Lensing Cluster Survey (RELICS) using a photometric selection technique (the Lyman break dropout selection). We aim at using the resulting galaxy candidates to estimate a new measurement of the luminosity function at $z \sim 10$. To achieve that, we develop `GLACiAR`, an open `Python`-based tool available on `GitHub`, which is designed to estimate the completeness and selection functions in galaxy surveys. The code is tailored for multiband imaging datasets aimed at searching for high-redshift galaxies through the Lyman Break technique, but it can be applied broadly. The code generates artificial galaxies that follow Sérsic profiles with different indexes and with customisable size, redshift and spectral energy distribution properties, adds them to input images, and measures the recovery rate. We finally apply `GLACiAR` to quantify the completeness and redshift selection functions for J-dropouts sources (redshift $z \sim 10$ galaxies). Our comparison with a previous completeness analysis on the same dataset shows overall agreement, but also highlights how different modelling assumptions for artificial sources can impact completeness estimates.

Declaration

This is to certify that:

- This thesis comprises only their original work towards the degree of Doctor of Philosophy, except where indicated in the Preface.
- Due acknowledgement has been made in the text to all other material used.
- The thesis is less than 100,000 words in length, exclusive of tables, maps, bibliographies, and appendices.

Daniela Patricia Carrasco Núñez

Preface

The majority of the work presented in this thesis is that of the author, however some of the work was undertaken as part of a collaboration. All resources used have been cited accordingly in the text. Specific details are listed below.

- Chapter 1, which presents a review of the history of the Universe and galaxy formation, is entirely the work of the author. All references are cited in the text.
- Chapter 2, which presents a review of high-redshift galaxies and selection techniques, is entirely the work of the author. All references are cited in the text.
- Chapter 3 presents a review of high-redshift galaxy surveys. All references are cited in the text. The selection technique applied on the BoRG dataset has been published in Bernard, Carrasco et al. [2016]. The author's contribution to this paper consisted of performing a parallel search from scratch, which included the reduction of the images and construction of the catalogues. The selection technique applied to the RELICS dataset is entirely the work of the author.
- Chapter 4 is based on the work published in Carrasco et al. [2018]. This was supervised by Michele Trenti, with input, comment, and suggestions from Simon Mutch, and Pascal Oesch, who also provided advice on the code that served as a starting point.
- Chapter 5 presents a review of the galaxy luminosity function at high-redshift. All references are cited in the text. It also includes the application of the code from Chapter 4 on the galaxy candidates from Chapter 3, which is entirely work of the author. The comparison of these results to Bernard, Carrasco et al. [2016] was supervised by Michele Trenti.

- The conclusions in Chapter 6 are entirely the work of the author.

A list of peer-reviewed publications related to the topic of this thesis in which the author is a part of are listed below. The participation in these articles consisted of feedback on the analysis techniques, as well as comments and suggestions on the text of the manuscripts.

- Acebron et al. [2018]
- Calvi et al. [2016]
- Cerny et al. [2018]
- Cibirka et al. [2018]
- Paterno-Mahler et al. [2018]
- Salmon et al. [2017]
- Salmon et al. [2018]

Acknowledgements

It is difficult to try and fit into these pages all the people that have helped me to get here, but I will try. Firstly, I would like to thank my supervisor, Prof. Michele Trenti, for taking me as his student after more than one year through my PhD. Thank you for always taking the time to help me, answer my questions, or anything else I needed. Your guidance, patience, and support have been immensely important. Thank you for being so selfless and always accommodating and trying to help me as much as possible.

Thank you to Prof. Stuart Wyithe for taking me as his student and giving me the opportunity to come and work at the University of Melbourne. Without you, this incredible experience would have not been possible. Many thanks also to Prof. Rachel Webster for being a great role model and source of inspiration. Thank you to Dr. Rachael Livermore. Our brief time working together was a pleasure. I really appreciate your selflessness, either with your time, knowledge, or space (the office). Thanks to Dr. Dan Coe, and Dr. Larry Bradley, and all the people at STScI that made my time there really pleasant. It filled me with the very much needed energy boost half way through my PhD. Thank you to the rest of the people who I collaborated with and that somehow helped with this thesis. Stephanie Bernard, for her help on our high-z galaxies search; and Pascal Oesch, for selflessly sharing his code.

Thank you to all the people from the School of Physics. In particular, to all the good friends I made there. Thanks to Ángela for spending your time here in Melbourne with me. Those cups of tea (and muffins) while chatting about life are such great memories. Thank you for listening to me, for being my confidant and letting me be yours. I miss you immensely, but I am happy that you are doing what you enjoy, with your family and friends in your beloved Bogotá. Thanks to Rob for receiving me with open arms

when I started my PhD. Thank you also for the lessons about footy and cricket. I guess I paid back the favour by teaching you about the best soccer team in the world, Chile. Thanks to my good friend Justine for those walks and conversations while looking for hot chocolate. Thanks for those writing sessions. Even though they were few, they did help. Thanks to Noura for being such a great officemate, for showing me your life and letting me be part of it. Thank you for being a sister. Thanks to Sarah for all those lunches filled with interesting conversations. You are such a smart and compassionate person. Many thanks to all those incredibly strong and supportive women from the Astro department, Mahsa, Stephi, Lilli, Sinem. Big thanks also to George and Daniel Flynn. It's always great to share a laugh, a beer and/or a coffee with you. To the friends back home. Cata and Charito for always taking time to chat on Skype. To Elo, Carla, Javi, Ibarrita, and specially Marce. Your messages always draw a smile to my face. Thank you Esteban for being there in the important moments.

A huge thanks to my friends Laurence and Kim. Laurence, you have been the greatest support I have had during my time in Melbourne. You have helped me without questioning or judgement. You have been such great source of support. I hope I can one day repay so much kindness. And all the teasing aside, you are an amazing friend. Kim, I cannot stress enough how glad I am we met. You are such a thoughtful person, always worried about me, sending me cake or funny posts. You and Laurence have made me feel like part of your little family with Brian and Peggy. I cannot express how grateful I am for being fortunate enough to call you my friends. Thank you also to María for her encouragement and shared laughs.

A special thanks to Dan for being so incredibly supportive, patient, and thoughtful. Even though this academic world is different to what you are used to, you have been great. Thank you for always understanding that weekends meant *working on the thesis* for me, for believing in me, and for spoiling me with all the dinners and sweets. I feel immensely fortunate to have you in my life.

Finally, the biggest acknowledgement goes to my family. This would have not been possible without them. Thank you to my parents for their unconditional support. It has been incredibly hard being physically far from you, but I've always felt you are by my side. Thank you to Rodrigo and Matías for always being proud of me, and lightening up my days with their random jokes. Special thanks to Tomás, who inspires me everyday to be a better person and to keep going. Thank you for all those conversations on the phone. You have no idea how helpful they are and how our silly jokes brighten my days. You inspire me, and I am your biggest admirer. Most important of all, thank you for keeping me updated with the newest memes and viral videos.

Contents

List of Figures

List of Tables

1

Introduction

The Universe and its mysteries have always fascinated humans. Since the first civilisations, humans have studied the sky and its wonders, and have applied that knowledge in their pursuits. The Ancient Greeks studied constellations and the shape of Earth. The precise calendars of the Mayans were created using their knowledge of Astronomy. Perhaps less known are the Incas, who also developed sophisticated calendars from their studies of the cosmos, where they applied this knowledge to activities such as agriculture [Carlson, 1976]. Often overlooked are the earliest civilisations known, the first peoples of Australia. Several tribes had a particular interest in the Milky Way, and phenomena such as eclipses, tides, and the solar dusk and dawn were noticed and given an explanation by them as well [Norris, 2016].

Enormous efforts have been made throughout history to improve our understanding of the Universe. These efforts have led to important discoveries, including predicting phenomena such as eclipses almost a millennium ago; the Sun as the centre of the Solar System, first with Plato in the second century and confirmed by Copernicus over 500 years ago and the discovery of the expansion of the Universe just two decades

ago. As our technology improves, we are ever closer to a time in which we can form a comprehensive picture of the formation and evolution of the Universe.

We know that it all started with the Big Bang, followed by the expansion of the Universe. This expansion is known as Cosmic Inflation and is predicted to have occurred very early on. This expansion was exponential, with space growing much faster than the speed of light. This process explains why, at large scales, the Universe appears flat and homogeneous. At the end of the inflationary period, new particles began to form. As the Universe cooled, the Universe began to form neutral atoms and became transparent. These atoms decoupled from photons, allowing us to observe the photons today as Cosmic Microwave Background radiation. Small variations and instabilities in the very early Universe, formed likely during inflation, were the seeds of what we know as stars and galaxies today. These stars and galaxies formed from only primordial hydrogen and helium, but processes such as supernovae and feedback began to produce heavier atoms. The first stars and galaxies formed larger structures such as clusters and superclusters, and over time more complex objects such as black holes formed. Eventually, in orbit of one of the billions of stars inside the Milky Way galaxy, Earth was formed.

Below we provide a more detailed summary of the history of the Universe with a particular focus in the first galaxies.

Gravitational interactions play a key role in the formation and evolution of the Universe. Albert Einstein provided an equation that unified the description of gravity as a property of space-time. This is the General Relativity field equation, which can be written as

$$R_{\mu\nu} - \frac{1}{2} g_{\mu\nu} R = 8\pi G T_{\mu\nu} + g_{\mu\nu}, \tag{1.1}$$

where the left side describes spatial curvature and the right side the energy content.

To solve 1.1, certain assumptions are required. We assume the Universe is homogeneous and isotropic over large scales, which is known as the *cosmological principle*. Using the Robertson-Walker metric[1], the distance in space-time can be written as:

$$ds^2 = dt^2 - a(t)^2 \left(\frac{dr^2}{1 - kr^2} + r^2 d\theta^2 + r^2 sin^2\theta d\phi^2 \right). \tag{1.2}$$

[1]We will be using geometric units, i.e., $c = t_H = D_H = 1$.

$a(t)$ is the so-called scale factor of the Universe, which is a parametrisation of the relative expansion of the Universe; k is the curvature, a value of 0 is for a flat Universe, 1 for open, and -1 is closed; ds is a spacetime unit; t is time; and r, θ, and ϕ are the spatial comoving coordinates.

The field equations of General Relativity yield the equations of motion:

$$\left(\frac{\dot{a}}{a}\right)^2 = \frac{8\pi G}{3}\rho - \frac{k}{a^2} + \frac{\Lambda}{3} \tag{1.3}$$

and

$$\frac{\ddot{a}}{a} = -\frac{4\pi G}{3}(\rho + 3P) + \frac{\Lambda}{3} \tag{1.4}$$

G is the gravitational constant; ρ is the mass density; P is the pressure; and Λ is the cosmological constant.

If we consider photons in equation 1.2, where $ds = 0$, and a flat Universe, we obtain

$$dt^2 = a^2(t)dr^2. \tag{1.5}$$

The dependence of the scale factor $a(t)$ on t varies with time. For example, the scale factor at early times follows a function of $a \propto t^{1/2}$, which later changes to $a \propto t^{2/3}$. The value of $a(t)$ depends on the energy density in the Universe. At early Universal times, the dominating form of energy is radiation, while matter dominates at later times. The Hubble parameter, $H(t)$, measures the rate of the expansion of the Universe,

$$H(t) = \frac{\dot{a}}{a}, \tag{1.6}$$

and

$$H^2 = \left(\frac{\dot{a}}{a}\right)^2 = \frac{8\pi G}{3}\rho - \frac{k}{a^2} + \frac{\Lambda}{3}. \tag{1.7}$$

The age of the Universe today, t_0, can be calculated as

$$t_0 = H_0^{-1} \int_0^\infty \frac{dz}{(1+z)H(z)} \tag{1.8}$$

The Hubble parameter in the current time is called the Hubble constant, and it is indicated by a "0", H_0.

H_0 is often written as a function of a new dimensionless parameter, h,

$$H_0 = h \cdot 100 \frac{\text{km}}{\text{s} \cdot \text{Mpc}} \tag{1.9}$$

The density parameter indicates the density of the Universe, and it is defined as

$$\Omega \equiv \frac{\rho}{\rho_c} \equiv \Omega_R + \Omega_M + \Omega_\Lambda - \Omega_k \tag{1.10}$$

For a flat Universe, $\Omega_k = 0$, in which case we can obtain the critical density

$$\rho_c = \frac{3H^2}{8\pi G} \tag{1.11}$$

A density above this value of yields a closed Universe, and a value below it yields an open Universe.

Redshift is a measure of the scale of the Universe from when radiation was emitted by a certain source in comparison to its present value. For a photon that was emitted at a time t, with a wavelength of λ_{emit}, the photon we observe now will have a longer physical wavelength, λ_{obs} with z being the redshift.

$$1 + z \equiv \frac{\lambda_{obs}}{\lambda_{emit}} = \frac{a_0}{a(t)} \tag{1.12}$$

For a nearby source, i.e. $z \ll 1$, $a(t)$ can be expanded,

$$a(t) = a_0 - \dot{a}(t_0)(t_0 - t). \tag{1.13}$$

Using this definition of $a(t)$ and equations 1.6 and 1.12, we obtain the Hubble law,

$$z = H_0 r, \qquad z \ll 1, \tag{1.14}$$

Distances in Cosmology

Due to the expansion of the Universe, measuring distances in Cosmology is not straightforward[Riess et al., 1998]. To take the expansion of the Universe into account, the concepts of comoving distance and coordinates are used. Unlike proper distances, that measure the space between two objects at a specific time, comoving distances account for the expansion of the Universe. This means comoving distances and coordinates do not change with time, while proper distances do. Following Hogg [1999], we present the main equations describing useful measurements of distances.

The line-of-sight comoving distance, D_C, is the is the proper distance divided by the

scale factor,

$$Dc = \int_0^z \frac{dz'}{\sqrt{\Omega_M(1+z')^3 + \Omega_k(1+z')^2 + \Omega_\Lambda}} \tag{1.15}$$

The transverse comoving distance, D_M, is the distance between two objects in the sky, and can be defined as

$$D_M = \begin{cases} \frac{1}{\sqrt{\Omega_k}}\sinh[\sqrt{\Omega_k}D_C] & \text{for } \Omega_k > 0 \\ D_C & \text{for } \Omega_k = 0 \\ \frac{1}{\sqrt{|\Omega_k|}}\sin[\sqrt{|\Omega_k|}D_C] & \text{for } \Omega_k < 0 \end{cases} \tag{1.16}$$

The angular diameter distance is a measurement that relates the physical size of an object, D, and its angular size as measured by the viewer, θ.

$$D_A = \frac{D}{\theta}. \tag{1.17}$$

D_A can also be defined in terms of the transverse comoving distance, which depends on the Cosmology assumed,

$$D_A = \frac{D_M}{1+z}. \tag{1.18}$$

The luminosity distance, D_L, corresponds to the distance obtained from the relation between the flux emitted at a redshift z and the flux observed today,

$$D_L = \sqrt{\frac{L}{4\pi F}} = (1+z)D_M = (1+z)^2 D_A \tag{1.19}$$

Lookback time, t_L, is the time difference between the age of the Universe where the light at a redshift z was emitted, and the age of the Universe at the time of the observation. It is defined as

$$t_L = t_H \int_0^z \frac{dz'}{(1+z')\sqrt{\Omega_M(1+z')^3 + \Omega_k(1+z')^2 + \Omega_\Lambda}} \tag{1.20}$$

1.0.1 Constituents of the Universe

The Universe is predominantly composed of Dark Energy, Dark Matter, and only a small percentage of visible matter. The latest estimations for the their relative occurrences are $\sim 68\%$, $\sim 27\%$, and $\sim 5\%$, respectively [Planck Collaboration et al., 2018].

Visible matter is the matter we see every day. This matter is composed of protons, neutrons and electrons.

Dark Matter is a type of non-relativistic matter. Its existence was first proposed by [Zwicky, 1933]. While we cannot observe dark matter directly, evidence for the existence of Dark Matter includes the rotation curves of galaxies [Rubin et al., 1980] and gravitational lensing [e.g., Blandford and Narayan, 1992]. The elementary particle of Dark Matter is not known but predicted candidates are mainly types of Weakly Interacting Massive Particles, WIMPs [see Jungman et al., 1996].

Dark Energy is currently the least understood constituent of the Universe, and it is a strong candidate for what may drive the expansion of the Universe, where it can be defined as a candidate to be cosmological constant, Λ [Peebles and Ratra, 2003].

During different stages in the history of the Universe, different energy types have dominated over the rest, which dictates the behaviour of the scale factor and therefore the expansion of the Universe [e.g., Dodelson, 2003]. Some possible scenarios are listed below,

1. Radiation dominated, $a(t) \propto t^{1/2}$.
2. Matter dominated, $a(t) \propto t^{2/3}$.
3. Curvature dominated ($k < 0$), $a(t) \propto t$.
4. Cosmological constant dominated, $a(t) \propto \exp(\Lambda t/3)$.

1.0.2 ΛCDM model

This model is also referred to as the Standard Model of Cosmology. In this model, dark matter is cold, and the expansion of the Universe is driven by a cosmological constant, Λ. Hence the name, ΛCDM.

This model describes the universe as containing matter, radiation, and Dark Energy, whose combined energy density determines its expansion. These three kinds of matter-energy are modelled macroscopically as a perfect fluid and are thus completely determined by an energy density ρ and a pressure p, with different equations of state.

Simulations reproducing this model Universe formation with CDM particles show that the structure consists of filaments, walls with characteristic sizes of $R \sim 100h^{-1}$ Mpc, and voids. The overdensities are called dark matter halos.

Parameter	Value	Units
H_0	67.4 ± 0.5	km s^{-1} Mpc^{-1}
Ω_Λ	0.685 ± 0.007	N/A
Ω_M	0.315 ± 0.007	N/A
Ω_k	0.001 ± 0.002	N/A

Table 1.1: Estimated values for the cosmological parameters of the ΛCDM model according to Planck Collaboration et al. [2018].

One of the keys to the success of this model is because it is capable of reproducing observations such as the anisotropies in the CMB [e.g., Planck Collaboration et al., 2016]; data from Supernova type-Ia (SNIa) [e.g., Planck Collaboration et al., 2016]; Baryon Acoustic Oscillations observations [e.g., Planck Collaboration et al., 2016]; and the HST measurement of the Hubble parameter [e.g., Planck Collaboration et al., 2016], among others.

Conflicts using this model have arisen recently with for example tension between the results from Hildebrandt et al. [2017] and Planck or local measurements of H_0 being higher than that inferred from the CMB [Riess et al., 2016]. Another weakness is its current inability to probe the existence of Dark Energy.

The latest values for the cosmological parameters as measured by Planck Collaboration et al. [2018] are listed in Table 1.1

1.1 Early Universe

The Universe is 13.8 billion years old. Throughout this time, it has gone through several phases that have shaped what we observe nowadays. In this section we will describe the major milestones of the cosmic history of the Universe. A schematic diagram depicting these stages is shown in Figure 1.1.

The Big Bang can be defined as a gravitational singularity that thrust the Universe in to existence 13.8 billion years ago. Immediately after the Big Bang, the Universe was extremely dense and hot, with a temperature of the order of 10^{32}K. All particles were mixed together in a photo-baryonic fluid, and the Universe was opaque. At this time, there were no neutral atoms or even bound nuclei, as high energy photons destroyed any atom or nucleus. As the universe cooled to below the binding energies of typical nuclei, low-density elements started to from.

The standard Hot Big Bang scenario fails to account for some of the properties of the Universe about what we observe today. Examples include:

- The Flatness problem. This relates to the small random probability of the Universe being as flat as it is observed nowadays. For the total density parameter to be of order unity today, it must have been extremely close to 1 at earlier times, which means that a very precise *fine tuning* of this parameter was necessary.

- The Horizon problem. The Universe follows the cosmological principle, which means it is at equilibrium. In the Hot Big Bang model this would not be possible as particles would not have been in casual contact. Therefore, they would be unable to reach thermal equilibrium with such far away particles.

- The lack of monopoles. One of the relics of this scenario is monopoles. The predicted number of them means that they would have had to be detected, which they haven't.

These problems can be solved with a particular set of solutions to the Einstein's equation. However, the probability of these solutions occurring is nearly 0, which is known as a "fine tuning" problem. A more natural solution to the aforementioned issues is a theory that supports an exponential growth. This is an inflationary model, i.e. a model where $\ddot{a} > 0$. This would also explain macroscopic inhomogeneities and haloes as results of primordial microscopic inhomogeneities.

Inflation models started to appear in 1978, with Starobinsky [1980], however these models are very different to what modern inflationary models. The first paper to describe a more modern inflationary model was Linde [1982], and with some modifications, chaotic inflation was born [Linde, 1983]. This theory accounted for most of the problems of previous inflation models and is today considered the standard model. There remains no consensus on all of the small details regarding inflation, with numerous different models proposed, but there are enough common properties that allow us to describe an overview of the process.

In the most accepted models of inflation [e.g., Linde, 1983], the vacuum energy density was much higher than today, with Ω_Λ dominating the Hubble expansion. This expansion starts at the Planck time, $t_{Planck} = 10^{-43}$ seconds, while the total duration of inflation is $t \sim 10^{-30}$ seconds. It occurred when the strong nuclear force separated from the electroweak force. This expansion was exponential, with space growing much faster than the speed of light.

A manner in which Inflation can be defined is as the period when the Hubble length, in comoving coordinates, decreases.

$$a(t) \propto \exp(Ht) \tag{1.21}$$

The inflation period produced an accelerated expansion of the Universe driven by the high vacuum energy density, which by , would make

$$\frac{\dot{a}}{a} \approx \sqrt{\frac{\Lambda}{3}} \tag{1.22}$$

The details about what happened after the inflationary phase are not well understood, but it is expected that a reheating transition took place. In this phase the vacuum energy density is transformed into normal matter and radiation, which ends exponential expansion. It is presumed that the normal Friedmann evolution took place after this.

This process triggered sound waves that travelled across the primordial hot plasma. These inflationary perturbations lead to density perturbations that produced the collapse of Dark Matter haloes. The gasses inside them could cool and collapsed further to form the first stars and galaxies. Perturbations are sound waves propagating in plasma with time-independent amplitudes.

Before the epoch of Recombination, the so-called Big Bang Nucleosynthesis took place. This is an epoch of nuclear fusion, in which deuterium was formed from neutron and protons. Successive chains of fusion would form heavier nuclei. The synthesis of deuterium was expected to occur at a temperature of $\approx 6 \times 10^8$K, which corresponds to a Universe only $t = 300$ seconds old. After this time has passed and the Big Bang Nucleosynthesis process has ended, the Recombination epoch starts.

1.2 Recombination

The process of Recombination started when the temperature dropped to about $T \sim$ 3740K. During this period, the baryonic component of the Universe evolved from an ionised plasma to a gas of neutral atoms. This process can be mathematically described as the instant at which the number density of ions is equal to the number density of neutral atoms. This is closely related to the process by which the universe goes from being opaque to being transparent. Free electrons bonded with protons and formed atoms of neutral hydrogen. This neutral hydrogen was transparent to light, allowing photons to travel freely, forming the "observable Universe" at a redshift of $z \sim 1090$.

Before the period of Recombination, when the Universe was fully ionised, photons interacted primarily with electrons. The main interaction mechanism was Thomson scattering. The optical depth for the Thompson scattering implies that photons can propagate from the time of the last-scattering surface, at $z \sim 1000$, until the present

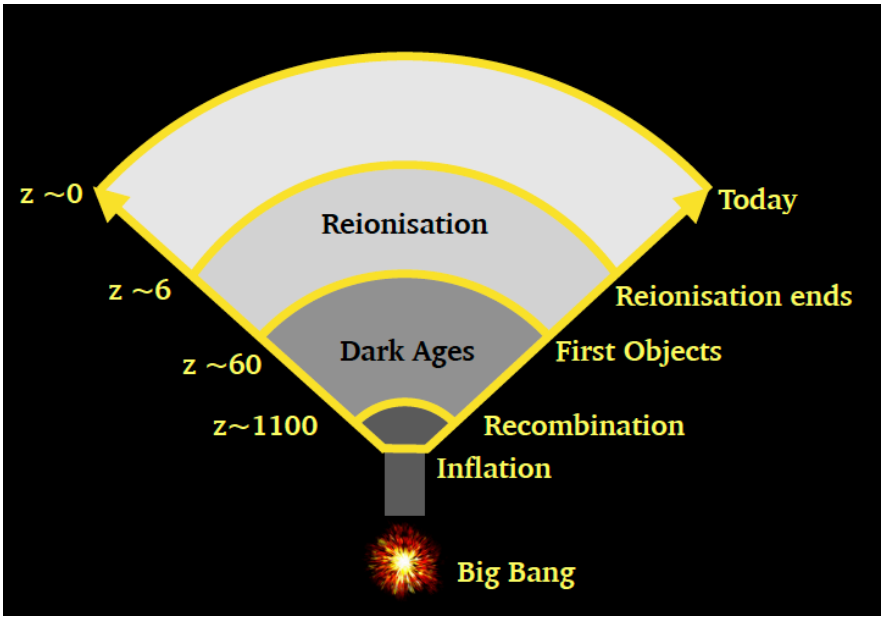

Figure 1.1: Schematic diagram showing the major milestones in the history of the Universe since the Big Bang.

day without being absorbed by light-matter interactions. It is important to note that this is only for photons with a wavelength larger than 1216Å because the absorption cross-section for Lyman-α photons is too large.

At the end of this epoch, photons and baryons had decoupled and baryons became pressure-free for the first time. Because of the gravitational interactions, they started following the distribution of Dark Matter and fell into their potential wells until they became gravitationally bound. However, their evolution was not identical, as baryonic matter interacts differently than dark matter, being subject to processes such as cooling, heating, and friction, among others.

1.3 Cosmic Microwave Background

Predicted by Gamow [1946] and observed for the first time by Penzias and Wilson [1965], the Cosmic Microwave Background (CMB) is a relic of thermal radiation from the early hot phase of the Universe, when matter and radiation were in thermal equilibrium. The cosmic expansion of the Universe caused these background radiation photons to cool to a temperature of $T \approx 2.73$K. As they are further redshifted they continue to lose energy.

The Thomson scattering optical depth, τ corresponds to the scattering of photons by

free electrons and it parametrises the total column density of free electrons along each line of sight that encounters the CMB radiation, i.e. it measures the opacity of free electrons from CMB radiation along the line of sight. This is observed as the amplitude of the polarisation of the CMB.

Photons can propagate from $z \sim 1000$ onward without interacting with matter. The redshift at which this occurs is known as the *surface of last scattering*. The exception to this is photons with a wavelength of $\lambda \leq 1216\,\text{Å}$ since the absorption cross section of these atoms is too large to escape matter interactions.

The physics behind CMB is well understood, and therefore allows us to study the standard cosmological model and determine its parameters with high precision.

According to the model of the Universe we have described, the Universe was inhomogeneous by the time of the surface of last scattering. Therefore, we expect that the CMB radiation would show evidence of inhomogeneities, which is observed in the form of small anisotropies. The scale of the expected anisotropies is determined by the constituents of the Universe. A Universe with Dark Matter would present a CMB with smaller anisotropies than a Universe with a larger amount of baryonic matter.

For a long time, fluctuations in the CMB were searched for, as these fluctuations are the precursors of the large scale structures we observe around us. Finally, the Cosmic Background Explorer Satellite [COBE; Mather et al., 1990] detected these fluctuations. They have been further constrained by the Wilkinson Microwave Anisotropy Probe [WMAP; Spergel et al., 2003, Hinshaw et al., 2013], and the Planck satellite [Planck Collaboration et al., 2016, 2018], and fluctuations have been measured to the order of $O(10^{-5})$. Figure 1.2 shows the temperature fluctuations $\mathcal{D}_\ell$ as a function of the multipole moment ℓ, which can be translated as angular scales using

$$\theta = \frac{360^\circ}{\ell}. \tag{1.23}$$

In the Figure, we can see fluctuations up to scales of $\sim 0.07^\circ$.

1.4 Gravitational instabilities

Gravitational instabilities are responsible for the evolution of structure in the Universe. When the Universe was dominated by matter, the regions with larger density would expand at a slower rate than the less dense regions. Therefore, these overdense regions

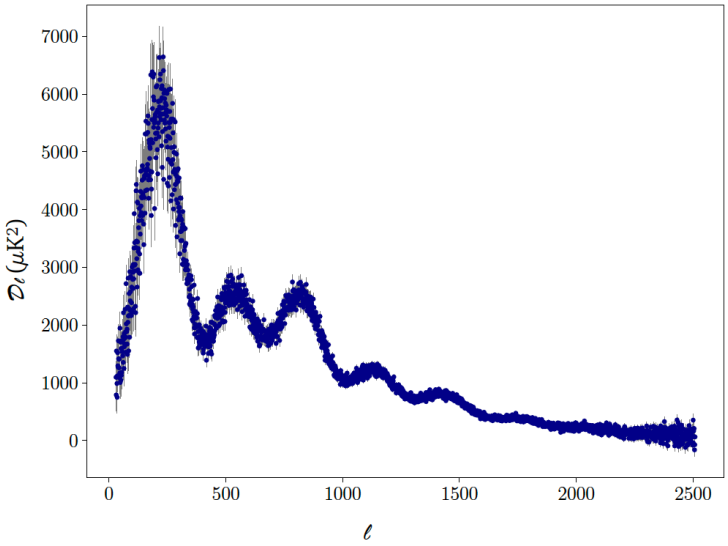

Figure 1.2: Temperature power spectrum of the CMB in the high-multipole likelihood $\ell = 30 - 2508$ from [Planck Collaboration et al., 2016]. The measurements are in blue and the error bars are in gray.

became the first structures, provided they collapsed and became gravitationally bound. On the other hand, less dense regions became continually less dense as the Universe expanded.

The origin of density fluctuations comes from quantum fluctuations from the Big Bang era that expanded to macroscopic scales during the inflationary epoch. Theoretical models suggest that all objects separated for $150h^{-1}$Mpc were outside the horizon after inflation, and thus were not able to interact. This strongly suggests that the seeds of the overdensities and voids present today had already formed before inflation took place [e.g., Einasto et al., 2011].

Acoustic oscillations in the fluid with coupled photons and baryons produced the peaks in the CMB angular power spectrum and the lower amplitude peaks in the matter power spectrum. This happened during the matter dominated epoch. The CMB anisotropies measured are very small, which implies that by the time the CMB photons last interacted with matter, presumably at $z \sim 1000$, the fluctuations were also small. Obviously, the perturbations grew over time, as the inhomogeneities we observe today are large in comparison. The growth of these density fluctuations are caused by self-gravity.

The power spectrum $P(k)$ can be used to describe the statistical properties of matter distribution in the Universe [Yu and Peebles, 1969, Peebles, 1973]. It describes the

level of structure as a function of the length scale $L \simeq 2\pi/k$, with k the comoving wave number. The initial power spectrum is a powerful tool in Cosmology, and it is predicted theoretically. The measurements made for later times can be compared with the predictions for the power spectrum, making it a powerful tool to understand the Universe.

The shape of $P(k)$ immediately after Inflation can be described as

$$P(k) \propto k^n, \tag{1.24}$$

with $n = 1$ in most inflation models. However, its shape changes after the end of this process.

The modifications of $P(k)$ depend on the type of dark matter, whether is cold dark matter (CDM) or hot dark matter (HDM). The difference between these two models is the velocity of the constituent particles. In the cold dark matter scenario, the dark matter particles are non-relativistic at the time they decoupled from other components of the Universe. Whereas in hot dark matter scenarios, the constituent particles are relativistic.

The proposed HDM particles are not able to produce the first fluctuations, and a smoother early Universe is predicted in this case. Therefore, HDM models cannot explain galaxy formation, which lead to structure formation that does not agree with observation. We can therefore exclude HDM as the dominant constituent of dark matter.

The CDM models predict a hierarchical formation of structures. Small overdensities overcome the expansion of the Universe and collapse first. These Dark Matter haloes merge together to form larger haloes where galaxies are formed. This process is still occurring, billions of years after the Big Bang, meaning galaxy formation still occurs.

The cosmological principle is only valid for large scales. At small scales, the Universe is far from being homogeneous and isotropic. The scale at which the Universe seems to be homogeneous is $R \gtrsim 200h^{-1}$Mpc [Schneider, 2015].

The inhomogeneity of the Universe at small scales is supported by all types of structures, including galaxy clusters, galaxies, and stars. The anisotropies are observed in the CMB, which shows fluctuations of about $\Delta T/T \approx 10^{-5}$ [Planck Collaboration et al., 2016].

The angular size $\Delta\theta$ of a temperature fluctuation in the CMB can be related to a physical size l on the surface of last scattering by

$$d_A = \frac{l}{\Delta\theta} \tag{1.25}$$

where d_A is the angular diameter distance (see equation 1.17) to the surface of last scattering.

By using this relation, the sizes of anisotropies on the CMB spectrum can be converted to current sizes. For example, some of the first fluctuations measured by the Cosmic Background Explorer Satellite [COBE Mather et al., 1990] had a proper size of $l >$ 1.6Mpc, which corresponds physical scales of $\gtrsim$ 1700Mpc today, which is larger than the known superclusters. With measurements of higher resolutions, the CMB fluctuations have been measured at $l \approx 0.004$Mpc, for example. This is of the order of superclusters, corresponding to $l \approx 40$Mpc.

1.4.1 Baryons and Dark Matter Haloes

Baryonic matter consists mainly of atomic nuclei and electrons. The collapse of the baryonic matter in the early Universe is expected to give way to the first stars. The characteristics and conditions for this to happen have been largely studied in Astrophysics, and they can be challenging as many aspects need to be taken into account.

Before recombination, baryons and photons were coupled, forming a fluid. This fluid does not follow Dark Matter gravitationally due to the pressure produced by the photons. In the Cold Dark Matter model, potential wells in non-baryonic Dark Matter form before decoupling, into which baryons may fall after decoupling because of gravity. Haloes form by the unification of less massive haloes (subhaloes) into more massive ones. Afterwards, the higher mass newly formed halo reaches a new equilibrium by relaxation, which can be violent or quiet.

Dark matter haloes are the most basic structure which matter collapses into, and this gravitational collapse is not the only ingredient that forms stars; a sufficient amount of cold dense gases required as well. In the Dark matter haloes that contain baryons in the form of gas, the baryons cool down by radiating photons and move towards the centre of the halo. This produces a change in the gravitational field, and the halo slightly contracts. The non-linear collapse of dark matter overdensities occurred on characteristic scales that became larger with time. Therefore, the typical collapsed halo mass grows with time.

The gas collapses in a quasi-spherical way. The large thermal pressure creates a peaked density distribution, suppressing collapse at small scales until the density in-

creases considerably. This gas will continue to collapse to proto-stellar densities before fragmentation occurs, for which the fragmentation process is not very relevant according to most studies [Glover, 2005]. The type of fragmentation will determine whether only one or several stars are produced in the Dark Matter haloes. If the dominant process continues to be quasi-spherical collapse, then only a single proto-star would form. On the other had, if a gravitationally unstable disk is formed, then the gas is prone to fragment into several stars.

There are two minimum mass thresholds for star formation, which are the Jean mass and the cooling mass. In the case of the first objects, the minimum mass is dictated by the cooling mass, which sets a lower limit on the halo mass of $\sim 5 \times 10^4$ $M_\odot$ at $z \sim 20$ [Loeb and Barkana, 2001]. The virial temperature of a collapsing cloud is determined only by its mass and its virialisation redshift. Therefore, if the virial temperature is high enough to produce a molecular hydrogen fraction of order of$\sim 5 \times 10^{-4}$, then the cloud will collapse [Tegmark et al., 1997]. The gas will heat up as a consequence of the collapse, either via adiabatic compression or due to shock heating.

The temperature of the gas plays a very important role. If the gas were unable to cool, there would be no further collapse, and consequently no gas fragmentation and star formation. The gas would simply persist in hydrostatic equilibrium and follow the density profile of the Dark Matter. The coupling between baryonic and Dark Matter induces momentum transfer between them hence their temperatures, T_b and T_d, evolve together. Cooling in the primordial gas had to rely on molecular hydrogen (H_2), since metal-line cooling common in local Universe star formation was not available. Therefore, to determine the cooling rate of the gas accurately, an understanding of the thermal and chemical evolution of the gas is required.

The pressure of the gas also plays an important role as it halts the collapse, maintaining the gas density constant. For the gas to collapse and eventually form the first stars, the baryons have to be able to dissipate energy rapidly through cooling.

The baryons and the potential wells of dark matter in which they were embedded in the early Universe will be the progenitors of the first small structures. These galaxies form after stars, and these first stars play a key role in this process by defining the initial conditions of the broader Universe.

1.4.2 End of the Dark Ages

The so-called Dark Ages are the period between Recombination and the formation of the first stars. Stars formed in the cooled gas of baryons in the aforementioned overdensities. In the cores of these halos, the density and temperature of the gas have to reach sufficiently high values to ignite nuclear fusion and burn brightly as a star. As previously mentioned, the haloes that host the first stars are expected to have a minimum mass of $5 \times 10^4 M_\odot$ at $z \sim 20$ according to Loeb and Barkana [2001], with other authors suggesting actual values of $\sim 10^5 - 10^6 M_\odot$ [Abel et al., 2002, Gao et al., 2007, Bromm and Yoshida, 2011].

The process of formation of primordial stars is not completely understood. However, what has been discovered points to the fact that the first stars were very massive. This is due to molecular hydrogen cooling properties, which keep the Jeans mass high. It is expected that with higher resolution simulations some of the gaps around the knowledge of this process are filled.

In the primordial small haloes, the first stars could have formed at redshift $z \simeq 55-60$, which is the redshift at which the first mini-haloes encompassed all of the required ingredients [Bromm et al., 2009, Trenti and Stiavelli, 2009, Naoz et al., 2006].

As the cosmic density field in which the first stars formed are expected to be strongly clustered [Gao et al., 2007], feedback effects from these stars are crucial in the formation of the galaxy. They are the most likely source of the first heavier elements produced in stars and galaxies we observe today. It is expected that the imprint of these processes could be observed.

Stars: Population II and Population III

The first stars formed from hydrogen and helium only as this was the only gas available in the Dark Matter haloes. Since the heavy elements had not yet been created, these first stars are expected to have no metals. They are called Population III (Pop III) stars. Compared to the stars we observe now (with the same mass), they were hotter and more luminous and had shorter lifetimes - $\sim 2 - 4$ Myr [Schaerer, 2002].

Population III stars explode as supernovae and enrich the intergalactic medium [e.g. Nomoto et al., 2006]. As a result of these supernovae, the gas in the halo is likely to be blown outside of the halo, thus preventing further star formation. Apart from Dark Matter and primordial gas, the haloes also contain gas enriched with metals by the

Population III stars. These metal-enriched gasses are both more efficient in cooling and can eventually form Population II stars.

The search for stars that belong to this population has been a very active topic in Astrophysics. Finding them would further support the current theory of galaxy formation. Although some studies have claimed detection of these stars, such as in the recently discovered galaxy CR7 [Sobral et al., 2015], they have been questioned [Bowler et al., 2017b]. As yet, we have no definite detection of said stars.

1.4.3 First Galaxies

At the time of Recombination, around $z \sim 1090$, the Universe went from being opaque to transparent [Hinshaw et al., 2013]. Up to this point, baryons and photons had been coupled. Then, the baryons became pressure free and followed the density distribution of the dark matter. Since both baryons and photons interact differently when subjected to the same processes, they evolve in different ways. The photons were able to escape and travel, which we detect today as CMB.

The ΛCDM model (see Section 1.0.2), built with key input from CMB observations, provides a distribution of haloes where galaxies can form. The large scale structures we observe in the Universe today were produced by density fluctuations, which grew via gravitational instability. One of the remnants from the early fluctuations can be found in the temperature variations of the CMB [Smoot et al., 1992].

In order to understand the formation of galaxies, we must first be clear in defining what we consider to constitute a galaxy. For the purposes of our work, we will require that a galaxy consists of: a bound dark matter halo, with a potential well, with a stellar system inside that well. This system is often associated with an even larger gaseous circumgalactic medium [Shull, 2014].

Galaxies formed from the inhomogeneities in matter produced by the gravitational instabilities. From the ΛCDM model, we know that the formation of structures in the Universe is hierarchical, forming smaller sources first and larger structures only later in time through merging processes. The potential energy in the dark matter haloes heats up the gas, and if the gas is able to cool down by radiative processes it can collapse into dense structures. These are the first stars, which began to form at $z \sim 30$ [Loeb and Barkana, 2001].

The details of how and when exactly star formation was triggered is still an open discussion, but all studies agree that the gas supports star formation in galaxies. Galaxies

grow hierarchically from small to large objects. This is achieved by mergers of two or more haloes or by accretion of surrounding matter. When the gas in the halo cools down it can sink in the middle, and form a disk because of its angular momentum. After reaching a certain density, stars begin to form in a more efficient manner, producing galaxies.

The star formation process is regulated by feedback resulting in winds at large scales. These winds are produced by the stars exploding as supernovae and by accreting black holes from Active Galactic Nuclei (AGNs). The process of feedback and the interaction between the aforementioned types are not fully understood. However, it can be summarised that the supernova feedback is driven by the explosion of the star, which causes an increment in the temperature of the interstellar medium, halting star formation. Regarding AGNs, the cooling gas in the atmosphere surrounding galaxies is heated through radiation and this causes the rate at which the gas can cool to drop [Benson, 2010].

It is still unclear whether there are galaxies with only Population III stars or whether these ones gave way to Population II stars and formed the first galaxies afterwards [Maio et al., 2011]. According to [Johnson et al., 2008], most first galaxies hosted at least one primordial star after their formation. However, some of the mini-haloes that merged and formed the galaxies had already formed Population III stars before merging. This study also concludes that metal free galaxies are less likely to exist even in the first newly formed galaxies because of supernovae explosions that chemically enrich the system. Furthermore, recent simulations have indicated that heavy elements were produced and dispersed at a fast pace, which led to fast enrichment of the medium. All this evidence suggests that galaxies formed exclusively by Population III stars might not have existed.

1.5 Reionisation

As we have noted, the Universe went from being ionised to being neutral during Recombination. However, there must have been a process by which the Universe became ionised again, otherwise we would not be able to observe structures. This process is known as Reionisation.

Reionisation is not an instantaneous process, but the range of redshift at which it occurred is not yet entirely constrained. The most recent measurements of [Planck Collaboration et al., 2018] suggests a redshift of $z = 7.68 \pm 0.79$ as a mid-point value, with the whole process probably spreading over a period of the order of hundreds of

gigayears.

The mechanism that drives Reionisation is photoionisation. The sources responsible for these ionising photons is still not entirely clear. AGNs were a natural choice as they are bright sources. However, it has been found that the ionising flux required is insufficient if only provided by AGNs [Willott et al., 2010], due to the decline in the quasar luminosity function for $z > 3$. Nowadays, results lean towards the first galaxies [e.g. Yan and Windhorst, 2004, Kashikawa et al., 2006, Robertson et al., 2013] as likely sources. The first stars have a high temperature and energy, and they are much more efficient sources of ionising photons. However, individual stars are born in isolation, for which they are not the main contributors to the Reionisation process. Instead, we require groups of stars, in the first galaxies.

In the Dark Matter haloes, efficient star formation occurs and the first proto-galaxies form. The stars in these structures will ionise the intergalactic medium close to them. These ionised regions will keep expanding because there are more photons available. For very dense regions, i.e. regions with several haloes, the haloes with ionised hydrogen will overlap and coalesce until the entire Universe is ionised. These haloes of HII are sometimes referred to as bubbles.

In order to understand the role of galaxies in this process, it is necessary to estimate the total ionising radiation coming from galaxies, n_{ion}. Following the notation by Robertson et al. [2013], this can be expressed as the multiplication of three quantities:

- ρ_{UV}, the rest-frame UV continuum luminosity density, which quantifies the luminosity of galaxies at UV-continuum wavelengths in a given comoving volume of the Universe. It is important to note that the UV luminosity density is used due to the redshift of Reionisation. The light we observe from the galaxies responsible for the process comes from the UV part of the galaxies' spectrum.

- ξ_{ion}, the efficiency factor in converting the UV luminosity to Lyman-continuum emission, and

- f_{esc}, the escape fraction, which is the relative fraction of Lyman-continuum-ionising photons escaping from galaxies over the the fraction of UV-continuum photons which escape.

which leads to the production rate of ionising photons, $\dot{n}_{ion}$,

$$\dot{n}_{ion} = f_{esc} \times \rho_{UV} \times \xi_{ion} \tag{1.26}$$

This equation helps us understanding how many energetic UV photons were produced by young stars at early times and what fraction of photons capable of ionising hydrogen outside galaxies escaped without being intercepted by clouds of dust and hydrogen from galaxies.

ξ_{ion} and f_{esc} are quantities that vary for each galaxy, but their average is attempted to be calculated.

The parameter ξ_{ion} can be derived from stellar population models based on assumptions regarding the properties of high-redshift galaxies.

The escape fraction is the portion of radiation that is able to escape from the host source. The sources responsible for Reionisation have to provide Lyman continuum photons with wavelengths < 912Å, as this is what ionises the hydrogen in the intergalactic medium. Therefore, in order to estimate f_{esc}, the emerging flux in this wavelength range has to be measured. This is a challenging task as f_{esc} is very small, $f_{esc} << 1$ at $z \leq 6$, and the escaping photons of the Lyman continuum flux can be absorbed by the intervening intergalactic medium in the line of sight. Nevertheless, this has been done for galaxies at $z \sim 3$ [e.g. Cooke et al., 2014], which is the redshift limit for this method since at higher redshifts the intergalactic absorption is too high. As mentioned before, this parameter is not equal for all galaxies. In fact, it has proven to considerably vary from galaxy to galaxy. However, the characteristic values found at $z \sim 3$ are in the range $0.1 \lesssim f_{esc} \lesssim 0.2$. A link with the slope of the spectrum, β has been proposed that can also be used to estimate f_{esc}. The values inferred for f_{esc} show it evolves with the redshift in the range $z = 6 - 10$ [e.g., Kuhlen and Faucher-Giguère, 2012].

An alternative form for $\dot{n_{ion}}$ [Robertson et al., 2010, Duncan and Conselice, 2015] is given by

$$\dot{n}_{ion} = f_{esc} \times \rho_{SFR} \times \kappa_{ion} \tag{1.27}$$

where ρ_{SFR} is the star formation rate density, and κ_{ion} is the ionising photon production rate per unit of star formation.

In order to connect equations 1.26 and 1.27 to the ionisation state of the intergalactic medium, it is also necessary to take into account recombination, which depends on inhomogeneities, typically accounted through the introduction of a clumping factor, C_H. This can be used to estimate a minimum star formation rate per unit of comoving volume, ρ_{SFR} by counting how many photons are needed and estimating recombination through the clumping factor [Madau et al., 1999, Shull et al., 2012].

The galaxies that existed during the Reionisation epoch emit the radiation that will

ionise the medium. The amount of radiation required to ionise the Universe cannot be accounted for considering only bright galaxies [Robertson et al., 2015] since faint galaxies dominate the photon budget according to the shape of the luminosity function. It is clear that both quasars and the very brightest galaxies are too rare to significantly contribute to the overall ionising photon budget [e.g. Dijkstra et al., 2004]. On the other hand, several studies have shown that faint galaxies make a significant contribution to the ionising photon budget during Reionisation [Wise et al., 2014].

Several studies have explored this area, trying to constrain the faintest luminosity of galaxies that can entirely ionise the Universe. Possible scenarios include either galaxies as faint as $M_{UV} \sim -10$ being responsible for the ionisation of the intergalactic medium, or a strong evolution of ξ_{ion} or f_{esc} [Kuhlen and Faucher-Giguère, 2012]. A compromise between these scenarios is currently accepted, with faint galaxies playing an important role, with the escape fraction also being larger at early times [Kuhlen and Faucher-Giguère, 2012]. Robertson et al. [2013] find that in order to match the observational constraints on cosmic Reionisation, the galaxy population needs to have a steep power-law luminosity function to continue up to magnitudes of at least $M_{UV} < -13$. Bouwens et al. [2015a] showed that the evolution of the ionising emissivity, n_{ion} (equation 1.26) at $z > 6$ is matched by a similar evolution in the UV luminosity density. They also find a faint end-limit of $M_{UV} < -13$. Agreeing with Kuhlen and Faucher-Giguère [2012], they acknowledge the possibility of evolution in ξ_{ion} or f_{esc} and that $z > 6$ galaxies are more efficient at releasing Lyman-continuum radiation. This matches current observations as spectroscopic analysis of a galaxy at $z = 7.05$ showed a value of ξ_{ion} larger than normal [Stark et al., 2015].

1.5.1 Observational constraints

Currently, there are only a few observational constraints on the epoch of Reionisation. One is the measurement of the Thomson scattering optical depth of the primordial CMB photons. Another is the Lyman-α forest at $z \approx 2.5 - 6.5$. Other less powerful observational constraints include the intergalactic medium at $z \lesssim 6$, Ly-α emitters and Gamma Ray Bursts. Below we focus on the first two constraints.

The Thomson scattering optical depth can be related to a redshift during which Reionisation occurred. This process is complete by $z \sim 6$. A value of $\tau = 0.088$ of the CMB, and HeII reionisation at $z \sim 3$ with $\tau = 0.044$ leave half of the observed optical depth, $\tau \approx 0.043$. This is explained by ionisation at higher redshifts, which likely requires an epoch of partial ionisation [Pritchard et al., 2010, Shull et al., 2012]. Consequently, a value of $\tau = 0$ implies no reionisation, while larger values imply early

Reionisation. The first detection of τ was made by the Wilkinson Microwave Array [WMAP; Spergel et al., 2003] by measuring the CMB polarisation. Previously, only lower limits had been set by measuring the Lyman-α absorption in quasars [Pryke et al., 2002, Fan et al., 2006].

The latest value of the Thomson scattering optical depth is of $\tau = 0.054 \pm 0.007$ [Planck Collaboration et al., 2018]. Combined with other measurements, this favours a late and fast reionisation. The Universe is entirely ionised by $z \sim 6$, but less than 10% of it is ionised by $z \sim 10$. This corresponds to a period of ~ 450 Myr. The previous measurement was $\tau = 0.058 \pm 0.012$ [Planck Collaboration et al., 2016]. Although a useful constraint regarding the evolution of the Reionisation process, the Thomson scattering reveals little information about the responsible sources, its duration or how it propagated to fill the whole Universe.

According to the last measurements of Planck Collaboration et al. [2018], instantaneous reionisation occurs at a redshift of $z_{reion} = 7.68 \pm 0.79$. It is important to note that instantaneous reionisation is a theoretical term in which it is assumed that Reionisation happened in an instant, but this is only for the purpose of the models. This is unlikely to be how it happened, but it can be an approximation of the mean redshift of Reionisation. These results combined show that most of the reionisation activity takes place at $z \lesssim 15$.

The Lyman-α forest at $z \approx 2.5 - 6.5$ also provides constraints for the Epoch or Reionisation. Discrete absorption features in the spectra of quasars should be observed if residual regions of neutral hydrogen are present. This is the so-called Lyman-α forest. Studies have shown that quasars at $z \leq 6$ have a complete Gunn-Peterson trough. This indicates that Reionisation is complete by $z = 6$.

Mitra et al. [2015] use the values found by τ from Planck Collaboration et al. [2016] and combine it with observations of high-redshift quasar absorption spectra, finding that reionisation is almost complete for $5.8 \lesssim z \lesssim 8.5$.

1.6 Luminosity Function

The luminosity function can be defined as the number density of objects as a function of luminosity. Constraining the galaxy luminosity function is important as it can provide an insight to the populations of galaxies at different redshifts. Consequently, we will be able to better understand galaxy evolution, star formation history, and the roles of galaxies in processes such as Reionisation. Ultimately, this can help us understand our

own Milky Way's formation.

Formally, if $\tilde{\phi}(L)dL$ is the number of galaxies per unit volume for a given luminosity range $[L, L + dL]$ at a given redshift, the total density of galaxies ν can be defined as:

$$\nu = \int_0^\infty \tilde{\phi}(L)dL. \tag{1.28}$$

The relation between absolute magnitude and luminosity is:

$$M - M_\odot = -2.5\log_{10}\left(\frac{L}{L_\odot}\right) \tag{1.29}$$

where M is the bolometric magnitude of an object, $M_\odot$ is the magnitude of the Sun, L is the luminosity of the same object, and $L_\odot$ is the luminosity of the Sun. The absolute magnitude is defined as the intrinsic magnitude of a source as if it was placed at a distance of 10 pc away from Earth.

We can use equation 1.29 to re-write equation 1.28 in terms of magnitude, which is what we will use throughout this chapter,

$$\nu = \int_{M_{min}}^\infty \phi(M)dM, \tag{1.30}$$

where M_{min} is the lower limit for a galaxy's magnitude, which is un uncertain value, and

$$\tilde{\phi}(L)dL = \phi(M)dM \tag{1.31}$$

The parameter $\phi(M)$ corresponds to the differential luminosity function, and it is different from the integrated luminosity function, $\Phi(M)$. They are related by

$$\Phi(M) = \int_{M_{min}}^M \phi(M')dM' \tag{1.32}$$

Throughout this study, we will use the term *luminosity function* to refer to $\phi(M)$.

1.6.1 Schechter

The shape of the luminosity function for galaxies has been historically described in an analytic manner by the empirical relation defined by Schechter [1976]:

$$\tilde{\phi}(L) = \left(\frac{\phi^*}{L^*}\right)\left(\frac{L}{L^*}\right)^{\alpha} \exp(-L/L^*), \tag{1.33}$$

where ϕ^* is a number per unit volume that specifies the normalisation of the distribution; L^* is a characteristic luminosity above that marks the transition between an exponential distribution (bright galaxies), and a power law (faint galaxies), α being the slope of the latter or also called faint-end slope; these three parameters describe the shape of the curve, and they can be determined by the observed data.

In order to express the LF in absolute magnitude, equations 1.28, 1.29, and 1.30 can be combined and rearranged, obtaining:

$$\phi(M) = 0.921\phi^* 10^{0.4(\alpha+1)(M^*-M)} \exp(-10^{0.4(M^*-M)}) \tag{1.34}$$

Equivalent to L^*, M^* is the characteristic magnitude at which a break is produced and the slope of the distribution starts to decrease exponentially for brighter galaxies. Figure 1.3 shows the Schechter function plotted for three different values of the slope $\alpha = -1, -2, -3$, for $M^* = -21$ and $\phi^* = 5 \times 10^{-6}$.

Colloquially, the part of the luminosity function with galaxies more luminous than M^* is referred to as the bright end, while the part with galaxies dimmer than M^* is known as the faint end. Both ends of the luminosity function present challenges in terms of observations. As it can be seen, galaxies in the bright end are less abundant, therefore wider areas of the sky are needed in order to find them. On the other hand, deeper surveys are necessary for the faint end.

The Schechter function has proven to be accurate for field galaxies in several surveys, regardless of the nature of the galaxies. In the past, surveys with thousands of low redshift galaxies have fitted Schechter functions reasonably well to their data. Some examples include the Stromlo-APM survey [Loveday et al., 1992], CfA Redshift Survey for all the galaxies [Marzke et al., 1994b] and for different morphological types [Marzke et al., 1994a], and Las Campanas Redshift Survey [Lin et al., 1996], among others. This work has been extended nowadays to higher redshift galaxies, with the Schechter

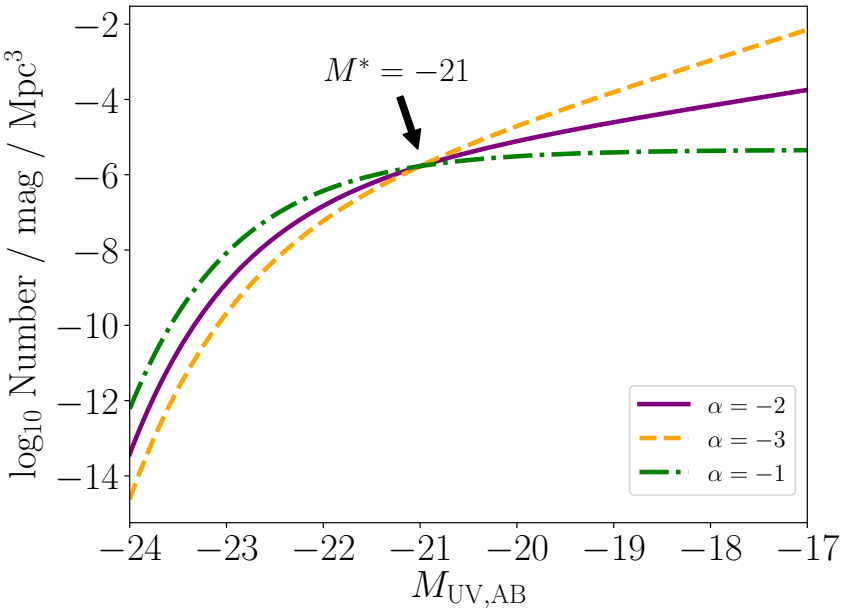

Figure 1.3: Schechter function for three different values of the slope $\alpha = -3$ (yellow dashed line), $\alpha = -2$ (purple solid line), and $\alpha = -1$ (green dashdotted line). The value for M^* is -21, and ϕ^* is 5×10^{-6}.

function still being the most popular fit [e.g. Bouwens et al., 2015b, Bowler et al., 2015, Finkelstein et al., 2015], although alternative functional forms have been proposed too [e.g. Bowler et al., 2015, Ono et al., 2017].

1.6.2 Applications

The statistical nature of the luminosity function makes it suitable for the study of galaxy populations. In fact, it can be seen as a snapshot of galaxy populations at a certain time. This allows for a wide range of applications related to the evolution and formation of galaxies. As described in the famous paper by Schechter [1976], and in the review of Binggeli et al. [1988], the applications include the determination of the mass density within a certain space provided that the dependence of mass on luminosity is specified [e.g.: Shapiro, 1971, Pérez-González et al., 2003]; the estimation of spatial clustering by converting the observed angular correlation function [e,g,: Skibba et al., 2014, Farrow et al., 2015]; and the estimation of the number of intervening absorbers at a certain redshift that produce the Lyman-α forest in high-redshift quasars or galaxies [e.g.: Bahcall, 1975, McQuinn and White, 2011]; among others.

In addition to offering the opportunity of photon budget counts to infer information

about the Epoch of Reionisation, the differential evolution of continuum versus line emission (Ly-α) luminosity functions can probe reionization in a powerful way. This is very relevant nowadays due to larger samples of galaxy candidates within the redshift range at which the Reionisation process was finishing [e.g. Bradley et al., 2012, Schmidt et al., 2014, Calvi et al., 2016] and recent discoveries of galaxies at redshifts close to the beginning of it [e.g. Coe et al., 2013, Zitrin et al., 2014, Oesch et al., 2016]. The information obtained from the luminosity function can shed some light on the Reionisation period, for which most of the details of its mechanisms are still unknown. For instance, the attenuation in observed galaxies during the late stages of this period can give us clues about the intergalactic neutral hydrogen content, a key feature of the end of the Reionisation epoch [Dijkstra et al., 2007]; parameters such as the hydrogen fraction and the Thomson scattering optical depth can also be calculated [e.g.: Ishigaki et al., 2018]; as well as constraining the size distribution of HII regions from the distribution of Lyman-α galaxies [Furlanetto et al., 2006]. Other measurements and constraints of parameters can be obtained from studies of the Lyman Break Galaxies combined with quasars and CMD measurements for a better picture, as it is done in Greig and Mesinger [2017].

To summarise, the luminosity function presents a neat alternative to measuring the evolution of a single galaxy across time, which is unfeasible; or to infer the galaxy star formation history with a high level of details, which is challenging for distant objects near the detection limit of telescopes. Instead, it is possible to measure statistical properties of populations of galaxies across different epochs and compare them [e.g.: Blanton et al., 2001]. However, obtaining the luminosity function of certain objects such as quasars or stars is not a trivial task. For this to be done, a large unbiased sample of a portion of the sky is needed, which is difficult and is limited by a variety of factors. For example, reaching faint magnitudes is a strong limitation.

Star Formation Rate

The Star Formation Rate (SFR) can be defined as the mass of stars formed per unit time in galaxies. The formation of stars occurs over a finite period of time, therefore it is expected to change with redshift. Several efforts have been made in order to constraint the SFR across the history of the Universe.

The SFR can be estimated from the light emission of the galaxies at different wavelengths, and it is equal to the luminosity in a particular wavelength divided by a factor whose value depends on said wavelength. This is because different parts of the elec-

tromagnetic spectrum are sensitive to different ranges of stellar masses, types, and processes occurring in the galaxy. To understand the full picture of the SFR across times, the idea is to trace the evolution of the light emission from the far-UV to the far-IR of the galaxy population as a whole.

The results of SFR have large uncertainties, and they need to be corrected for certain phenomena. The presence of dust has a large impact and should be taken into account when calculating the SFR. For example, the UV light in galaxies is absorbed by dust in the star-forming regions and in the interstellar medium. In fact, only a small fraction of UV-photons are detected, having to apply correction of up to a factor of 5 in order to estimated the SFR from this light. The amount of dust absorption is also proportional to the FIR luminosity, a phenomenon that needs to be considered in the corrections as well.

For an individual galaxy, the star formation rate can be estimated from its luminosity [Kennicutt, 1998]. Studies such as Lilly et al. [1996], Madau et al. [1998], Kennicutt [1998], among others were pioneers in this matter. The procedures to do this are based in two principles.

- The UV light is a popular indicator of the SFR and it is frequently used for high redshift galaxies due to the observed wavelength. In a galaxy with significant ongoing star formation, this is dominated by short-lived massive stars, and is therefore nearly independent of the galaxy history. This process dominates the galaxies' UV-continuum. Therefore, the UV light from galaxies is used as a traces or star formation.

- Surrounding dust is absorbed and heated by young stars and it then radiates in the FIR. Therefore, FIR can be used as a tracer of star formation.

As summarised in Madau and Dickinson [2014], the conversion factor between the intrinsic Far Ultraviolet (FUV) specific luminosity L_ν(FUV) (before extinction, or corrected for extinction) and the global star formation rate can be expressed as

$$SFR = \kappa_{FUV} \times L_\nu(\text{FUV}). \tag{1.35}$$

Where κ_{FUV} is the conversion factor, and it depends on the history of star formation, metallicity, initial mass function and the exact FUV wavelength.

With the corresponding conversion factor, the same can be done for the Infrared

emission. This way we can obtain the total star formation rate,

$$SFR_{tot} = \kappa_{FUV} \times L_{\nu}(\text{FUV}) + \kappa_{IR} \times L_{\nu}(\text{IR}). \tag{1.36}$$

Following the same idea, the star formation rate history of the Universe can be estimated from the luminosity function by integrating over it to get a total luminosity from all galaxies at a certain wavelength. This is typically done in the UV because at higher redshift it can still be observed. Apart from the aforementioned dust correction, another key ingredient to calculate SFR is the initial mass function (IMF), which corresponds to the initial mass distribution at the time of birth of stars. The total SFR can be estimated by adopting an IMF to connect it to the UV/FIR emission.

The star formation rate density (SFRD or ψ) is the SFR per unit comoving volume. As a function of redshift, it indicates how much mass in the form of stars has been created at any time. The star formation rate density can be inferred from a luminosity-weighted integration of the relevant luminosity functions across time.

Using the analogue equation to 1.35 for the IR in conjunction with equation 1.36, the star formation rate density can be obtained.

Despite the big efforts, the star formation history of the Universe has not yet been fully constrained. A recent attempt was completed by Madau and Dickinson [2014], where they find that the star formation rate density peaked $\sim$ 3.5Gyr after the Big Bang, and dropped exponentially at z $<$ 1 (see Figure 1.4). However, all studies rely heavily on the assumptions made in order to correct from the observed samples to the full populations. This ultimately depends on the luminosity function, from which would have to be known for each redshift bin.

1.7 Galaxies at High Redshift

The study of galaxies at high redshift can shed light on the evolution of the Universe, the Reionisation process, formation of first galaxies, among others. Therefore, finding these galaxies is an important task. In the last decade, there has been an important improvement regarding the redshift of the galaxies we are able to find, with redshifts of $z \sim 11$ as the current limit. However, these are limited cases, and even for galaxies at $z > 7$, it is believed we are missing a non negligible fraction of galaxies.

Studies of individual sources at $z > 7$ are extremely difficult with currently available technology, for which the statistical studies are more frequent. Furthermore, in order

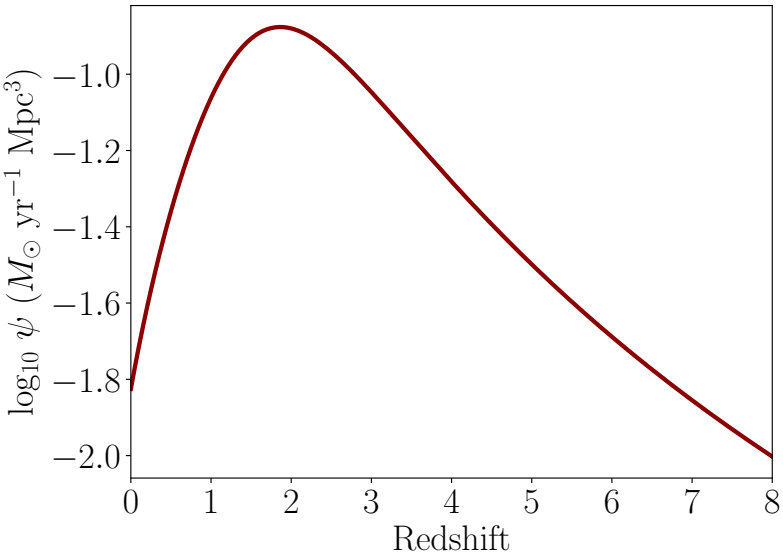

Figure 1.4: History of cosmic SFRD according to Madau and Dickinson [2014]. The red line shows the best fitting function to all the data collected for SFR at different redshifts.

to understand global phenomena, the study of the luminosity function, which requires a census of galaxies, is more appropriate.

Finding galaxies and counting them is important, but in order to characterise the galaxy population, we also need to account for the sources that we are missing. In order to do that, completeness simulations are performed. These allow us to estimate the efficiency of galaxy surveys and selection techniques by placing mock galaxies in the survey images and analysing source detection rates. This is a crucial factor in measuring the luminosity function with precision.

1.8 Thesis outline

As seen in this chapter, galaxies are fundamental in many important processes, particularly in Reionisation. Therefore, estimating the amount of galaxies during this time and their contribution to the process is very important. This is well constrained at lower redshifts. However, while large samples of photometrically identified galaxy candidates are now known at $z \lesssim 6$, at redshifts beyond this the Lyman break moves into the near-infrared, while the galaxies themselves rapidly become too faint for detailed spectroscopy. At high redshifts ($z \sim 8 - 10$) only a handful of robust high redshift candidates are known and only a few are spectroscopically confirmed. As a result the luminosity function of these galaxies is poorly understood. This motivates the work in

this thesis.

This project focuses on the development of an algorithm that estimates the completeness and source recovery in galaxy surveys. We create `GLACiAR` , an open python tool to estimate the completeness and selection function in multi-band imaging surveys. We also use a photometric selection technique in order to find galaxy candidates at $z \sim 10$ in Hubble Space Telescope galaxy surveys. We apply `GLACiAR` to these galaxy surveys and use the results combined with the galaxy candidates we find in order to constrain the bright end of the luminosity function at $z \sim 10$.

The outline of the thesis is as follows. We first describe high-redshift galaxies in Chapter 2, with an overview on their formation history, observed properties, and selection techniques. In Chapter 3 we describe some important galaxy surveys carried out mostly with the Hubble Space Telescope. We focus on the surveys BoRG and RELICS, for which we perform a photometric search in order to find $z \sim 10$ galaxy candidates. In Chapter 4 we introduce the the completeness simulation code we have written and explain the details. Chapter 5 presents a review of the galaxy luminosity function at high-redshift, with focus on its current state. We also apply our code `GLACiAR` to the galaxy candidates from 3 and calculate a point for the UV luminosity function at $z \sim 10$. Finally, Chapter 6 consists of a summary of the thesis and future work.

2

Galaxies at High-Redshift

High redshift galaxies present a unique opportunity to look into the past. Due to the finite nature of the speed of light and the expansion of the Universe, we are able to observe the light from these galaxies that originated at earlier times.

We can infer important information regarding processes such as star formation and Reionisation by studying galaxies. The development of new technologies in terms of observations and simulations has allowed us to push the frontier from our local Universe to the time at which galaxies first formed, at redshift $z \gtrsim 10$, when the Universe was approximately 500 Myr old.

Several efforts both observational and theoretical have been made in order to understand high redshift galaxies. Due to the challenges of studying objects at high redshifts, the next generation of telescopes is expected to produce important results and help constrain the properties of this epoch.

In this chapter, we give an overview of galaxy spectra and photometry and the main

techniques to find these galaxies. We also discuss some of the observed properties of high-redshift galaxies and recent results.

2.1 Galaxy spectra

To summarise the features of a spectrum we refer to Kirchoff's laws [Carroll and Ostlie, 2006]. They can be summarised as it follows:

- An object in the state of a hot solid or dense gas produces a continuous spectrum.
- A hot, diffuse gas produces emission lines.
- A cool, diffuse gas between a source of continuous spectrum and the observer produces absorption lines.

Through the analysis of the lines in the spectrum of a source, one can determine the gases in it or in the medium in which their light propagates. The characteristic atomic and molecular features are referred to as emission or absorption lines. Because of the Doppler effect and the expansion of the Universe, photons coming from distant sources are redshifted (see equation 1.12).

In the case of galaxies, one can expect a spectrum composed of a superposition of the stars within the galaxy. Further, emission and absorption lines are also expected, as products of the interstellar and intergalactic media. Exact features of the spectral light distribution depend on the properties of the galaxy.

The continuum radiation component of galaxy spectra originates from the blackbody spectra of stars and, consequently, its shape varies for each galaxy. This continuum lies under absorption and emission lines that are present in galaxies. For example, some galaxies present a break in the spectrum, which is called Balmer break ($\lambda = 4000$Å). This appears in the spectra of cooler stars from late-B and beyond due to their cool emissions. Hotter stars, on the other hand, are strong emitters of UV radiation. Elliptical galaxies present a strong break at said wavelength, which is caused by the their characteristic lack of hot stars, and a blanket absorption of high energy radiation from metals in stellar atmospheres. The continuum below the Balmer break comes from late-O and early-B stars [Leitherer, 2009].

Another important component of galaxy spectra is the Lyman-continuum (LyC). It corresponds to the photons that are emitted at a wavelength of $\lambda < 912$Å. As seen in Section 1.5 these are the photons that ionise the media. They are absorbed by hydrogen, helium, and dust in the interstellar medium of the galaxy. The fraction of

these photons that escape is the f_{esc}, which is a crucial part of many fundamental processes such as Reionisation. According to Leitherer et al. [1999], $\sim$ 10% of the luminosity radiation emitted by a standard star-forming galaxy comes from this section. Following we describe two important features of high-redshift galaxies, which are used in order to find them both spectroscopically and photometrically.

2.1.1 Lyman-α emission line

The Lyman-α line originates from the Lyman series, which is a series of radiative transitions in the hydrogen atom produced by electrons going from a higher level (orbital $n \geq 2$) to the ground state ($n = 1$). Specifically, the Lyman-α emission line is produced by the spontaneous decay from $n = 2$, the first excited state, to $n = 1$.

The Lyman-α line is resonantly scattered. Resonant scattering occurs when the energy of a photon matches the energy difference between the ground state and the lowest excited state of an atom. Afterwards, the atom de-excites, an another photon with the same energy is scattered. In the case of Lyman-α, the energy difference between the levels is of 10.2eV, which corresponds to a wavelength of $\lambda = 1215.67$Å.

The Lyman-α transition is the most basic transition of the hydrogen atom, and therefore this emission line is ubiquitous in astrophysical objects. Whenever photons with the corresponding energy are around, this line is produced.

Tracing cosmic hydrogen through its Ly-α emission has been done for a long time in Astrophysics. This emission provides an important probe for studying the distribution and properties of the neutral, atomic hydrogen in the local interstellar medium. It carries information about the column density and velocity distribution of the hydrogen atoms [Brasken and Kyrola, 1998].

As summarised by Dijkstra [2014], the Lyman-α emission line can be produced by two phenomena.

- Ionising radiation, which is emitted by type O and B stars. These photons ionise the dense gas surrounding them. When this gas is recombined, an important fraction of this recombination radiation emerges as the Lyman-α emission line. Therefore, this line is a tracer of young stellar populations or star forming galaxies.

- Photons emitted by collisionally excited HI, which is also referred to as *cooling radiation*.

In galaxies, the first phenomenon seems to be dominant, although it has been suggested that it becomes less relevant at higher redshifts. Some hydrodynamic simulations have found that the cooling radiation can be of up to $\sim 50\%$ at $z \sim 6$ [Dayal et al., 2010, Yajima et al., 2012]. However, these values are difficult to constrain and very sensitive to measurement parameters.

The lack of the Lyman-α line indicates the presence of neutral hydrogen as interstellar HI clouds are extremely opaque to it. The Ly-α photons can be absorbed and scattered many times in these clouds. Consequently, there is a high probability that these photons get absorbed by dust grains in evolved galaxies.

As we previously saw, a key estimator for Reionisation is the measurement of Lyman-α emission from galaxies, since the lack of their detection implies that the intergalactic medium surrounding them is neutral. The observed drop in the fraction of galaxies exhibiting Lyman-α emission can indicate a rapidly evolving intergalactic medium neutral fraction.

2.1.2 Lyman-alpha forest

The light from the galaxies travels towards us throughout the Universe, hence any medium the photons pass through imprints information about its gases and chemical composition. Most of the lines present in the Lyman-α forest are produced by neutral hydrogen present in the intergalactic medium, which means that the absorption occurs at a rest wavelength of $\lambda = 1216$Å, but we observe them at different wavelengths depending on their redshift. Figure 2.1 shows a diagram of the spectrum of a galaxy with Lyman-α emission and some absorption lines produced by neutral hydrogen in the intergalactic medium. If the galaxy is at a redshift high enough, the light will encounter so many of this neutral hydrogen that the absorption lines will eventually produce the Lyman-α forest.

Resonant scattering occurs at the wavelength of Lyman-α. This is broadened into the Gunn-Peterson trough [Gunn and Peterson, 1965] by both the velocity distribution and width of the line. The latter is the dominant effect, causing an extension of the absorption towards the red side [Miralda-Escudé, 1998].

The absorption is produced by the Lyman-α transition of neutral hydrogen as it has a large cross-section. It is called a forest as the sharp absorption lines resemble one in the spectrum. This forest is observed in quasars as well as in galaxies. The clouds that produce the absorption lines become more common at high redshifts so the absorption

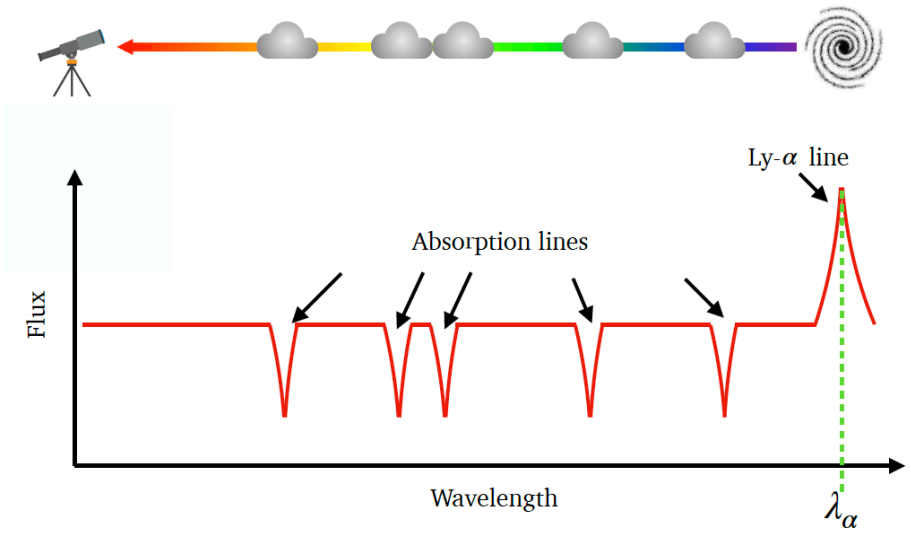

Figure 2.1: Diagram of a galaxy spectrum with a Lyman-α emission line and absorption lines. The emission line is produced in the galaxy at $\lambda_\alpha = 1216$Å and it is observed at a redshifted wavelength. The absorption lines are produced by neutral hydrogen (clouds in the diagram) in the intergalactic medium between the galaxy and the observer. They are also produced at a rest wavelength of $\lambda_\alpha = 1216$Å, but are observed at different wavelengths because of their redshift. These absorption lines will eventually produce the Lyman-α forest if the galaxy is at a redshift high enough for its light to encounter enough of them in its path to the observer.

lines become more dense resulting in the Lyman-α forest. Several studies have been performed in order to study the Lyman-*alpha* forest and its evolution [e.g. Kim et al., 1997, Riediger et al., 1998, Bolton et al., 2017]. As a matter of fact, it has been found that its density increases with redshift by $\sim (1+z)^{2.2}$ [e.g., Kim et al., 2001]

As illustrated in Schneider [2015], the Lyman-α forest can be subdivided depending on the depth of absorption, which also depends on the size of the column density of neutral hydrogen (N_H) that produces the absorption:

- Narrow lines, $N_H \lesssim 10^{17} cm^{-2}$.

- Lyman-limit systems, $10^{17} cm^{-2} \lesssim N_H \lesssim 2 \cdot 10^{20} cm^{-2}$. As we will expand on later, if $N_H \gtrsim 10^{17} cm^{-2}$, neutral hydrogen absorbs most of the radiation at a wavelength of $\lambda \lesssim 912$Å. This wavelength corresponds to the photons capable of ionising hydrogen. Anything below this limit will get absorbed, thus the name of these systems.

- Damped Lyα systems, $N_H \gtrsim 10^{20} cm^{-2}$. This type of hydrogen produces a broad absorption line.

2.1.3 Lyman-α emitters

As indicated by its name, a Lyman-α emitter (LAE) is a young galaxy that emits Lyman-α radiation. A prevalent fraction of their overall light emitted shortwards of Lyman-α is reprocessed into the line which hence outshines the continuum by a significant margin. The UV part of their spectra is very bright with not much obstruction by dust.

An abrupt reduction of the detected Lyman-α flux has been consistently measured at $z > 6$. This emission is stronger with redshift up to $z \sim 6$, but it decays afterwards [Stark et al., 2010, Caruana et al., 2012]. This can be related to the Reionisation process as this would absorb the emission radiated. However, more studies are needed in order to draw a strong conclusion.

2.2 Selection Techniques

The techniques used for finding high-redshift galaxies will depend on the type of galaxies, the data set, and the filters available, among other factors. The majority of selection techniques are based on spectroscopic information of the objects. As previously discussed, the spectra of astronomical objects provide the information needed to study a source. Therefore, any method that classifies astronomical sources relies on their spectral characteristics, even if they cannot be measured in detail, i.e., even if the electromagnetic spectrum is not directly observed.

Photometric or imaging techniques study the sources in a certain band that corresponds to a particular wavelength range in the spectrum. The magnitude observed in a band is ultimately the flux emitted by the object in that range of the spectrum. This provides information about particular features of the spectrum, and information such as the redshift and chemical composition can be inferred.

An important difficulty for performing photometry is Earth's atmosphere, which presents regions opaque to certain wavelengths where most of the light is absorbed, and produces scattering. The atmosphere is transparent to only a small percentage of the electromagnetic radiation, presenting only a few *atmospheric windows*, one big one in the optical range and several small ones in near and mid-infrared ranged. Most of the night-sky background in the red and hear infrared is due to airglow produced by OH radicals in the high atmosphere and consequently the photometry filters are modelled to correspond with the atmospheric windows.

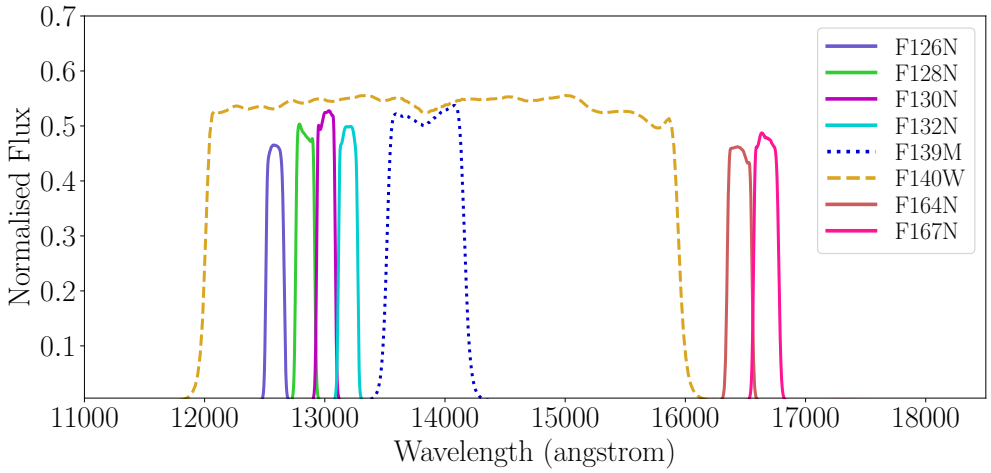

Figure 2.2: *Hubble Space Telescope* WFC3 IR transmission curves of the narrow filters F126N, F128N, F130N, F132N, F164N, and F167N. For comparison, we show a wide filter, F140W (dashed gold line), and a medium filter, F139M (dotted blue line).

As expected, this field has had advances tied to the improvements of observational technology. The launch of the *HST* and, in particular, the installation of WFC3, have yielded many high-z galaxy candidates, with the amount of candidates dramatically growing in the last decade. Below, we describe the most commonly used methods to find high-redshift galaxies.

2.2.1 Narrow-band Photometry

This is an imaging technique that relies on the detection of the emission lines. This technique involves taking images in a narrow-band filter and at least one other broad band filter, or another close narrow-band filter, and comparing them. Depending on the redshift that the survey is targeting, the target emission lines are different as well, H-α, [OII], and Ly-α. For high-redshift galaxies, the filters tend to fall near the infrared. Figure 2.2 shows six narrow IR filters from the Wield Field Camera 3 (WFC3) from *HST*. Along with them, a medium and a wide filter are in the plot for comparison.

After having the same area of the sky surveyed with both - or more - filters, they are then compared. If the object is exceedingly bright in the narrow filter, it suggests the existence of an emission line. At high redshift, this technique is highly dependent on the design of the narrow band filters as the wavelength at which the observations would fall around $\sim 9000 - 10000\,\text{Å}$ for a galaxy at $z \sim 7 - 8$.

Due of the narrow wavelength they cover, the redshift range they encompass is small,

which translates into a smaller cosmological volume of the observed field. This also makes them less effective in terms of the amount of galaxies they can find. Another disadvantage is the fact that this technique is only capable of finding a particular population of high redshift galaxies, which is the one that presents strong Lyman-α emission in the majority of cases for high-redshift galaxies.

In terms of the advantages, Mesinger and Furlanetto [2008] mention the reduction of the sky background, the efficiency in selecting galaxies at a known redshift, and the higher signal-to-noise ratio by focusing on an emission line. Because it relies in the identification of an emission line, the ratio of spectroscopic confirmation is high, but the samples of these galaxies is biased.

Narrow-band photometry has been used successfully for lower redshift galaxies, mainly for searches up to redshift $z \sim 6$ [e.g. Steidel et al., 2000, Ouchi et al., 2003, Malhotra and Rhoads, 2004]. For example, Ouchi et al. [2003] used it to find LAEs at $z \sim 4.8$. Furthermore, galaxies in the redshift range between $z \sim 5-7$ have been mainly found with this technique, such as Ouchi et al. [2010] who studied LAEs at $z = 6.6$ from the Subaru/XMM-Newton Deep Survey field, where they use a narrow-band filter, $NB921$, with a central wavelength of $\lambda_c = 9196\,\text{Å}$ and a FWHM of $132\,\text{Å}$. However, for higher redshifts, $z \gtrsim 7$ the success rate of this technique dramatically decreases.

A major disadvantage of narrow-band photometry comes from the opacity of Earth's atmosphere. The atmospheric windows mentioned above only allow for certain wavelengths to be observed, which translates into galaxies at only certain redshift ranges that can be identified with this technique. The identification of the Lyman-α line is possible for galaxies at $z \sim 4.5, 5.7, 6.5, 7.7, 7.9, 8.1, 8.8, 9.8$, and 10. The redshift ranges in between are not visible from the ground, from where the narrow-band surveys have been carried out.

2.2.2 Lyman-Break Galaxies

Technically, Lyman-Break galaxies are galaxies that are selected by using this technique. These galaxies are at redshift $z \gtrsim 3$, where the far-UV spectrum is observed at optical wavelengths. They are characterised by a break in their spectrum produced by absorption, the Lyman break. This is a discontinuity produced at $\lambda = 912\,\text{Å}$ by the stellar atmosphere of massive stars as a result of the hydrogen ionization edge. This break is accentuated by the photoelectric absorption of the interstellar HI gas, which is abundant in young galaxies, and by intervening HI gas. The Lyman-α forest also contributes to this break in the rest range of $\lambda = 912 - 1216\,\text{Å}$, making it more pronounced

for galaxies at $z \gtrsim 4$ [Giavalisco, 2002].

The nature of LBGs is expected to be associated with starburst galaxies. A characteristic feature of their spectra is a strong UV continuum emission caused by the formation of massive young stars of type O and B, which suggests recent star formation episodes. They also present strong interstellar absorption lines due to low ionisation stages of C, O, Si, and Al, and of prominent high-ionisation stellar lines of HeII, CIV, SiIV, and NV [Giavalisco, 2002].

In their spectrum there are strong interstellar absorption lines due to low-ionisation stages of metals, and high-ionisation stellar lines. The identification of these lines can help the spectroscopic confirmation of Lyman-Break galaxy candidates. Even if the Lyman-α line is not present due to Reionisation. Observations show that the fraction of LBGs with strong Lyman-α emission increases up to $z \approx 6$ [e.g., Stanway et al., 2003].

Some studies have been performed on populations of LBGs at different redshifts to study their evolution. For example, Vanzella et al. [2009] performs a systematic study of LBGs at higher redshift, $z > 4$. They observe similar outflows than at lower redshifts. In general, spectra seem to change very little. [Stark et al., 2009] also studied these galaxies at higher redshift, $4 \lesssim z \lesssim 6$, and they don't find a strong evolution among the redshift bins, neither in stellar masses nor in the ages of galaxies. They also find that a likely scenario in terms of star formation is an episodic rate. That means that the star formation rate is increased during certain periods and it is not constant. Shapley et al. [2003] finds consistency with massive star formation related to the size of HII clouds. They also found evidence for gas for LBGs at $z \sim 3$.

2.2.3 Photometric Redshift estimation

As we saw have seen, galaxies present characteristic features in their spectra. With the spectroscopic observations of several galaxies, templates can be generated by putting the features of the galaxies together. These templates can then be fitted to observations of the galaxies and a redshift can be estimated according to these fits. In order to have good estimations, the more bands used the better the chance to estimate the redshift accurately.

When a substantial number of filters are used, this technique proves to be very effective. One of the highest redshift galaxies ever found [$z \sim 11$ Coe et al., 2013] was classified with this technique.

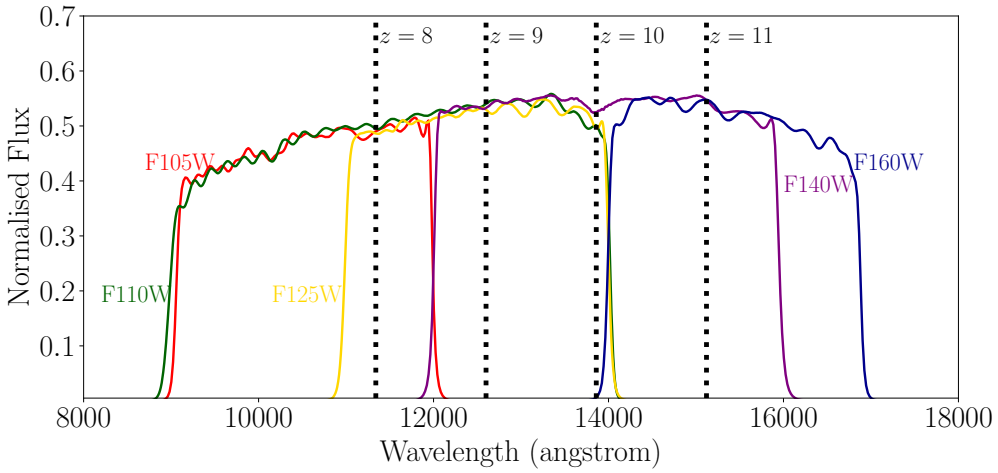

Figure 2.3: Transmission curves of *Hubble Space Telescope* WFC3 IR wide filters. The filters are F105W (red), F110W (green), F125W (yellow), F140W (purple), F160W (blue). On top of the filters, a dotted black vertical line indicates where the Lyman break would be produced at the corresponding redshift. Flux would be expected starting from that vertical line towards the right end of the plot (larger wavelengths).

2.2.4 Lyman break technique

Sometimes referred to as dropout *technique*, this selection method was first put into practice by Steidel and Hamilton [1993]. It has been by far the most successful technique in order to find high-redshift galaxy candidates in studies such as Hildebrandt et al. [2007], Bouwens et al. [2011], Bradley et al. [2012], and Calvi et al. [2016].

The technique is based in the discontinuity in the spectrum of galaxies below the Lyman limit (see Section 2.2.2). First, photons with $\lambda < 912\,\text{Å}$ are absorbed due to the ionisation of the hydrogen by the photons of massive hot stars present in host galaxies. Further, if the galaxy is far enough from us, there will be absorption between $\lambda = 912 - 1216\,\text{Å}$, which is produced by galaxies located between the emitting host galaxy and us. Therefore, it can be summarised as a search for objects that show little to no flux below those rest-frame wavelengths. The wavelength of the filters will dictate the redshift range of the selected galaxies. Figure 2.3 shows the transmission curves of five *HST* WFC3 wide IR filters. The dotted black vertical line shows where the Lyman-break is expected for the corresponding redshift. Flux from the galaxies is expected from that point to the right., i.e. at higher wavelengths.

In order to select galaxies with this method, three or more broad-band filters are needed. A generalised description of the method follows. Images are taken with three

filters whose central wavelengths are λ_1, λ_2, and λ_3, the last one being the so-called *detection band*. To optimise the search λ_1 should cover the region of the spectrum of $\lambda_{rest} \lesssim 912$Å, λ_2 should be situated in the range $\lambda_{rest} \sim 912 - 1216$Å to identify the Lyman-$\alpha$ forest, and $\lambda_3 \gtrsim 1216$Å, to measure the stellar continuum beyond the break. From here, there will be two colours available, C_1 and C_2, defined as $C_1 = m_{\lambda_1} - m_{\lambda_2}$, and $C_2 = m_{\lambda_2} - m_{\lambda_3}$. Based on templates or population synthesis models of star-forming galaxies, the expected colours can be calculated. The other condition, which is the one that gives the name to this technique is the requirement that no flux is found in λ_1. In the case of λ_2, depending on the redshift (and the Lyman-α forest associated with the redshift), flux can or cannot be present. On the other hand, flux must be observed in λ_3 as this is the detection band. Methods to ensure no flux is observed depend on the survey, but commonly relate to the signal to noise ratio. This technique can be extended to as many filters as available, with the more filters the better redshift estimation.

This technique has some similarities with the photometric redshift estimation technique. They both derive from galaxy spectra and its characteristics. However, they are not the same. Photometric redshift estimation uses templates of galaxies and fits them to the observed photometry. This is useful when many bands are available. Instead, the case of the dropout method is a better option when fewer bands available, and it relies in the Lyman-break phenomenon which is mostly based in only one characteristic of the spectra.

2.2.5 BzK

This method targets other populations of galaxies at redshift $1.4 \leq z \leq 2.5$. As previously summarised in Section 2.2.4, the Lyman-break colour selection method is better suited for galaxies that are actively forming stars. Therefore, the criteria for the dropouts will overlook other kind of galaxies; the galaxies with passive stellar population. In order to find these galaxies, a new criteria was introduced by Daddi et al. [2004], which is a selection based on three bands, the B-, z-, and K-band filters. By constructing a colour-colour diagram, $(B - z)_{AB}$ vs $(z - K)_{AB}$, it is possible to distinguish two populations. The B-band corresponds to the rest-frame UV part of the spectrum, therefore, the $(B - z)$ is expected to be higher for passive galaxies. The $\lambda_{emit} = 4000$Å Balmer break is located towards the red from the z-band. In the case of passive galaxies, the break is large, producing a redder colour, while for star-forming galaxies, it is weaker. Therefore, galaxies in the upper right corner showing red colours in both scales have an absence of star formation. On the other hand, the galaxies in

the upper left corner, characterised by a bluer $(B-z)$ and a weaker red in the $(z-K)$ colour, are actively forming stars.

This method has been applied in several studies, such as Daddi et al. [2005], Kong et al. [2006], McCracken et al. [2010], among others.

It is important to note that some star-forming galaxies can be found by this and the Lyman-break method. However, the most active galaxies are missed by BzK because of their $(z-K)$ colour since the 4000Å-break is not present in their spectrum.

2.2.6 Contaminants

The use of photometric selection techniques has been very successful and prolific for finding galaxy candidates. However, a further complication that must be considered in photometric samples is contaminants. As these objects are selected based on their colours, there is a non-negligible chance that sources of a different nature but with similar colours are selected. The main sources that can be wrongly classified as LBGs include emission line galaxies, stellar sources, and galaxies at $z \sim 2$ [e.g. Stanway et al., 2008, Bowler et al., 2012].

Stellar sources with low surface temperatures have similar colours to high-redshift galaxies and therefore pass the dropout criteria. Stars are point sources, while galaxies are extended. However, when the angular resolution is not high enough to resolve them, they look like point sources and can be mistaken for stars [Stanway et al., 2003, Bouwens et al., 2006, Ouchi et al., 2009]. At higher redshift $z \gtrsim 9$, however, the contamination from stars becomes negligible, specially with *HST*, with intermediate redshift galaxies the main source of contamination.

Several techniques have been proposed in order to avoid these contaminants. Some of them include the use of filters that do not overlap, as the colour can flatten out as a function of redshift in some redshift ranges when filters overlap [Stanway et al., 2008]; very deep observations blueward of the spectral break are also very helpful to distinguish between a true non-detection for an high-z object and a faint continuum for an interloper [Bouwens et al., 2015b].

Heavily obscured $z \sim 2$ galaxies show a break in the spectra that is not produced by many other kind of galaxies, except for heavily dust-obscured galaxies at about $z \sim 2$. Despite this, it is highly effective as these galaxies are not very common. Additionally, as pointed out in Giavalisco [2002], Balmer break galaxies at $1.3 \leq z \leq 2.5$ can mimic the colours of $z \sim 6$ galaxies in filters chosen to select the Lyman break.

Vulcani et al. [2017] performed an exhaustive study regarding contaminants in LBG selections at $z \sim 5 - 8$. They find that the dropout selection contains small quantities of contaminants. These numbers remain relatively constant across different samples, but as the redshift increases, the relative weight compared to the number of dropouts grows significantly as less candidates are detected.

An example is the recent study by Livermore et al. [2018], where they followed-up observations for two candidates from the sample by Calvi et al. [2016]. This followup involved the observation of the candidates with the F098M band from *HST*. One of these candidates showed measurements consistent with a high redshift galaxy, while the brightest object probed to be a more likely a galaxy at $z \sim 2$. This makes a difference in the luminosity function, where the fit presented by Calvi et al. [2016] was more consistent with a departure from the Schechter form. However, the removal of the brightest candidate shows a more consistent fit with a Schechter form.

Galaxy candidates can be discriminated by their size, which can help avoid contaminants. Holwerda et al. [2015] find that the interlopers have approximately 4 times larger sizes than the galaxies at $z \sim 9 - 10$.

Looking at the future and the at $z \sim 10$ galaxy candidates, we expect larger fractions of contaminants [Vulcani et al., 2017], of even $\sim 50\%$. In the case of *JWST* this should be solved by the ability this will have to observe efficiently at rest-frame optical wavelengths for sources at $z > 10$ and therefore making it easier to exclude contaminants.

2.2.7 Spectroscopy

Spectroscopic confirmation of high-redshift galaxies depends almost entirely in the detection of the Lyman-α line. As seen in Section 1.5, this line is attenuated by neutral hydrogen, making it difficult to be observed.

The way spectroscopy works is by observing the electromagnetic spectrum of the object and locating the emission lines, if applicable. When the lines are located, they can be identified in term of which emission line they are and then they can be compared to the rest wavelength. This way, the redshift can be calculated using equation 1.12.

This method is primarily used to confirm known galaxy candidates. Although in principle it is the most precise way of finding the galaxies, it is not widely used as such. This is because it requires much longer exposure times than imaging in order to get a reasonable signal-to-noise ratio. It also typically requires the previous knowledge of the position of the object within the field.

Jiang et al. [2017] used the Magellan telescopes in Las Campanas, Chile, in order to perform spectroscopy over a portion of the sky of ~ 4 square degrees previously observed by several surveys. Their campaign is expected to take spectra ~ 400 bright LAEs at $z \approx 5.7 - 6.5$, and a significant amount of LBGs at $z \geq 6$. So far, they have been able to take spectra of 32 bright LAEs. A campaign like this takes years.

Spectroscopy has proven to be difficult for galaxies at $z \gtrsim 7$ [e.g. Treu et al., 2012, González-López et al., 2014], with only a handful of confirmations out of hundreds of candidates. Those include Pentericci et al. [2011], where out of a sample of approximately 20 photometric candidates at redshift $z \sim 7$, they could just confirm the redshift of 5 of them, with only 2 of them having bright Lyman-α emission lines. This can be better explained in terms of a rapid evolution of the neutral hydrogen fraction from $z \sim 6$ to $z \sim 7$.

One of the complications of performing spectroscopy in high-redshift galaxies and that can account for a portion of the unconfirmed galaxies is because of the observations and their reduction. High spectral resolution cannot be used because then the emission is spread over too many IR detector pixels and the signal to noise suffers. On the other hand, when low resolution spectroscopy is used, a sizeable fraction of the spectrum is dominated by the residuals from night sky emission line subtraction which can wipe out any signal. This becomes a problem at $z \sim 6$ and worsens for higher redshifts.

This is the most reliable method, although especially when it comes to high-redshift galaxies, it can't always confirm or rule out the nature of the candidate. Confirmation can be complicated when it comes to high-redshift galaxies as the signal-to-noise is low, even with the long exposure times used. Another challenge that is presented when it comes to spectroscopy is that not the whole spectrum can be measured, but only a portion of it. Therefore, if the estimation of the redshift is too far off, the emission line won't lie within the observed range. Furthermore, the Lyman-α forest means that no emission or absorption line can be observed for wavelengths lower than the Lyman-alpha emission line, making detection available mainly for objects for which the Lyman-alpha line can be observed. Another issue is that the Lyman-alpha line can be sometimes compromised by the dust in the intergalactic medium.

In a recent study, Livermore et al. [2018] does a follow up observation of two candidates from Calvi et al. [2016]. They confirm one of the candidates as a probable $z \sim 8$ galaxy, and rule out the other candidate, which has an apparent magnitude of $m_{H160} = 24.81$. This was a very bright galaxy candidate for $z \sim 8$. The elimination of such candidate now brings the data of the bright-end of the LF down, closer to Schechter function, as opposed to previous claims from Calvi et al. [2016] that measured

a power-law decline for the bright-end of the LF at said redshift.

2.2.8 Samples and bias

Selection bias is an important issue that needs to be taken into account when performing systematic searches and using the results to characterise the high redshift galaxy population. Because of the colour cuts, some populations can be favoured. If, for example, there is any overlap between the red and blue filters, as between I814 and J110, the dropout colour as a function of redshift can flatten into a *colour plateau* [Stanway et al., 2008].

A thorough study into this issue by Stanway et al. [2008] conclude that the samples recovered with a LBG-based technique only select a certain kind of population, ignoring or missing others such as quiescent galaxies. Although this study focuses on galaxies at $z \sim 5$, it can be extended to galaxies at higher redshift. This is an important issue to consider when finding galaxy samples. This motivates our next chapter where we code a completeness estimator.

2.3 Luminosity Function of Galaxies

2.3.1 Evolution of the Luminosity Function with Redshift

Just as the galaxies and their properties evolve with time, the luminosity function is not constant for all redshifts as we can see in the changing values of parameters such as M^*, ϕ^*, and α. In order to understand galaxy evolution and formation in a global way it is necessary to have a picture of the statistical properties of galaxies across all times.

Regardless of the possible discrepancies in the shape of the luminosity function at high-redshift, the majority of studies still fit a Schechter function to it in order to understand whether there is evolution in the parameters with the redshift. Following this, most of studies we refer to use this fit and their corresponding parameters.

It is important to acknowledge that the luminosity function parameters vary even when samples at the same redshift are compared. This tells us that the redshift is not the only feature that affects galaxy evolution. We can see, for example, that magnitudes and sizes of the samples also play an important role. However, these are not physical properties of the galaxies but rather limitations of the samples. However, there are physical properties that determine different shapes of the luminosity function. The

type of galaxy, such as blue and red have a different evolution in terms of their luminosity function with redshift [e.g.: Faber et al., 2007]; the morphology of galaxies [e.g.: Ilbert et al., 2006]; and the environment in which they are immersed [e.g.: Xia et al., 2006]. Some studies have also researched the relationships between two or more of these features [e.g.: Mo et al., 2004, Tempel et al., 2011].

The picture of the relationship between the luminosity function of galaxies and redshift has developed with time as the capabilities of telescopes have improved. As expected, the first statistical studies for galaxies were performed using low redshift samples, limiting any statistical study to the present Universe. Not only was the redshift a limitation but so was the number of galaxies used in these studies. Johnston [2011] presents a summary of relevant low and intermediate redshift surveys and their results in terms of luminosity function parameters. We can see in that review that prior to the year 2000, most of the studies were performed with samples of galaxies at redshift $z \lesssim 0.2$ and samples with numbers well below 20,000 [e.g. Marzke et al., 1994b, Lin et al., 1996, Zucca et al., 1997, Folkes et al., 1999]. Consistently, efforts to reach higher redshifts ($z \lesssim 1.5$) had samples of up to 2,000 galaxies [e.g. Lilly et al., 1995, Ellis et al., 1996, Lin et al., 1999]. After this period, significant improvements were achieved, not only in the number of galaxies for these type of surveys, but also in the magnitudes and redshift ranges reached [e.g. Fried et al., 2001, Cohen, 2002, Wolf et al., 2003]. In the early 2000s there were considerable improvements and the frontiers were pushed to samples of above 100,000 galaxies for redshifts of $z \lesssim 0.2$, particularly successful with the release of SDSS [York et al., 2000]. Following, we highlight some of the main studies of the luminosity function of galaxies at low and intermediate redshifts organised by publication date. We then also present in more depth studies for high-redshift in Section 2.3.1.

Wolf et al. [2003] performed a study over $\sim 25,000$ galaxies in the redshift range $0.2 < z < 1.2$ for galaxies of different spectral energy distributions (SEDs). This study finds that the shape of the luminosity function does depend on the adopted SED type, but not on the redshift. They determine that up to $z \sim 1$ the shape does not change if a non-evolving given SED type is assumed. Furthermore, the redshift evolution of the values for M^* and ϕ^* depend on the SED type. Another important conclusion from this study is the fact that the evolution of the luminosity density depends substantially on the rest-wavelength considered. It is essential to consider this when comparing luminosity function fits among different redshifts. Accordingly, Wolf et al. [2003] estimates that for the optical bands B and r, the integrated luminosity remains constant between $z = 1.1 - 0.5$ and then drops by $\sim 30\%$ from $z = 0.5$ to $z = 0$. In the case of the near-UV, the integrated luminosity drops from $z \sim 1$ to $z \sim 0$ by a factor of six, with

a great part of that drop occurring for $z \lesssim 0.6$. This evolution is shallower compared to what was found previously [Lilly et al., 1995], but still within the earlier confidence limits. As we can see, the results are different depending on the rest-frame wavelength at which the measurements are performed. In agreement with these results, Loveday [2004] find significant evolution in the luminosity function of r-band selected galaxies from SDSS DR1 at redshifts $z < 0.3$, and Ilbert et al. [2005] find again a dependence with the bands on the evolution of the luminosity function for the redshift range of $z \sim 0 - 2$. The results found by this study for the bright end are also consistent with what is found by Wolf et al. [2003]. In case of the faint end, both studies disagree, which is attributed by the authors to the different selection methods. Ilbert et al. [2005] finds that the value of M^* changes with the rest-wavelength and the redshift which can be summarised as a stronger brightening with bluer luminosity functions. This study also finds a steepening of the slope α from $z = 0.05$ to $z = 1$, which is independent from the band.

As demonstrated by Wolf et al. [2003], the rest wavelength in which the luminosity function is measured can deliver different results. If the same telescope covering the same wavelength is used to observe galaxies at different redshifts, the rest wavelength at which galaxies are observed will be different. Therefore, in order to compare luminosity function results, it is of crucial importance to understand this and take it into account when comparing results at different redshifts. Because of telescopes capabilities, most of the low redshift galaxies are observed in the IR, while higher redshift galaxies are observed in the UV. The UV luminosity function has not been widely studied in the low redshift range due to the limitations by the atmospheric cut off, which requires these large area surveys to be made with space telescopes, which is very costly. At higher redshifts this same intrinsic wavelength range is observed in the optical or the IR. In Madau and Dickinson [2014], they compare recent results for both wavelength ranges, arriving at the following conclusions. First, that the IR luminosity functions cut off less steeply. Second, that the IR luminosity functions show higher luminosities in the bright end. This can be attributed to the fact that the dust content increases with larger star formation rates, inducing preferential obstruction in the brightest galaxies. It is important to clarify that the IR LF anf the UV LF fundamentally measure different properties. The former is an estimates the stellar mass function, while the latter measures the star formation rate distribution.

Gabasch et al. [2004] used a sample of $5,500$ galaxies in the redshift range of $0.5 < z < 5.0$. Their results show that the faint-end slope of the luminosity function does not evolve significantly with redshift, and it is constant within the confidence range. Depending on the bands used, the value varies between $\alpha = -1.07 \pm 0.04$ and $\alpha =$

-1.25 ± 0.03, but they find no evidence supporting a steeper slope ($\alpha \leq -1.6$) at $z \sim 3$ or $z \sim 4$, which differed from previous studies such as Steidel et al. [1999], and Ouchi et al. [2004]. In regards of the parameters M^* and ϕ^* they do find a more pronounced evolution with redshift. M^* becomes brighter with redshift, with a variation of ~ 3.1 magnitudes in the redshift range of $z \sim 0.5 - 5.0$ for the UV, and about 0.5 magnitudes fainter in redder bands. On the other hand, ϕ^* decreases a similar amount for all bands, being that about $\sim 80\% - 90\%$.

The first study that used the far ultraviolet (FUV) band, at 1500 Å from the *Galaxy Evolution Explorer Survey* [GALEX; Morrissey et al., 2007] to measure the luminosity function was Arnouts et al. [2005]. They used a spectroscopic sample of about 1,000 galaxies in the far ultraviolet band. The redshift range of the galaxies is $0.2 \leq z \leq 1.2$. They also use the HDF data to extend the analysis to $z = 3$. Their results show that there is a larger evolution for M^* in the range $z \approx 0 - 1$ than at a higher redshift range, $z \approx 1 - 3$. There is a strong dependency of this value with redshift. From $z \approx 1.2$ to $z \approx 0$, the value range is $-20.15 \leq M^* \leq -18.00$, reaching a $\Delta M^* \sim 2.0$. For the rest of the redshift values examined in that study, $1.75 \leq z \leq 3.5$, the evolution is smaller, with a difference of $\Delta M^* \sim 1.0$ and values $-21.1 \leq M^* \leq -20.3$. In regards to the faint-end slope, the results are weakly dependent on the redshift, with the values smaller (i.e., steeper slope) for higher redshift. Depending on the redshift bin and the detection method, the results cover the range $-1.65 \leq \alpha \leq -1.2$ for the redshift range $0.2 \leq z \leq 3.0$.

Dahlen et al. [2007] perform a study on the evolution of the UV luminosity function of galaxies aiming to estimate the star formation rate. They use data from the Great Observatories Origins Deep Survey [GOODS; Giavalisco et al., 2004], only including observations from GOODS South (GOODS-S). They study the luminosity function focusing on two rest-frame wavelengths, 1500Å and 2800Å. In the first, the redshift range is $0.92 \leq z \leq 2.37$. The characteristic magnitude they find goes approximately from $M^* \approx -19.5$ to $M^* \approx -20.5$, showing a strong evolution of about 1 magnitude. The faint-end slope is consistent with previous results, $\alpha = -1.48^{+0.34}_{-0.29}$. In terms of ϕ^*, the results are around $\phi^* \sim 2.9, 3.1, 3.3 \times 10^{-3}\mathrm{Mpc}^{-3}\mathrm{mag}^{-1}$, depending on the redshift bin. This evolution seems to flatten at $z \gtrsim 1.7$.

Oesch et al. [2010] measured the evolution of the UV luminosity function (far ultraviolet, 1500 Å) from the *Hubble Space Telescope* WFC3/UVIS data. This data has better resolution and fainter limiting magnitudes than *GALEX*, which was the only telescope used for these type of studies. Their galaxy candidates are in the redshift range of $z \sim 0.75 - 2.5$, and they were selected by estimating their photometric redshift in 13

bands for the lower redshift ones, and with the dropout techniques for the higher redshift ones. M^* becomes fainter by 1.5 magnitudes from $z \sim 2.5$ to $z \sim 0.5$, going from $M^* \sim -21$ at $z \sim 3$ to $M^* \sim -18$ at $z \sim 0$. The parameters α and ϕ^*, however, remain constant for the same redshift range, although ϕ^* actually shows a weak decline towards higher redshifts. The faint-end slope is considerably steep, with values of $\alpha \lesssim -1.5$, in agreement with what Arnouts et al. [2005] previously found. In the local Universe ($z \sim 0$) however, the faint-end slope seems to reach flatter values, of around $\alpha \sim -1.2$.

Cucciati et al. [2012] performed a study also in the FUV in the redshift range of $0.05 \leq z \leq 4.5$, but reaching fainter magnitudes than Arnouts et al. [2005] as they do not use *GALEX*. Instead, they use data from VLT, which allows for better resolution and deeper magnitudes. Their values for α are consistently larger than most studies as they present in their article, with values of $\alpha \sim -1$ for redshifts of $0 \leq z \leq 1.7$. At higher redshift, they find that the slope becomes steeper, reaching values of $\alpha \lesssim -1.7$, which is consistent with other studies reaching faint limiting magnitudes. They attribute the differences in the faint-end slope to the magnitude limit from their sample, which allows them to go fainter. In the case of the parameters M^*, for lower redshift, $0 \leq z \leq 1.2$, seem to not vary much, with values fluctuating between $M^* \sim -18.3$ and $M^* \sim -19.0$ in the FUV band and similar results for the NUV band up to $z \sim 0.6$, and being approximately 0.5 magnitudes brighter for $0.6 \leq z \leq 1.2$. At higher redshifts, the value keeps getting brighter, with values close to $M^* \sim -21.0$ in the FUV band, which is even brighter than previous works [e.g. Arnouts et al., 2005]. In the case of ϕ^*, it appears to reach a peak value of $\phi^* = 9.53 \times 10^{-3}\mathrm{Mpc}^{-3}$ at $z \sim 0.7$ for the FUV band, with a similar situation happening in the NUV band, only with a value of $\phi^* = 9.48 \times 10^{-3}\mathrm{Mpc}^{-3}$ at $z \sim 0.9$. It then declines up to $\phi^* = 1.72 \times 10^{-3}\mathrm{Mpc}^{-3}$ at $2.5 \leq z \leq 3.5$, equivalent to a reduction of a factor of ~ 40. This is lower than previous studies had found.

Alavi et al. [2014] studied a sample of strongly lensed galaxies at $1 \leq z \leq 3$, prioritising the intrinsic luminosity of the galaxy candidates over the number of objects in order to be able to reach deeper magnitudes. They had 58 Lyman-break galaxies in the magnitude bin of $-19.5 < M_{1500} < -13$, approximately a factor of 100 larger than previous redshifts at the same redshift. The maximum likelihood parameters show a value of $\alpha = -1.74 \pm 0.08$ for these galaxies with a redshift of $z \sim 2$. This is smaller than previously found by Cucciati et al. [2012], and slightly smaller but in closer agreement with Arnouts et al. [2005]'s results. In terms of M^*, Alavi et al. [2014] found a magnitude of $M^* \approx -20$, in close agreement with Cucciati et al. [2012] and Arnouts et al. [2005].

In summary, for low and intermediate redshifts, the faint-end slope seems to be con-

sistently steep, with values of $\alpha \sim -1.6$ for most studies. However, a few studies claim that this steepness is caused by the shallow nature of the samples, and the deeper samples would reveal larger values for α. Nowadays, most studies agree that for low redshift ($z = 1$ to today), the characteristic magnitude is fainter for lower redshift, and that these values depend on the rest-wavelength. [Beare et al., 2015]. In regards to ϕ^*, the consensus is that it has remained approximately constant in this same redshift range. Both parameters, M^* and ϕ^* show less consensus towards higher redshifts as exemplified above.

The infra-red luminosity functions show even less consensus, as the observations are not particularly powerful, even at $z \approx 1$ or $z \approx 2$. As Madau and Dickinson [2014] explains, *Spitzer* studies would only reach magnitudes barely fainter than M^* for these redshifts. Therefore, their estimations are not completely reliable. For example, in the far infra-red, the biggest disagreements come from the measurements of α, where the results vary considerably, with results going from $\alpha \sim -1.2$ to $\alpha \sim -1.8$.

In the past, there have discrepancies regarding the extent of the evolution of the luminosity function with redshift. For example, Madau et al. [1996] claimed to have found a difference in the luminosity functions at $z \sim 3$ and $z \sim 4$, which was later refuted by Steidel et al. [1999] where no evidence for the aforementioned evolution was found. Nowadays, we know the latter statement is true.

Shifting towards intermediate and high redshift, Ouchi et al. [2004] studied the UV luminosity function with a large sample of LBGs at $z = 4$ and $z = 5$ from the Subaru Prime Focus Camera [Suprime-Cam; Miyazaki et al., 2002]. They have a photometric sample of LBGs at $z = 3.5 - 5.2$ and derive its luminosity function at $\langle z \rangle = 4.0, 4.7, 4.9$. When comparing their results with the ones from $z = 3$ from Steidel et al. [1999], they found no significant variation between $z = 3$ and $z = 4$. However, they did seem to encounter a larger number of faint galaxies at $z = 4$, with a slope value of $\alpha = -2.2$, smaller than the value of $\alpha = -1.6$ from Steidel et al. [1999]. Even within a high uncertainty, Ouchi et al. [2004] also found that there seems to be an increase in bright galaxies with time, predicting more bright galaxies at lower redshifts. The characteristic luminosity they derived shows values of $M^* \sim -21$ to $M^* \sim -20$. Regarding ϕ^*, the values fluctuate between $\phi^* = 1.2 - 2.8 \times 10^{-3}\mathrm{Mpc}^{-3}$.

Iwata et al. [2007] used a sample of ~ 850 LBGs at $z \sim 5$ to study the UV luminosity function. Comparing with results from other articles [Ouchi et al., 2004, Gabasch et al., 2004, Takeuchi et al., 2005, Bunker et al., 2006], they found no significant change in the bright end for the number density from $z \sim 5$ to $z \sim 3$. On the other hand, they do find a slightly larger faint-end slope than previous works [e.g.: Ouchi et al., 2004], with

a value of $\alpha = -1.48$, which is more in agreement with what is found in Sawicki and Thompson [2006].

The bright end of the LF shows a significant evolution at $5 < z < 6$ [Stanway et al., 2003, McLure et al., 2009]. This evolution is not completely accounted for by the evolution in the normalisation parameters ϕ^*, requiring the evolution of M^* as well. This results are in agreement with subsequent studies such as Finkelstein et al. [2015] in the redshift range $z = 4 - 5$.

An interesting topic of discussion is the dependency among these parameters. The amount of variables means that a range of values can be valid and at least one of the parameters is fixed by the calculations. For example, Bouwens et al. [2015b] find results that are consistent with an evolution in both ϕ^* and α. However, they argue that with the current surveys, changes in ϕ^* and α can be interchangeable by changes in M^*.

All the aforementioned studies show the fact that even though the luminosity function is fairly well constrained at low and intermediate redshift, there are still discrepancies in the value of the parameters. This helps exemplify what happens at higher redshifts, where the limiting absolute magnitudes reached are considerably fainter than at lower redshifts. Consequently, studies will show more discrepancies in terms of the parameters and even the shape of the luminosity function, which motivates the next section.

Studies of high-z LF

Up to redshift $z \sim 5 - 6$, the parameters of the luminosity function have been extensively examined, with the shape showing no sign deviating from a Schechter function. However, due to the small size of galaxy samples towards higher redshift, the uncertainties are large and the measurements are not equally reliable. Furthermore, the samples can have larger fractions of contaminants. This, combined with the size of the samples make the results for the luminosity function more uncertain. For example, current photometric samples of $z \sim 7$ and $z \sim 8$ include hundreds of galaxies, and they are expected to have contamination levels of 7% and 10% respectively [Stark, 2016, Vulcani et al., 2017]. However, it is important to note that having a large sample is not enough to avoid biased measurements. The size of the area covered by these is important as well because of the cosmic variance [Trenti and Stiavelli, 2008], which can have a considerable impact in the estimation of the parameters for the luminosity function in deep high-redshift surveys.

Below we summarise some relevant studies about the measurement of the parameters

of the luminosity function.[1]

Different results have been found for high-redshift galaxies, with some studies suggesting that the luminosity function deviates from a Schechter shape following a double power law [e.g.: Bowler et al., 2015, O'Shea et al., 2015] or a single power law distribution. For example, Finkelstein et al. [2015] found that at $z = 8$ a single power law is as good a fit as the Schechter function. More recently, Ono et al. [2017] found an excess of bright galaxies in a study with galaxies in the redshift range of $z \sim 4 - 7$ which cannot be modelled by a Schechter function. What makes their results different, they claim, is that they are able to separate high-redshift AGNs from high-redshift galaxies. This study finds that a better fit is provided by a double power-law or a lensed Schechter function. Recent efforts have focused on the high-redshift end [e.g.: Bowler et al., 2015, McLeod et al., 2016, Ishigaki et al., 2018]. This has also been driven by the new galaxy candidates at high-redshift from galaxy surveys.

Studies about the high redshift luminosity function ($z \sim 7{-}8$) started to appear about ten years ago [e.g. Bouwens et al., 2008, Oesch et al., 2009, Grazian et al., 2011], and they were performed with only a handful of galaxy candidates. Over time the amount of galaxy candidates increased, currently with some candidates at redshift $z \sim 9 - 10$ [e.g. Bouwens et al., 2014, Calvi et al., 2016, McLeod et al., 2016], which has allowed us to place some constraints in the UV luminosity function at this redshift.

The steepness of the luminosity function for faint galaxies at high redshift ($z \gtrsim 6$) is of particular interest in our work as low-luminosity galaxies are expected to contribute considerably in the Reionisation process. The fraction of their contribution can be derived from the number of faint galaxies, which is dictated by the value of α. It is expected that the values are steeper at high redshift ($z \gtrsim 5$), but the value itself is not well constrained. Ishigaki et al. [2018] has found a very steep value ($\alpha \sim -2.0$) for a study performed on the galaxies of the HFF at $z \sim 6 - 10$. Other studies suggest a value closer to ($\alpha \sim -1.7$) [Bouwens et al., 2015b]. This, however, is even less reliable because as it was shown by Grazian et al. [2011], the results on the faint end of the LF are highly dependent on the completeness simulations adopted. The aforementioned study [Finkelstein et al., 2015] finds a dependence of the slope parameter α with the redshift, with $d\alpha/dz = -0.19 \pm 0.04$ for $z = 4 - 8$. Similarly for ϕ^*, the change with redshift found is $d\log\phi^*/dz = -0.31 \pm 0.07$. These results would suggest that the faint end slope becomes steeper at larger redshift and the number density decreases, which is in agreement with previous results.

[1] Note that the values of ϕ^* mentioned in this section have not been converted to the same cosmology.

We will discuss the latest and most relevant studies of the UV luminosity function at high-redshift ($z \sim 6 - 10$) and its evolution below.

McLure et al. [2013] study the UV luminosity function at redshift $z \sim 7-8$ combining deep and wide-area data from *HST*. The deep data allows them to go to faint magnitudes of $M_{1500} = -16.75$ for $z = 7$ and $M_{1500} = -17.0$ for $z = 8$. At these redshifts they find a steep faint-end slope, with values of $\alpha = -1.90$ and $\alpha = -2.02$ respectively. As previously explained, because of the free parameters, the evolution in the luminosity function between these two redshift values could be attributed to either a luminosity evolution alone or to include an evolving density as well. This study also included the first attempt at constraining the faintness of the luminosity function at $z = 9$. Their measurements suggested that the luminosity density evolution from $z = 8$ to $z \simeq 9$ is steeper than expected for a linear trend with cosmic time.

Finkelstein et al. [2015] perform a measurement and analysis of the UV luminosity function at $z \sim 4 - 8$ using *HST* data combining both wide-area and deep surveys, with $\sim 7,500$ galaxy candidates. Their best fit for the Schechter parameters show almost no evolution in M^* with a result of $dM^*/dz = -0.12 \pm 0.09$. However, the value for the characteristic magnitude has a large uncertainty as the galaxy candidates in the bright end of their luminosity function are only brighter by 1-2 bins, therefore not allowing for a tight constraint. This absence of evolution is in disagreement with previous studies such as McLure et al. [2013] or Bouwens et al. [2011]. Unlike M^*, α and ϕ^* do show an important evolution with redshift as mentioned above. The faint-end slope becomes steeper at higher redshift while the number density decreases. This is very significant, with almost a factor of ~ 20 in the characteristic density over less than 1 Gyr. Interestingly, their data at redshift $z \sim 4-5$ is in agreement with the majority of previous studies as mentioned before, as well as the faint-end slope for higher redshifts. However, the bright end suggests a larger amount of galaxies with those magnitudes at $z \gtrsim 6$ than for ground-based studies [e.g. Willott et al., 2013]. For $z \sim 6$ they found a value of $M^* = -21.23$, different from the $M^* \sim -20.0$ found in other studies [e.g. McLure et al., 2009]. At higher redshifts $z \gtrsim 7$, both the characteristic number density and the faint-end slope seem to be consistent with most studies as well, but M^* is brighter.

As in the aforementioned studies, Bouwens et al. [2015b] used *HST* data from both wide-area and deep surveys to study the UV luminosity function. They covered about double the area that McLure et al. [2013] did and around three times the area that Finkelstein et al. [2015] comprised. They construct a sample of over $10,000$ galaxy candidates in the redshift range $z \sim 4 - 10$, with almost 700 sources at $z \sim 7 - 8$ and 6

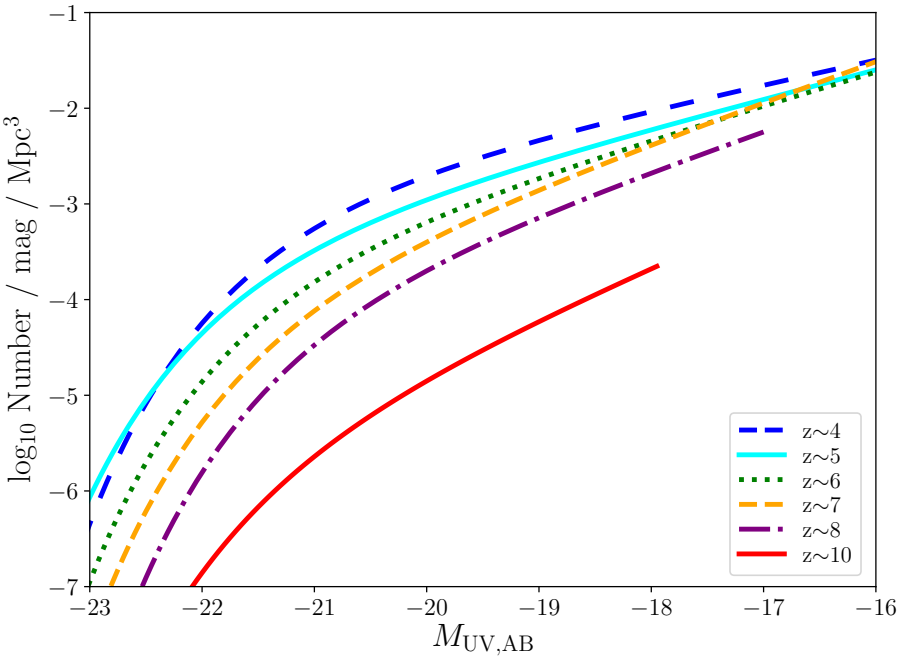

Figure 2.4: Luminosity function for $z \sim 4, 5, 6, 7, 8, 10$ calculated by [Bouwens et al., 2015b] using a SWML fit to the galaxy candidates from the *HST* data sets CANDELS, HUDF09, HUDF12, ERS, and BORG/HIPPIES.

candidates and $z \sim 10$. Figure 2.4 shows the results for the LF found in this study for redshifts $z \sim 4, 5, 6, 7, 8, 10$. Their exhaustive examination of the Schechter fit reveals a broad agreement with their previous studies in the main measurements [e.g. Bouwens et al., 2011], but still shows some significant differences. One is a less pronounced evolution of M^* with redshift, something that is also found by Finkelstein et al. [2015]. Depending on the redshift, we see that for $z = 6.8, 7.9, 10.4$ the calculated characteristic magnitude is $M^* = -20.61, -20.19, -20.92$ respectively, which is slightly brighter than previous studies. For the same redshifts, the ϕ^* presents a value of $0.46 \times 10^{-3}\text{Mpc}^{-3}$, $0.44 \times 10^{-3}\text{Mpc}^{-3}$, and $0.013 \times 10^{-3}\text{Mpc}^{-3}$. It is important to note that the $z \sim 10$ sample is very small and the values for M^* and α were fixed. It can be seen that the normalisation becomes larger with time, i.e. larger for smaller redshifts. This evolution appears to be the dominant one. For the values of the faint-end slope, they find it becomes steeper with redshift, with $\alpha = -1.64$ at $z \sim 4$ to $\alpha = -2.02$ at $z \sim 8$. As previously mentioned, the evolution of the parameters is not clear in regards to their contribution in the evolution of the luminosity function as a whole. In fact, this study suggests that the combination of the evolution in ϕ^* and α can produce the same results as an evolution in M^* in noisy data. This offers an explanation as to why previous study suggest a more pronounced evolution of M^* with redshift.

McLeod et al. [2016] searched for $z = 9-10$ galaxy candidates in data from the *Hubble* Frontier Fields survey and CLASH. They find 33 sources with photometric redshift $z \gtrsim 8.4$. The main findings of this study are that the evolution of the luminosity function from $z \sim 8$ to $z \sim 9$ is smooth. This evolution can be described either by pure luminosity evolution or by pure density evolution. The first would be accounted for a dimming of 0.5 magnitudes in M^* while the second would require drop of a factor of $\simeq 2$ in ϕ^*. They extend this and conclude that the luminosity function can be described by a smooth transition from $z \sim 6$ until at least $z \sim 10$.

Ishigaki et al. [2018] performs a study with the *Hubble* Frontier fields data, where we find ~ 450 galaxy candidates in the redshfit range $z \sim 6 - 10$. They find a steep faint-end slope, with $\alpha \sim -2$. The values of the parameters M^*, ϕ^*, and α are consistent with previous studies such as Bouwens et al. [2015b] and McLeod et al. [2016].

We can conclude that for the redshift range of $z \sim 6 - 10$, the number density of galaxies has consistently be shown to decline. However, there is clearly more work to do regarding the study of the luminosity function, particularly at higher redshifts, $z \gtrsim 8$, where the uncertainties are quite high and the evolution of the luminosity function has not been entirely understood. Whether it is an evolution in luminosity, in density or in both has not been established yet. In terms of the faint-end slope, which is crucial in order to understand the Reionisation process, the values are around $\alpha \sim -2$. However, it is extremely important to constrain this value, because small differences such as a slope of $\alpha \lesssim -2$ leads to formally divergent luminosity densities.

Comparing with lower redshift galaxies, the overall space density decreases at $z \gtrsim 4$. However, the factor by which this happens is different for the faint end and the bright end. The bright end shows a significantly larger drop than the faint end. This implies that faint galaxies were more numerous in the past, therefore they could be responsible for the Reionisation. As it can be seen, even though great progress has been made towards understanding the contribution of galaxies in the process of Reionisation, we are still far from fully understanding the entire process and how galaxies take part in it.

Numerical simulations and theoretical modelling suggest that the luminosity function flattens at some point or even turns over for magnitudes fainter than $M_{UV} = -17$ [e.g. O'Shea et al., 2015]. This is because star formation becomes progressively less efficient in low-mass Dark Matter haloes, and it eventually ceases when the atomic cooling limit is reached. In the high redshift range, this is very difficult to observe with the current technology. So far, the faintest luminosities reached by surveys have not shown evidence for a turnover, but if it happens it is expected to be at fainter magnitudes than observed.

Livermore et al. [2017] found new galaxy candidates at $z \sim 6, 7, 8$ in the Hubble Frontier Fields which are lensed and intrinsically faint. This is remarkable as it extends the sample up to faint magnitudes of $M_{UV} = -12.5, -14.5, -15$ for the respective redshift ranges. This study finds that the faint-end slope is consistent with a single power law at faint luminosities, with no apparent turnover up to at least a magnitude of $M_{UV} = -11.1$. This is in agreement with some studies that did not find the turnover either [Finkelstein et al., 2015, e.g.]. Even though this study is at low redshift, Alavi et al. [2014] analyses the UV luminosity function for a sample of 58 strongly lensed LBGs at $1 \leq z \leq 3$. They also find no turnover up to a faint magnitude of $M_{1500} \sim -13$. Bouwens et al. [2017], however, claims that the turnover would occur at higher luminosities ($M_{UV} > -14.2$ with 68% confidence), and that it cannot be constrained at such faint luminosities as Livermore et al. [2017] found.

2.3.2 Simulations

The evolution of galaxies is governed by processes that are not fully understood such as star formation, feedback, and gas cooling, among others. With a complete comprehension of these processes, simulations can reproduce observable properties that can be measured today, in particular the luminosity function. Having the observables, and the initial conditions, the subgrid physics recipes on the simulations are adjusted such as that the observed results can be reproduced. This can shed a light on the details of these processes. The types of simulations can be categorised into two main families, one being semi-analytic models (SAMs) and the other one being hydrodynamical (numerical) simulations.

Hydrodynamical simulations solve the equations of gravitation and hydrodynamics for the particles in it. The arrangement and distribution of these particles are generally approached in two different ways: Eulerian and Lagrangian. The first discretises the space, consisting of a grid fixed in space populated by the particles; while in the second the mass is discretised, using particles for the gas which flow. Nowadays, other variations of these approaches are used as well, becoming more common.

Although more accurate than SAMs, hydrodynamical simulations are computationally expensive. SAMs follows a different procedure using analytic techniques for the description of the processes involved. One important difference is the manner in which galaxies are represented. In hydrodynamic simulations, a galaxy is represented by particles, allowing details about the hydrodynamics and gravitational mechanisms in play. On the other hand, galaxies are treated as unresolved objects in SAMs, focusing on its integrated properties. Regardless of these differences, recent studies have found that

the results can be in good agreement, and differences found in previous studies can be attributed to the different parameters adopted. [e.g. Neistein et al., 2012].

The larger degrees of approximations involved in SAMs make this method less computationally intensive by using a set of simplified equations for bulk components instead of solving fundamental equations for particles. Rather than tracking the evolution of individual particles, it focuses on general quantities, such as the amount of gas that accretes into halos [Somerville and Davé, 2015].

Semi-analytic models approach the behaviour of dark matter by using results from N-body simulations and the baryonic matter with analytic simplified equations [Hirschmann et al., 2012]. Despite relying on approximations, this method has produced successful results for galaxies in large cosmological volumes. Semi-analytic models of galaxy formation are an important tool for understanding the properties of galaxy populations in large cosmological volumes such as their luminosity distributions, star formation rates, morphology, among others.

In summary, semi-analytical models are less computationally expensive than hydrodynamical simulations, but they compromise in the detailed description of the gas physics and rely on empirical laws or idealised laws for galaxy formation properties. They are a great tool for reproducing statistical properties but hydrodynamical simulations are the preferred method for reproducing the individual properties of galaxies.

Simulations and the luminosity function

Reproducing observed properties such as the luminosity function is a main goal of simulations. The luminosity function is one of the key observable properties of galaxies along with the mass function. It can give us insight to different processes by comparing observations with theoretical results. However, this is not straightforward. A sample of galaxies can be limited in different ways, for example by volume or by magnitude (flux). Furthermore, certain of the physical initial conditions play an important role in how the luminosity function is going to look. For example, many of the results of the shape depend on physical properties such as stellar feedback. However, simulations and observations are both important, because by comparing observable and theoretical models we can gain insight in to processes involved in the formation and evolution of galaxies.

Observations of the luminosity function at the epoch of Reionisation do not provide enough information about faint galaxies which is explained by the limitations of tech-

nology. Simulations are then key to understanding what happens at these magnitudes. This is important because the amount of faint galaxies can suggest whether they are responsible for the production of photons that ionised the environment, or whether the involvement of brighter galaxies is needed for this process. As extensively discussed in the previous Section, the slope for the faint end of the luminosity function remains an active topic of discussion. For example, although most studies support a flattening or turnover, the magnitude at which this happens and the slope of the flattening are still open questions.

Liu et al. [2016] studied the luminosity function of galaxies in the redshift range of $z \sim 5 - 10$ by using MERAXES [Mutch et al., 2016]. This is a semi-analytic model, specially designed for studying galaxy formation during the Epoch of Reionisation. This study finds that the slope of the predicted UV luminosity function remains steep below current detection limits, becoming flat for $M\_UV > -14$ and declining for $M_{UV} \sim -12$. They also find that the majority of UV flux is coming from bright galaxies ($M_{UV} < -13$) for the redshift range of the study. For galaxies at $z \geq 7$, the dominant contributors are the ones with magnitudes in the range of $-17 \lesssim M_{UV} \lesssim -13$. When comparing to observed luminosity function fits by Bouwens et al. [2015b], they are in excellent agreement with the simulation's results. The comparison is expanded to fainter luminosities, where Atek et al. [2015] has data up to $M_{UV} = -15.25$ at $z \sim 7$, and the simulation is still in good agreement. Taking advantage of these agreements the results can be expanded to predict the shape of the luminosity function for fainter luminosities where data is yet to be collected.

The Renaissance Simulation [O'Shea et al., 2015], a hydrodynamical based simulation, is also in good agreement with recent observations. Interestingly, it predicts a rather flat slope for low luminosities that does not agree with the extrapolated shape from fitting a Schechter function to observations.

Ceverino et al. [2017] used the FirstLight Project, a high-resolution database of simulated galaxies around at $z \geq 6$, in order to study the UV luminosity function at said redshift. Their results are in good agreement with the observed data for $z \sim 10$ and they find that the UV luminosity function starts to flatten below $M_{UV} > -14$, attributing this flattening to stellar feedback. They also find that the power-law slope evolves rapidly with redshift, with a value of $\alpha \simeq -2.5$ at $z = 10$.

As we can see, simulations tend to be in good agreement with the observations. The main results predict a flattening of the luminosity function at $M_{UV} > -14$, and a pronounced faint end slope. This is broadly related to feedback processes and decreased efficiency in cooling as the halo virial temperature approaches $T_{vir} = 1 \times 10^4$K.

2.4 First Galaxies and their observed properties

Defining a galaxy is already a complicated task when they are at lower redshift, but doing so at the time of the formation of the first galaxies is considerably more complex. As discussed in Bromm and Yoshida [2011], the definition of first *galaxy* can be different depending on the point of view, whether theoretical or observational. The first galaxies can refer to galaxies with zero metallicity, or hosts to predominantly Pop III stars; or it can refer to the galaxies that first formed. The epoch at which galaxy formation started is still uncertain, but it is expected to be at a around a redshift of $z \sim 40$ [Stiavelli and Trenti, 2010].

Interestingly, the former definitions do not refer to the same type of objects, as the galaxies that first formed are not the most chemically poor. As they formed in areas with strong clustering, stars there have gone through their cycle and have given way to Population II stars and have contaminated the environment [e.g. Wise and Abel, 2008].

Details on how the first galaxies formed and evolved are complex and elusive. However, observations of galaxies close to the time of formation can help us understand some of the mechanisms. Following we present some relevant properties that have been observed.

2.4.1 UV slope

The UV light in the spectrum of a galaxy is determined by the massive stars it hosts and the dust that exists in the galaxy. Therefore, properties of these first massive stars such as their mass and star formation rates can be deduced from the value of the UV slope provided the L_{UV} is known and a grid of stellar population synthesis models is assumed.

As mentioned in Section 2.1, the slope of the UV continuum in galaxy spectra is parametrised as β. One of the reasons why the UV continuum slope is relevant in the study of galaxies is its correlation with three important properties. As summarised by Dunlop et al. [2013], β has been shown to be a good tracer of dust extinction, as it is well correlated with excess far-infrared emission from dust; it is a function of age as well; and it is also an indicator of metallicity. Therefore, the value of β being known, the value of one of said properties can be estimated if the remaining two properties are also known from observations or models.

The main assumption is that the UV continuum slope and the flux density follow a

power law,

$$f_\lambda \approx \lambda^\beta \tag{2.1}$$

with f_λ being the flux density and λ the wavelength. By definition, using the frequency ν instead of the wavelength λ,

$$f_\nu \simeq \nu^{(\beta+2)}. \tag{2.2}$$

Therefore galaxies with a flat spectral slope in f_ν have a value of $\beta = -2.0$.

What has been found is that high-redshift galaxies tend to present less absorption than their low redshift counterparts. A few studies have also pointed out that this is true for low luminosity galaxies as well. The first estimations of this spectral index include Bouwens et al. [2003] and Stanway et al. [2005]. The latter opened the possibility of bluer values of $\beta < -2.0$, which had been the assumed value in earlier studies. However, more recent studies showed values of $\beta \sim -1.5$ for luminous galaxies, which are more consistent with redder colours. Several studies cited below explore the theory of the luminosity and the spectral index having a correlation.

Bouwens et al. [2009] carried out a systematic study over $\sim$ 1400 galaxies in the redshift range of $z \sim 2 - 6$ using multi-wavelength broadband imaging data. They found that the UV continuum keeps the trend of being bluer at $z \sim 6$ than at $z \sim 3 - 4$ by ~ 0.5. They also found that this was true for low luminosity galaxies. Although this study had mainly bright galaxies in their sample at $z > 5$, which made it hard to extend their conclusions for low luminosity galaxies, posterior studies confirmed their findings.

An important dependency to explore is β-M_{UV}. If such dependency exists at high-redshift, it could imply that a relationship between metallicity and luminosity of galaxies is established at early times. Due to the challenges the observation of faint high-redshift galaxies present, few studies have covered the $\beta - M_{UV}$ dependency at $z \gtrsim 6$ [examples include Finkelstein et al., 2012, Rogers et al., 2013, Dunlop, 2013, Rogers et al., 2014, Bouwens et al., 2014]. Studies at intermediate redshift, $4 \leq z \leq 6$, find a colour-magnitude dependency, with low luminosity galaxies emitting more blue light than their intrinsically brighter counterparts. At $z \gtrsim 6$, a consensus has not been reached yet. Studies such as Bouwens et al. [2014] do find a relationships, while other studies, including Finkelstein et al. [2012] and Rogers et al. [2013] find no evidence for this dependency.

Wilkins et al. [2016b] used hydrodynamic simulations to predict the values of the UV continuum slope for galaxies in the Reionisation epoch in the redshift range of $z = 8 - 15$. Depending on the model used, the values they obtain for β vary between

~ -2.7 and ~ -2.45. They also find an evolution of the value of beta of ~ 0.15 towards bluer colours when moving from $z = 8$ to $z = 15$. In another study, Wilkins et al. [2016a] used *HST* and *Spitzer* data of five $z \sim 10$ galaxy candidates and characterised their slope finding a value of $\langle\beta\rangle - 2.1$, which is not considerably bluer than the observed value of $\langle\beta\rangle \sim -1.7$ of galaxies at lower redshift, $z < 8$. This shows that there is some dust attenuation even at this high value of redshift. Furthermore, Watson et al. [2015] observed a galaxy at $z = 7.5$ with the Atacama Large Millimeter Array (ALMA), and found that the spectral slope of the galaxy was consistent with a value of $\beta = -2.0$, unexpectedly blue for a galaxy at high redshift.

Because the dependence of β with galaxy properties such as dust, star formation, metallicity, among other, it is hard to draw conclusions about the nature of the star populations of these galaxies unless spectroscopy is available.

2.4.2 Composition

The chemical composition of galaxies is of great importance. The metallicity of early galaxies at this redshift can help elucidate, for example, whether galaxies with only Pop III stars existed.

Simulations suggest that small β values, $\beta \lesssim -2.5$, are a feature of very-low metallicity and dust-free objects [Dunlop et al., 2013]. Although values of $\beta \lesssim -2.5$ have been scarce, there are some examples. Finkelstein et al. [2012] found values of $\langle\beta\rangle - 2.68$ for faint galaxies at redshift $z \sim 7$, which is consistent with a young, dust-free population of low-metallicity stars ($0.2Z_{\odot}$). This would agree with the theory where the first galaxies are dwarf faint galaxies with low metallicity.

2.4.3 Star Formation Rates and Dust

UV continuum slopes have been shown to correlate with dust content of galaxies in the local Universe up to redshift $z \sim 2$ [e.g. Meurer et al., 1995, Daddi et al., 2004]. Therefore, the measurement of the slopes at high-redshift can help us constrain the fraction of dust in early galaxies. This is closely linked with the star formation rate because UV light is absorbed by dust. We need to be able to estimate the dust contribution in order to estimate star formation rates accurately.

Salmon et al. [2015] studied the average properties of a sample with galaxy candidates within the redshift range $3.5 < z < 6.5$ from the CANDELS GOODS-S field. The properties of these galaxies are studied by fitting Spectral Energy Distribution (SEDs)

templates and deriving the physical properties of such galaxies. They find almost no evolution of the star formation rates with the stellar mass. Their findings are consistent with an increasing star formation history for lower redshifts. However, the specific star formation rate increases from $z = 4$ to $z = 6$.

The values found by Wilkins et al. [2016a] for galaxy candidates at $z \sim 10$ are larger than would be expected from galaxies with no dust, inferring that there is still some dust attenuation even at $z \approx 10$. Watson et al. [2015] is another example that supports this conclusion since they find a significant amount of gas in a galaxy at $z = 7.5$.

2.4.4 Sizes and Morphologies

Despite the challenge of the small apparent sizes of galaxies at high redshift, some studies have attempted to measure them [e.g., Oesch et al., 2010, Shibuya et al., 2015, Holwerda et al., 2015]. The latter article analyses six $z \sim 9-10$ galaxy candidates, and finds that their sizes are in agreement with extrapolations from low-redshift galaxies, which predict sizes of approximately 0.6 kpc. A similar size is found by Oesch et al. [2010], with a radius of ~ 0.7 kpc for a sample of LBGs at $z \sim 7-8$. They also compared their results to LBGs down to $z \sim 4$ and see only a very slow size evolution. Similarly, Curtis-Lake et al. [2016] measured the evolution of galaxy sizes and morphology for a sample of galaxies in the redshift range of $4 < z < 9$, finding a negligible evolution of the sizes with the redshift. They also find no evolution of disturbed galaxies with redshift. This same study raises an important point when measuring the sizes of galaxies; the widely used software for source identification, `SExtractor` [Bertin and Arnouts, 1996] systematically underestimates the sizes for large galaxies.

Some studies have looked into this topic using simulations. This is a good complement to observations and it can help with the comparisons. Liu et al. [2017] uses a semi-analytic model to predict the sizes and evolution of $z > 5$ galaxies. They find that their predicted sizes are in agreement with the bright candidates found at $z > 7$.

Bowler et al. [2017a] finds a weak evolution of the radii with bright magnitudes when only using the single component galaxies, which becomes steeper if the galaxies have multiple components. Bright galaxies appear to have considerably larger sizes than the faint ones, which they explain because of the multiple component nature of these. The size ranges for the half-light radii are $r_{1/2} = 0.2 - 3.2$kpc. The fainter galaxies show a size of $r_{1/2} \sim 0.5$kpc, consistent with other studies.

Regarding morphology, most studies agree that high-redshift galaxies ($z \simeq 7$) show

clumpy and disturbed morphologies. Bowler et al. [2017a] argue that the multiple components observed in these galaxies are physically associated. According to them, it is likely that these components are classified as separate sources when observed by a telescope with higher resolution such as *HST*. The clumpy objects they find tend to be the brightest in the sample as well. They conclude that this suggests clumpy star formation or merging galaxies. The latter would explain the high luminosity of these galaxies more easily as a similar phenomenon is observed at lower redshifts. The conclusion that these clumps are physically associated is also supported by the higher specific star formation rate, which would imply that the environment - whether a merger or a starburst - is triggering a higher density of star formation.

2.5 Summary

We have presented an overview of the photometric and spectroscopic features of high redshift galaxies, with a focus on Lyman Break Galaxies and their properties.

The most popular and successful technique used to spectroscopically confirm high-redshift galaxy candidates are based on the detection of the Lyman-α line. Because of the increasing amount of neutral hydrogen at early redshifts, it is not a surprise that there is a drop in the detection of galaxies at $z > 6.6$, as this line sometimes cannot be detected.

The studies of the Reionisation epoch and the galaxy luminosity function at the corresponding redshift have suggested that faint galaxies are responsible for ionising their environment, with magnitudes as faint as $M_{UV} \sim -13$, along with an evolution in the escape fraction.

Despite the challenges to study galaxies at high redshift, many of their properties have been studied and we already have a picture of how they are expected to be. They have proven to be clumpy and irregular, with dust, which suggests that star formation is still occurring at redshifts of $z \sim 7$.

Important progress is expected with the improvements in the next generation of telescopes, allowing us to measure the galaxies responsible for Reionisation and their properties.

Photometric selection techniques are being used for galaxies at $z \sim 10-12$ nowadays, but spectroscopy has not gone above $z \sim 8$, and it likely won't be able to if it relies on Lyman-α emission line detection, due to reionisation.

This motivates our work in the next chapter, where we apply the dropout technique to find high redshift galaxy candidates.

3

Searching for High-Redshift Galaxies

Observing the sky has interested humans since the beginning of time. Major efforts have been made in order to be able to comprehend the Universe. Modern telescopes have allowed us to reach faint limits, and we are close to observing the Universe at the time of formation of the first galaxies. This has driven a growth in the field of the search for galaxies, which has had a remarkable evolution in the last 20 years.

Most of the high redshift surveys have been carried out with *HST*, which revolutionised the search for high redshift galaxies, pushing their discovery from redshift $z \sim 3$ Giavalisco et al. [1996] to current galaxy candidates as high as $z \sim 11$ [Coe et al., 2013, Oesch et al., 2016]. The installation of the Wide Field Camera 3 (WFC3) with a state-of-the-art near-infrared detector played an important role in this revolution, allowing us to have a glimpse of the first galaxies and their evolution during the epoch of Reionisation.

Because of the distribution of objects with respect to their intrinsic luminosity (see

Chapter 5 for a review on the galaxy luminosity function), finding both bright and faint galaxies is challenging. Bright galaxies tend to be rare, therefore large areas of the sky compared to the typical instrumental field of view need to be observed. Conversely, faint galaxies are much more common, but they present a difficulty in their lower intrinsic magnitudes, requiring ultradeep exposures.

Different techniques have been used when designing the surveys in order to make them more efficient and reach magnitudes as faint as possible and/or cover wider areas. One of these techniques consists of using the magnification produced by the strong gravitational lensing phenomena to find intrinsically dim galaxies. This is achieved by observing in fields that contain massive objects such as galaxy clusters. The gravitational lensing effect will make possible the detection of galaxies that are too faint to be observed otherwise. Alternatively, surveys that focus on bright objects do not require such deep magnitude limits. Therefore these observations are shallower, but they focus on covering large areas.

In this chapter we present an overview of the *HST* and the WFC3, with a description of some important galaxy surveys whose aim has been to find distant galaxies. We then provide a summary of successful surveys that used this telescope. Additionally, we describe two surveys we use in this thesis, BoRG and RELICS. Finally, we describe our search for galaxies at $z \gtrsim 8$ in these surveys and present the candidates found. The results for the BoRG search have been published in Bernard, Carrasco et al. [2016]. We refer throughout this study to AB magnitudes [Oke and Gunn, 1983].

3.1 HST

The launch of the 2.4 m *Hubble Space Telescope* (HST) in low-Earth orbit ($\sim$ 550 km) in 1990 prompted a revolution in Astronomy as its observations led to some groundbreaking discoveries. After multiple servicing missions, currently, there are four main instruments that are operating. These are the Advanced Camera for Surveys [ACS; Sirianni et al., 2005], the Wide Field Camera 3 [WFC3; Windhorst et al., 2011], the Cosmic Origins Spectrograph [COS; Froning and Green, 2009], and the Space Telescope Imaging Spectrograph [STIS; Woodgate et al., 1998].

3.1.1 Wide-Field Camera 3 - WFC3

In 2009, WFC3 was launched and installed in the telescope, replacing the previous camera, WFPC2. This camera, WFC3, features two UV/visible detecting CCDs, each

2048×4096 pixels, and a separate IR detector of 1024×1024.

Compared to its predecessor, Wide Field and Planetary Camera 2 (WFPC2), WFC3 has a higher resolution, a larger field of view and two channels: UV and IR, with a pixel scale of 0.04"/pix and 0.13"/pix for each channel, 2×2048×4096, and 1024×1024 field of view, respectively, and spatial resolution of $0''.04$ FWHM at 2000 Å to $0''.16$ FWHM at 16000 Å.

The camera has a two-channel configuration, with an Infrared Channel and a UVIS channel. This dual-channelling allows for a wide-wavelength coverage, with a range of $2000 - 17000$ Å.

The light from the telescope goes into WFC3 using a pick-off mirror, and is directed to either the UVIS or the NIR channel.

NIR Channel

The Near Infrared channel has a field of view of $123'' \times 137''$, with a wavelength range of $8500 - 17000$Å and 17 filters. They include wide filters, medium filters, and narrow filters.

The detector type is a crystalline photosensitive surface composed of mercury, cadmium and tellurium (HgCdTe). It has one megapixel.

UVIS Channel

The Ultraviolet-visible channel has a field of view of $162'' \times 160''$, with a wavelength range coverage of $2000 - 10000$Å and 63 filters. They include longpass filters, wide filters, medium filters, and narrow filters. The detector type is Charge Coupled Device (CCD), a low noise array of high sensitivity and 16 megapixels.

3.2 High-Redshift Galaxy Surveys

The rapid progress generated by *HST* in terms of obervational capabilities naturally led to the planning of galaxy surveys. Several successful surveys for high-redshift galaxies have been carried out by *HST*. Below is a summary.

- *Hubble Deep Fields [HDF; Williams et al., 1996].* The pioneer in this type of

survey, it was carried out in 1995. It was taken with the Wide Field/Planetary Camera 2 (WFPC2) with a total exposure time of 10 days. It consisted of a deep image of an area of approximately 5.3 arcmin^2 taken in four filters: U_{300}, B_{450}, V_{606}, I_{814}. The composed image (see Figure 3.1) is one of the most famous Astronomical images. It provided a deep view of the Universe, as it purposely avoided bright stars. Follow-up observations of the HDF included almost the whole wavelength spectrum, and over $3,000$ galaxies were observed. It motivated innumerable studies and discoveries, including spectroscopic measurements of many of these sources.

In 1998, the south portion of the sky was observed, giving way to the HDF South[1] [Gardner et al., 2000]. Instead of avoiding bright objects this time, the field contained a quasar. This was in order to be able to observe the absorption lines produced in the quasar spectrum by the galaxies in the field [e.g. Gunn and Peterson, 1965, Bahcall and Salpeter, 1965]. The requirement of having a quasar and galaxies and being observed by *HST* resulted in the observation of a field that had many bright stars. The photometric measurements for the galaxies was therefore more complicated than for HDFN and truncated its impact. The observations of WFPC2 were complemented with STIS and NICMOS.

The HDF observations had a significant impact in understanding galaxies. One of the main findings was about the morphology of high-redshift galaxies, which differs from those in the local Universe. It was found that the distribution of their morphologies departs from anything like the Hubble Sequence observed at low redshift.

- *Great Observatories Origins Deep Surveys [GOODS; Giavalisco et al., 2004].* This is technically a joint observation as it comprises two fields observed by several telescopes, GOODS-North and a small region of the Chandra Deep Field South (CDFS). Some of these telescopes included the Chandra satellite and Spitzer. Each field has a minimum observed size of around $16' \times 10'$. The fields were observed with the ACS (B_{435}, V_{606}, i_{775}, and z_{850} filters) at several epochs between the years 2003 and 2005. GOODS-North contains the HDFN region, and CDFS contains the HUDF region.

  This survey has led to a number of successful publications. Some of the most remarkable results include a thorough study about the metallicity of galaxies at $0.3 < z < 1.0$ [Kobulnicky and Kewley, 2004], first constraints on the UV luminosity function at $z \sim 6$ [Bouwens et al., 2006], and the stellar mass function of galaxies at $z \sim 5$ [Drory et al., 2005], among others.

[1] The original HDF was subsequently renamed HDF North, or HDFN.

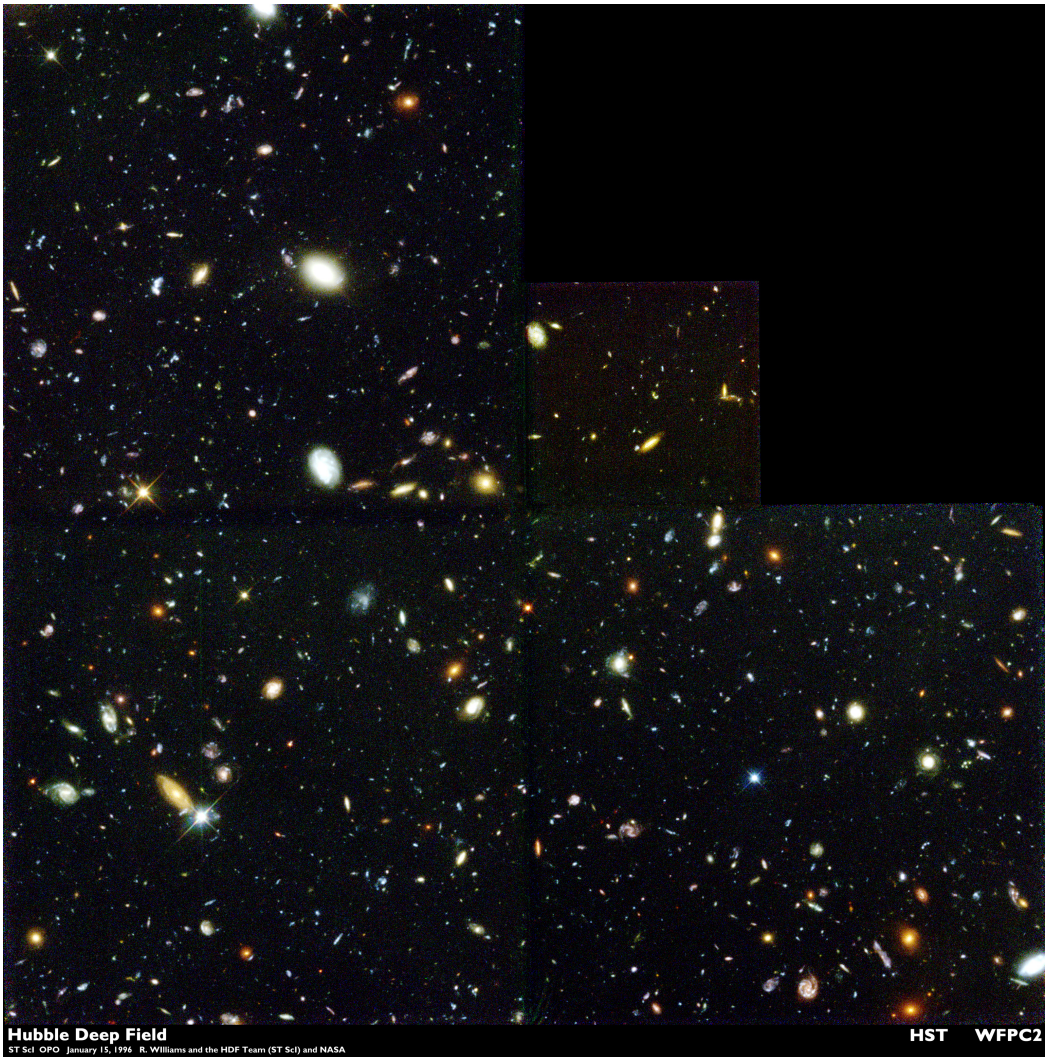

Figure 3.1: Combined image of the Hubble Deep Field. *Credit:* R. Williams (STScI), the Hubble Deep Field Team and NASA/ESA.

- *Hubble Ultra Deep Field [HUDF Beckwith et al., 2006].* In 2004, the Hubble Space Telescope again recorded the deepest image of the Universe. This was achieved with a newly installed camera, the Advanced Camera for Surveys, which was more powerful than WFPC2, with a field of view twice as large and a pixel size of $0''.05$, about half of the pixel size from WFPC2. The filter was taken with the same four filters as HDF, but reaching magnitude limits of about $m_{AB} \approx 29$. These allowed for the findings of galaxies up to redshift $z \sim 6$, which was ground-breaking. This image was also observed by NIR channel of WFC3 in the bands Y, J, and H. This allowed having comparably good data in the infrared and visible part of the spectrum.

  This survey helped understanding high-redshift galaxy populations which were found to be similar to the ones of galaxies at $z \sim 3$. This suggests that the galaxies evolved quickly in the first stages of the Universe. After the observations with WFC3, galaxies at even higher redshifts were found.

- *The Cosmic Assembly Near-IR Deep Extragalactic Legacy Survey [CANDELS Grogin et al., 2011, Koekemoer et al., 2011].* This survey uses both NIR and UVIS channels from the WFC3, and the ACS as well. WFC3/IR is the primary instrument, and ACS/WFC is used in parallel. It took $\sim 10\%$ of HST's available observing time for three years. Its main goals are studying the evolution of galaxies and black holes in the redshift range $z \sim 1.5-8$, and Type Ia supernovae (SNe Ia) at $z > 1.5$ to characterise Dark Energy. It observed five extragalactic fields that were previously observed in other surveys. These fields are GOODS-North, GOODS-South, COSMOS, EGS and UKIDSS/UDS. The survey includes Deep fields that comprise 133 arcmin^2 withing HDF North and Chandra Deep Field Shouth. They were imaged in the bands Y_{F105W}, J_{F125W} and H_{F160W} and have magnitude limits of $m_{AB} \approx 27.5$. CANDELS also include wide fields, which cover an area of 553 arcmin^2 and it is observed in two bands J_{F125W}, H_{F160W} with limit magnitudes of $m_{AB} \approx 26.6$.

  Several studies about high-redshift galaxies were done with CANDELS data. These include studies about the UV colours of galaxies at $z \sim 4-8$ [Finkelstein et al., 2012], their size and luminosity at $z = 7$ [Grazian et al., 2012], among others. Because this survey was primarily based on data from ground telescopes and only complemented by *HST* data, it covered a wide area which allowed the discovery of several bright galaxies at high-redshift, providing some of the best constraints on the bright-end of the luminosity function [e.g. Yan et al., 2012, Lorenzoni et al., 2013, Roberts-Borsani et al., 2016]. It is important to note that CANDELS data has not only been used for galaxies at high-redshift. Discoveries of faint AGNs at $z > 4$ [Giallongo et al., 2015], and a study aimed to track the

evolution of structure and activity of massive galaxies at $z = 1.4 - 3$ [Barro et al., 2013] are examples of this.

- *Cluster Lensing and Supernova survey with Hubble [CLASH Postman et al., 2012].* This is a 524-orbit multi-cycle treasury program that imaged 25 galaxy clusters with HST using 16 filters with ACS and WFC3/NIR. Five of these clusters were chosen because of their predicted highly effective lensing capabilities. Several interesting scientific results have been produced from the observations with CLASH. Significant progress has been made in terms of galaxy lensing [Meneghetti et al., 2014, Zitrin et al., 2015]. It also set a record when the highest redshift photometric candidate known at that point was found. This object is a $z \sim 10.7$ [Coe et al., 2013] galaxy candidate strongly lensed by a galaxy cluster, which produced three images of the source. These images were only able to be detected because of the strong lensing that magnified the source.

- *Extreme Deep Field [XDF; Illingworth et al., 2013].* Taken in 2012, this became the deepest image of the Universe. The observations were made in 9 filters, comprising NIR and visible wavelengths. It consists of 2963 separate images from the ACS and WFC3/IR. The XDF includes all data taken by Hubble on the small patch of sky first imaged as the Hubble Ultra-Deep Field (HUDF). The concept of the eXtreme Deep Field (XDF) resulted from the realization in late 2011 that all the data taken over the last 10 years with the Advanced Camera for Surveys and the WFC3 on the HUDF had not been combined into a single extremely deep image. This is what XDF is. All these images were combined in order to produce the deepest image of the sky, which covers now approximately 4.7 arcmin^2 up to a limiting magnitude of $m_{AB} \approx 31$. Data from XDF has been used in important publications such as the analysis and characterisation of galaxies at $z > 8$ [Oesch et al., 2013] and measurements of the UV luminosity function during the epoch of reionisation [Bouwens et al., 2015b].

- *HST Frontier Fields [HFF; Lotz et al., 2017a].* Community survey initiative of six deep fields centered on strong lensing galaxy clusters. Three of them are from Abell et al. [1989] and the other three are from the MACS survey [Ebeling et al., 2001]. Images of six deep blank fields adjacent to these clusters were also taken. The program was designed with the following science goals in mind: to reveal faint populations of $z = 5 - 10$ galaxies that are between 10 and 100 times fainter than the ones found with HUDF; to characterise the stellar populations of faint galaxies at high redshift and understand the stellar mass function at the earliest times; provide statistical morphological characterisation of star-forming galaxies at $z > 5$; find $z > 8$ galaxies stretched out enough by foreground clusters to measure

sizes and internal structure and/or magnified enough for spectroscopic follow-up. The magnitude limit of this survey is approximately $m_{AB} \sim 29$, depending on the band. Because of the strong lensing, it can be expected to observe highly magnified regions 10-100 times fainter than the limit magnitude. Both cameras WFC3 and ACS were used for this survey, with the filters being B_{F435W}, V_{F606W}, I_{F814W}, Y_{F105W}, J_{F125W}, JH_{F140W}, H_{F160W}, and JH_{F140W}. The last observations were carried out by the end of year 2016. Important results have been obtained from this data, including a measurement of the $z \sim 6-10$ UV luminosity function [Ishigaki et al., 2018], a detailed comparison among different strong lensing models [Meneghetti et al., 2017], and studies on the sizes of faint galaxies [Bouwens et al., 2017].

In the next sections we describe two surveys carried out by HST whose data we used.

3.3 BoRG

3.3.1 Overview

The Brightest of Reionizing Galaxies HST/WFC3 survey [BORG; Trenti et al., 2011, 2012] is a large Hubble Space Telescope (*HST*) program whose aim is to identify bright ($m_{F125W} \gtrsim 27$) galaxies at $z \gtrsim 7.5$. This survey complements other efforts to find high redshift galaxies, which are deeper in magnitude, but smaller in covered areas.

The observations for BoRG started in the Hubble Cycle 17, in 2010, and continued until 2016. Its focus on galaxies at $z \gtrsim 7.5$ (BoRG[z8]) was shifted to higher redshifts, optimising the search for candidates at $z \sim 9-10$ (BoRG[z10]) from 2015 onwards.

BoRG[z8] comprises 78 fields with a total area of ~ 350 arcmin^2. On the other hand, BoRG[z10] covers ~ 550 arcmin^2 over 120 independent lines of sight.

BoRG is a pure-parallel survey, which means that the data are acquired while Hubble is pointing at primary spectroscopic observations. This helps avoid a well-known problem in these kind of searches known as *cosmic variance*. This concept can be understood as sample variance, where limited areas in surveys are potentially affected by systematic uncertainties due to large-scale structures. This typically introduces additional systematic uncertainty that is at least of the order of the Poisson noise [Trenti and Stiavelli, 2008]. Any property or function calculated for a sample of objects found in any constrained volume will be affected by cosmic variance as it is assumed this calculations are from a homogeneous portion of the sky. While in surveys as GOODS or HUDF,

cosmic variance accounts for $\sim 25\%$ uncertainty, BoRG avoids this problem by using random locations in the sky. This also brings some challenges, such as the depth and image quality being non-uniform. It is important to clearly account for cosmic variance because it can bias the results. In order to correct for this effect, surveys can either sample substantially large parts of the sky so structures and voids that may be present can be averaged out, or there can be several random pointings so in case large-scale structures are present the variance can be statistically estimated. The latter approach is taken by BoRG.

3.3.2 Observational Strategies

Below, Table 3.1 shows the wavelengths of the filters used by the BoRG survey. Figure 3.2 shows the transmission curves for the filters used in BoRG[z8] (top panel).

Filter Name	Pivot Wavelength (Å)[1]	FWHM (Å)	Usage
F350LP	5846[2]	3500	BoRG[z10]
F606W	5997	2340	BoRG[z8]
F600LP	7444[2]	6000	BoRG[z8]
F098M	9864	1700	BoRG[z8]
F105W	10552	3000	BoRG[z10]
F125W	12486	3000	BoRG[z8], BoRG[z10]
F140W	13923	4000	BoRG[z10]
F160W	15369	2900	BoRG[z8], BoRG[z10]

Table 3.1: *HST* filters used in the BoRG survey with their pivot wavelength, and full width half maximum (FWHM). The top three bands are from WFC3/UVIS while the rest of them are from WFC3/IR.
[1] Pivot Wavelength is a measure of the effective wavelength of a filter [Tokunaga and Vacca, 2005].

We describe the observational strategies for both BoRG[z8] and BoRG[z10]. The main difference is related to the filters used in order to optimise the search for galaxy candidates, which depends on the targeted redshift. We focus more extensively on BoRG[z8] since this is the data we will work with.

BoRG[z8]

The observations are made with the IR channel from the WFC3, with the exception of one band used from the UVIS channel. An important design feature of this survey is

[2]Longpass filters block all blue light and permit all light longer than a nominal wavelength up to the CCD red cut-off through.

that it is planned to have a minimum amount of artefacts and low-redshift interlopers. Since the galaxy candidates at the aformentioned redshift are expected to be Y_{F098M} dropouts, this is one of the bands used in the survey. They are also complemented by the J_{F125W} and H_{F160W} bands, where flux is expected. One optical filter, V_{F606W} is used in order to distinguish the galaxy candidate from lower-redshift interlopers. In a small amount of fields, the band V_{F600LP} is used instead. which come from another pure-parallel program.

The field sensitivities are individual for each field, but the median magnitude limits at 5σ detection are $m_{F606W} = 26.9$, $m_{F600LP} = 26.4$, $m_{F098M} = 26.8$, $m_{F125W} = 26.7$, and $m_{F160W} = 26.3$. The median exposure times are $t_{exp} = 2647, 2334, 4515, 2205, 1405$ seconds, respectively. The exposure time between filters has been allocated by keeping the relative depths approximately constant, within the constraints imposed by the primary program.

BoRG[z10]

In order to optimise the search for galaxies at $z \sim 9 - 10$, the filters used here are $F350LP$, Y_{F105W}, J_{F125W}, JH_{F140W}, H_{F160W}. The new filters are optimised to differentiate galaxies at $z \sim 9-10$ from their contaminants and artefacts. WFC3 pointings in BoRG[z10] have variable exposure times, from $t_{exp} \sim 7000 - 19000$ seconds, depending on the number of orbits which is determined by the primary program.

3.3.3 Results

The BoRG survey has been very successful. Studies performed with BoRG data have led to several photometric galaxy candidates at $z \gtrsim 7.5$, such as Bradley et al. [2012], Calvi et al. [2016]; Bernard, Carrasco et al. [2016]. Furthermore, follow-up spectroscopical confirmation has also been pursued [Treu et al., 2013, Livermore et al., 2018]. The most relevant measurements of the UV luminosity function for high-redshift galaxies have included BoRG data [e.g Bouwens et al., 2015b, Finkelstein et al., 2015, McLeod et al., 2016].

Its data has also been used for studies in different areas, such as finding Milky Way late-type dwarf stars [Holwerda et al., 2014].

3.4 RELICS

3.4.1 Overview

The Reionisation Lensing Cluster Survey [RELICS; Coe et al. 2018, in prep.] aims at analysing 46 fields strongly lensed by 41 massive clusters in order to efficiently search for and study magnified high-redshift galaxies. It covers approximately 207arcmin^2. RELICS targeted high mass clusters according to their Sunyaev Zeldovich [Sunyaev and Zeldovich, 1972] mass estimates in the Planck catalogue [Planck Collaboration et al., 2016]. Previous results of high-redshift galaxies observed by *HST* with magnitudes brighter than $m_{F160W} \gtrsim 25.5$ are rarer than expected. Objects with fainter magnitudes are extremely difficult to follow-up spectroscopically with the current technology. Therefore, the RELICS strategy is to search for galaxies whose brightness has been magnified by strong gravitational lensing. This way, the number of galaxy candidates in the epoch of Reionisation can be actually analysed spectroscopically, which allows for a better understanding of this process.

The 41 clusters selected for this survey have been observed in the NIR (with NICMOS or WFC/IR). A total of 21 of these galaxy clusters have masses similar or greater than the HFF clusters and were included within the 34 most massive clusters according to Planck observations [Planck Collaboration et al., 2016]. The rest of the galaxy clusters were chosen regarding their previous observational status with *HST*, i.e. prioritising galaxy clusters that had been previously observed with this telescope. Their mass estimates as measured by X-ray observations and other techniques were also considered.

In comparisons with CANDELS, CLASH and other surveys, it has been predicted that RELICS would observe around $40 - 200$ galaxy candidates at $z \gtrsim 9$ and ~ 170 candidates at $z \sim 8$. The first search is described in Salmon et al. [2018], where they used photometric redshift fitting codes in order to find candidates. This study identified 321 candidates in the redshift range of $z \sim 6-8$. A remarkable result is the discovery of some extremely bright candidates with magnitudes as bright as $m_{F160W} \approx 23$. Interestingly, only 8 of the candidates are at $z \sim 8$. We perform our own search in this data, which is shown in Section 3.6.

In addition to the *HST* imaging, Spitzer IRAC programs have been born from RELICS (PI Bradaĉ, PI Soifer). The IRAC 3.6μm and 4.5μm bands have proven to be useful in the photometric redshift estimations. Because of their wavelength, they can help distinguish between $z > 5$ galaxies and dusty galaxies at lower redshift.

3.4.2 Observational Strategies

Below, Table 3.2 shows the wavelengths of the filters used by the RELICS survey. Figure 3.2 shows the transmission curves for the filters used in RELICS (bottom panel).

Filter Name	Pivot Wavelength (Å)	FWHM (Å)
F435W	4328	729
F606W	5997	1566
F814W	8057	1657
F105W	10552	3000
F125W	12486	3000
F140W	13923	4000
F160W	15369	2900

Table 3.2: *HST* filters used in the RELICS survey with their peak wavelength and full width half maximum (FWHM). The top three bands are from ACS, while the rest of them are from WFC3/IR

RELICS observed 46 fields comprising 41 clusters, with five of them being observed with additional pointings. All the clusters are observed in two orbits of *HST* with WFC3, and it uses the same seven filters as HFF, which cover the wavelength range of $4000 - 17000$Å. From the NIR channel, the filters F105W, F125W, F140W, and F160W are used. Furthermore, available data from previous observations with ACS is used for 23 clusters. For the remaining 18 clusters, observations are made with 3 orbits in total in the filters F435W, F606W, and F814W.

The observations are split into two epochs separated by approximately a month for variability search. Twenty additional orbits were allocated for variability Target of Opportunity follow up.

3.4.3 Results

With the observations finished in October 2017, the majority of the data has not been exploited yet. However, some studies have started to see the light. A particularly exciting result from this survey is the discovery of a $z \sim 10$ galaxy candidate whose image has been stretched out by gravitational lensing Salmon et al. [2018]. This is the first galaxy candidate at such high-redshift that occupies such large area, presenting a unique opportunity for resolving stellar populations during the Reionisation epoch.

Along the lines of one of the aims of the survey, several lens models have been pro-

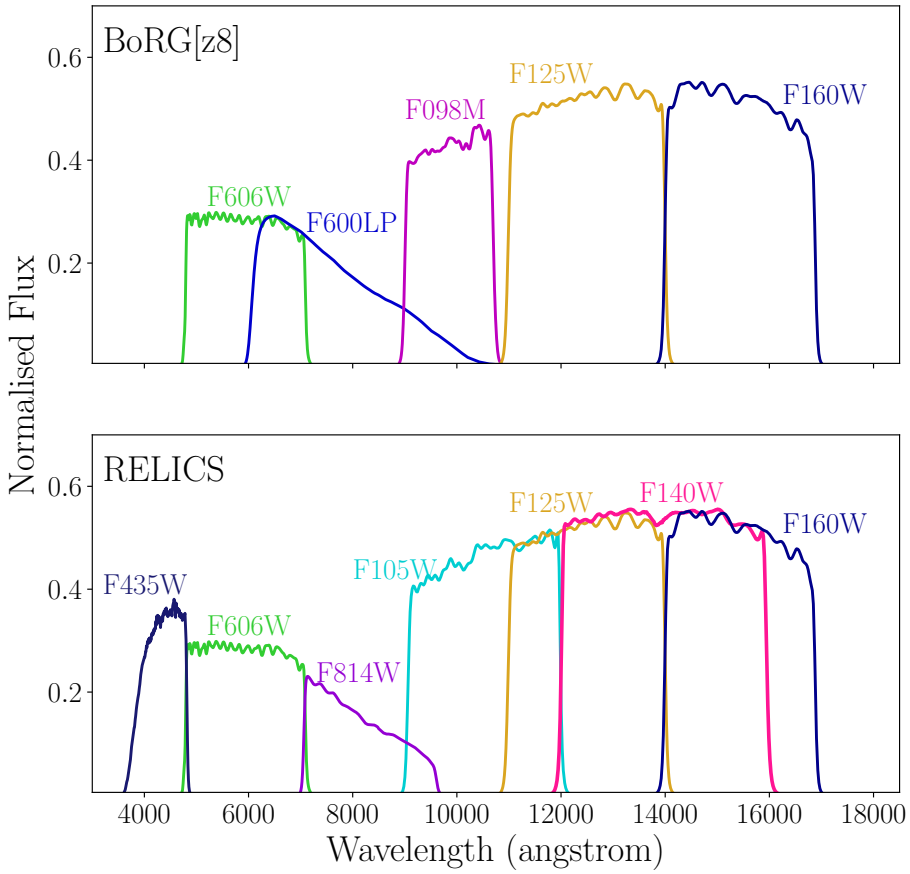

Figure 3.2: Transmission curves for the sets of *HST* filters used in BoRG[z8] (top panel) and RELICS (botom panel). It is clear that both surveys cover approximately the same wavelength range. However, RELICS has two more filters, one of them, F140W, in the range of the Lyman break for galaxies at $z \gtrsim 8.5$. This improves the selection at those redshifts.

duced and applied to study mass estimates for some of the galaxy clusters [Acebron et al., 2018, Cerny et al., 2018, Paterno-Mahler et al., 2018, Cibirka et al., 2018].

If the predictions regarding the number of high-redshift galaxy candidates that will be found in this data are correct, this will be an important improvement in the field. This will help constrain the data in the UV luminosity function. Otherwise, if the predictions are proven to be too high, that will shed some light on strong lensing, where important improvements will need to be made in order to understand the lack of high-redshift galaxy candidates being lensed by galaxy clusters.

3.5 Our search: BoRG

We applied a selection technique for redshift $z \sim 10$ by searching for J-dropouts in the survey BoRG[z8]. The results of this selection were published in Bernard, Carrasco et al. [2016].

As explained previously, the aim of this survey is to identify galaxies at $z \sim 8$, hence the filters used for the observations are not optimised for redshift $z \sim 10$. Consequently, finding high redshift galaxies can be more challenging as the bands are not ideal. BoRG[z10] includes the band $F140W$, whose coverage is between $F125W$ and $F160W$ in terms of the wavelength. This is relevant as the Lyman break is expected to be observed in this wavelength range for galaxies at redshift $z \gtrsim 10$. Thus, the flux received in the $F140W$ gives a better insight of the nature of the galaxy. For instance, if there is flux only in $F160W$, but no detection in $F140W$, it is very likely that the detected object is an artefact. In the case of our data, we do not have that distinction, only having $F160W$ to discriminate regarding detection.

It is important to note that we do not expect to see such a strong drop in Lyman-break galaxies at high redshift compared to Lyman-α emitters as photons longwards of 1216Å are not so effectively scattered by neutral hydrogen. If the drop at $z \sim 8$ is of physical origin, we can infer information about the evolution of star forming galaxies as well as the intergalactic medium and Reionisation.

3.5.1 Source Identification

In order to identify the galaxy candidates, we use `SExtractor` [Bertin and Arnouts, 1996], a program geared towards the reduction of large scale galaxy-survey data. It identifies sources by finding peaks of luminosity in given images, making the distinction between background and sources. The program receives a list of parameters in order

to detect said sources. These parameters include thresholds for the minimum size or signal-to-noise, for example.

Because the images from BoRG are taken with a range of channels and instruments, some processing needs to be done in order to have a pixel to pixel correspondence and be able to analyse sources. The reduced images for the BoRG[z8] survey are public, and they were produced using `Multidrizzle` [Koekemoer et al., 2003] along with the inverse variance maps. `Multidrizzle` is a software aimed at combining dithered observations. Since the drizzling process introduces correlated noise, RMS maps were created from the weight maps, and then normalised in order to account for that noise. This is done for each field and filter by measuring the noise in the image at random positions not associated with detected sources and comparing the measurement with the value inferred from the RMS map, which is then be corrected by a factor to match the measurement. The factors obtained are on average ~ 1.1 for the IR filters and ~ 1.4 for the optical/UV filters.

Given the characteristics of the sources we are aiming to find, we perform what is called a dual-mode search. This identification search mode consists of using one of the bands as detection band. This is the band where flux from the source is expected. Afterwards, the flux for the images taken in the rest of the bands is measured in the same positions where sources were found. This way, there is information on the flux for objects that have no flux in some or all the rest of the bands.

The procedure for one field is as follows:

1. Run `SExtractor` on the science image that was observed with the detection filter.

2. Run `SExtractor` in dual mode on the rest of the science images. This modality uses the catalogue produced in Step 1. It measures the photometry on the position where a source was detected in the detection band image.

3. A catalogue with the information in all bands is compiled.

We use equation 1.12, plus the wavelength at which the Lyman-break occurs, 1216Å, and the target redshift range, $z \sim 10$. This indicates that the wavelength at which this feature would be observed at $\lambda_{obs} \sim 13376$Å, and flux would be expected for greater wavelengths. Considering the peak wavelength and FWHM of the bands available for BoRG[z8], $F160W$ (also called H_{160}) is the most suitable. Therefore, this will be our detection band.

`SExtractor` is run over the science images and a catalogue with the characteristics

of the detected sources is produced. The properties included in the catalogue can be chosen by the user and, in our case, we require information regarding the magnitudes and fluxes, sizes, coordinates, signal-to-noise, and stellarity.

The information we use to find the dropouts is the magnitude, colours and signal-to-noise (S/N). We clarify that for the magnitude we use `MAG_AUTO`, for the colours (subtraction of one magnitude minus another one) we use `MAG_ISO`, and for the signal-to-noise we define it as:

$$S/N = \frac{\texttt{FLUX\_ISO}}{\texttt{EFLUX\_ISO}} \tag{3.1}$$

Also, we only consider objects that have a signal-to-noise above or equal to 8.0, $S/N \geq 8.0$.

3.5.2 Criteria

The criteria we use is aimed at finding galaxies at redshift $z \gtrsim 9-10$ and avoid as many contaminants as possible. Due to the lack of an intermediate band between $F125W$ and $F160W$ that could provide a second measurement of the flux to avoid artefacts (as they are expected to show on only one band), we have to be careful with the object detection only on the H band. With that purpose, we apply a further criteria, which consists of excluding all sources with stellarity greater than 0.95, meaning highly circularly-shaped objects. They can not only be artefacts, they can also be stars with unique colours similar to the galaxies we are aiming to find.

The specific criteria are summarised below.

1. $J_{125} - H_{160} > 1.5$,
2. $S/N_{160} \geq 8$,
3. $S/N_V < 1.5$,
4. $S/N_{098} < 1.5$,
5. `CLASS_STAR`<0.95.

where J_{125} is the magnitude in the band $F125W$; H_{160} is the magnitude in the band $F160W$; S/N_{160}, S/N_{098} are the signal-to-noise in the bands $F160W$, $F098M$ respectively; S/N_V, is the signal-to-noise in the bands $F606W$ or $F600LP$, depending on the availability.

Criterion 1 is the colour cut that ensures there is a strong break between the magni-

tudes J_{125} and H_{160}. This is a conservative value when compared to the typical applied in surveys $J_{125} - H_{160} > 1.2$ [e.g., Bouwens et al., 2015b].

Criterion 2 corresponds to the detection threshold required. This is also a conservative approach in order to ensure real detections in the $F160W$ band.

Criteria 3 and 4 are imposed to rule out objects that present some flux in optical bands, where no flux is expected.

The `CLASS_STAR` parameter measures the probability that a source is a point source (probability 1) or an extended object (probability 0). Consequently, criterion 5 is aimed at avoiding stars. Since the available filters are not optimal for this search, we have adopted the aforementioned criteria, which are conservative when compared to other searches. Our aim is to minimise the fraction of contaminants.

3.5.3 Results

After applying all the selection criteria from above and performing a final step of visual examination, we arrive at a sample of 6 galaxy candidates. Further analysis was performed in Bernard, Carrasco et al. [2016], and some candidates were excluded based on their size and magnitudes, constructing a final catalogue of 3 candidates, which are shown in Figure 3.3. These candidates are from the fields *borg_ 0240-1875*, *borg_ 0456-2203*, and *borg_ 1153+0056*. Their properties can be summarised as:

- *borg_ 0240-1875_ 25*: $RA = 40.1195$, $Dec = 18.9726$, $m_{160} = 26.2$, $S/N_{160} = 8.1$, `CLASS_STAR` $= 0.7$, and $J_{125} - H_{160} > 2.53$. The effective radius of this source is $r_{eff} = 0''.13$, the absolute magnitude is $M_{AB} = -21.1$, which corresponds to a luminosity of $L = 1.20 \times 10^{29}$erg s^{-1} Hz^{-1}. The SFR is 13.76 M$_{\odot}$yr^{-1}. This object shows no flux in any of the other bands apart from H_{160}. It is smaller than the PSF of the image, which suggests it could be a point-source and therefore a contaminant. However, its low stellarity is a good indicator.

- *borg_ 0456-2203_ 1091*: $RA = 73.9774$, $Dec = 22.0372$, $m_{160} = 26.1$, $S/N_{160} = 8.1$, `CLASS_STAR` $= 0.5$, and $J_{125} - H_{160} > 2.47$. Its effective radius is $r_{eff} = 0''.24$, and its absolute magnitude is $M_{AB} = -21.4$, equivalent to a luminosity of $L = 1.58 \times 10^{29}$erg s^{-1} Hz^{-1}. The SFR is 18.14 M$_{\odot}$yr^{-1}

- *borg_ 1153+0056_ 514*: $RA = 178.1972$, $Dec = 0.9270$, $m_{160} = 26.3$, $S/N_{160} = 8.0$, `CLASS_STAR` $= 0.0$, and $J_{125} - H_{160} > 2.64$. It has an effective radius of $r_{eff} = 0''.23$, and an absolute magnitude of $M_{AB} = -21.2$, equivalent to a luminosity of

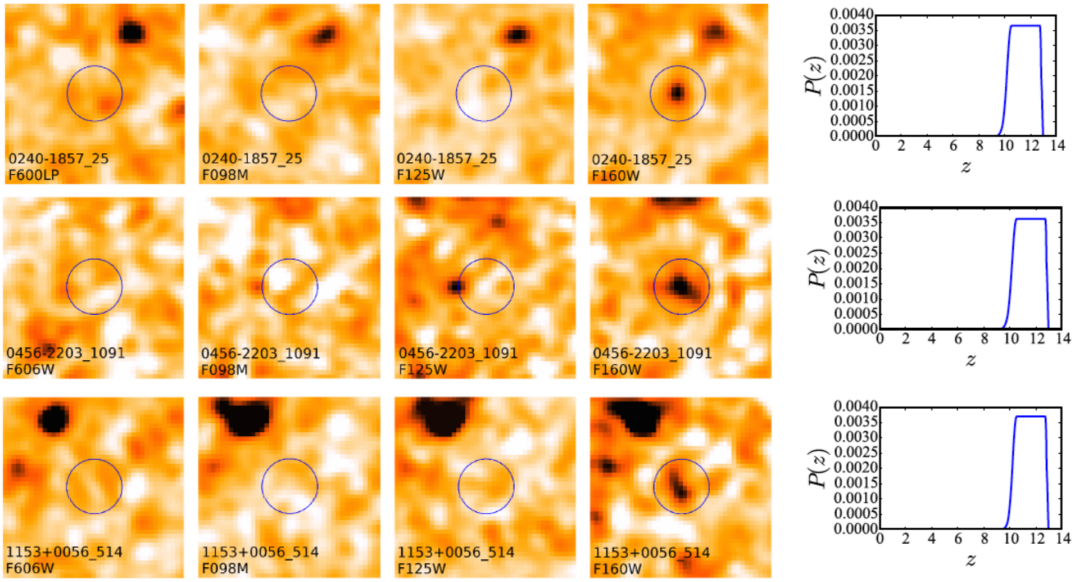

Figure 3.3: Final galaxy candidates at $z \sim 10$ from the BoRG[z8] dataset. The image size is $3''.2 \times 3''.2$. The last column to the right shows the redshift probability distribution $P(z)$ vs. z from BPZ. *Credit:* Bernard, Carrasco et al. [2016].

$L = 1.31 \times 10^{29}$erg s^{-1} Hz^{-1}. The SFR is 15.09 M$_\odot$yr^{-1}

The results of this search are also summarised in Table 6.1.

The sizes of the objects were calculated from the observed half-light radius measured by `SExtractor` . The intrinsic source size is then estimated with this radius and by taking into account the effects of the PSF broadening and surface brightening limits as described in Calvi et al. [2016]. These findings favour compact sizes for high-redshift galaxies, which is in agreement with studies such as Holwerda et al. [2015].

The star formation rate for the candidates was inferred using equation 1.35, with the conversion factor from UV luminosity to SFR $\kappa_{UV} = 1.15 \times 10^{28}M_\odot$yr^{-1}/erg s^{-1} Hz^{-1} [Madau and Dickinson, 2014]. The values we obtain, log(SFR) ~ 1.2M$_\odot$yr^{-1} are in good agreement with the findings of high-redshift galaxies [e.g., Smit et al., 2012, Rowan-Robinson et al., 2016].

The probability distribution for the three candidates is shown in the right panel of Figure 3.3. This was calculated using BPZ [Benítez, 2000], and by fitting SED templates described in Oesch et al. [2007]. For BPZ, a flat prior on redshift was assumed, motivated by the uncertainty in the density of sources at intermediate redshifts with colours similar to those of $z \gtrsim 9$ galaxies. Our candidates are only detected in the H_{160} band, and their probability is flat over the range $z \sim 10 - 13$. Other candidates were rejected

when applying this step to them as they showed non-negligible probabilities of being lower redshift galaxies. The likelihood of the three final candidates being at $z \gtrsim 10$ are strong.

These galaxy candidates will be used to estimate new data on the bright end of the luminosity function in Chapter 5. It is important to note that the absolute magnitude was calculated assuming a redshift of $z \sim 10$.

This is a remarkable finding as the design of the BoRG[z8] survey was optimised to fin $z \sim 8$. However, we still find a strong pool of candidates that are suitable for follow-up observations.

3.6 Our search RELICS

We applied a selection technique for finding galaxies at redshift $z \sim 8$, $z \sim 9$, and $z \sim 10$. The same procedure regarding source identification we used for BoRG[z8] in Section 3.6 is followed for this survey.

Because the bands available are similar to the ones from BoRG, we use a similar selection criteria, with colour cuts and signal-to-noise.

3.6.1 Criteria

The criteria used to find the galaxies are described below. They were designed after Bouwens et al. [2015b] criteria by adapting them to our bands. As our previous selection for BoRG, we include requirements for solid detection in the bands where flux is expected, absence of flux for the bands in the blue part of the spectrum (passed the Lyman-break), and colour cuts. These colour cuts are aimed to measure the intrinsic colour of the object and the amplitude of the Lyman break in the expected wavelength. We also apply the stellarity cut as we did the BoRG dataset.

- For $z \sim 8$
    1. $S/N_{435} < 1.5$,
    2. $S/N_{606} < 1.5$,
    3. $S/N_{125} \geq 6$,
    4. $S/N_{140} \geq 6$,
    5. $S/N_{160} \geq 4$,

6. $m_{105} - m_{125} > 0.45$,
7. $m_{105} - m_{125} > 1.5(m_{125} - m_{160}) + 0.45$,
8. $m_{125} - m_{160} < 0.5$,
9. `CLASS_STAR` < 0.95.

In this redshift range, the Lyman-break is expected at $\lambda \geq 10944$Å. Therefore, flux is expected in the $F125W$, $F140W$, and $F160W$ filters. However, the flux in the latter can be weaker because of then spectral shape of galaxies, and therefore we relax this threshold. The colour cuts in 6 and 7 are designed to search for a break in between the $F105W$ and $F125W$ bands. The colour in 8 is imposed to discriminate galaxies that show an abrupt break in the spectrum in the bands $F125W$ and $F140W$. The detection band in this search is $F140W$.

- For $z \sim 9$
  1. $S/N_{435} < 1.5$,
  2. $S/N_{606} < 1.5$,
  3. $S/N_{140} \geq 6$,
  4. $S/N_{160} \geq 4$,
  5. $m_{105} - m_{140}) > 1.5$,
  6. $(m_{105} - m_{140}) > 5.33(m_{140} - m_{160}) + 0.7$,
  7. $m_{140} - m_{160}) < 0.3$,
  8. `CLASS_STAR` < 0.95.

  In this redshift range, the Lyman-break is expected at $\lambda \geq 13376$ Å. The first 3 criteria are the same as for $z \sim 8$ galaxy candidates, while 4 requests for a smaller threshold because of galaxy spectra. The criteria in 5, and 6 are aimed at detecting a break $F105W$ and $F140W$ bands. The colour in 7, similar to the previous case, excludes galaxies that show an abrupt break in the spectrum in the bands $F140W$ and $F160W$. The detection band in this search is $F140W$.

- For $z \sim 10$
  1. $S/N_{435} < 1.5$,
  2. $S/N_{606} < 1.5$,
  3. $S/N_{105} < 1.5$,

4. $S/N_{160} \geq 6$,
5. $(m_{125} - m_{160}) > 1.3$,
6. `CLASS_STAR` < 0.95.

In this redshift range, the Lyman-break is expected at $\lambda \geq 10944$Å. As before, the first three criteria are in order to select sources that show no flux in the blue side of the spectrum. Criterion 4 is to ensure a strong detection in the $F160W$ band, which is the detection band, while criterion 4 is a colour cut that ensures a considerable break in the spectrum.

3.6.2 Results

After the application of the selection criteria described above, we obtain a catalogue of 12 candidates at $z \sim 10$, and 9 candidates at $z \sim 9$. However, after visual inspection, we conclude most of these objects are artefacts, and we find no reliable $z \sim 9 - 10$ candidates.

We tried some variations of the criteria for finding candidates at $z \sim 9$ and $z \sim 10$ because of the lack of candidates. These variations included lowering the threshold for non-detections (2.0 instead of 1.5), and the colour cuts. However, the amount of candidates did not improve considerably, and we did not obtain any strong candidates. For $z \sim 10$, we do not use $F140W$ in the first instance, in order to cover a wider redshift range. Some candidates could show different levels of flux, depending on the redshift, so we have a visual inspection. Regardless, we again do not find any strong galaxy candidates.

The reasons as to why there are no galaxies beyond $z \sim 9$ are not well understood yet, but some possibilities are discussed in the next Section. This is similar to the results of Oesch et al. [2018], where only four reliable candidates were found at this redshift within an explored area of ~ 800 arcmin^2.

In terms of $z \sim 8$, we arrive at a catalogue of 3 candidates after visual inspection. However, our final catalogue is composed by only 2 of these candidates, as the third one has a photometric redshift of $z \sim 2$ determined by an alternative search (see Section 3.6.2). The candidates are:

- $RXC142+44-par\_1852$: $RA = 25.8006$, $Dec = 44.5631$, $m_{160} = 26.51$, $m_{140} = 26.97$, $m_{125} = 26.51$, $m_{105} = 99.00$.
- $RXC0232-44\_401$: $RA = 30.0917$, $Dec = -44.3421$, $m_{160} = 25.98$, $m_{140} =$

26.06, $m_{125} = 26.96$, $m_{105} = 27.14$.

Because of the lensing nature of the survey, the magnitudes are likely to be affected by magnification. Therefore, we abstain from calculating properties such as the SFR.

It is important to note that the volume cannot be adequately calculated as the lens models have to be considered for lensed fields. However, we estimate the corresponding volume at each redshift range assuming a flat-field area in order to give a constraint. The volumes are $\sim 4.3 \times 10^5 \mathrm{Mpc}^3$ at $z \sim 8$, $\sim 3.9 \times 10^5 \mathrm{Mpc}^3$ at $z \sim 9$, $\sim 3.5 \times 10^5 \mathrm{Mpc}^3$ at $z \sim 10$.

Alternative Search

An alternative search was performed by Salmon et al. [2017], where they used photometric redshift estimations using the software EAZY [Brammer et al., 2008] and BPZ [Benítez, 2000, Benítez et al., 2004, Coe et al., 2006] for each cluster field. They focus on the selection of galaxies at redshift $z \gtrsim 6$, finding 8 candidates at $z \sim 8$ and no candidates at higher redshift. This is consistent with our findings, which could suggest an abrupt decline in the luminosity function density at higher redshift. However, this can also be attributed to the poorly understood lensing effects in terms of the volume the images cover in comparison to their blank field counterparts, or the way in which photometry changes because of lensing-caused phenomena such as intracluster light.

Two of our candidates are included in their sample, which we show in Figure 3.4. It is important to note that these candidates have a lower signal-to-noise compared to BoRG candidates as we require $S/N > 6$ for RELICS. The photometric redshift estimation for our remainder candidate performed in the alternative search was $z \sim 2$, suggesting it was an interloper. Therefore, we consider our final sample composed by the two candidates that are found also in the alternative search. The other 5 candidates were not identified in our sample because they did not pass our colour cut criterion. A relaxation of this value can be an improvement for our selection criteria. However, we opt for a more conservative approach.

3.7 Summary

We have introduced the observation of high-redshift galaxies with *HST*, giving a brief overview of the WFC3, which is the current camera used for most of these observations. We also presented a summary of several relevant fields that shaped the recent records

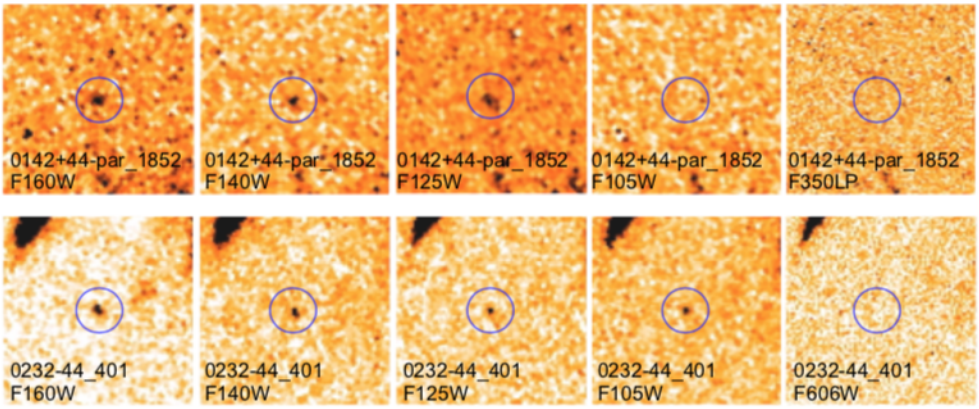

Figure 3.4: Galaxy candidates at $z \sim 8$ from the RELICS dataset that were selected with our selection criteria and are also part of the catalogue in Salmon et al. [2017].

of galaxy discoveries. Furthermore, we have expanded in the workings and features of two surveys, BoRG[z8] and RELICS. BoRG is a survey that aims at finding bright galaxies at high-redshift, $z \gtrsim 7.5$. The strategy consists of making parallel observations of random fields with *HST*. On the other hand, RELICS observed 41 of the most massive galaxy clusters. The goal of this survey is to find high-redshift galaxies at $z \gtrsim 9$ that are intrinsically faint but magnified. Data from these surveys was used to find high-redshift galaxies. We used the dropout selection technique in order to find galaxies at $z \gtrsim 9 - 10$ in BoRG[z8]. Even though the filters used there are optimised to find galaxies at $z \sim 8$, they can also be used for higher redshift. Because of this, we use a selection criteria which is on the conservative side. After the application of the criteria and visual inspection, we end up with 6 candidates, which are reduced to 3 after further inspection in Bernard, Carrasco et al. [2016]. We apply a similar dropout criteria to the RELICS survey. In this case, we find 3 galaxy candidates at $z \sim 8$, and no candidates for higher redshifts. This is an interesting result as it can imply that the luminosity function density declines at $z \gtrsim 9$, that the estimation of volume for gravitationally lensed fields is off, or that the photometry is distorted. Regardless, any of these results are interesting for the planning of upcoming surveys.

4

Completeness Simulations: GLACIAR

Finding galaxies has been a priority in Astrophysics since the construction of modern telescopes. The launch of the *Hubble Space Telescope* (HST) and the installation of the Wide Field Camera 3 [WFC3; Windhorst et al., 2011] in it enabled rapid progress in this area, and led to highly efficient galaxy surveys. Currently, the observation limit has been pushed towards almost the actual time of formation of the first galaxies, at around $z \sim 10$, or ~ 13.4 Gyr lookback time.

In order to understand the internal properties and physical processes that dominate galaxies, detailed studies of individual systems would be an optimal approach. However, due to the limitations of the available technology, spatially resolved studies of individual galaxies are still inaccessible at high redshift, $z \gtrsim 6$. Current studies are limited to finding these objects primarily using broad-band imaging, and thorough examinations cannot be performed on them as individuals yet. Several spectroscopic observation campaigns have been performed to identify emission lines from high-redshift galaxy candidates, and only a few have succeeded ([e.g. Oesch et al., 2016, Zitrin et al., 2014, Coe

et al., 2013]). Accordingly, the majority of studies focus on building photometric samples. Still, this approach gives valuable information, as it provides a statistical insight (that can account and correct for sample contamination), and allows us to estimate the luminosity function. The luminosity function is crucial in order to understand galaxy formation and galaxy evolution and its connection to the assembly and growth of dark matter halos. To measure the luminosity function it is imperative to understand and quantify the recovery fraction of the galaxies we are observing. However, due to the resolution limit of telescopes, not all galaxies will be recovered by the implemented selection methods. Thus, the task of quantifying the fraction of galaxies these studies are unable to find is very important. This is not only relevant for the luminosity function, but also to understand the selection biases, i.e. the type of populations that are being preferentially recovered with the selection methods.

This chapter describes the algorithm we created to estimate the completeness in galaxy surveys, GaLAxy survey Completeness AlgoRithm, `GLACiAR` , [Carrasco et al., 2018]. The algorithm is written in Python, and it simulates galaxies following user-defined features. It then places these mock galaxies into science images and their recovery rates can be studied. This open source code can also be used to study the kind of populations that are being preferentially recovered by a specific selection method, and it can be used to fine-tune the selection criteria in case of redshift estimation, for example. Another option that can be exploited is the study and modification of the best parameter for the source identification software.

The organisation of the chapter is as follows. An overview of the subject is presented, along with previous work in the area. Afterwards, details of the concepts needed to create the simulated galaxies, such as the luminosity profile, are outlined. In Section 4.4 we explain how the artificial galaxies are produced, reviewing their spectra, the positions in which they are placed, convolution, the addition of the sources to the real data and their identification. Then, the required specifications for the code, including files and parameters needed for the code to run. It follows a description of the produced files, including the images, catalogues, segmentation maps, tables, and plots. We finally touch on redshift selection, which we explain with one example. Section 4.1.1 puts all the pieces from above together and a detailed description of the software is given here. Finally, we discuss about the future of the code and how it can be applied to other surveys and the inclusion of the gravitational lensing effect.

4.1 Overview

A simple diagram of the outline of `GLACiAR` is presented in Figure 4.1. The code works as follows: simulated galaxy stamps are created following a Sérsic luminosity profile. The set of requirements include the parameters (described in Section 4.5.2), which mainly define the physical characteristics of the artificial galaxies; the science images of the survey for which the completeness is going to be calculated; and the parameters file for running the Source Identification software, which in the case of the first release is `SExtractor` [Bertin and Arnouts, 1996]. Depending on the configuration required for it, the user might need to provide the rms maps or weight images. We expand more on this in Section 4.5.1.

The motivation for developing `GLACiAR` stems from the fact that there are several high-redshift galaxy surveys, and completeness simulations are needed for all of them. Until now, this has been done independently for each team analysing the data, but there is no available open-access tool to easily reproduce the results by the community. Thus, our aim is to have one open code that can be applied to these surveys and unify this process. This will be very helpful as it will allow for insightful and comprehensive comparisons between different studies.

4.1.1 Description of the code structure

In order to estimate the completeness of a survey, it is necessary to quantify the fraction of galaxies that are not being detected. To do this, we wrote a `python` code that simulates artificial galaxies with the features of galaxies that are being studied. These simulated objects are added to the images of the survey. Afterwards, a source identification software is run over the original science images and the images with the simulated sources. This way, both catalogues can be compared and the fraction of recovered artificial galaxies can be measured.

A simulated galaxy is created by following the recovered characteristics given by the user through a parameters file (see Section 4.5.2). The software first reads the parameters and creates a galaxy following a luminosity profile described in section 4.3.

The first step is to read the number of times this process is repeated. There are four main components to this: number of iterations n_i, redshift n_z and magnitude bins n_m, and number of fields n_f. For each redshift bin, there are n_m magnitude bins, and for each magnitude bin there are n_i iterations. This whole process is done for all fields.

Figure 4.1: Overview of main steps in the `GLACiAR` code.

Therefore, the total number of times a new image N_T is created corresponds to:

$$N_T = n_f \times n_z \times n_m \times n_i. \tag{4.1}$$

For each image, there is also a number of galaxies placed in it, n_g. Going down in hierarchy can be represented as $n_f \rightarrow n_z \rightarrow n_m \rightarrow n_i \rightarrow n_g$

The code first enters a loop that runs for each field, i.e. n_f times. After that, there is another loop for the redshift bins n_z. In that step, the spectrum of a galaxy is created with the given input redshift. Then, according to the redshift, the effective radius of the galaxy is assigned, R_{eff}. This scales inversely with the redshift by $(1 + z)$ as it is explained in Section 4.5.2. Then, all possible required combinations of artificial galaxies are created. The amount of possible galaxies N_G will depend on the number of possible inclination angles, n_θ, the amount of possible eccentricities n_e. For each type of galaxy (i.e. Sérsic index), this number is:

$$N_G = n_\theta \times n_e \tag{4.2}$$

It is important to note that there are some characteristics of a galaxy that will only scale the flux in each band while maintaining the distribution of the luminosity, i.e. the ratio among the value of the pixels. We consider this in order to save time when creating the artificial galaxies and multiply the source pixels by a scale factor. For example, galaxies with different Sérsic indexes will have different distributions of light so, in that case, a new set of galaxies for every inclination angle and every eccentricity is needed. It happens the same with the redshift, eccentricity, and inclination angle. For the redshift, this is because the luminosity profile depends on the effective radius R_{eff}, as we can see in equation 4.4.

There is one special case that can be specified in the parameters file, which corresponds to $n = 4$, or a de Vaucouleur profile ([de Vaucouleurs, 1948]). The motivation for this special case comes from the fact that the majority of elliptical galaxies are expected to have this kind of profile. These elliptical galaxies tend to be circular, and it could be the case that the user wants a distribution of galaxies with different Sérsic indexes, where one of them is $n = 4$. The user could want the galaxies with $n \neq 4$ to have a range of eccentricities and inclination angles, but still want the de Vaucouleur type of galaxies to be only circular shaped. In that case, the boolean parameter de_Vaucouleur is set to 'True' and the galaxies with $n = 4$ are only circular.

After the array with the set of galaxies is generated and saved, the code continues ahead. For each set of galaxies, there is an assigned input magnitude. This is not technically its final input magnitude as that will vary with the slope of the spectrum β described in Section 4.4.1. With the preliminary assigned magnitude m_0, the code now enters a loop for the number of iterations n_i. Realistically, each of the galaxies in each iteration will have a different slope, but this is computationally expensive, so we take a slightly different approach. For each iteration, we keep β fixed. This yields a similar distribution of beta for the total amount of galaxies at that redshift and magnitude. The only difference is that they are being placed in the same image. It is important to note that each iteration is not significant on its own. We only break the number of galaxies inserted into iterations and save them in different images to avoid overcrowding them and distorting the background measurements and therefore photometry. For this reason, a fixed β in each iteration makes no substantial difference. The code generates a random number following a Gaussian distribution

$$\phi(x) = \frac{1}{\sigma\sqrt{2\pi}} e^{-(x-\mu)^2/2\sigma^2} \tag{4.3}$$

where μ is the mean of the distribution, and σ is the deviation of the distribution. Both are chosen by the user. Afterwards, all the specifications needed to generate a mock spectrum are given. With the central wavelength of the detection band, the redshift, preliminary input magnitude, and β, the spectrum is set.

In Figure 4.2 we see an example spectrum. We also see four *HST* filters. Depending on the filter (wavelength, transmission efficiency, width), the amount of light collected by it will vary. `GLACiAR` takes that into account, so after producing the spectrum, the code then enters the loop for the number of bands, and the amount of light expected to be observed in each filter is calculated. To do so, the response curves are required. As detailed in 4.5.1, `GLACiAR` includes some filters, the most used ones for *HST*, but the user can add their own following the format. Depending on the given β the expected magnitude varies. Thus, the preliminary input magnitude will not be necessarily equal to the magnitude input in the detection band, and it will change slightly with the β. As this is the actual magnitude we are concerned about, we use the preliminary input magnitude as a guide, but record and work with the final input magnitude. After the calculation of the expected magnitude in each filter, we transform that into flux by using equation 4.11. We know that the total flux only changes the stamp by a scale factor, and not the distribution of this. Thus we record the factor that makes up for the difference between the input magnitude of the stamp (which we set to $m_{AB} = 24.0$), and the final input magnitude. We then generate three arrays the size of the amount of inserted galaxies: one with the (x_0, y_0) position of the galaxies (see section 4.4.2); one

with random numbers in the range of the amount of available/required eccentricities; and the same for inclination angles.

For each galaxy now there is an indicator of its position, eccentricity and inclination angle. These are all individual for each galaxy. There is also a common feature for all the galaxies in one iteration, which is the factor for which the flux has to be scaled that is associated with the slope of the spectrum, β.

For each of these bands, the original image taken with that filter is open. Also, a new empty array with the size equal to the size of the image (in terms of pixels) is created, while the array corresponding to the image and its respective header are stored as well. Then, if the expected measured magnitude of a galaxy in a certain band is fainter than 50, $m_{AB} \geq 50$, the frame (new empty array) is saved as such, i.e. with all cells values equal to 0 for the corresponding band. If not, the galaxies are placed in this empty frame.

Each galaxy will have its own eccentricity and inclination angle. The module first takes the random numbers corresponding to the eccentricity and inclinations. Each set of created galaxies has a galaxy for each possible combination of these two features and the Sérsic index. Knowing these three parameters for each galaxy, the corresponding stamp is assigned according to the input eccentricity slice, inclination angle slice and n. As mentioned before, for $n = 4$ there is the possibility of no eccentricity or inclination angle required, in which case the other two features are not taken considered, and the standard galaxy produced for the corresponding R_{eff} is assigned. These galaxies are taken from the stamp set, scaled according to the flux difference, convolved with the corresponding PSF, and then placed in (x_0, y_0) in the new empty frame. What the module returns is the new frame with the corresponding galaxies. This new frame is added to the respective image in that band, and there we have our new image, i.e. an image with the observed data plus new galaxies. After this, the created frame with the new simulated galaxies is added to the image that was saved and stored before and it is saved with the same header. As pointed out in 4.6.1, this new image is only saved temporarily as it consumes a large amount of space.

Now, the new image information is ready to be extracted. In order to do so, `SExtractor` runs on the original image first, creates a catalogue as explained in Section 4.6.2, and then runs over all the new images. In fact, the process of the identification of the sources is embedded in the loop of the number of bands. Thus, for each band, the catalogue and respective segmentation maps are generated, according to the parameters set by the user for the sources to be identified with `SExtractor`. After this is done for all bands in one iteration, the code identifies the status of each of the sources placed in

that iteration. This information is recorded in the tables described in Section 4.6.4. A file ready to save the information of all the inserted sources is open for each redshift bin. For each iteration, all the inserted galaxies are saved with their input and output features along with their detection and blending status. In the same way, another file with the information recovered from the simulated galaxies is saved. The information is obtained by finding the ID number corresponding to that source, which is obtained from the segmentation maps by looking over a grid of dimension 7×7 pixels with the centre in the pixel where the galaxy was initially intended to be placed. By looking at this area, the code decides whether an object is indeed detected or not, and if detected, its blending status can be found as well. Now, the next section is only done depending on whether the user wants to add a dropout technique selection. If so, the colours and signal-to-noise S/N of the object are examined, and if they pass a selection criteria they are flagged as dropout. This status also goes in the text file mentioned before.

After repeating this process for each redshift bin and the embedded magnitude bins, there is another text file that has been opened, which will store the statistics. In this case, there is a line for each magnitude bin. All the iterations are considered within each of these lines. To do so, we count the number of total inserted galaxies with the corresponding features, i.e. $n_i \times n_g$. After that, we count the number of galaxies for each detection status over all the performed iterations, and calculate the number of them considered recovered. That includes mock galaxies detected and isolated, blended with fainter objects, and blended with brighter objects that are overlapped by 25% or less. The next column includes all the galaxies that were classified as dropouts in the redshift range expected (if requested), and then the fraction of recovered galaxies, the fraction of dropouts, and the fraction of dropouts over recovered.

There is an extra step, which includes plotting. A final product of `GLACiAR` is a plot for each field that contains the input magnitude as x-axis and the redshift as the y-axis. There is also a plot produced in case the dropouts option was chosen as True. Again, this module `plot` can be modified to satisfy the user requirements.

4.2 Completeness

We define the completeness as the fraction of successfully identified sources over the total number of sources.

In our case, we slice this in magnitude and redshift bins. Therefore, the recovery fraction is estimated for each redshift and each magnitude, being a function of them.

4.2.1 Previous Work

When constructing the luminosity function with observational data, the completeness and source recovery efficiency need to be estimated. As stated before, the lack of unification for this procedure is a problem as it is done in a different manner for every survey. Furthermore, the way this is done in some cases is not comprehensive and cannot be revised, potentially making it challenging to reproduce results independently.

Two main approaches have been implemented for completeness simulations in the past. Both of them involve inserting mock galaxies into the observed images and studying the recovered fraction. The main difference of these methods originate in the type of simulated galaxy. The first technique uses images of galaxies acquired in observations with similar characteristics but for example at a lower redshift, that are modified or rescaled to fit the desired properties of the sample to simulate. Examples of this method include Bershady et al. [1998], Imai et al. [2007], and Cristóbal-Hornillos et al. [2009]. The second approach consists of the creation of artificial light profiles from theoretical models of the expected surface brightness profiles. Examples of luminosity function studies utilising this approach are Bowler et al. [2015], Oesch et al. [2014], and Jiang et al. [2011], among others.

For `GLACiAR`, we use the second approach due to its flexibility in terms of the features required for the simulated galaxy. Since we do not have a full understanding of the population of galaxies at high-redshift yet, it is possible that the dominant population has certain characteristics that are not commonly observed at lower redshifts. If the first method is used, images of these galaxies are needed and it's possible they may not be available, or the sample may not be complete enough. Also, there is the possibility that we want to explore different populations, and in that case, being able to tweak the parameters is a very important feature. Both methods are appropriate if used only for one case as they can be tailored for that. But, if an approach that can be modified according to the needs of different surveys with different features is required, the second approach is by far more appropriate.

We describe the luminosity profile of our artificial galaxies in the following section.

4.3 Sérsic profile

Galaxies have a luminosity distribution, which describes the light emitted by the galaxy as a function of its radius. This distribution is not uniform, and in fact, it can be described by an empirical model. This model was first proposed in [Sérsic, 1968], and it

is called the Sérsic luminosity profile. The definition of the light intensity as a function of the radius can be described by the formula

$$I(R) = I_e \exp\left\{-b_n\left[\left(\frac{R}{R_eff}\right)^{\frac{1}{n}} - 1\right]\right\}, \tag{4.4}$$

with I_e being the intensity at the radius that encloses half of the total light, R_{eff}; n is the Sérsic index, which describes the shape of the profile, i.e. the concentration factor of the light; and b_n is a constant defined in terms of this index, which follows from our choice to normalise the profile with I_e.

To obtain the luminosity of a galaxy within a certain radius, we follow the approach by Graham and Driver [2005] integrating equation (4.4) over a projected area $A = \pi R^2$,

$$L(< R) = \int_0^R I(R')2\pi R' dR' \tag{4.5}$$

We obtain

$$L(< R) = I_e R_{eff}^2 2\pi n \frac{e^{b_n}}{(b_n)^{2n}}\gamma(2n, x) \tag{4.6}$$

where $\gamma(2n, x)$ is the incomplete gamma function, defined as:

$$\gamma(2n, x) = \int_0^x e^{-t} t^{2n-1} dt \tag{4.7}$$

and

$$x = b_n \frac{R}{R_{eff}}^{\frac{1}{n}}. \tag{4.8}$$

To calculate b_n we follow Ciotti [1991], and taking the total luminosity we obtain:

$$\Gamma(2n) = 2\gamma(2n, b_n) \tag{4.9}$$

where Γ is the complete gamma function, defined as:

$$\Gamma(2n) = (2n-1)! \tag{4.10}$$

From 4.3, the value of b_n can be obtained.

There are two particular cases of this profile that are relevant, as they can correlate with the morphology of the galaxies. These two cases are described below:

$n = 1$, this is an exponential profile, and it is been shown to describe dwarf ellipticals

and galaxy disks.

$n = 4$, this corresponds to a de Vaucouleurs profile [de Vaucouleurs, 1948], and it characterises mainly bright elliptical galaxies.

4.4 Generation of artificial galaxy stamps

The generation of the artificial galaxies is broken down into modules. First, a modelled galaxy stamp is created. The description of the stamp is below.

We consider a grid of equal size as the stamp. The cells in this grid correspond to pixels. Therefore, the value in each of the cells is the flux of the galaxy in the corresponding pixel. In Section 4.3, we have explained the brightness profile that will be used. As seen in equations 4.4 and 4.6, the variables on which the luminosity depends are I_e, the effective radius R_{eff} and the Sérsic index, n. The last two parameters, R_{eff} and n, are chosen by the user, whereas the first one is calculated from equation 4.3 since the value of $L(< R)$ is known. The total flux of the artificial galaxy is inputted by the user as the desired magnitude, which can be transformed into flux by the following equation:

$$F_x = 10^{\left(\frac{m_{x,0}-m_x}{2.5}\right)}, \tag{4.11}$$

where F_x is the flux in the band x, m_x the magnitude in the same band, and $m_{x,0}$ is the zeropoint magnitude in that band as well.

For a simulated galaxy, the flux for each pixel is calculated following equation 4.6. To do so, the radius R we consider is the size of the galaxy. The concentration of the luminosity in the centre will be dictated by the value of n. Since the integral (equation 4.6) is considered for an infinite size, there will be some lost flux when we integrate this value over a determined radius. However, since the distribution of the light in a realistic galaxy is accumulated in the centre of the galaxy, the total flux that is lost is negligible. The radius R_{eff} scales with the redshift, which is explained in more detail below. This means that for a different redshift bin, there will be a different light distribution, same with a different n. As we can see in 4.4, and 4.6, we integrate the flux for each pixel, where R is the distance from the pixel to the centre of the galaxy. This is computationally expensive, thus we re-use the generated sources as much as possible, i.e. produce stamps of them that can be scaled for some with different characteristics, for example, a galaxy with the same n, R_{eff}, inclination angle, eccentricity, but different flux.

The diameter of the stamp d_S is determined by the user-defined values of R_{eff} and

$size_pix$, and it is calculated as

$$d_S = R_{eff} \times size\_pix \times 325. \tag{4.12}$$

This is an arbitrary measurement, where 325 is the scale factor needed for a galaxy stamp with default BoRG galaxy to have a diameter of 28 pixels. This was chosen after trying different sizes and comparing to sizes of real galaxies. The dependency on the effective radius implies that for low redshift galaxies the stamp size will be larger. This is because an important fraction of the flux can be loss for extended galaxy if the its size is not taken into account.

4.4.1 Spectrum

In order to estimate the flux expected to be measured in each filter, a mock spectrum of a galaxy is created. The required parameters for the creation of the spectrum are: redshift; magnitude; lambda detection, which is the central wavelength in angstroms of the detection bands; and β, which defines the slope of the spectrum.

The module that constructs the spectrum is `creation_of_galaxy.write_spectrum`. An array corresponding to the wavelength, in Angstroms, is created, with a range of $\lambda = 0 - 30000$ in steps of 1 Å. The flux F of the spectrum is defined as a function of the wavelength λ as

$$F(\lambda) = \begin{cases} 0 & \lambda \leq 0 \\ a\lambda^{\beta} & 1216 \leq \lambda \end{cases} . \tag{4.13}$$

This spectrum corresponds to the one of Lyman break galaxies (see Chapter 3), which is based in the existence of a break at a rest wavelength of $\lambda = 1216$Å produced by the absorption of photons by neutral hydrogen in the Universe. This spectrum is then normalised in order to match the required flux. In fact, the flux assigned to it is arbitrary, being a preliminary input magnitude, which will later change with the β. This will only change the cells values by a scaling factor, therefore it is not relevant while creating the source as it means that the shape of the spectrum will not change, only its *height* in the y-axis. The spectrum is temporarily saved in a .fits file 'spec.fits'. An example of a spectrum produced by `GLACiAR` can be seen in Figure 4.2 along with the galaxy corresponding to that spectrum inserted into the science images of the BoRG survey BoRG-0835+2456 for the four filters of the survey: F606W, F098M, F125W, and F160W. The characteristics of the galaxy consist of a Sérsic index $n = 4$, an apparent magnitude of $m_{AB} = 24.0$, inclination angle $i = 0°$, and eccentricity $e = 0°$.

The relevance of this spectrum is because the estimated flux of the galaxy in each

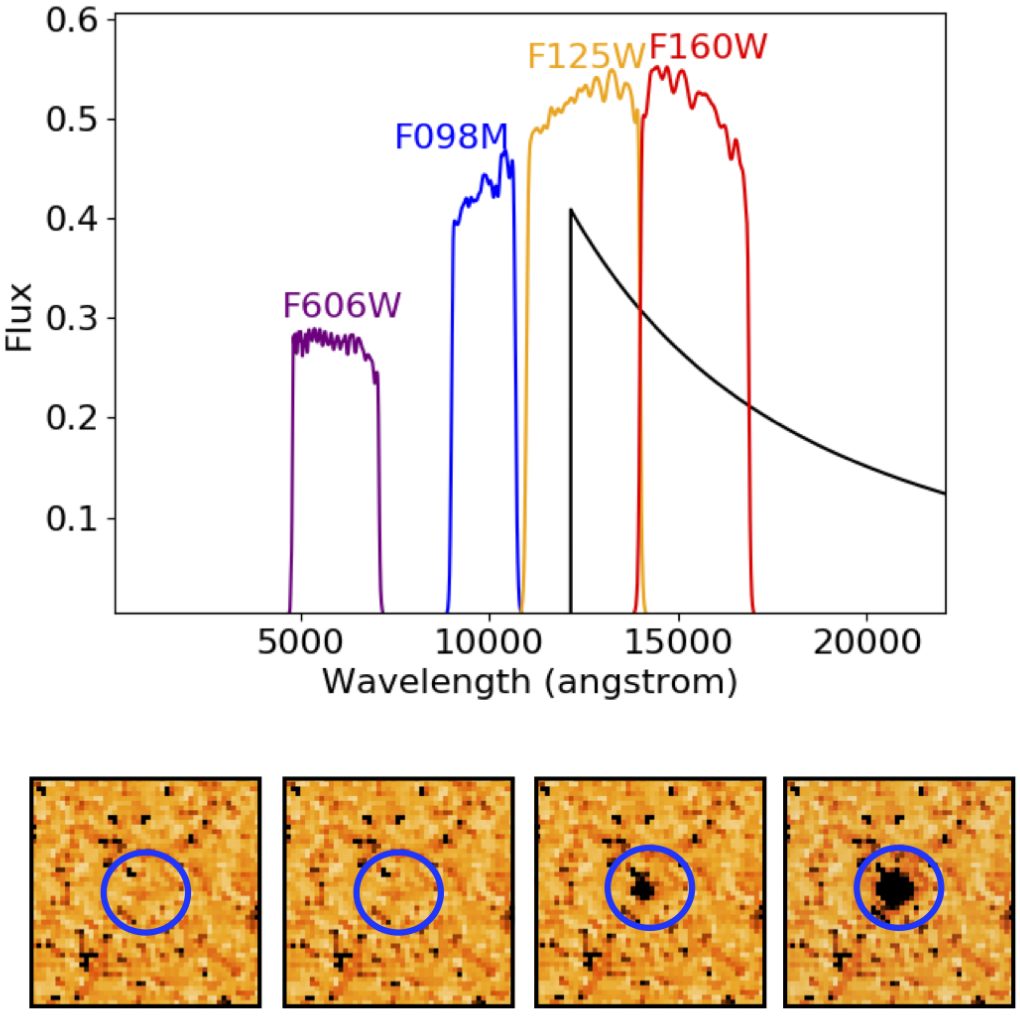

Figure 4.2: *Top:* Spectrum of a simulated galaxy at $z = 10$ and with $\beta = -2.0$ produced by `GLACiAR` in arbitrary units of flux as a function of wavelength, with four *HST* filter transmission curves superimposed (F098M, F125W, F160W, and F606W). *Bottom:* Source from above inserted into the F606W, F098M, F125W, and F160W science images (from left to right) from field BoRG-0835+2456 assuming a $n = 4$ surface brightness profile and $m_{AB} = 24.0$ with no inclination and circular shape. The stamps have a size of 3.6"×3.6".

band will be measured from here. To do this, the code uses the module `pysysp` from `pyPI`, which calculates the amount of flux received for each filter. This module contains some bands already, and we include some more in the folder *Filters*. What there is in the files is the response of the filter as a function of the wavelength. This, together with the saved simulated spectrum gives an estimated measured magnitude.

4.4.2 Position

The position of the galaxy corresponds to the pixel in which the centre of the galaxy is placed. This is, in mathematical terms, a pair of points (x, y) that follows a random distribution of the same size as the image.

The only limitation for the placement of the galaxy is the avoidance of the edges in the image. Frequently, the science images are tilted with respect to a square in the fits file. As a result, the edges contain sections of the image that have no information as it is an area that has not been observed. There are also cases in which the images are taken with different cameras but have the same size, with the smaller of these images having pixels with zero flux. Placing sources there will introduce uncertainties as it, for instance, could modify the measured values for the background. In order to avoid this, the value of pixels from the science image are checked. When a pair of pixel coordinates is randomly generated, the value of the pixel in the observed image $\texttt{data}[x_0, y_0]$ is checked, and if the value is 0, it is discarded as that is the value on the edges of the image, therefore a new pair is generated. It is important to note that not all pixels where $\texttt{data}[x_0, y_0] = 0$ are part of the edges, there are some of these within the observed data. However, since they are in random positions, this condition does not introduce any bias. It can be argued that this will alter the results as it could produce that the bad pixels are avoided. However, this is not a problem because the simulated sources can still occupy some of those pixels since the condition is only imposed for the central one. Therefore, other parts of the created source can be on one or more of those pixels. In fact, this was tested by avoiding the edges by imposing geometric conditions and using the $data[x_0, y_0] \neq 0$ and the results do not vary any more than a normal deviation from the finite amount of iterations.

When the amount of n_g of pairs of coordinates is reached, the random number generator stops. The format in which the positions are generated is an array of the size of $[2, n_g]$, where 2 is the coordinates x and y, and n_g is the length or number of positions, having $2 \times n_g$ elements.

4.4.3 Convolution

The point spread function (PSF) describes the imaging system response to a point input.

Reproducing the way in which the galaxies will be observed requires that the mock galaxy is convolved with a point spread function (PSF). This PSF is unique for each filter as it takes the instrumental response into account.

In order to do the convolution, we first need the image with the PSF, which we get with the Tiny Tim HST PSF Modelling code[1] for the surveys done with *HST*. The software includes a folder 'psf' that contains some of the more used bands for *HST*. If the user is working with filters not listed in the code, the corresponding files can be added to that folder.

The convolution is done with the Python module `convolution.convolve`, from `Astropy`, which is a direct convolution algorithm.

After the convolution the galaxies are added to the images in the positions (x,y) described in 4.4.2.

4.4.4 Addition of the galaxy stamp

Adding the simulated galaxies to the science image is the next step after having generated the stamps and storing their central positions in the science image. In order to place the galaxies, the science image is opened and its data and header are stored. A new empty array with the same dimensions as the data is created. The galaxy stamp that matches the requirements for the simulation (i.e. eccentricity, inclination angle, redshift, among others) is added to the new empty array in the position that was generated by the code. The stamp has to actually be multiplied by a scaling factor, which correspond to the difference between the standard flux with which the stamps were generated, and the input flux that is defined by the slope of the spectrum β. The frame is then added to the science image and the new image with the simulated galaxies is temporarily saved.

The bottom row of Figure 4.2 shows a galaxy stamp inserted into the science images of the BoRG survey BoRG-0835+2456.

[1] http://www.stsci.edu/hst/observatory/focus/TinyTim

4.4.5 Identification of the sources

In order to identify the sources, we use the software `SExtractor` [Bertin and Arnouts, 1996]. This software finds the peaks of luminosity in the image and demarcates between background and sources with its properties such as size. This is run over the observed science images, which are the processed and reduced images taken by *HST*, and it creates a catalogue with the real sources. It then does the same for the new images, which are the original science images with the addition of artificial galaxies created by `GLACiAR` in the process that was explained above. A comparison is needed in order to distinguish the new found sources from the old ones. As expected, the addition of sources can change the value of the background and produce small differences in the measured characteristics of a source, hence comparing the two catalogues is not a trivial process. The optimal procedure would be to superpose both catalogues and flag the sources that are found inside a certain limit, but that is not effective in terms of computational resources. Instead, we use the segmentation maps.

The segmentation maps are images of the same size as the observed images with information of the identified sources and the background. All the pixels with values of zero are what `SExtractor` considered background, while the rest of the pixels are assigned an integer value, which corresponds to the ID of the detected source. Comparing these maps allows the identification of newly detected sources. We will call the segmentation maps of the real sources *original image segmentation maps*, and the ones of the images with the simulated galaxies included *new simulated segmentation maps*. However, to compare them is not straightforward. Ideally, a source that is repeated in both segmentation maps would have the same ID number identification, but that is not the case. Furthermore, if there is blending of two or more sources, it is possible that the original source changed shape, size, luminosity, or other features. Instead of trying to identify the original sources, the approach is to identify the simulated new ones. In order to do that, the list of the position that was assigned to the galaxy is used to check whether a source was identified in that position in the new images. This approach raises two issues.

First, the artificial galaxy could have been placed on top of an older source as there is no limitation to avoid old sources. This issue is related to blending and it is discussed in Section 4.4.5. The second issue is that the artificial galaxy can be off by a certain distance from the recorded input position. Since measuring distances is computationally expensive and inefficient we implement a search grid approach.

In detail, the software goes to the position in which the galaxy was initially placed

(x_0, y_0) and searches for the value of this position in the new segmentation maps over a grid of 7×7 pixels, i.e. the search encompasses all pixels $[x_0 - 3 : x_0 + 3, y_0 - 3 : y_0 + 3]$. If the value of all those pixels in the new segmentation map is equal to 0, the source is classified as 'Not detected', which in the catalogue corresponds to a flag of 3. If not, a second check to ascertain the status of the source is carried out. As mentioned before, there is the possibility of the artificial source being blended (see Section 4.4.5). To first distinguish whether an object is blended or detected in isolation (i.e. with no blending and labelled as 0), the code searches for values different than 0 in the new segmentation map over the same 7×7 grid, $\texttt{NSM}[x_0 - 3 : x_0 + 3, y_0 - 3 : y_0 + 3]$ and it records them. If more than one value is different from 0, the value closest to the central pixel in which the galaxy was placed (x_0, y_0) is recorded. Now, after obtaining this new ID number, `GLACiAR` finds all the pixels that have that value, demarcating the source. It then flags all those pixels, (x_{NG}, y_{NG}), and goes to the original segmentation map where it checks the values of those pixels, $\texttt{OSM}[x_{NG_0} : x_{NG_n}, y_{NG_0} : y_{NG_n}]$. If all the values are 0 (the sum of all the values is 0), the object is labelled as detected and isolated, ($\texttt{label} = 0$) since there was no object previously there. If that is not the case, the object is classified as blended.

It is important to note that the search grid can be easily changed by the user.

Blending

Blending is a considerable issue in the detection of sources as classifying an object is a complex task. Summarising what was explained above, the code enters to check blending if the value of any of the pixels in which the new source is identified is different from zero. If that is the case, it checks the magnitude of the old source and the degree of blending, that means, the percentage of physical overlapping. This process is divided into three steps:

1. Identifying the old source by checking its ID number.

2. Comparing the magnitudes: the code opens and reads the catalogues of the original science images and identifies the object that has the ID number obtained in step 1. The magnitude (`MAG_AUTO`) is recorded and compared to the input magnitude of the new artificial source with which is blended. If the original source is fainter, the object is considered detected and it is labelled as blended with a fainter object ($\texttt{label} = 1$).

3. Checking blending with brighter object: This stage is only entered by the objects

that are blended with a previously known brighter object. However, since the concept of blending is not straightforward, the fact that two sources are next to each other does not mean they are physically blended or that the photometry will change.

After some tests, we came up with something that takes into account the percentage of physical overlap and also the change in the initial brightness. The code finds all the pixels with the number of the old source that was previously in the location of the new source and counts them. Then, it compares them to the amount of pixels covered by the new source. If the difference is over 25%, or in other words, if the amount of overlaps of the two sources is over 25%, the objects are considered as not identified. In the same vein, if the input magnitude and the detected magnitude differ by over 25%, the object is discarded and considered as not identified. If only one of these conditions is not reached, the object is considered as not blended as well.

We allow the blending with fainter previous objects and consider them detected anyway as the impact this is going to produce in the photometry is not considerable and it will not affect the colours of the source. We expand more on this later.

A comprehensive diagram of the code is shown in Figure 4.3 where blending is explained in more detail.

4.5 Requirements

The code has been programmed for `Python` version 2.6 and 2.7. It uses the packages `Numpy` [Oliphant, 2006], `Astropy` [Price-Whelan et al., 2018], `SciPy` [Jones et al., 2001], `pysysp`[2], `matplotlib` [Hunter, 2007], `pickle` , yaml [3]

`GLACiAR` also requires as a list of files and a set of parameters to fill out. These are described in Sections 4.5.1 and 4.5.2, respectively.

4.5.1 Files

Described below are the files needed to run `GLACiAR` .

- Science images: All the .fits files with the observed images of the survey including all the fields and filters in which the fields were observed. It typically includes

[2]https://github.com/mdusilva/pysysp
[3]https://yaml.org

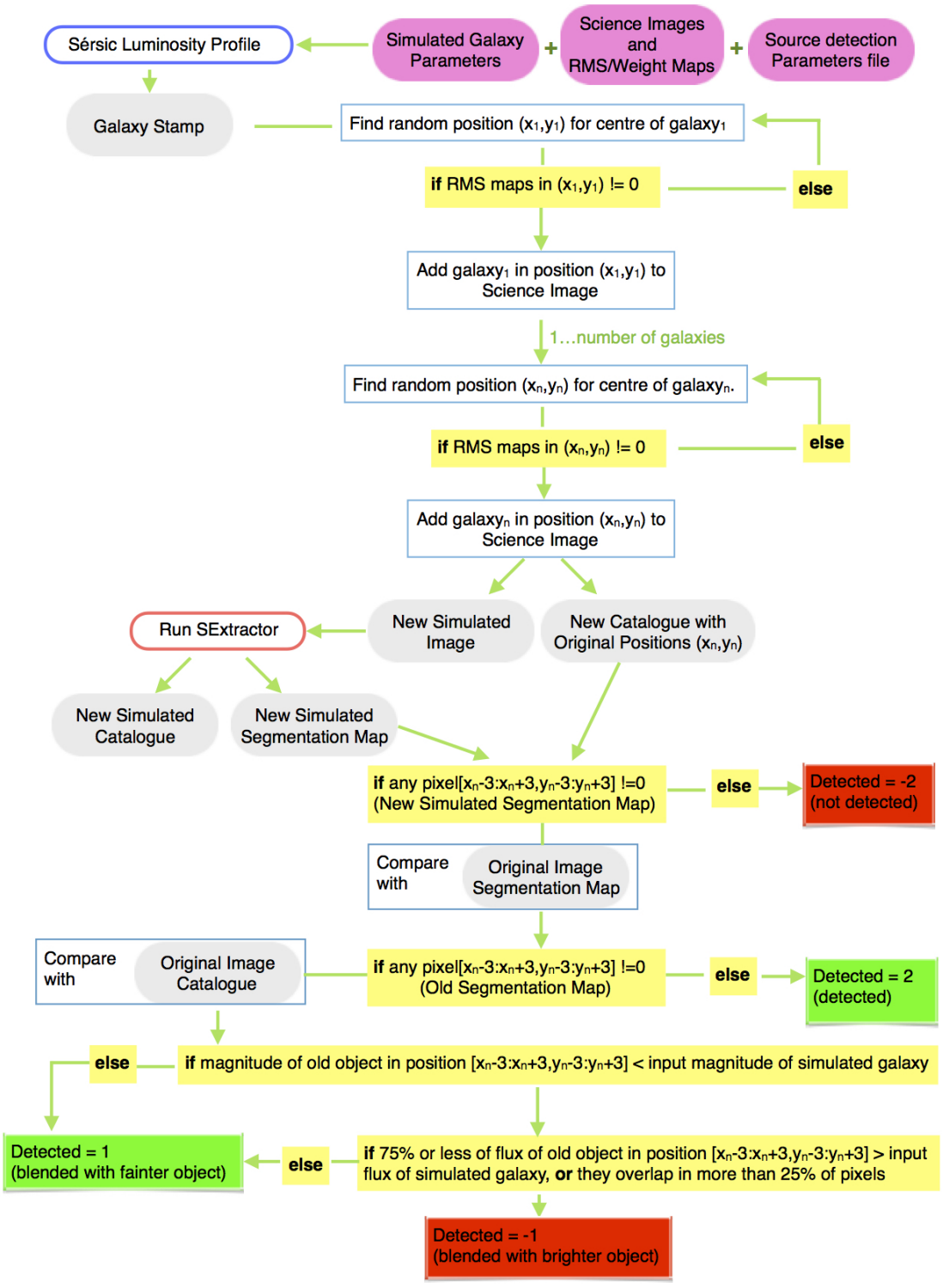

Figure 4.3: Detailed diagram of the steps followed by `GLACiAR`

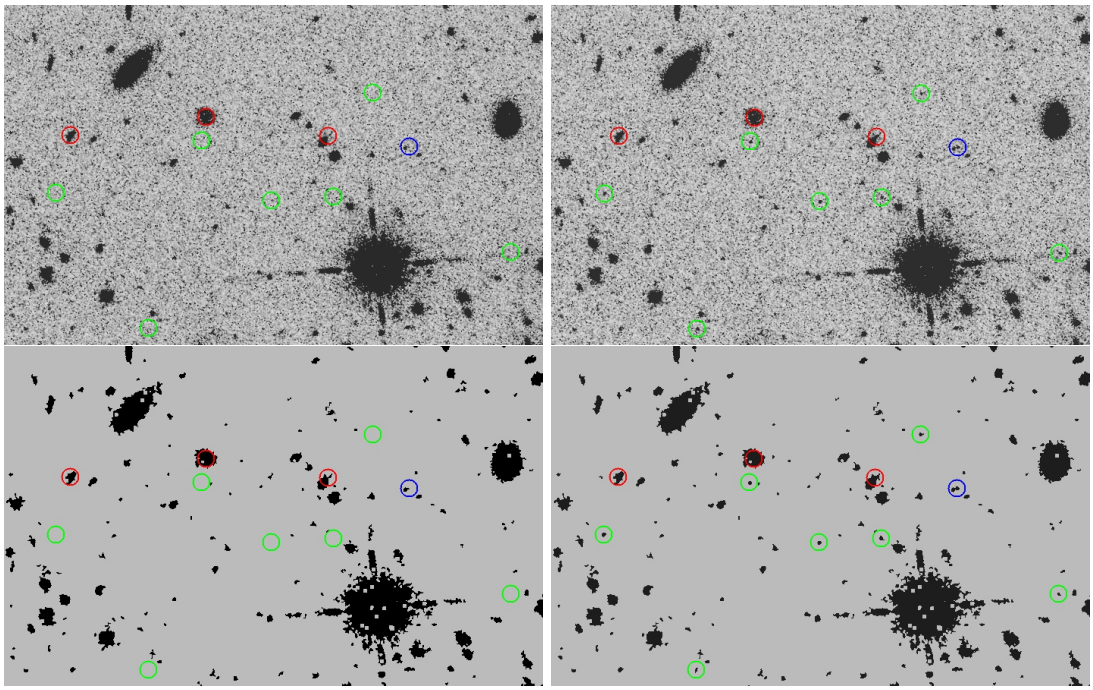

Figure 4.4: Illustration of `GLACiAR`'s application to BoRG field *borg_*0835+2456. *Top left:* Original science image. *Top right:* Science image plus simulated galaxies with an input magnitude of $m_H = 26.0$ indicated by coloured circles. *Bottom left:* `SExtractor` Segmentation map for the original science image. *Bottom right:* Segmentation map after running `SExtractor` on the image that includes simulated galaxies. The colour of the circles encodes detection of the simulated sources with green indicating recovery for an isolated galaxy, blue recovery but source blended with a fainter object. Detection failures are shown in red.

several fields and several filters, although one of each is enough if that is needed.

- List: Text file with the names of the fields from the survey. This list is given as an input parameter (see Section 4.5.2). This list has a minimum length of 1, i.e. the name of one field.

- `SExtractor` parameters: As explained in section 4.4.5, one of the steps of the code involves running `SExtractor` on the images (original and with simulated galaxies). To run the software, a file defining the parameters is required. There is an example provided under the folder 'SExtractor_files', which will be used if no other file is provided, but it is recommended for the user to change it according to their observations.

- RMS maps or weight maps: These are frames having the same size as the science image that describe the noise intensity at each pixel. They are defined as:

$$weight = \frac{1}{variance} = \frac{1}{rms^2} \tag{4.14}$$

  Although they are necessary only if required for the `SExtractor` parameters, it is strongly recommended that one of these is used, as it will improve the source detection.

- PSF: As mentioned in Section 4.4.3, this corresponds to the image of the PSF that we are going to use to convolve with our simulated galaxy. It depends on the instrument, telescope, and filter. Some PSFs are included with `GLACiAR` , but the user should add their own if needed.

4.5.2 Parameters

There is a set of parameters that define the features of the simulations. Some of these parameters are required, while other can be left blank and assigned a default value.

- n_galaxies: Number of galaxies. In every image, the simulation will place a determined number of galaxies per iteration. After that, the image will be saved and the source identification software will be run on it. In summary, this parameter is the amount of galaxies per image. (`default` = 100)

- n_iterations: Number of iterations. For each redshift and magnitude, n_galaxies will be placed in an image. The number of times this is done corresponds to this parameter. (`default` = 100)

- mag_bins: Number of bins for the input apparent magnitude. The completeness

is studied over a magnitude range divided by a certain number of bins, which are defined by this parameter. For example, for a simulation run from $m_1 = 24.0$ to $m_2 = 25.0$ in steps of 0.2, there will be 6 bins. (`default` = 20)

- min_mag: Brightest magnitude for the artificial galaxies. This is the brightest magnitude that the sources of the simulation will have. (`default` = 24.1)

- max_mag: Faintest magnitude for the artificial galaxies. This is the faintest magnitude that the sources of the simulation will have. (`default` = 27.9)

- z_bins: Number of bins for the input redshift. The completeness is studied for a range of redshifts, which are divided by a number of bins. These bins are defined by this parameter. For example, for a simulation run from $z_1 = 9.5$ to $z_2 = 10.5$ in steps of 0.2, there will be 6 bins. (`default` = 15)

- min_z: Minimum redshift of the simulated galaxies for the required redshift range. (`default` = 9.0)

- max_z: Maximum redshift of the simulated galaxies for the required redshift range. (`default` = 11.9)

- n_bands: Number of filters the survey images have been observed through. If not specified, it will raise an error.

- detection_band: Band in which the detection of the objects is performed. This is the band in which `SExtractor` is run on first. After detecting the sources in this band, the photometry is performed on the rest of the bands in the area where the sources were identified. The images taken in this band will be where the simulated galaxies are first put in. If not specified, it will raise an error.

- lambda_detection: Central wavelength in angstroms of detection_band (above). If not specified, it will raise an error.

- bands: Name of the bands from n_bands. The detection band has to be the first band listed here. If not specified, it will raise an error.

- zeropoints: Zeropoint value corresponding to each band. The values must follow the same order as bands. The default value is 25 for each band, but the user should provide their own.

- gain_values: Gain values for each band. The values must follow the same order as bands. If not specified, it will raise an error.

- list_of_fields: Text file containing the name of the fields where the simulation is going to be run. Even if there is only one field, it has to be listed in this format.

If not specified, it will raise an error.

- R_eff: Effective radius in kpc for a simulated galaxy at $z = 6$. It is the half light radius, i.e. the radius within half of the light emitted is enclosed. This value changes with the redshift as $(1 + z)^{-1}$. (`default` = 1.075 kpc)

- beta_mean: Mean value for a Gaussian distribution of the slope of the spectrum as explained in Section 4.4.1. (`default` $= -2.2$).

- beta_sd: Standard deviation for a Gaussian distribution of the slope of the spectrum as explained in Section 4.4.1. (`default` $= 0.4$).

- size_pix: Pixel scale for the images (`default` $= 0.08$).

- path_to_images: Directory where the images are located. The code will create a folder inside it with the results. If not specified, it will raise an error.

- image_name: Name of the images. They all should have the same name with the band written at the end, as follows: 'image_name+field+band.fits'. The images have to be coaligned on the same pixel scale before running the code. If not specified, it will raise an error.

- types_galaxies: Number indicating the amount of Sérsic indexes. (`default` $= 2$).

- sersic_indexes: Value of the Sérsic index parameter n for the number of types_galaxies (`default` $= [1, 4]$).

- fraction_type_galaxies: Fraction of galaxies corresponding the the Sérsic indexes given (`default` $= [0.5, 0.5]$).

- ibins: Number of bins for the inclination angle. The inclinations can vary from 0° to 90°, i.e., if 10 bins are chosen, the variations will be of 9°. One bin indicates no variation of inclination angle. (`default` $= 1$).

- ebins: Number of bins for the eccentricity. The values can vary 0 to 1, i.e., if 10 bins are chosen, the variations will be of 0.1. One bin indicates only circular shapes (`default` $= 1$).

- min_sn: Minimum S/N ratio in the detection band for an object to be considered detected by `SExtractor`. (`default` $= 8.0$)

- dropouts: Boolean that indicates whether the user wants to run a dropout selection (`default` $= False$).

- de_Vacouleur: Boolean that indicates whether the user wants to make an exemption for de Vaucouleur galaxies. If true, galaxies with $n = 4$ will only have circular

Parameter	Type	Units	Default Value
n_galaxies	Integer		100
n_iterations	Integer		100
mag_bins	Integer		20
min_mag	Float	magnitude	24.1
max_mag	Float	magnitude	27.9
z_bins	Integer		20
min_z	Float	redshift	9.0
max_z	Float	redshift	12.0
n_bands	Integer		Required
lambda_detection	Float	Angstrom	Required
detection_band	String		Required
bands	String List		Required
zeropoints	Float List	magnitude	Required
gain_values	Float List	e^-/count	Required
list_of_fields	String		Required
R_eff	Float	kiloparsec	1.075
beta_mean	Float		-2.2
beta_sd	Float		0.4
size_pix	Float	arcsec/pixel	0.08
path_to_images	String		Required
image_name	String		Required
types_galaxies	Int		2
sersic_indices	Int List		2, 4
fraction_type_galaxies	Float List		0.5, 0.5
ibins	Float		1
ebins	Float		1
min_sn	Float		8.0
dropouts	Boolean		True
de_Vacouleur	Boolean		True

Table 4.1: Summary of the parameters needed to run `GLACiAR` . It includes the units and the default value.

shape (`default` = $False$).

Figure 4.5 shows an example of four galaxies produced by `GLACiAR` before and after being added to the science image. They have features which were all produced given the parameters requested by the user.

4.6 Output

The code produces a set of files, images and tables. Some of them are deleted for space storage reasons, while others are kept as a final result. We outline them in the following

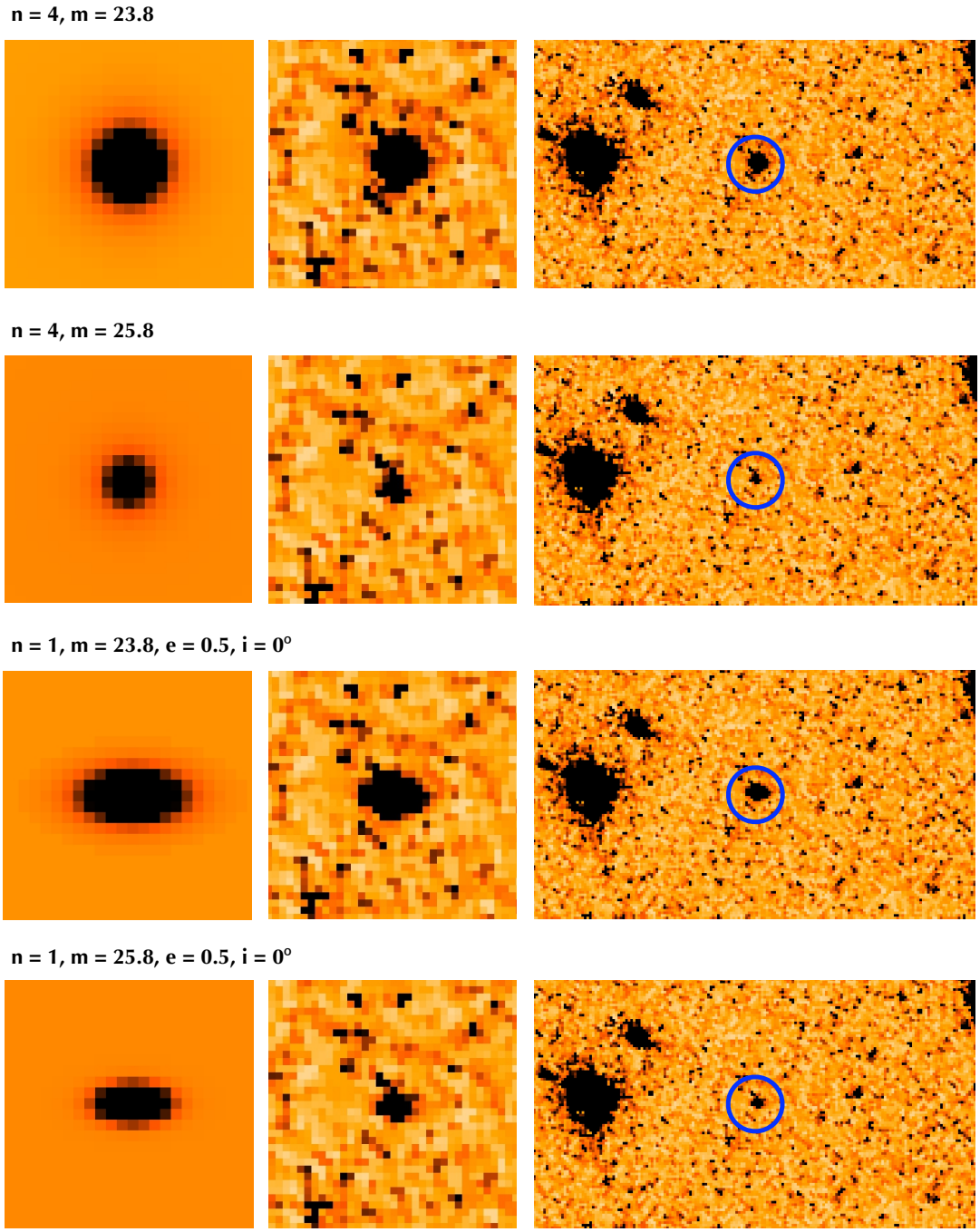

Figure 4.5: Example of different types of galaxies produced by GLACiAR. The left panels show a zoom of the galaxies placed on a constant background (box size 35×35 pixels), while the middle and right panels show them inserted in a typical science image (F160W for the field BoRG-0835+2456) with box sizes ($2.8'' \times 2.8''$ and $5.0'' \times 2.8''$ respectively). From top to bottom we see an artificial galaxy with a Sérsic index of 4, and total input magnitude $m_{AB} = 23.8$; an artificial galaxy with Sérsic index of 4, and magnitude $m_{AB} = 25.8$; an artificial galaxy with Sérsic index of 1, magnitude $m_{AB} = 23.8$, eccentricity of 0.5, and inclination angle of 0.5 degrees; and an artificial galaxy with Sérsic index of 1, magnitude $m_{AB} = 25.8$, eccentricity of 0.5, and inclination angle of 0 degrees. The first two ones have a circular shape, while the latter two are elliptical.

subsections in order of appearance.

4.6.1 New Images

The new images are the created images that contain the original observed data from the survey with the simulated galaxies added. Each iteration in the simulation produces one image per band. These are saved and then deleted immediately after `SExtractor` runs on them.

4.6.2 `SExtractor` Catalogues

As explained in Section 4.4.5, the sources are identified with `SExtractor` . This process generates two sets of files. One of them is the catalogues, which are described in this section, and the other one corresponds to segmentation maps, described in Section 4.6.3.

The catalogues generated by `SExtractor` include a list with all the sources identified in the images and their parameters. Due to the structure of the code, the first file created for a field of the survey contains the information of the real sources as it is run on the original science image. Besides this, for each iteration of the simulation a catalogue with the information of the sources is created. The header of the catalogue is shown below:

4.6.3 Segmentation maps

A segmentation map is a map with the definition of the location of a source and its extension found by a source identification software. In this case, they are produced by `SExtractor`. For `GLACiAR`, they can be classified in two groups: the segmentation maps from the original science images of the survey, and the ones from the images that include the simulated galaxies.

- Together with the old catalogues of the sources a segmentation map is created. This corresponds to a *.fits* file of the same size as the original image. This map makes the distinction between background and sources by labelling the pixels considered part of the background with a value of 0 and the pixels that belong to a source with a value of an integer. This integer is the ID number of the source in the catalogue (see Section 4.6.4), thus all the pixels forming one source have the same value. This value has no other meaning than the ID number which is the way in which a the found properties of a source can be correlated to their physical

1	NUMBER	Running object number	
2	FLUX_ISO	Isophotal flux	[count]
3	FLUXERR_ISO	RMS error for isophotal flux	[count]
4	MAG_ISO	Isophotal magnitude	[mag]
5	MAGERR_ISO	RMS error for isophotal magnitude	[mag]
6	FLUX_APER	Flux vector within fixed circular aperture(s)	[count]
11	FLUXERR_APER	RMS error vector for aperture flux(es)	[count]
16	MAG_APER	Fixed aperture magnitude vector	[mag]
21	MAGERR_APER	RMS error vector for fixed aperture mag.	[mag]
26	FLUX_AUTO	Flux within a Kron-like elliptical aperture	[count]
27	FLUXERR_AUTO	RMS error for AUTO flux	[count]
28	MAG_AUTO	Kron-like elliptical aperture magnitude	[mag]
29	MAGERR_AUTO	RMS error for AUTO magnitude	[mag]
30	KRON_RADIUS	Kron apertures in units of A or B	
31	BACKGROUND	Background at centroid position	[count]
32	X_IMAGE	Object position along x	[pixel]
33	Y_IMAGE	Object position along y	[pixel]
34	ALPHA_J2000	Right ascension of barycenter (J2000)	[deg]
35	DELTA_J2000	Declination of barycenter (J2000)	[deg]
36	A_IMAGE	Profile RMS along major axis	[pixel]
37	B_IMAGE	Profile RMS along minor axis	[pixel]
38	THETA_IMAGE	Position angle (CCW/x)	[deg]
39	FWHM_IMAGE	FWHM assuming a gaussian core	[pixel]
40	FWHM_WORLD	FWHM assuming a gaussian core	[deg]
41	FLAGS	Extraction flags	
42	CLASS_STAR	S/G classifier output	
43	FLUX_RADIUS	Fraction-of-light radii	[pixel]

Table 4.2: Header of the `SExtractor` catalogues produced by `GLACiAR` . The first column corresponds to the number of the column, the second is the name of the parameters, the third is a definition, and the fourth corresponds to the units (if applicable).

position. This file is kept.

- The images with the simulated galaxies will produce new segmentation maps with the same characteristics. The only difference with the catalogue described above is that it includes the new detected sources. It is important to note that original sources are not necessarily the same in the new catalogue in terms of magnitude, size, shape, or other properties. Accordingly, the ID numbers are not connected with the previous ID numbers.
  This file is discarded in order to save space.

4.6.4 *GLACiAR catalogues*

The main results produced by `GLACiAR` can be summarised in three tables. These contain the information of the inserted galaxies, including their input properties and their output status and properties as well. They are described below.

1. This is a table that contains information on the statistics of the result. The purpose of this table is to show the statistics in terms of the recovered sources and the high-redshift candidates if specified. It basically counts the amount of sources inserted per redshift bin and magnitude bin. From the inserted sources, it keeps track of the amount of that qualifies for each detection status (i.e. blending and detection status), and it calculates the amount of total recoveries over all the inserted simulated sources, $C(m)$. Also, if specified, it counts the number of dropouts for each bin, and calculates the fraction of these over the total amount of inserted galaxies, $S(z, m)$, and over the recovered dropouts in the desired redshift range over the number of recovered simulated galaxies $C(m)S(z, m)$. Table 4.3 shows an example of its structure with a brief description of the columns.

z[a]	m[b]	N_Obj[c]	S(0)[d]	S(2,1)[e]	S(-1)[f]	S(-2)[g]	S(-3)[h]	N_Rec[i]	N_Drop[j]	Rec[k]	Drop[l]
9.0	24.1	300	218	50	26	4	2	268	0	0.89	0.0
9.0	24.3	1000	751	169	62	13	5	920	0	0.92	0.0
9.0	24.5	1500	1112	257	94	26	11	1369	0	0.91	0.0
⋮	⋮	⋮	⋮	⋮	⋮	⋮	⋮	⋮	⋮	⋮	
10.0	24.1	300	211	63	17	5	4	274	101	0.91	0.34
⋮	⋮	⋮	⋮	⋮	⋮	⋮	⋮	⋮	⋮	⋮	
11.8	27.9	600	0	0	72	34	494	0	0	0.0	0.0

Table 4.3: Example of the file produced by the simulation with the statistics for each redshift and magnitude. This is a simulation run for a magnitude range of $m = 24.0 - 28.0$ and a redshift range of $z = 9.0 - 11.8$.

[a] Input redshift of the simulated galaxy.
[b] Median value of the magnitude bin.
[c] Number of objects inserted for the corresponding redshift and magnitude bin in all the iterations.
[d] Number of artificial sources recovered by `SExtractor` that were isolated.
[e] Number of artificial sources recovered that were blended with a fainter object.
[f] Number of artificial sources recovered that were blended with a brighter object.
[g] Number of artificial sources that were detected by `SExtractor` with a S/N under the required threshold.
[h] Number of artificial sources that were not detected by `SExtractor`.
[i] Number of recovered artificial sources: $(d + e)$.
[j] Number of artificial sources that passed the dropout selection criteria
[k] Fraction of not recovered artificial sources : i/c.
[l] Fraction of artificial sources that passed the selection criteria: j/c.

2. Complementary to the previous table, the algorithm produces another table with the each one of the inserted sources, their positions, the input magnitude, the

Initial Mag[a]	iteration[b]	ID Number[c]	Input Magnitude[d]	Output Magnitude[e]	Id Status[f]
24.1	1	319	25.922	26.255	0
24.1	1	213	25.922	26.088	0
⋮	⋮	⋮	⋮	⋮	⋮
27.9	10	39	26.952	23.627	-1
27.9	10	0	26.952	-99.000	-3

Table 4.4: Example of the file produced by the simulation with information of all the simulated galaxies.

[a] Magnitude corresponding to the input flux for the star. This is not the same as [d] since the input magnitude changes depending on the β value and size of the object.
[b] Iteration number.
[c] Identification number given by `SExtractor` after it runs on the image with the simulated galaxies. This number is unique for every iteration for a given magnitude and redshift.
[b] Magnitude corresponding to the added flux inside all the pixels that the source includes.
[e] Magnitude of the source found with `SExtractor` after it runs on the image with the simulated galaxies.
[f] Integer number that indicates whether a source has been recovered and/or is blended.

blending status, and the detection status. Several tables (one for each redshift step) are produced with all the galaxies that were placed in the simulations at that redshift. It provides an insight to understand the characteristics or reasons to detect or miss an object. It also yields their detected magnitude in the detection band, and their size. In summary, it gives us information about how this source is detected instead of the input information about it. The structure is shown in Table 4.4.

3. One last table, which is useful for redshift selection, is produced. Given that the number of bands is variable this table is released in a Python-specific compact binary representation (using the `pickle` module). It contains the ID of the object, input magnitude, status, magnitudes in all bands, and S/N for each band as well. This is an important file for redshift estimations/selection techniques. Similar to the previous tables, it contains information about the output/measured characteristics of the detected objects. It also encloses all the magnitudes in different bands, so it is especially useful for photometric estimations. Unlike the other two tables, this is not an ASCII file as that is not efficient because it is resource intensive.

4.6.5 Plots

Our code also produces a plot of the completeness and two extra plots if the 'dropouts' parameters is set to 'True'. The first plot corresponds to the completeness function (or recovered sources) $C(m)$ as a function of the magnitude and the redshift. The second

and third plot are the $S(z, m)$ and $S(z, m)C(m)$. This is only produced in case the dropout technique is applied, but given the tables produced by `GLACiAR` , it is easily calculable with the final catalogues. Examples of these plots can be in seen in Chapter 5, in Figures 5.1 and 5.3.

4.7 Redshift Selection

An important feature of `GLACiAR` is the option of applying a selection technique or another type of redshift estimation. Since the information used to estimate redshift relies on the magnitude in each/any of the bands in which the survey is taken, the information given by the software is what the user needs.

With the produced catalogues (see Section 4.6.4), most of the commonly used techniques can be performed in order to estimate the redshift.

We provide the selection adapted from Bouwens et al. [2015b] and Bernard, Carrasco et al. [2016]that we have used to run our example:

$S/N_{160} \geq 8.0$

$S/N_V < 1.5$

$S/N_{098} < 1.5$

$J_{125} - H_{160} > 1.5$

4.8 Modules

The code is made of several modules which are called by a main module, `completeness.py`. A description of them follows.

- `write_conf_files.py`: This module is used in `run_sextractor.py`, and it reads the `SExtractor` parameters file (see Section 4.5.1), which contains the requirements to identify the sources. Following that file, it writes new temporary configuration files for each band. These are used when `SExtractor` is run.
- `run_sextractor.py`: This module is called by `completeness.py`, and it calls `write_conf_files.py` to write the `SExtractor` parameters file for each band. It then distinguishes between the detection band and the other bands. It runs the first on the detection band, identifies the sources, and runs then `SExtractor` in dual mode. This means that the photometry is performed on the location of the

sources found in the detection band. This is crucial so then all the sources can be compared and have their information in all the bands.

- `creation_of_galaxy.py`: This module performs most of the mathematics processes involved in the code. It calculates the flux for each of the pixels following the Sérsic profile. Accordingly, it performs all the required operations for the profile. It also generates the random positions for the simulated sources, generates the mock spectrum and calculates the expected flux for that spectrum in a given band.

- `blending.py`: It identifies the detection and blending status of a source. It does this by comparing segmentation maps, the ones from the original science image and the ones with the simulated sources. It also extracts information from the catalogues when needed in order to compare magnitudes for the blending status. It runs for each iteration, so it retrieves a list with all the galaxies in that iteration and their status.

- `dropouts.py`: If the parameters dropouts is set to 'True' by the user, this module is called by `blending.py`. This is a more specific module as it is only useful in case of dropouts. The one we include has the selection criteria from BoRG Bernard, Carrasco et al. [2016], but it can be modified. It receives information on the magnitudes and status of all sources and then, depending on their colours and signal-to-noise, classifies the objects.

- `plot_completeness.py`: This module produces the plots. It always produces the plot of $C(m)$ as a function of redshift and magnitude. Depending on the requirements by the user, it will produce a plot of $S(s, m)$ and $S(s, m)C(m)$ as well.

- `completeness.py`: This is the main module that runs the code. This module manages the files and calls `creation_of_galaxy.py` to perform the mathematical operations in order to calculate the flux for the simulated galaxies and expected magnitudes. It also calls `run_sextractor.py` to run the source identification software on the images as well as `plot_completeness.py` in order to produce plots. On its own, this module produces the features of the artificial galaxies according to the input parameters (see Section 4.5.2). It opens the images, creates the stamps with the calculated fluxes, places the galaxies in the given positions, and adds them to the science images. Then it calls the module to run `SExtractor`, and records the statistics regarding the recovery of sources and also the individual status and extracted properties of the simulated objects. It then produces the final tables and plots.

4.9 Application of GLACiAR to HUDF12

In this Section, we present the application of the code to the Hubble Ultra Deep Field 2012, [UDF12 Koekemoer et al., 2013, Ellis et al., 2013] and study the source recovery here.

4.9.1 UDF12

The UDF12 campaign is an extension to the HUDF observations (see Section 3.2 for a description of HUDF) which covered an area of 11.0arcmin^2. The previous survey (UDF09 hereafter) comprised observations in the four *HST* bands, F105W, F125W, F140W, and F160W. UDF12 doubles the exposure times and quadruples the exposure in the F105W filter. From the combination of the new exposures and from reprocessing the previously obtained observations, the 5σ limiting magnitudes achieved are of $m_{105} = 30.0$, $m_{125} = 29.5$, $m_{140} = 29.5$, and $m_{105} = 29,5$ (AB magnitudes,as measured in $0''.4$ diameter apertures). The main goal of the UDF12 observations was to find high-redshift galaxies, improving the UV continuum slope at $z \sim 7-8$ and creating new samples of gaalaxies at $z \sim 9-10$.

4.9.2 Results

We study the completeness $C(m)$ of the survey for the redshift range $m_{160} = 24.0-32.0$ using GLACiAR default parameters. In Figure 4.6 we can see a steady and slow fall of the completeness fraction up to magnitudes of $m_{160} \sim 29.8$, after which it shows a more about drop from $C(m) \sim 0.6$ to $C(m) \sim 0.0$ in about 1.5 magnitudes. It is important to note that the 50% occurs at magnitude $m_{160} = 30$, which is 0.5 magnitudes fainter than the 5σ detection limit. In general, this is the results we expected. An interesting result is that the completeness fraction does not go above $\gtrsim 0.8$. We conclude that this is due to the field and our blending conditions. Because the magnitude limit of this field is deep ($m_{160W} \sim 29.5$), the images are more crowded. Therefore, artificial sources placed on top of real sources are more likely to considerably change their flux and be classified as blended not recovered.

In order to study the redshift selection function $S(z, m)$ and $C(m)S(z, m)$ we require a dropout selection criteria. We follow the literature for $z \sim 10$ galaxy candidates in UDF12 and adapt the compilation from Bouwens et al. [2015b]. We use one colour cut, a non-detection condition and a minimum signal to noise for the identification band. Our final criteria is summarised below.

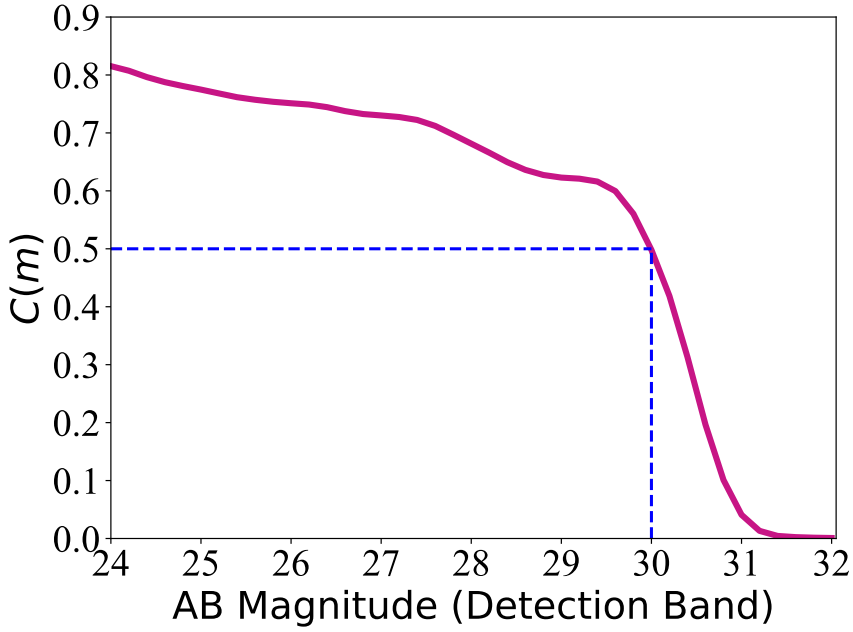

Figure 4.6: Completeness as a function of the magnitude $C(m)$ calculated by `GLACiAR` for the band filter F160W in the UDF12 field (purple solid line). The blue dashed line corresponds to $C(m) = 0.5$.

1. $S/N_{105} < 1.5$,

2. $S/N_{160} \geq 8$,

3. $(m_{125} - m_{160}) > 1.2$,

Although this can be considered a basic model, and it can certainly be changed by making a more exhaustive choice of the redshift selection criteria. For example, including cuts in the colour $JH_{140} - H_{160}$ or refinements for the colour $J_{125} - H_{160}$.

The results are shown in Figure 4.7. As it can be seen here, the highest recovery fraction is around 0.4. This is due partly to the condition of non-detection in $F105W$, $S/N_{105} < 1.5$. This excludes a large fraction of galaxies that might have some flux in this band. Furthermore, as discussed above, UDF12 is a very crowded field. The artificial colour of galaxies are more likely to be affected by nearby sources. We also think this is why galaxies at brighter magnitudes show a smaller fraction of recovered dropouts. This is something that can be solved by changing some of the deblended parameters. As expected, $S(z, m)$ is noisy for faint magnitudes ($m_{160} \gtrsim 30.8$), and this is because this fraction is computed only over the small fraction of artificial galaxies recovered at this magnitude.

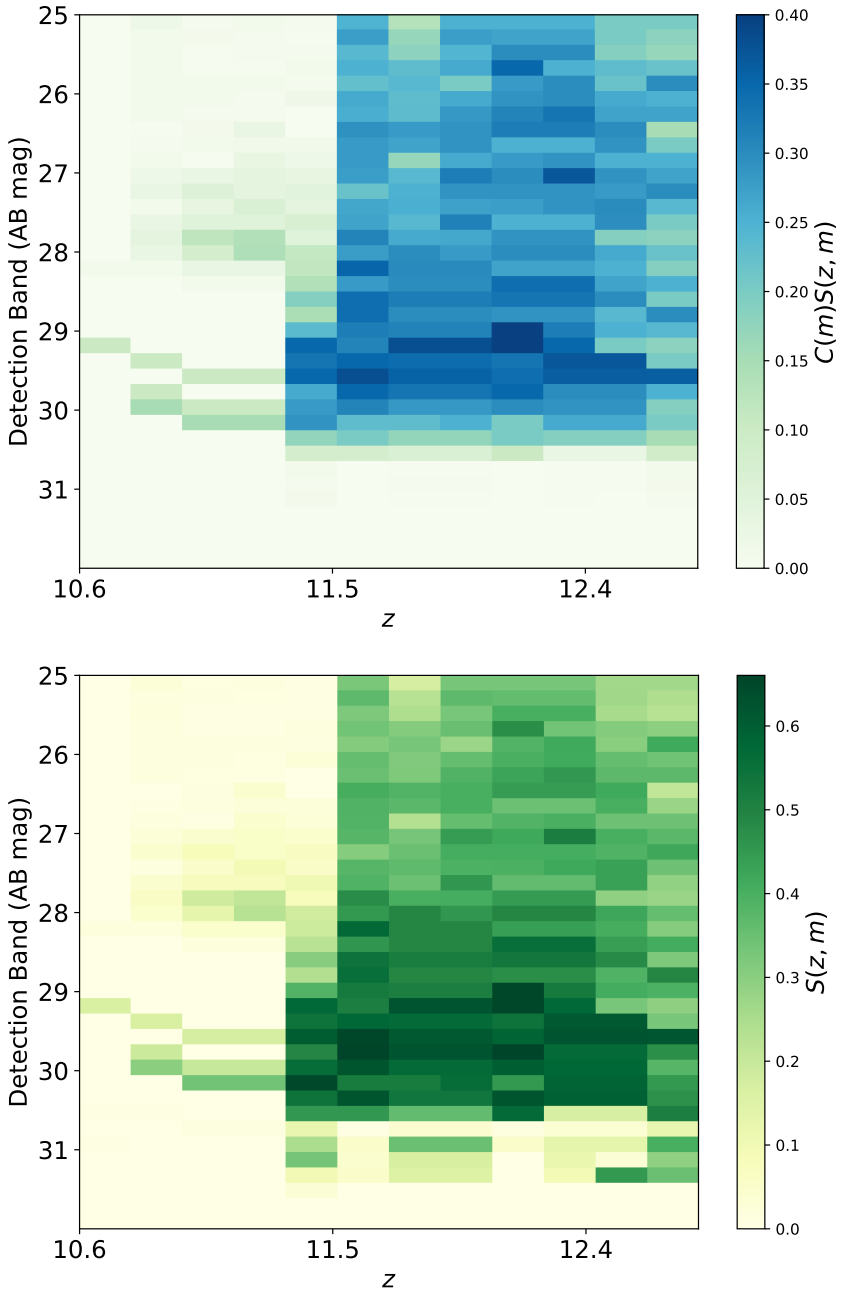

Figure 4.7: Dropout selection for UDF12 produced by our `GLACiAR` for a selection criteria aimed at finding $z \sim 10$ galaxy candidates. The top panel shows the dropouts found from all the artificial galaxies inserted ($C(m)S(z,m)$). The bottom panel shows the dropouts found from the recovered artificial galaxies inserted ($S(z,m)$).

Configurations	Fraction $n = 1$	Fraction $n = 4$	beta_mean	R_eff
Config_1	0.5	0.5	-2.0	1.075
Config_2	1.0	0.0	-2.0	1.075
Config_3	0.0	1.0	-2.0	1.075
Config_4	0.5	0.5	-1.8	1.075
Config_5	0.5	0.5	-2.6	1.075
Config_6	0.5	0.5	-2.0	2.0
Config_7	0.5	0.5	-2.0	0.5

Table 4.5: Configurations with different sets of parameters of GLACiAR.

It would be interesting to produce a larger range of parameter sets covering more values for all the properties changed in Table 4.5. This can be done with GLACiAR in a very clear manner.

As it can be seen in this example, applying GLACiAR to UDF12 is straightforward. The parameters are easily changed as well as the dropout selection criteria. This can be useful when comparing results and choosing selection techniques.

4.9.3 Assumptions

An interesting point is to check how much the recovery fraction changes depending on the assumptions made regarding morphology, spectral energy distributions or sizes. In order to do this, we run the simulation for different configurations, which are listed in Table 4.5.

The results of the recovered sources for each one of the configurations are show in Figure 4.8. As we can see, the parameter configurations we tested for assumptions regarding the properties of the artificial galaxies do not produce big changes in the completeness results, $C(m)$. This is expected as we chose realistic sets of parameters, with no extreme cases. The biggest differences are produced when applying the configurations that vary the size of the mock galaxies, Config_6 and Config_7. We attribute this to the fact that smaller galaxies will be easier to identify with GLACiAR as the flux concentrates in the central pixels, helping avoid contamination of flux from other sources since the galaxy will spread out over fewer pixels. Another interesting result is that the variation in β does not change the results for completeness in a considerable manner, being almost identical at fainter magnitudes. For brighter magnitudes, $m_{160} \gtrsim 29.5$, the smaller β yields a slightly larger fraction of recovery. In the case of galaxy Sérsic indices, they overlap in 2 magnitudes, having different results in terms of the largest recovery fraction for different magnitude ranges.

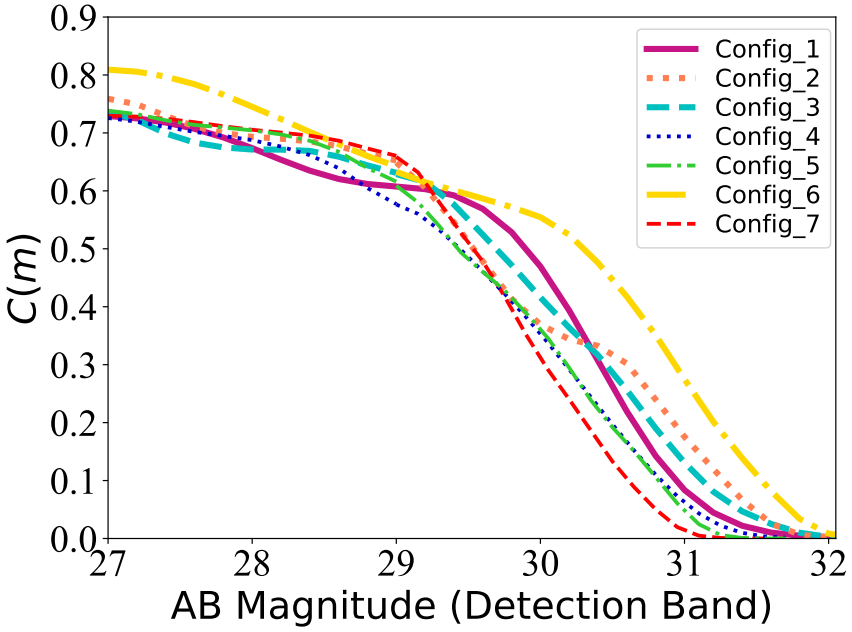

Figure 4.8: Completeness as a function of the magnitude $C(m)$ calculated by `GLACiAR` for the band filter F160W in the UDF12 field for different sets of parameters. These configurations are described in Table 4.5.

4.10 Limitations

`GLACiAR` was created to be implemented in *HST* multi-band imaging galaxy surveys focused on high-redshift ($z \gtrsim 6$) Lyman-break galaxies. It can certainly be used for other types of surveys. However, it is important to discuss its limitations.

`GLACiAR` is tailored for higher-redshift galaxies. When a galaxy is simulated, its spectrum is a smooth slopped UV source with a strong break. Parameters such as the location of the break or the slope are chosen by the user. This spectrum is aimed at reproducing star forming galaxies at high-redshift ($z \gtrsim 6$). Features on the spectrum such as the nebular line emission present in some high-redshift galaxies are not accounted for and therefore `GLACiAR` might not produce accurate results.

The code is also not optimised to generate samples of very compact galaxies, i.e., galaxy stamps for cases where the effective radius of the galaxy is similar to the pixel scale. In these cases, the flux will be concentrated in only a few pixels and their identification will become difficult.

The assumptions made by our code, such as assuming all the galaxies will present the Lyman break, or the lack of emission lines, among others, are not what it's observed in

the sky. However, it is important to note that as long as the simulated galaxies mimic the galaxies in the survey and the selection technique is the same, `GLACiAR` will do a good job indicating the fraction of recovered galaxies.

4.11 Future

`GLACiAR` is a completeness simulation tool that can be applied to different surveys. The parameters of the code can be easily adapted to fit the requirements of *JWST*. As the majority of high-redshift galaxy surveys can use our code, comparisons and studies can be more easily performed and better understood.

The main additions or modifications planned for the future of `GLACiAR` are the incorporation of strong gravitational lensing (explained below), and the replacement of `SExtractor` by `photutils` [Bradley et al., 2016]. This is a package of Astropy that provides tools for detecting and performing photometry of astronomical sources. The inclusion of `photutils` is motivated by the fact that it is a `python` module, therefore `GLACiAR` would not depend on using any external software.

Another modification that would make the code apt for an even wider range of surveys is incorporation of flexible spectra. Instead of only allowing for Lyman-break galaxies, it is possible to change the code and allow for the spectrum to be an input. This would make the code better suited for low-redshift galaxies or certain populations of galaxies with special features in the spectrum.

An interesting exercise would be the application of `GLACiAR` to synthetic *JWST* observations. This can be of particular relevance for planning future observations as it can help constrain the number of expected galaxy candidates, for example.

4.11.1 Lensing

An important addition to the code will be the incorporation of the strong gravitational lensing phenomenon. This event affects the observed properties of the galaxy that is behind a lens.

This is relevant as several successful surveys focus on finding galaxies that are being lensed. This gives us insight into objects that are intrinsically faint, and that in many cases we would not be able to observe. The gravitational lensing effect will not only change the observed properties of the galaxy, but it will also affect the observed volume. This can no longer be directly estimated, because the massive object in between acts as

a natural telescope, changing the observed volume. It now depends on the gravitational potential well, which will also depend upon other features. Therefore observing behind massive objects such as galaxy clusters gives as an insight into this population.

4.12 Summary

`GLACiAR` is an algorithm developed in order to have a unified tool for completeness estimations in galaxy surveys. Today, all the galaxy surveys that have been performed have their own way of estimating the completeness which can prevent us from fully understanding the missing galaxies and the resulting statistics. Our goal was to solve this problem by creating a `Python`-based open source easily adaptable for different surveys that can do that. The relevant part is that it not only can be applied to current surveys, but that it can be used for the future surveys carried out by `HST`.

We have described how the algorithm `GLACiAR` works, providing a detailed description of the steps involved in the code, the required parameters and files, the output files, the output tables and what they can be used for. We describe how the galaxies are created, giving details on the luminosity profile, the size, the magnitude, etcetera, and how these are measured by `GLACiAR`. We have also tested the code on the *HST* UDF12 observations. After this, we are ready to implement and apply this code to our data set from BoRG[z8] and our corresponding high-redshift galaxy candidates.

Future improvements to the code include the incorporation of the strong gravitational lensing phenomenon and the replacement on `SExtractor` by a `python` based package for source identification.

5

UV Luminosity Function

Celestial objects such as stars, quasars, and galaxies have an intrinsic luminosity that correlates with certain physical properties. The luminosity function describes the probability of finding an object of a given luminosity per unit volume, and is one of the most fundamental observable properties in astronomy. The work presented in this chapter is focused on the luminosity function of galaxies, which has a wide range of applications in Astrophysics, including understanding galaxy formation and evolution.

In this chapter, we first present an introduction and formal definition of the luminosity function. Afterwards we present the Schechter function, which is an analytic expression widely used to fit the shape of the luminosity function. We also discuss its evolution with redshift and its implications. We then summarise the main results at higher redshifts, $z \gtrsim 7$, with emphasis on recent findings, particularly with *HST*. Afterwards, we present our measurement for the galaxy luminosity function at $z \sim 10$, which is obtained by using the galaxy candidates from Bernard, Carrasco et al. [2016] (see Chapter 2) with data from BoRG[z8]. We use our code, `GLACiAR` (see Chapter 4) in order to estimate the completeness and dropout selection function we obtain with these galaxy candidates.

With these values we can calculate the effective volume and, from it, our own improved estimate of the luminosity function. We then compare our results to the results obtained in the Bernard, Carrasco et al. [2016], where they used the same galaxy candidates but a different completeness simulation. We finally summarise our findings in Section 5.2.

5.0.1 Fitting the Luminosity Function

Fitting the luminosity function is a complex task. Its challenges include the flux-limited samples of galaxies, the observational bias, and the need to distinguish between physical and observational variations, among others. Consequently, the methods need to take this into account.

Different approaches can be taken in order to measure the luminosity function. They can be divided into two categories, parametric and non-parametric. A parametric approach has benefits such as being relatively simple easy to implement, but it has some disadvantages as well. In particular because it assumes the luminosity function has a shape that can be analytically represented. As an alternative to this approach there are non-parametric methods, where no shape is assumed. The most basic toy-model estimator is part of this category, where the luminosity function is estimated by just counting the number of objects in a certain volume, i.e. $\phi = N/V$.

All methods have their advantages and disadvantages. Parametric methods such as Sandage et al. [1979] assume a form of the luminosity function, which is sensible but has not yet been confirmed. On the other hand, the problem with non-parametric maximum likelihood is the amount of free parameters and the increased computational challenge. Below we summarise the main methods for fitting the luminosity function.

The Classical Method

The classical method uses the number of objects inside a given volume $\Phi = N/V$. It was used in the first studies regarding luminosity functions [van den Bergh, 1961, Kiang, 1961], but it was only explained more formally later on [e.g. Schechter, 1976].

As its name suggests, this is a basic method that was used in the first studies of the luminosity function. It consists of estimating the volume of the sample up to a certain magnitude limit m_{lim}, which is given by the depth of the survey. The volume depends on the absolute magnitude, $V(M)$. Then the number of galaxies is divided in bins of magnitudes, and they are individually divided by $V(M)$.

$$N_{bin} = \int_{M1}^{M2} dM V_{lim} = \Phi(M) V_{lim} \tag{5.1}$$

This estimator is very limited, as it assumes that the sources are uniformly distributed in the Universe. Furthermore, it does not take into account the position in the bin, losing valuable information. Most of the standard non-parametric approaches used in order to measure the luminosity function are variations of this method.

5.0.2 V/V_{max}

This method is based on the classical method explained above. It was first proposed by Schmidt [1968] in a flux limited sample of quasars. It consists of performing a sum over the N objects in the sample, divided by V_{max}, which is a maximum volume over which an object at a maximum redshift could be observed. V_{max} is the maximum volume for each galaxy, and it depends on the survey limits, distribution of sources in space and the way detectability depends on distance.

$$\phi_{bin=i} = \sum_{bin=i}^{N} \frac{1}{V_{max}(M_i)} \tag{5.2}$$

Sometimes, this method is referred to as V/V_{max} [Wall and Jenkins, 2012]. V is the volume that corresponds to the actual redshift at which a source is observed. Therefore, V/V_{max} is a measure of the position of the source within the observable volume V_{max} or fraction of the available volume occupied by the source. The value V/V_{max} can take values between 0 and 1. Therefore, it is easy to see that this method is a type of weighted histogram. It is important to note that V/V_{max} estimates the actual limit of a survey, and calculating it can be difficult. This method in particular considers a weight inversely proportional to the luminosity of the object which statistically compensates and corrects for incompleteness.

Advantages of this method include the fact that the errors for different bins are not correlated and they are easy to calculate, and it is a good approximation if the size of the bins is small. In terms of the disadvantages, there is loss of information when summing over all the sources in a luminosity or magnitude bin, also, the sources are distributed in space in an even or uniform manner. As this is not true, some adaptations are required when using it.

ϕ/Φ Method

The term ϕ/Φ was introduced by Binggeli et al. [1988], but the actual method was first proposed by Turner [1979] and Kirshner et al. [1979]. It aims to consider the spatial inhomogeneities that would otherwise distort the parameter $\phi(M)$. The basic idea is to measure the ratio of the number of galaxies with absolute magnitudes between M and $M + dM$ to the total number of galaxies brighter than M in volume dV at a given location. Using these definitions and calculations that are out of the scope of this thesis, one can arrive at the conclusion that the ratio of ϕ/Φ is independent of any inhomogeneities in the distribution of galaxies.

$$\int \frac{\phi(M')}{\Phi(M')} dM' = \log\Phi(M) \tag{5.3}$$

This method is in principle non-parametric, but many of the studies do assume a parametric shape for $\phi(M)$, which is normally the Schechter form.

This technique is used because of its relative simplicity. One of the main advantages is that it takes care of the inhomogeinities in the distribution of galaxies. However, there is a large statistical noise associated with ϕ/Φ which is a considerable disadvantage.

Maximum Likelihood Estimator

First proposed by Sandage et al. [1979], the Maximum Likelihood Estimator (MLE, or sometimes referred to as STY) is widely utilised. It assumes a parametric model of the luminosity function. As mentioned before, the most popular of these parametrisations is the Schechter function [Schechter, 1976].

This approach is similar to the previous one, ϕ/Φ. They both consider a quotient in order to cancel the density function out. In this case, the number of galaxies brighter than a certain absolute magnitude M is divided by the total number of galaxies at a given distance or redshift. This corresponds to the probability that a galaxy at a certain distance is brighter than M. This probability has to first be converted into an analytical expression with parameters to be fixed by a maximum likelihood technique in order to calculate the luminosity function $\phi(M)$.

The most common approach here is to assume spherical symmetry. This way density function doesn't need to be removed and it can be solved at the same time as $\phi(M)$.

This method relies on the fact that a specific form of the luminosity function can be assumed and the data can be fit to such a form.

The C-Method

Developed by Lynden-Bell [1971], the C^- estimator is a maximum likelihood method. It was applied to a sample of quasars by Jackson [1974] and a revised version was proposed as a good method for galaxies by Choloniewski [1987]. This method consists of producing a cumulative luminosity function with discrete jumps at the location of each galaxy. From there, it is possible to recover the integral luminosity function from where the differential luminosity function can be obtained.

The advantages of this technique are that it does not involve underlying assumptions on the distribution, and neither does it require binning.

Assumptions in this method are spherical symmetry, that the luminosity function has the same form throughout the whole line of sight, and that the sample should be ordered in luminosity.

Step-wise maximum likelihood

The Step-Wise Maximum Likelihood [SWML; Efstathiou et al., 1988] can be defined as a non-parametric equivalent of the MLE method. It was created to overcome the inconvenience of the MLE technique of being unable to test how well a parametrisation fits the data. This method parametrises $\phi(M)$ as a series of N steps, and it provides a suitable representation of the data.

This is popular technique, used also by Finkelstein et al. [2015] to obtain their luminosity function measurements. They also use a parametric version and compare the results, which are in good agreement. A SWML approach is considered in Bouwens et al. [2015b]. Its advantage is that it does not rely on the assumption of a simple functional for $\phi(M)$ and it allows the incorporation of effects such as sample incompleteness [Willmer, 1997].

5.1 Our Results

We can now use our completeness simulation estimator, `GLACiAR` (see Chapter 4) combined with the galaxy candidates from the BoRG survey (see Chapter 2) in order to

estimate a new point in the bright end of the luminosity function at $z \sim 10$.

5.1.1 Completeness

Completeness simulations are necessary when measuring the galaxy luminosity function. The characteristics of the survey, where the galaxy candidates are found, and the selection technique used have an impact on the amount of selected candidates. This will have a direct impact on the luminosity function measurements. Therefore, the completeness of the sample has to be determined and added to the number count.

The most common approach for estimating the completeness involves adding artificial galaxies and studying their recovery fraction. These artificial galaxies can be modelled in different manners. The two main techniques consist of creating artificial galaxies where the flux is determined by the luminosity profile, with the other method using images of real galaxies and matching their features to the galaxy candidates. Our code uses the former approach, modelling artificial galaxies following a Sérsic profile [Sérsic, 1968].

5.1.2 Application of the Code

We refer the reader to Chapter 4 in order to understand the functioning of the code presented in this thesis. As a brief summary, `GLACiAR` estimates the completeness of a galaxy survey $C(m)$ by creating artificial galaxies following a Sérsic brightness profile [Sérsic, 1968] and adding them to the observed images of the survey. These sources have different redshifts and magnitudes. Then, a source identification software [`SExtractor` Bertin and Arnouts, 1996] runs over the original and simulated images producing catalogues with the identified sources. These catalogues are then compared in order to measure the fraction of recovered objects. A redshift selection algorithm can also be applied over these catalogues to find galaxies at a certain redshift. The fraction of recovered galaxies at that redshift versus the galaxies that actually exist at that redshift $S(z, m)$ can be also estimated with our code.

In order to apply the code, we write a list with the fields that form the survey, which is described in Chapter 3. We then fill out the parameters file with the features of the artificial galaxies we require.

The following table contains the parameters we used to run the program:

As detailed in Chapter 3, the survey used four bands: H_{160}, J_{125}, Y_{098}, and the optical

Parameter	Value
n_galaxies	100
n_iterations	100
mag_bins	21
min_mag	24.0
max_mag	28.0
z_bins	13
min_z	9.6
max_z	12.0
n_bands	4
lambda_detection	15369.14
detection_band	f160w
bands	- f160w - f098m - f125w - f606w
zeropoints	- 25.9463 - 25.6674 - 26.2303 - 26.0691
gain_values	- 2008.803039 - 4208.810304 - 2205.871521 - 4698
list_of_fields	../list.txt
R_eff	17.5
beta_mean	-2.2
beta_sd	0.4
size_pix	0.08
path_to_images	../
image_name	hlsp_borg_hst_wfc3_par
types_galaxies	2
sersic_indices	- 1 - 4
fraction_type_galaxies	- 0.5 - 0.5
ibins	10
ebins	10
min_sn	8.0
dropouts	Yes
de_Vacouleur	Yes

Table 5.1: Summary of the parameters used to run `GLACiAR` on the BoRG[z8] survey.

band V_{600} or V_{606}. The fact that some fields have a different optical band means that it is more efficient to run the code twice: one for the fields taken with V_{600}, and another one for the fields taken with V_{606}. We run the code for two sets of fields, depending on the optical band available for them. In Table 5.1, we show the parameters file used for the group of fields that have V_{606} band observations available.

As we explained before, the galaxy search performed here is the one carried out by Bernard, Carrasco et al. [2016], aiming to find galaxies at $z \gtrsim 10$. Therefore, we ask for a spectrum slope β Gaussian distribution with a mean of $mean = -2.2$, and a standard deviation of $\sigma = 0.4$. This is a number for high-z galaxies supported in studies such as [Bouwens et al., 2015b]. We also do this to compare with the previous simulation performed for the same survey with slightly different code.

5.1.3 Completeness $C(m)$

The results we obtain for the completeness for one of the fields, *borg_ 0440-5244*, are shown in Figure 5.1. Since we have access to their results, we use this field as an example to compare to the results in the figures from Bernard, Carrasco et al. [2016]. As expected, the completeness only depends on the magnitude and not on the redshift. This is because the recovered magnitude will only depend on the final input magnitude in the detection band which is independent from the redshift.

In Figure 5.2, we show a slice at redshift $z = 10$ of the completeness $C(m)$ to help visualise it more clearly. The value of the completeness goes up to $\sim 90\%$ for the brightest galaxies. This means that even at such bright magnitudes, not all galaxies will be detected. This is because the likelihood of detection a galaxy is not only a function of the magnitude as there are other phenomena that play a role. To analyse the reasons we have undetected sources we look into their status, and we see that the majority of them are blended with another source, primarily a brighter one. Therefore, according to the definition of successful recovery adopted in `GLACiAR` , we will never be able to recover 100% of the galaxies at any redshift. The fraction of recovery stays stable (variations of $\Delta C(m) \lesssim 5$) up to $m_{H160} = 25.2$, dropping to 80% at $m_{H160} = 25.6$, 70% at $m_{H160} = 25.8$, and 20% at $m_{H160} = 26.2$, being technically 0 for $m_{H160} \gtrsim 27.0$. At a magnitude of $m_{H160} = 26.0$, the detection is of $C(m) = 47\%$, and extrapolating, we find that $C(m) = 50\%$ is reached at a magnitude of about $m_{H160} = 25.98$. It is interesting to note that according to the *Hubble Space Telescope* Exposure Time Calculator (ETC), this signal-to-noise limit is achieved at a magnitude of $m_{H160} = 26.1$ for a source with the characteristics given above. These two limits, our 50% completeness and the magnitude given by the calculator, are shown in Figure 5.2 in blue and red colours,

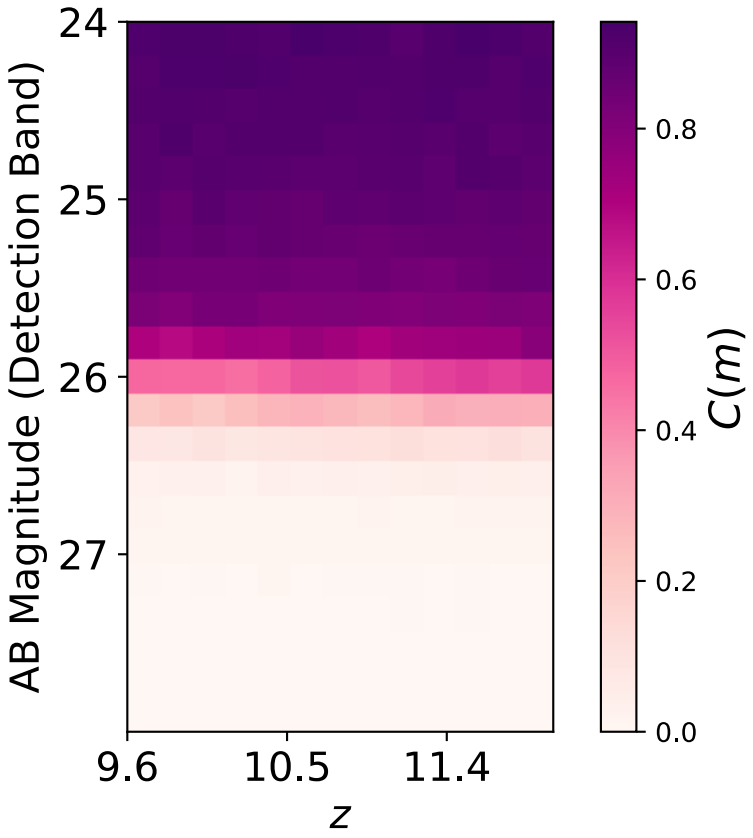

Figure 5.1: Completeness $C(m)$ as a function of the redshift z and the intrinsic magnitude m.

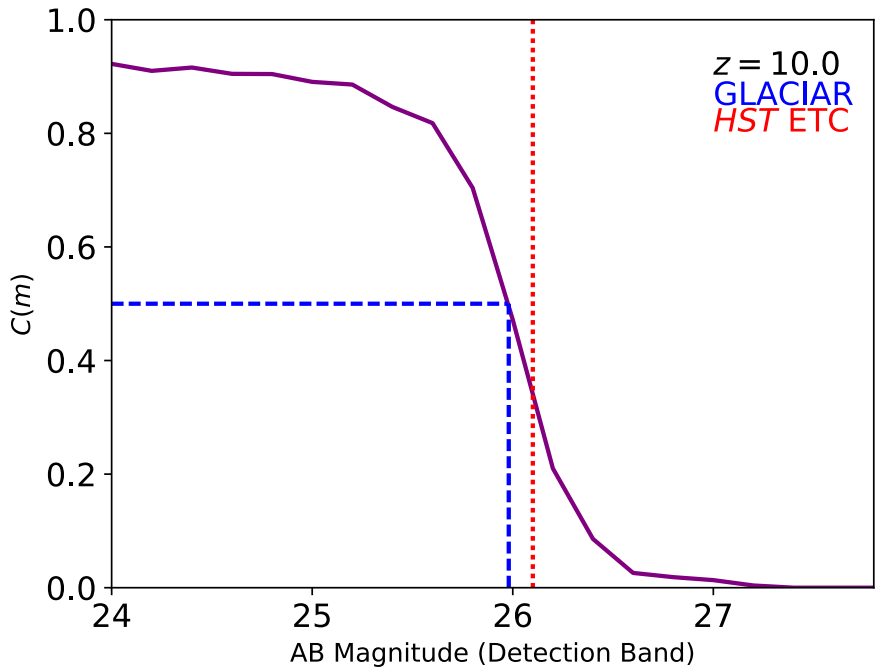

Figure 5.2: Completeness $C(m)$ as a function of the redshift z and the intrinsic magnitude m for $z = 10$.

respectively.

5.1.4 *Dropouts* $S(z, m)$ *and* $S(z, m)C(m)$

The results after the dropout selection criteria described in Chapter 2 is applied are shown in Figure 5.3. As with Figure 5.1, these results are only for one field, *borg_0440-5244*, which is chosen for comparison purposes. The rest of the fields show similar results. The figure shows the selection function results out of all the inserted objects $C(m)S(z, m)$ and out of only the recovered objects $S(z, m)$.

As we can see, the recovery fraction over all the galaxies $S(z, m)C(m)$ reaches a maximum value of 64%, which is at brighter magnitudes ($m_H \lesssim 25.5$) and at a redshift of $z > 10$. At fainter magnitudes, the selection function recovery drops, finding almost no objects after $m \sim 26.5$. However, if we only consider the objects found with the redshift selection only from the recovered objects, i.e. $S(z, m)$, we see things somewhat differently. Recoveries are still happening at faint magnitudes, $m \gtrsim 26.5$. In particular, there is a high value for a magnitude of $m_H \sim 27.5$. This can be explained because of the few objects that were recovered at that redshift, and from those few, most of them were found in the correct redshift range. This is more related to a small likelihood of recovering objects at that magnitude rather than having particularly complete samples.

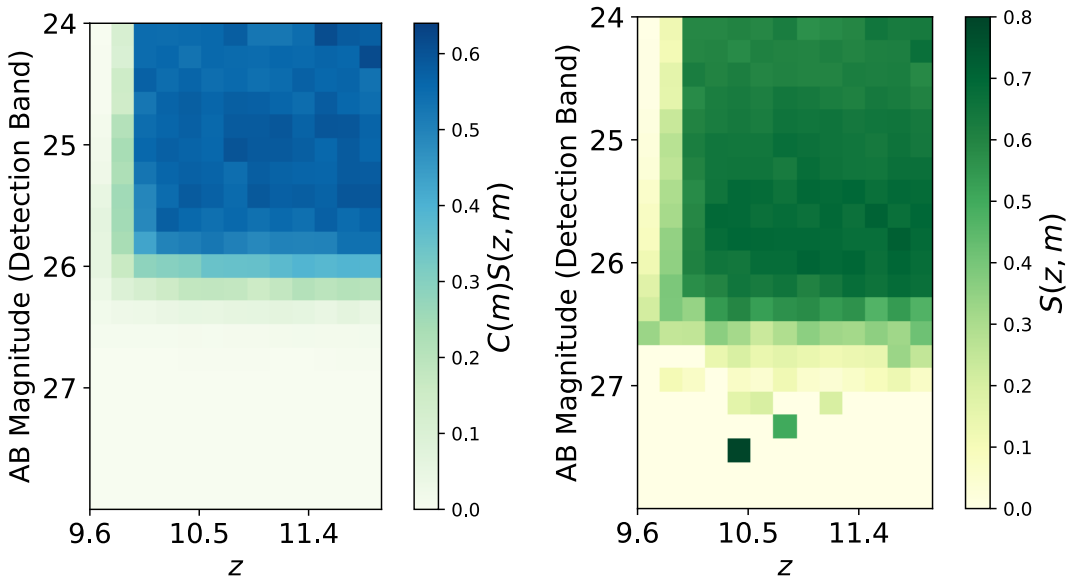

Figure 5.3: Dropouts selection plots produced by our code for the BoRG field *borg_0440-5244* for redshift $z \sim 10$. The left panel shows the dropouts found from all the galaxies inserted ($C(m)S(z,m)$), while the right panel shows the fraction of recovered dropouts ($S(z,m)$) for artificial sources that are successfully identified in the detection band. Note that the right panel becomes noisy for $m_{AB} > 27.0$ since $S(z,m)$ is computed only using the small number of faint artificial galaxies that are identified with success. The left panel does not suffer from such noise, instead.

i.e., it is noise. In terms of the redshift dependence, things do not change considerably In the case of $S(z, m)$, the maximum value is more of the order of $\sim 80\%$, and higher values go up to fainter magnitudes than $S(z, m)C(m)$. This is expected as it means that the objects that are being recovered at this magnitude are actually real dropouts instead of contaminants or dropouts with altered photometry.

5.1.5 Effective Volume

The effective volume of a survey can be defined as:

$$V_{eff}(m) = \int_0^\infty S(z, m)C(m)\frac{dV}{dz}dz, \tag{5.4}$$

where dV/dz is the comoving volume at that redshift, escalated by the area of the survey. We can calculate this in a discrete manner for each magnitude bin. $C(m)$ is the completeness fraction of the survey for a given magnitude. This is calculated by `GLACiAR`. The function $S(z, m)$ is the recovered fraction of objects for a determined magnitude and redshift. This can be calculated directly by `GLACiAR` if the selection technique used is dropouts, and if not, all the information needed for it is given to the user. The users only need to apply their redshift selection method and obtain these parameters. Actually, our code can give the fraction $S(z, m)C(m)$ directly, which is the number of dropouts for a given redshift over the number of detected sources at that magnitude.

In order to calculate $V_{eff}(m)$, the value of dV/dz is required. Following the cosmological concepts from Hogg [1999], the comoving volume V_C is the volume factoring in the expansion of the Universe. Therefore, it is the volume that encompasses a number density of non-evolving objects locked into Hubble flow that are constant with redshift. The comoving volume element dV_C in a solid angle $d\Omega$ and a redshift interval dz can be defined as:

$$dV_C = D_H\frac{(1+z)^2 D_A^2}{E(z)}d\Omega dz \tag{5.5}$$

where D_H is the Hubble distance, defined as:

$$D_H = \frac{c}{H_0}, \tag{5.6}$$

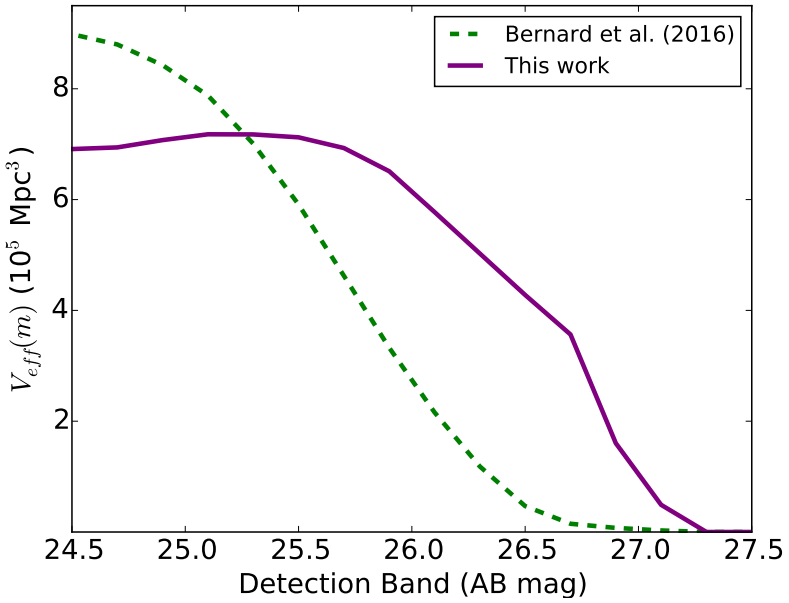

Figure 5.4: Effective Volume of the BoRG[z8] survey calculated as a function of the apparent magnitude in the H band m_H. The green dashed line corresponds to the results from Bernard, Carrasco et al. [2016], and the purple solid line is from this work.

with c being the speed of light, and H_0 the Hubble time; D_A is the angular diameter distance, which corresponds to the ratio between physical and angular size; and $E(z)$ is a function which is defined by the redshift and cosmological parameters as follows:

$$E(z) = \sqrt{\Omega_M(1+z)^3 + \Omega_k(1+z)^2 + \Omega_\Lambda} \tag{5.7}$$

All these parameters depend on the adopted cosmology.

Using the equations described above, we calculate the volume dV/dz and scale it by the area covered by the survey. We do this for every magnitude bin and in this way, we obtain the results shown in Figure 5.4

We compare our results in terms of the calculated effective volume $V_{eff}(m)$, which we get following equation 5.4. The value for $S(z,m)C(m)$ has been given by `GLACiAR`, from all the fields combined. We can calculate dV/dz, with the volume of the survey as a function of the apparent magnitude m. The results from our simulation are shown in Figure 5.4 (solid purple line) compared to the results in Bernard, Carrasco et al. [2016] (green dashed line). As expected from our comparison regarding the selection function recovery results (see Section 5.1.4). `GLACiAR` obtains a smaller volume for

brighter magnitudes $m_{H160} = 24.0 - 25.3$ with values of about $V_{eff}(m_{H160} = 24.0 - 25.9) \sim 7 \times 10^5 \mathrm{Mpc}^3$. The values drop more abruptly for fainter magnitudes, reaching an effective volume of $V_{eff}(m_{H160} = 26.5) = 7 \times 10^4 \mathrm{Mpc}^3$, and dropping to zero for fainter magnitudes. On the other hand, Bernard, Carrasco et al. [2016] results reach a value of $V_{eff}(m_{H160} = 24.5) \sim 9 \times 10^5 \mathrm{Mpc}^3$, which then declines in a more gradual fashion, crossing lines with our results at $m_{H160} = 25.3$ and continue decreasing up to $m_{H160} \sim 26.5$ and beyond, where it is similar to what we obtain.

We are unable to determine which code is correct since there is no point for an absolute comparison. However, we can explain why the differences originate, which is mainly due to how we classify blended objects. We placed objects in the same position as a simulation from Bernard, Carrasco et al. [2016] and examined their recovery status. The only difference was produced by the sources that were classified as blended in one of the codes. The code used in Bernard, Carrasco et al. [2016] considers blending only based on the distance between the two objects. This distance is measured from the central position found by `SExtractor` . In the case of `GLACiAR` , the blending is measured considering the segmentation maps, comparing positions, overlap of sources, and flux loss (see Section 4.4.5 for a detailed explanation). Brighter objects tend to cover more pixels and therefore the method used in Bernard, Carrasco et al. [2016] would not account for that and can potentially consider objects not blended because they are at a certain distance despite them overlapping in the image. `GLACiAR` , on the other hand, does account for this by using the fraction of flux loss and overlapping pixels. This is why we recover fewer brighter objects but more fainter objects. The decline of the curve and virtual no recovery of sources is due to the magnitude limit of the survey, with the noise causing faint sources to blend in. Given the lack of any other public code for completeness and source recovery simulations, it is not possible to investigate further the discrepancies observed here.

Intrinsic versus observed magnitude

It is important to note that the calculations we do here are all as a function of the intrinsic magnitude, which in `GLACiAR` would correspond to the input magnitude. When observations of a galaxy are made, the magnitude we measure is the observed magnitude, which might be different from the intrinsic magnitude. In Figure 5.5 we can see that the observed magnitude tends to be fainter than the intrinsic magnitude. The effective volume is a function of the magnitude, therefore the magnitude we use is significant. When the calculations for the luminosity function with galaxy candidates are made, the effective volume is one of the parameters used here hence the manner in which

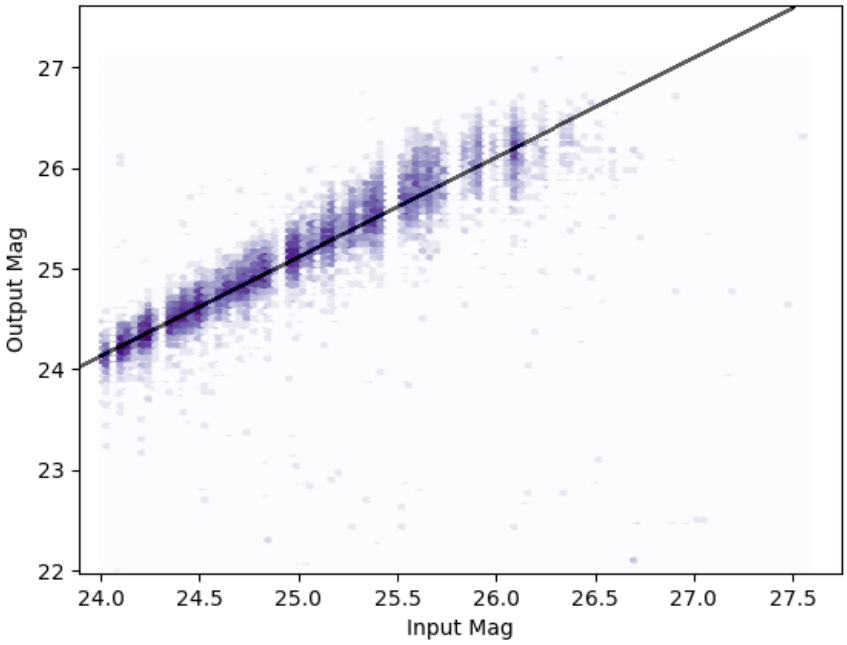

Figure 5.5: 2D histogram showing the input magnitude versus the output magnitude for simulated galaxies in the BoRG[z8] survey. The black line shows where magnitudes are equal. The scale for the amount of objects is logarithmic. It can be seen that the majority of the sources are recovered at fainter galaxies, with the difference ranging between $0.2 - 0.5$, which increases with fainter magnitudes. After $m_{H160} \sim 26.5$ there is only spurious sources since most of them are not recovered.

$V_{eff}(m)$ is calculated will directly impact the results. Since the calculations for the luminosity function are made with the observed magnitude of the galaxy candidates, ideally we would want to have our results as a function of the observed magnitude as well. However, the amount of objects inserted with a certain observed magnitude is not a quantity we can measure. Therefore, in order to calculate our results as a function of an observed magnitude, we must take a different approach. We define the following quantities:

$\phi_{\rm int}(m_{\rm int}, z)$: LF intrinsic at redshift z.

$\epsilon(m_{\rm int}, m_{\rm obs}, z)$: probability of recovering a magnitude $m_{\rm obs}$ for a source with $m_{\rm int}$ at redsift z.

$S(m_{\rm int}, m_{\rm obs}, z)$: Probability of redshift selection for a source with $m_{\rm int}$ and redshift z that is recovered as $m_{\rm obs}$ and redshift z.

$N_{obs}(m_{\rm obs})$: Number density of galaxies at $m_{\rm obs}$.

we can define $N_{obs}(m_{\rm obs})$ as:

$$N_{obs}(m_{\rm obs}) = \int_{m_{\rm min}}^{m_{\rm max}} \int_{z_{\rm min}}^{z_{\rm max}} \phi_{\rm int}(m_{\rm int}, z)\epsilon(m_{\rm int}, m_{\rm obs}, z)S(m_{\rm int}, m_{\rm obs}, z)dzdm_{\rm int} \quad (5.8)$$

We fix z and define $CS(m_{obs})$ (completeness $\times$ selection) such that

$$N_{\rm obs}(m_{\rm obs}) \equiv \phi_{\rm int}(m_{\rm obs}) \times CS(m_{\rm obs}) \quad (5.9)$$

where

$$CS(m_{\rm obs}) = \frac{\int_{m_{\rm int}}^{m_{\rm obs}} \phi_{int}(m_{\rm int}, z)\epsilon(m_{\rm int}, m_{\rm obs}, z)S(m_{\rm int}, m_{\rm obs}, z)dm_{\rm int}}{\phi_{\rm int}(m_{\rm obs})} \quad (5.10)$$

As can be seen, this depends on the LF shape. Using a regular function like the one from Mason et al. [2015] results in considerably different results than a flat LF, for example. This is an important issue for future work. When assuming a flat shape, we get results that are very similar to what we obtain when using the $m_{\rm int}$. The user has available all the resources in case they want to calculate it in a different manner.

5.1.6 Luminosity Function

The luminosity function is calculated with the three galaxy candidates from BoRG[z8] described in Section 3.6. We plot the results obtained with our code for these galaxy candidates, and the results with the same candidates but with a completeness simulation performed using the code explained in Oesch et al. [2014] along with previous studies on the luminosity function with different data. The final plot can be seen in Figure 5.6. The values we obtain for the LF are listed in Table 5.2. From the figure, the red star corresponds to the point estimated with the 3 BoRG candidates, while the other 2 red arrows show upper limits estimated from the lack of candidates. The error bars are 1σ Poison errors, and limits are 1σ upper limits.

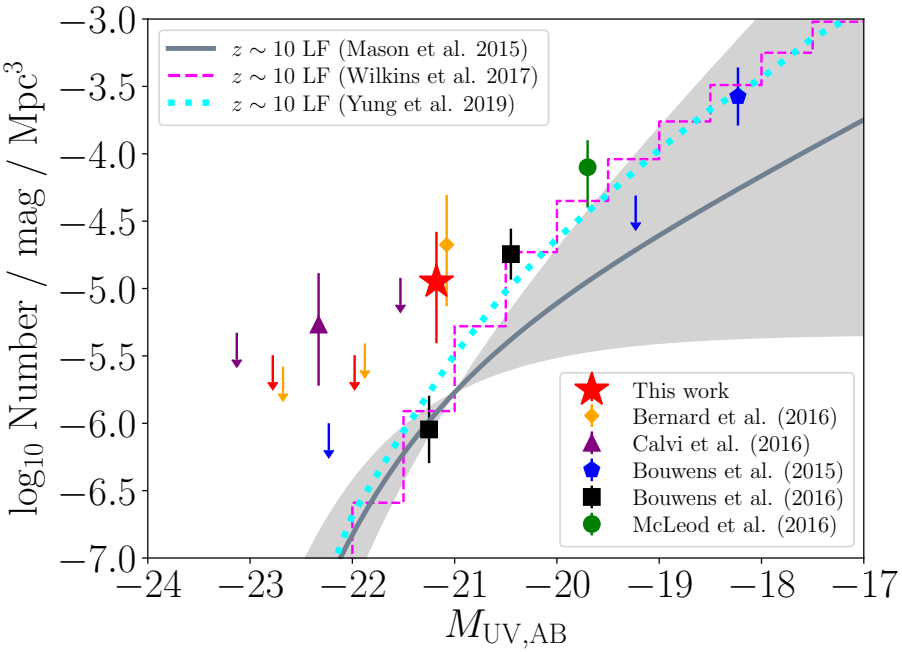

Figure 5.6: Step-wise UV LF at $z \sim 10$. The red star and upper limits correspond to the calculations with our new volume and galaxy candidates from Bernard, Carrasco et al. [2016], whose points are in orange and shifted 0.1 magnitudes in order to compare them. The other values are Bouwens et al. [2016], Bouwens et al. [2015b], Calvi et al. [2016], McLeod et al. [2016], The overplotted gray line indicates the $z \sim 10$ LF from the theoretical model of Mason et al. [2015], with shaded region being the 68% contour of its $\phi*$ uncertainty. We also present the predictions for the LF from hydrodynamical simulations [Wilkins et al., 2017], and a semi-analytic model [Yung et al., 2019]. Our new effective volume estimations from `GLACiAR` reduce the BoRG's survey tension with other literature data and theoretical modelling.

5.1.7 Comparison to previous simulations

We have access to both the results and code in Bernard, Carrasco et al. [2016], which means we can compare our results and understand where differences are generated.

When comparing to the results found on Bernard, Carrasco et al. [2016], we notice the magnitude dependencies differ. We recover a smaller fraction of objects at brighter magnitudes, but a larger fraction in the magnitude range of $m = 25.3 - 26.5$. This is interesting as this is the range where most of these galaxies are expected to be found.

In our case, we recover a smaller effective volume at magnitudes brighter than 25.3, while it is larger for magnitudes in the range between $m = 25.3 - 26.5$. This is expected as the only factor that changes in our calculations is $C(m)S(z, m)$, and this is also what shapes the curve we obtain.

M_{AB}	$\log_{10}/\mathrm{mag}/\mathrm{Mpc}^3$
-21.2	-4.95
-22.0	-5.49
-22.8	-5.48

Table 5.2: Values for the luminosity function at $z \sim 10$ calculated from the BoRG[z8] data and `GLACiAR` simulations.

5.1.8 Validation

There are two small but interesting variations compared to the results obtained by our code. The apparent magnitudes of the galaxy candidates used to measure the LF are $m_{160} = 26.1, 26.2, 26.3$. This is relevant since the main differences of our code with to that used in Bernard, Carrasco et al. [2016] are produced in this area (see Figure 5.4). As mentioned before, our code tends to recover a higher fraction of objects at these magnitudes, up to 50% more depending on the magnitude. This is due to the different manner in which `GLACiAR` classifies a blended object. The main concern that can arise in this case is that the objects we are recovering are not the objects that were placed in there in the first place or their photometry has been altered due of a blending that `GLACiAR` did not classify as such. However, that these objects are not only detected but also recovered as dropouts means that the code finds them successfully, and that their photometry was not modified enough to be removed from the sample.

A second validation of the code is the calculation of the data points for the luminosity function. Assuming that the candidates found in Bernard, Carrasco et al. [2016] are indeed high-z galaxies, and that the LF follows a distribution as from Mason et al. [2015], Wilkins et al. [2017], or Yung et al. [2019], our completeness method brings the data point lower, placing the lower error bar being inside the 68% confidence on the estimation of ϕ. The luminosity function obtained with their galaxy candidates would be in slightly better agreement with Mason et al. [2015] (see Figure 5.6 and Table 5.2), from $10^{-4.7}$ to $10^{-4.95}$ in Number/mag/Mpc^3. This is not an extremely large change, and that is expected as our code follows a similar structure as Oesch et al. [2014] and it makes similar assumptions. Interestingly, despite the big difference between both codes in the magnitude range where there BoRG candidates are, the difference in terms of the measured LF is less considerable.

We are not particularly concerned about the two upper limits as they only show the highest possible value, but give no insight on the minimum, which is our focus in this case.

An interesting point made by Grazian et al. [2011] regarding completeness simulations

when estimating the galaxy luminosity function is that the parameter α has a critical dependence with the half light radii of the artificial galaxies used for the the simulations. Our application of `GLACiAR` to BoRG data is not significantly affected by this issue. In fact, the faint end is more dependent on the completeness simulations used, while the bright end is more limited by the amount of objects found [Dunlop, 2013]. And, as we see in Figures 5.4 and 5.6, the difference in the estimated effective volume does not impact the LF as much. We can assume from here that variations in the morphology or spectral energy distribution choices would not change the results prominently.

5.2 Summary

We have given a summary of the luminosity function, including the equations that describe it, focusing our approach on the Schechter function, which is an empirical analytic description. This function is characterised by three parameters, which are calculated according to the observed data. We have given a brief summary of the values found in the literature for said parameters, and we have discussed the main discrepancies in them.

We run our completeness simulation code, `GLACiAR` , and used the galaxy candidates from Bernard, Carrasco et al. [2016] along with the results for $C(m)S(z,m)$. With these, we have calculated the effective volume $V_{eff}(m)$ for the BoRG[z8] survey and therefore we have re-run the calculations for the data for the luminosity function. Our code shows an improved agreement with Mason et al. [2015] compared to the previous code, although within the error limits. We are able to understand where the differences originate, mainly involving the classification of blended sources. This demonstrates the importance of using open completeness simulations and using a single system in order to estimate measurements for luminosity functions.

6

Conclusions

The focus of this thesis is high redshift galaxies, with particular emphasis on their search in galaxy surveys, the study of completeness and recovery simulations, and measurements of the luminosity function.

The main product of this work is an open `Python` based tool that estimates the source recovery in galaxy surveys, `GLACiAR` . A summary of the findings and future work related to this thesis are described in this Chapter.

6.1 Final Results

We searched for high redshift galaxies ($z \gtrsim 8$) in two *HST* galaxy surveys. Afterwards, we developed a general-purpose, public code to estimate source recovery and completeness of these galaxy candidates that can be applied in similar cases. With the information obtained from these simulations and the galaxy candidates from the surveys, measurements of the galaxy luminosity function can be made. The luminosity

function is very relevant in the study of galaxies as it can help better understand their formation, properties, evolution, and, of particular interest, the role galaxies played in the Reionisation process.

6.1.1 Search for high redshift galaxies

We have performed a search for high redshift galaxies at $z \gtrsim 10$ using data from two surveys, BoRG[z8] and RELICS. The searches and resulting data used are described in Chapter 3. Both surveys were carried out with *HST*. These surveys both aim to find high-redshift galaxies, although their approaches are different. BoRG[z8] looks for the brightest of the high redshift galaxies by observing random points in the sky, covering a large total area. RELICS focuses on fields with galaxy clusters, which produce strong gravitational lensing in the observed area. This phenomenon has a magnification effect on the objects behind the galaxy clusters, allowing us to observe sources that would otherwise be too faint to observe.

Our searches were performed using the Lyman break selection technique. This relies on finding a break in the spectrum of the galaxy known as the Lyman break, which is produced by the absorption of neutral hydrogen. This absorption occurs at a rest-frame wavelength of $\lambda < 912$ Å, and at $\lambda < 1216$ for galaxies at $z \lesssim 4$ [Giavalisco, 2002]. With our focus at $z \sim 10$, we expect the latter break to be present in our candidates.

The selection criteria applied for the surveys has three main features. First, the requirement of strong signal-to-noise in the detection band. Second, the non-detection of flux in the bands that are towards the blue part of the spectrum from the Lyman break. Third is the colour cuts, which measure the strength of the Lyman-break. In addition to the these criteria, avoiding point-like sources, and a visual inspection, will leave us with the final catalogue of galaxies.

The initial result of the BoRG[z8] survey was a catalogue of 6 candidates at $z \sim 10$. When further considering the sizes and magnitudes of the candidates, Bernard, Carrasco et al. [2016] arrived at a sample of 3 candidates.

For the RELICS survey, we find no galaxy candidates at $z \sim 9-10$, and 3 candidates at $z \sim 8$. We compare our results to a search carried out using photometric redshifts, and they have the same results for $z \sim 9-10$, and find 8 candidates at $z \sim 8$. These candidates include 2 of the candidates we found. The remaining 5 candidates were not selected by our technique due to the colour cuts criteria, making our selection more conservative.

	0240-1875_25	*0456-2203_1091*	*0456-2203_1091*
R.A. (deg)	40.1195	73.9774	178.1972
Dec. (deg)	18.9726	22.0372	0.9270
m_{160}	26.2	26.1	26.3
S/N_{160}	8.1	8.1	8.0
Stellarity	0.7	0.5	0.0
r_e	$0''.13$	$0''.24$	$0''.23$
M_{AB}	-21.1	-21.4	-21.2
$log_{10}(SFR)M_\odot yr^{-1}$	1.139	1.259	1.179

Table 6.1: Summary of the high-redshift galaxy candidates from BoRG[z8] and their main properties.

6.1.2 Recovery and Completeness Simulations

In order to use the galaxy candidates in estimations of the luminosity function, we need to estimate the effective volume of the surveys. This requires the measurement of the completeness fraction $C(m)$, and the selection function, $S(z, m)$, corresponding to the fraction of recovered galaxies at a certain magnitude and redshift. These quantities are normally computed by performing completeness simulations.

A completeness simulation is usually carried out by including mock galaxies at a certain redshift z and apparent magnitude m, then studying their recovery using the selection process used to find the observed candidates. These simulations are typically done by either including altered images of real galaxies; or by modelling galaxies following a luminosity profile and other given features. These simulations tend to be done separately for each survey, and no public tool is available, leading to problems when analysing and comparing data. We follow the galaxy-modelling approach, and write a `Python`-based completeness simulation tool, `GLACiAR`. `GLACiAR` has been published [Carrasco et al., 2018] and is available to the public. This code models galaxies following a Sérsic luminosity profile and other parameters input by the user, and places them in the images of a galaxy survey. It then applies a user-defined selection technique, and measures the completeness $C(m)$ and recovery fraction $S(z, m)$ at different redshifts and magnitudes by iterating these two properties of the artificial galaxies.

The advantages of having a tool such as `GLACiAR` include the ability to compare results for galaxies with different properties, and the flexibility of modelling these galaxies. Studies of how these properties can affect calculations for the effective volume, and consequently, the luminosity function, can also be performed.

We applied `GLACiAR` to two different *HST* surveys. In Section 4.9 we show its appli-

cation on the UDF12 field. In Section 5.1.2, we apply the code to the BoRG[z8] survey and use its results along with the galaxy candidates for new measurements of the LF at $z \sim 10$.

6.1.3 Galaxy luminosity function measurements

The galaxy luminosity function is the count of galaxies per luminosity bin in a given volume. This is a very important tool to help us understand the evolution and formation of galaxies and their properties at a given time, among other important questions.

The galaxy luminosity function has been traditionally described by an analytic function known as the Schechter function. This is described in Chapter 5. At lower redshifts ($z \lesssim 7$), this function has been studied and constrained to a high level of confidence. For higher redshift, however, it is only recently taking shape. Recently hundreds of galaxies have been observed at $z \sim 8$, with studies of the luminosity function at this redshift still underway. Nevertheless, there is general agreement that the luminosity function is also described by the Schechter function, but constraints on the bright end in particular are still needed. For again higher redshift, $z \gtrsim 9$, there are not yet enough galaxy candidates, and the study of the luminosity function is a very active topic.

Both our searches aimed at finding candidates at high redshift and using them to better understand the luminosity function. The two surveys used in this thesis are complementary, as we can use their results to investigate different parts of the luminosity function. BoRG is aimed at finding the bright galaxy candidates, while RELICS, due to the gravitational lensing phenomenon, can potentially find objects with less bright intrinsic magnitudes.

We used the BoRG[z8] candidates and our completeness simulation tool `GLACiAR` to estimate the effective volume and the luminosity function (see Table 5.2). This had been previously done by Bernard, Carrasco et al. [2016] with the same galaxy candidates and a different completeness simulation tool. We compare results and find that ours are improved and in better agreement with theoretical estimations (see Figure 5.6). Since we have access to the simulations used in Bernard, Carrasco et al. [2016], we can compare and understand the causes of the differences in our results, which we explain in detail in Chapter 5. This emphasises the value of an open tool such as `GLACiAR` for completeness simulations.

While no suitable candidates were found in the RELICS survey, an upper limit on the luminosity function can still be calculated. However, lensed fields present a differ-

ent challenge, with the effects of this phenomenon needing to be incorporated in the completeness simulation tool. `GLACiAR` still does not have this capacity, therefore we abstain from applying it to this survey.

6.2 Future work

The recent result in the findings of high redshift galaxies are pushing towards the observation of the first galaxies. We can continue expanding on this work.

6.2.1 JWST

The launching the the *JWST* is expected to drastically improve our capacity to find high redshift galaxies the same way *HST* did it when the redshift frontier was $z \sim 2$. First galaxies are expected to have formed at around $z \sim 10 - 15$, a redshift limit that *JWST* is expected to be able to cover. `GLACiAR` was designed with this in mind, and therefore is easily applied to fields observed with *JWST*.

An interesting exercise would be applying `GLACiAR` to synthetic observations from *JWST* to study the source recovery. This can be done to predict the number of expected galaxies, for example.

Despite *JWST* capabilities, not all galaxies will be observable. Faint galaxies, which are likely to have a bigger impact in the Reionisation process, will still be beyond our reach. Gravitational lensing will still therefore play an important role in finding additional high redshift galaxies.

6.2.2 Gravitational Lensing

It is clear how valuable a gravitational lensing tool is in the study of galaxies. Surveys such as CLASH [Postman et al., 2012] and the *Frontier Fields* [Lotz et al., 2017b] are good examples. However, it is important to note that the lack of comprehensive completeness simulations in lensed fields also continues to be an obstacle when studying the luminosity function.

The lack of high redshift candidates in RELICS is puzzling. Some studies show consistent results in terms of the luminosity function, for which we would expect more candidates. One possible explanation is the effective volume covered by the survey because of effect of gravitational lensing. Therefore, completeness simulations are crucial

in order to understand the lack of galaxy candidates and discriminate among the possible explanations.

This motivates the implementation of gravitational lensing capability to our completeness simulation tool, which is currently in preparation.

6.2.3 Source Identification Software

The source identification software used in this release of `GLACiAR` is `SExtractor`. Although this program is fit for purpose, it is an external program run with `GLACiAR`, which can increase processing times. To improve the peformance of `GLACiAR`, future releases will look to utilize `photutils` instead [Bradley et al., 2016], which is a `Python`-based source identification package.

6.3 Final Remarks

We summarise by reiteraiting that exciting times are ahead with the launch of *JWST*. We expect the discovery of galaxies at $z \gtrsim 9$ in quantities that will allow us to further constrain the luminosity function in order to have a better understanding of galaxies, and our universe.

Bibliography

T. Abel, G. L. Bryan, and M. L. Norman. The Formation of the First Star in the Universe. *Science*, 295:93–98, Jan. 2002. doi: 10.1126/science.295.5552.93.

G. O. Abell, J. Corwin, Harold G., and R. P. Olowin. A Catalog of Rich Clusters of Galaxies. *The Astrophysical Journal Supplement Series*, 70:1, May 1989. doi: 10.1086/191333.

A. Acebron, N. Cibirka, A. Zitrin, D. Coe, I. Agulli, K. Sharon, M. Bradač, B. Frye, R. C. Livermore, G. Mahler, B. Salmon, K. Umetsu, L. Bradley, F. Andrade-Santos, R. Avila, D. Carrasco, C. Cerny, N. G. Czakon, W. A. Dawson, A. T. Hoag, K.-H. Huang, T. L. Johnson, C. Jones, S. Kikuchihara, D. Lam, L. Lovisari, R. Mainali, P. A. Oesch, S. Ogaz, M. Ouchi, M. Past, R. Paterno-Mahler, A. Peterson, R. E. Ryan, I. Sendra-Server, D. P. Stark, V. Strait, S. Toft, M. Trenti, and B. Vulcani. RELICS: Strong-lensing Analysis of the Massive Clusters MACS J0308.9+2645 and PLCK G171.9−40.7. *ApJ*, 858:42, May 2018. doi: 10.3847/1538-4357/aabe29.

A. Alavi, B. Siana, J. Richard, D. P. Stark, C. Scarlata, H. I. Teplitz, W. R. Freeman, A. Dominguez, M. Rafelski, B. Robertson, and L. Kewley. Ultra-faint Ultraviolet Galaxies at z 2 behind the Lensing Cluster A1689: The Luminosity Function, Dust Extinction, and Star Formation Rate Density. *ApJ*, 780:143, Jan. 2014. doi: 10.1088/0004-637X/780/2/143.

S. Arnouts, D. Schiminovich, O. Ilbert, L. Tresse, B. Milliard, M. Treyer, S. Bardelli, T. Budavari, T. K. Wyder, E. Zucca, O. Le Fèvre, D. C. Martin, G. Vettolani, C. Adami, M. Arnaboldi, T. Barlow, L. Bianchi, M. Bolzonella, D. Bottini, Y.-I. Byun, A. Cappi, S. Charlot, T. Contini, J. Donas, K. Forster, S. Foucaud, P. Franzetti, P. G. Friedman, B. Garilli, I. Gavignaud, L. Guzzo, T. M. Heckman, C. Hoopes, A. Iovino, P. Jelinsky, V. Le Brun, Y.-W. Lee, D. Maccagni, B. F. Madore,

R. Malina, B. Marano, C. Marinoni, H. J. McCracken, A. Mazure, B. Meneux, R. Merighi, P. Morrissey, S. Neff, S. Paltani, R. Pellò, J. P. Picat, A. Pollo, L. Pozzetti, M. Radovich, R. M. Rich, R. Scaramella, M. Scodeggio, M. Seibert, O. Siegmund, T. Small, A. S. Szalay, B. Welsh, C. K. Xu, G. Zamorani, and A. Zanichelli. The GALEX VIMOS-VLT Deep Survey Measurement of the Evolution of the 1500 Å Luminosity Function. *ApJ*, 619:L43–L46, Jan. 2005. doi: 10.1086/426733.

H. Atek, J. Richard, J.-P. Kneib, M. Jauzac, D. Schaerer, B. Clement, M. Limousin, E. Jullo, P. Natarajan, E. Egami, and H. Ebeling. New Constraints on the Faint End of the UV Luminosity Function at z ˜ 7-8 Using the Gravitational Lensing of the Hubble Frontier Fields Cluster A2744. *ApJ*, 800:18, Feb. 2015. doi: 10.1088/0004-637X/800/1/18.

J. N. Bahcall. Splittings in quasar absorption lines. *ApJ*, 200:L1–L3, Aug. 1975. doi: 10.1086/181883.

J. N. Bahcall and E. E. Salpeter. On the Interaction of Radiation from Distant Sources with the Intervening Medium. *ApJ*, 142:1677–1680, Nov. 1965. doi: 10.1086/148460.

G. Barro, S. M. Faber, P. G. Pérez-González, D. C. Koo, C. C. Williams, D. D. Kocevski, J. R. Trump, M. Mozena, E. McGrath, A. van der Wel, S. Wuyts, E. F. Bell, D. J. Croton, D. Ceverino, A. Dekel, M. L. N. Ashby, E. Cheung, H. C. Ferguson, A. Fontana, J. Fang, M. Giavalisco, N. A. Grogin, Y. Guo, N. P. Hathi, P. F. Hopkins, K.-H. Huang, A. M. Koekemoer, J. S. Kartaltepe, K.-S. Lee, J. A. Newman, L. A. Porter, J. R. Primack, R. E. Ryan, D. Rosario, R. S. Somerville, M. Salvato, and L.-T. Hsu. CANDELS: The Progenitors of Compact Quiescent Galaxies at $z \sim 2$. *ApJ*, 765:104, Mar. 2013. doi: 10.1088/0004-637X/765/2/104.

R. Beare, M. J. I. Brown, K. Pimbblet, F. Bian, and Y.-T. Lin. The z< 1.2 Optical Luminosity Function from a Sample of 410,000 Galaxies in Bo#1255tes. *ApJ*, 815: 94, Dec. 2015. doi: 10.1088/0004-637X/815/2/94.

S. V. W. Beckwith, M. Stiavelli, A. M. Koekemoer, J. A. R. Caldwell, H. C. Ferguson, R. Hook, R. A. Lucas, L. E. Bergeron, M. Corbin, S. Jogee, N. Panagia, M. Robberto, P. Royle, R. S. Somerville, and M. Sosey. The Hubble Ultra Deep Field. *AJ*, 132: 1729–1755, Nov. 2006. doi: 10.1086/507302.

N. Benítez. Bayesian Photometric Redshift Estimation. *ApJ*, 536:571–583, June 2000. doi: 10.1086/308947.

N. Benítez, H. Ford, R. Bouwens, F. Menanteau, J. Blakeslee, C. Gronwall, G. Illingworth, G. Meurer, T. J. Broadhurst, M. Clampin, M. Franx, G. F. Hartig, D. Magee,

M. Sirianni, D. R. Ardila, F. Bartko, R. A. Brown, C. J. Burrows, E. S. Cheng, N. J. G. Cross, P. D. Feldman, D. A. Golimowski, L. Infante, R. A. Kimble, J. E. Krist, M. P. Lesser, Z. Levay, A. R. Martel, G. K. Miley, M. Postman, P. Rosati, W. B. Sparks, H. D. Tran, Z. I. Tsvetanov, R. L. White, and W. Zheng. Faint Galaxies in Deep Advanced Camera for Surveys Observations. *The Astrophysical Journal Supplement Series*, 150:1–18, Jan. 2004. doi: 10.1086/380120.

A. J. Benson. Galaxy formation theory. *Phys. Rep.*, 495:33–86, Oct. 2010. doi: 10.1016/j.physrep.2010.06.001.

S. R. Bernard, D. Carrasco, M. Trenti, P. A. Oesch, J. F. Wu, L. D. Bradley, K. B. Schmidt, R. J. Bouwens, V. Calvi, C. A. Mason, M. Stiavelli, and T. Treu. Galaxy Candidates at $z \sim 10$ in Archival Data from the Brightest of Reionizing Galaxies (BORG[z8]) Survey. *ApJ*, 827:76, Aug. 2016. doi: 10.3847/0004-637X/827/1/76.

M. A. Bershady, J. D. Lowenthal, and D. C. Koo. Near-Infrared Galaxy Counts to J and K ˜ 24 as a Function of Image Size. *ApJ*, 505:50–73, Sept. 1998. doi: 10.1086/306130.

E. Bertin and S. Arnouts. SExtractor: Software for source extraction. *A&AS*, 117:393–404, June 1996. doi: 10.1051/aas:1996164.

B. Binggeli, A. Sandage, and G. A. Tammann. The luminosity function of galaxies. *ARA&A*, 26:509–560, 1988. doi: 10.1146/annurev.aa.26.090188.002453.

R. D. Blandford and R. Narayan. Cosmological applications of gravitational lensing. *Annual Review of Astronomy and Astrophysics*, 30:311–358, Jan. 1992. doi: 10.1146/annurev.astro.30.1.311.

M. R. Blanton, J. Dalcanton, D. Eisenstein, J. Loveday, M. A. Strauss, M. SubbaRao, D. H. Weinberg, J. E. Anderson, Jr., J. Annis, N. A. Bahcall, M. Bernardi, J. Brinkmann, R. J. Brunner, S. Burles, L. Carey, F. J. Castander, A. J. Connolly, I. Csabai, M. Doi, D. Finkbeiner, S. Friedman, J. A. Frieman, M. Fukugita, J. E. Gunn, G. S. Hennessy, R. B. Hindsley, D. W. Hogg, T. Ichikawa, Ž. Ivezić, S. Kent, G. R. Knapp, D. Q. Lamb, R. F. Leger, D. C. Long, R. H. Lupton, T. A. McKay, A. Meiksin, A. Merelli, J. A. Munn, V. Narayanan, M. Newcomb, R. C. Nichol, S. Okamura, R. Owen, J. R. Pier, A. Pope, M. Postman, T. Quinn, C. M. Rockosi, D. J. Schlegel, D. P. Schneider, K. Shimasaku, W. A. Siegmund, S. Smee, Y. Snir, C. Stoughton, C. Stubbs, A. S. Szalay, G. P. Szokoly, A. R. Thakar, C. Tremonti, D. L. Tucker, A. Uomoto, D. Vanden Berk, M. S. Vogeley, P. Waddell, B. Yanny, N. Yasuda, and D. G. York. The Luminosity Function of Galaxies in SDSS Commissioning Data. *AJ*, 121:2358–2380, May 2001. doi: 10.1086/320405.

J. S. Bolton, E. Puchwein, D. Sijacki, M. G. Haehnelt, T.-S. Kim, A. Meiksin, J. A. Regan, and M. Viel. The Sherwood simulation suite: overview and data comparisons with the Lyman α forest at redshifts $2 \leq z \leq 5$. *MNRAS*, 464:897–914, Jan. 2017. doi: 10.1093/mnras/stw2397.

R. J. Bouwens, G. D. Illingworth, P. Rosati, C. Lidman, T. Broadhurst, M. Franx, H. C. Ford, D. Magee, N. Benítez, J. P. Blakeslee, G. R. Meurer, M. Clampin, G. F. Hartig, D. R. Ardila, F. Bartko, R. A. Brown, C. J. Burrows, E. S. Cheng, N. J. G. Cross, P. D. Feldman, D. A. Golimowski, C. Gronwall, L. Infante, R. A. Kimble, J. E. Krist, M. P. Lesser, A. R. Martel, F. Menanteau, G. K. Miley, M. Postman, M. Sirianni, W. B. Sparks, H. D. Tran, Z. I. Tsvetanov, R. L. White, and W. Zheng. Star Formation at z˜6: i-Dropouts in the Advanced Camera for Surveys Guaranteed Time Observation Fields. *ApJ*, 595:589–602, Oct. 2003. doi: 10.1086/377477.

R. J. Bouwens, G. D. Illingworth, J. P. Blakeslee, and M. Franx. Galaxies at $z \sim 6$: The UV Luminosity Function and Luminosity Density from 506 HUDF, HUDF Parallel ACS Field, and GOODS i-Dropouts. *ApJ*, 653:53–85, Dec. 2006. doi: 10.1086/498733.

R. J. Bouwens, G. D. Illingworth, M. Franx, and H. Ford. z 7-10 Galaxies in the HUDF and GOODS Fields: UV Luminosity Functions. *ApJ*, 686:230–250, Oct. 2008. doi: 10.1086/590103.

R. J. Bouwens, G. D. Illingworth, M. Franx, R.-R. Chary, G. R. Meurer, C. J. Conselice, H. Ford, M. Giavalisco, and P. van Dokkum. UV Continuum Slope and Dust Obscuration from z ˜ 6 to z ˜ 2: The Star Formation Rate Density at High Redshift. *ApJ*, 705:936–961, Nov. 2009. doi: 10.1088/0004-637X/705/1/936.

R. J. Bouwens, G. D. Illingworth, P. A. Oesch, I. Labbé, M. Trenti, P. van Dokkum, M. Franx, M. Stiavelli, C. M. Carollo, D. Magee, and V. Gonzalez. Ultraviolet Luminosity Functions from 132 z 7 and z 8 Lyman-break Galaxies in the Ultradeep HUDF09 and Wide-area Early Release Science WFC3/IR Observations. *ApJ*, 737:90, Aug. 2011. doi: 10.1088/0004-637X/737/2/90.

R. J. Bouwens, G. D. Illingworth, P. A. Oesch, I. Labbé, P. G. van Dokkum, M. Trenti, M. Franx, R. Smit, V. Gonzalez, and D. Magee. UV-continuum Slopes of >4000 z $\sim$ 4-8 Galaxies from the HUDF/XDF, HUDF09, ERS, CANDELS-South, and CANDELS-North Fields. *ApJ*, 793:115, Oct. 2014. doi: 10.1088/0004-637X/793/2/115.

R. J. Bouwens, G. D. Illingworth, P. A. Oesch, J. Caruana, B. Holwerda, R. Smit, and S. Wilkins. Reionization After Planck: The Derived Growth of the Cosmic Ionizing Emissivity Now Matches the Growth of the Galaxy UV Luminosity Density. *ApJ*, 811:140, Oct. 2015a. doi: 10.1088/0004-637X/811/2/140.

R. J. Bouwens, G. D. Illingworth, P. A. Oesch, M. Trenti, I. Labbé, L. Bradley, M. Carollo, P. G. van Dokkum, V. Gonzalez, B. Holwerda, M. Franx, L. Spitler, R. Smit, and D. Magee. UV Luminosity Functions at Redshifts z $\sim$ 4 to z $\sim$ 10: 10,000 Galaxies from HST Legacy Fields. *ApJ*, 803:34, Apr. 2015b. doi: 10.1088/0004-637X/803/1/34.

R. J. Bouwens, P. A. Oesch, I. Labbé, G. D. Illingworth, G. G. Fazio, D. Coe, B. Holwerda, R. Smit, M. Stefanon, P. G. van Dokkum, M. Trenti, M. L. N. Ashby, J.-S. Huang, L. Spitler, C. Straatman, L. Bradley, and D. Magee. The Bright End of the z $\sim$ 9 and z $\sim$ 10 UV Luminosity Functions Using All Five CANDELS Fields*. *ApJ*, 830:67, Oct. 2016. doi: 10.3847/0004-637X/830/2/67.

R. J. Bouwens, P. A. Oesch, G. D. Illingworth, R. S. Ellis, and M. Stefanon. The $z \sim 6$ Luminosity Function Fainter than -15 mag from the Hubble Frontier Fields: The Impact of Magnification Uncertainties. *ApJ*, 843:129, July 2017. doi: 10.3847/1538-4357/aa70a4.

R. A. A. Bowler, J. S. Dunlop, R. J. McLure, H. J. McCracken, B. Milvang-Jensen, H. Furusawa, J. P. U. Fynbo, O. Le Fèvre, J. Holt, Y. Ideue, Y. Ihara, A. B. Rogers, and Y. Taniguchi. Discovery of bright z âĽČ 7 galaxies in the UltraVISTA survey. *MNRAS*, 426:2772–2788, Nov. 2012. doi: 10.1111/j.1365-2966.2012.21904.x.

R. A. A. Bowler, J. S. Dunlop, R. J. McLure, H. J. McCracken, B. Milvang-Jensen, H. Furusawa, Y. Taniguchi, O. Le Fèvre, J. P. U. Fynbo, M. J. Jarvis, and B. Häußler. The galaxy luminosity function at z $\sim$ 6 and evidence for rapid evolution in the bright end from z $\sim$ 7 to 5. *MNRAS*, 452:1817–1840, Sept. 2015. doi: 10.1093/mnras/stv1403.

R. A. A. Bowler, J. S. Dunlop, R. J. McLure, and D. J. McLeod. Unveiling the nature of bright z âĽČ 7 galaxies with the Hubble Space Telescope. *MNRAS*, 466:3612–3635, Apr. 2017a. doi: 10.1093/mnras/stw3296.

R. A. A. Bowler, R. J. McLure, J. S. Dunlop, D. J. McLeod, E. R. Stanway, J. J. Eldridge, and M. J. Jarvis. No evidence for Population III stars or a Direct Collapse Black Hole in the z = 6.6 Lyman-α emitter 'CR7'. *MNRAS*, 469:448–458, Apr. 2017b. doi: 10.1093/mnras/stx839.

L. Bradley, B. Sipocz, T. Robitaille, E. Tollerud, Z. VinÃŋcius, C. Deil, K. Barbary, H. M. GÃijnther, M. Cara, M. Droettboom, A. Bostroem, E. Bray, L. A. Bratholm, T. E. Pickering, M. Craig, G. Barentsen, S. Pascual, adonath, J. Greco, W. Kerzendorf, StuartLittlefair, L. Ferreira, F. D'Eugenio, and B. A. Weaver. astropy/photutils: v0.3, Nov. 2016. URL `https://doi.org/10.5281/zenodo.164986`.

L. D. Bradley, M. Trenti, P. A. Oesch, M. Stiavelli, T. Treu, R. J. Bouwens, J. M. Shull, B. W. Holwerda, and N. Pirzkal. The Brightest of Reionizing Galaxies Survey: Constraints on the Bright End of the z ˜ 8 Luminosity Function. *ApJ*, 760:108, Dec. 2012. doi: 10.1088/0004-637X/760/2/108.

G. B. Brammer, P. G. van Dokkum, and P. Coppi. EAZY: A Fast, Public Photometric Redshift Code. *ApJ*, 686:1503–1513, Oct. 2008. doi: 10.1086/591786.

M. Brasken and E. Kyrola. Resonance scattering of Lyman alpha from interstellar hydrogen. *A&A*, 332:732–738, Apr. 1998.

V. Bromm and N. Yoshida. The first galaxies. *Annual Review of Astronomy and Astrophysics*, 49(1):373–407, 2011. doi: 10.1146/annurev-astro-081710-102608. URL `https://doi.org/10.1146/annurev-astro-081710-102608`.

V. Bromm, N. Yoshida, L. Hernquist, and C. F. McKee. The formation of the first stars and galaxies. *Nature*, 459:49–54, May 2009. doi: 10.1038/nature07990.

A. Bunker, E. Stanway, R. Ellis, R. McMahon, L. Eyles, and M. Lacy. Star forming galaxies at $z \sim 6$ and reionization. *New A Rev.*, 50:94–100, Mar. 2006. doi: 10.1016/j.newar.2005.11.006.

V. Calvi, M. Trenti, M. Stiavelli, P. Oesch, L. D. Bradley, K. B. Schmidt, D. Coe, G. Brammer, S. Bernard, R. J. Bouwens, D. Carrasco, C. M. Carollo, B. W. Holwerda, J. W. MacKenty, C. A. Mason, J. M. Shull, and T. Treu. Bright Galaxies at Hubble's Redshift Detection Frontier: Preliminary Results and Design from the Redshift z ∼ 9-10 BoRG Pure-Parallel HST Survey. *ApJ*, 817:120, Feb. 2016. doi: 10.3847/0004-637X/817/2/120.

J. B. Carlson. Book review: Archaeoastronomy in america: Archaeoastronomy in pre-columbian america. *Journal for the History of Astronomy*, 7(3):205–206, 1976. doi: 10.1177/002182867600700307. URL `https://doi.org/10.1177/002182867600700307`.

D. Carrasco, M. Trenti, S. Mutch, and P. A. Oesch. GLACiAR, an Open-Source Python Tool for Simulations of Source Recovery and Completeness in Galaxy Surveys. *Publications of the Astronomical Society of Australia*, 35:e022, June 2018. doi: 10.1017/pasa.2018.17.

B. W. Carroll and D. A. Ostlie. *An introduction to modern astrophysics and cosmology*. July 2006.

J. Caruana, A. J. Bunker, S. M. Wilkins, E. R. Stanway, M. Lacy, M. J. Jarvis, S. Lorenzoni, and S. Hickey. No evidence for Lyman α emission in spectroscopy of z > 7 candidate galaxies. *MNRAS*, 427:3055–3070, Dec. 2012. doi: 10.1111/j.1365-2966.2012.21996.x.

C. Cerny, K. Sharon, F. Andrade-Santos, R. J. Avila, M. Bradač, L. D. Bradley, D. Carrasco, D. Coe, N. G. Czakon, W. A. Dawson, B. L. Frye, A. Hoag, K.-H. Huang, T. L. Johnson, C. Jones, D. Lam, L. Lovisari, R. Mainali, P. A. Oesch, S. Ogaz, M. Past, R. Paterno-Mahler, A. Peterson, A. G. Riess, S. A. Rodney, R. E. Ryan, B. Salmon, I. Sendra-Server, D. P. Stark, L.-G. Strolger, M. Trenti, K. Umetsu, B. Vulcani, and A. Zitrin. RELICS: Strong Lens Models for Five Galaxy Clusters from the Reionization Lensing Cluster Survey. *ApJ*, 859:159, June 2018. doi: 10.3847/1538-4357/aabe7b.

D. Ceverino, S. C. O. Glover, and R. S. Klessen. Introducing the FirstLight project: UV luminosity function and scaling relations of primeval galaxies. *MNRAS*, 470:2791–2798, Sept. 2017. doi: 10.1093/mnras/stx1386.

J. Choloniewski. On Lynden-Bell's method for the determination of the luminosity function. *MNRAS*, 226:273–280, May 1987. doi: 10.1093/mnras/226.2.273.

N. Cibirka, A. Acebron, A. Zitrin, D. Coe, I. Agulli, F. Andrade-Santos, M. Bradač, B. Frye, R. C. Livermore, G. Mahler, B. Salmon, K. Sharon, M. Trenti, K. Umetsu, R. Avila, L. Bradley, D. Carrasco, C. Cerny, N. G. Czakon, W. A. Dawson, A. T. Hoag, K.-H. Huang, T. L. Johnson, C. Jones, S. Kikuchihara, D. Lam, L. Lovisari, R. Mainali, P. A. Oesch, S. Ogaz, M. Ouchi, M. Past, R. Paterno-Mahler, A. Peterson, R. E. Ryan, I. Sendra-Server, D. P. Stark, V. Strait, S. Toft, and B. Vulcani. RELICS: Strong Lensing Analysis of the Galaxy Clusters Abell S295, Abell 697, MACS J0025.4-1222, and MACS J0159.8-0849. *ApJ*, 863:145, Aug. 2018. doi: 10.3847/1538-4357/aad2d3.

L. Ciotti. Stellar systems following the R exp 1/m luminosity law. *A&A*, 249:99–106, Sept. 1991.

D. Coe, N. Benítez, S. F. Sánchez, M. Jee, R. Bouwens, and H. Ford. Galaxies in the Hubble Ultra Deep Field. I. Detection, Multiband Photometry, Photometric Redshifts, and Morphology. *AJ*, 132:926–959, Aug. 2006. doi: 10.1086/505530.

D. Coe, A. Zitrin, M. Carrasco, X. Shu, W. Zheng, M. Postman, L. Bradley, A. Koekemoer, R. Bouwens, T. Broadhurst, A. Monna, O. Host, L. A. Moustakas, H. Ford, J. Moustakas, A. van der Wel, M. Donahue, S. A. Rodney, N. Benítez, S. Jouvel,

S. Seitz, D. D. Kelson, and P. Rosati. CLASH: Three Strongly Lensed Images of a Candidate z $\sim$ 11 Galaxy. *ApJ*, 762:32, Jan. 2013. doi: 10.1088/0004-637X/762/1/32.

J. G. Cohen. Caltech Faint Galaxy Redshift Survey. XVI. The Luminosity Function for Galaxies in the Region of the Hubble Deep Field-North to z=1.5. *ApJ*, 567:672–701, Mar. 2002. doi: 10.1086/338226.

J. Cooke, E. V. Ryan-Weber, T. Garel, and C. G. Díaz. Lyman-continuum galaxies and the escape fraction of Lyman-break galaxies. *MNRAS*, 441:837–851, June 2014. doi: 10.1093/mnras/stu635.

D. Cristóbal-Hornillos, J. A. L. Aguerri, M. Moles, J. Perea, F. J. Castander, T. Broadhurst, E. J. Alfaro, N. Benítez, J. Cabrera-Caño, J. Cepa, M. Cerviño, A. Fernández-Soto, R. M. González Delgado, C. Husillos, L. Infante, I. Márquez, V. J. Martínez, J. Masegosa, A. del Olmo, F. Prada, J. M. Quintana, and S. F. Sánchez. Near-Infrared Galaxy Counts and Evolution from the Wide-Field ALHAMBRA Survey. *ApJ*, 696: 1554–1575, May 2009. doi: 10.1088/0004-637X/696/2/1554.

O. Cucciati, L. Tresse, O. Ilbert, O. Le Fèvre, B. Garilli, V. Le Brun, P. Cassata, P. Franzetti, D. Maccagni, M. Scodeggio, E. Zucca, G. Zamorani, S. Bardelli, M. Bolzonella, R. M. Bielby, H. J. McCracken, A. Zanichelli, and D. Vergani. The star formation rate density and dust attenuation evolution over 12 Gyr with the VVDS surveys. *A&A*, 539:A31, Mar. 2012. doi: 10.1051/0004-6361/201118010.

E. Curtis-Lake, R. J. McLure, J. S. Dunlop, A. B. Rogers, T. Targett, A. Dekel, R. S. Ellis, S. M. Faber, H. C. Ferguson, N. A. Grogin, D. D. Kocevski, A. M. Koekemoer, K. Lai, E. Mármol-Queraltó, and B. E. Robertson. Non-parametric analysis of the rest-frame UV sizes and morphological disturbance amongst L_* galaxies at $4 < z < 8$. *MNRAS*, 457:440–464, Mar. 2016. doi: 10.1093/mnras/stv3017.

E. Daddi, A. Cimatti, A. Renzini, A. Fontana, M. Mignoli, L. Pozzetti, P. Tozzi, and G. Zamorani. A New Photometric Technique for the Joint Selection of Star-forming and Passive Galaxies at $1.4 \lesssim z \lesssim 2.5$. *ApJ*, 617:746–764, Dec. 2004. doi: 10.1086/425569.

E. Daddi, M. Dickinson, R. Chary, A. Pope, G. Morrison, D. M. Alexander, F. E. Bauer, W. N. Brandt, M. Giavalisco, H. Ferguson, K.-S. Lee, B. D. Lehmer, C. Papovich, and A. Renzini. The Population of BzK-selected ULIRGs at z ˜ 2. *ApJ*, 631:L13–L16, Sept. 2005. doi: 10.1086/496918.

T. Dahlen, B. Mobasher, M. Dickinson, H. C. Ferguson, M. Giavalisco, C. Kretchmer, and S. Ravindranath. Evolution of the Luminosity Function, Star Formation Rate,

Morphology, and Size of Star-forming Galaxies Selected at Rest-Frame 1500 and 2800 Å. *ApJ*, 654:172–185, Jan. 2007. doi: 10.1086/508854.

P. Dayal, A. Ferrara, and A. Saro. The cool side of Lyman alpha emitters. *MNRAS*, 402:1449–1457, Mar. 2010. doi: 10.1111/j.1365-2966.2009.15995.x.

G. de Vaucouleurs. Recherches sur les Nebuleuses Extragalactiques. *Annales d'Astrophysique*, 11:247, Jan. 1948.

M. Dijkstra. Lyα Emitting Galaxies as a Probe of Reionisation. *Publications of the Astronomical Society of Australia*, 31:e040, Oct. 2014. doi: 10.1017/pasa.2014.33.

M. Dijkstra, Z. Haiman, M. J. Rees, and D. H. Weinberg. Photoionization Feedback in Low-Mass Galaxies at High Redshift. *ApJ*, 601:666–675, Feb. 2004. doi: 10.1086/380603.

M. Dijkstra, J. S. B. Wyithe, and Z. Haiman. Luminosity functions of Lyα emitting galaxies and cosmic reionization of hydrogen. *MNRAS*, 379:253–259, July 2007. doi: 10.1111/j.1365-2966.2007.11936.x.

S. Dodelson. *Modern cosmology*. 2003.

N. Drory, M. Salvato, A. Gabasch, R. Bender, U. Hopp, G. Feulner, and M. Pannella. The Stellar Mass Function of Galaxies to $z \sim 5$ in the FORS Deep and GOODS-South Fields. *ApJ*, 619:L131–L134, Feb. 2005. doi: 10.1086/428044.

K. Duncan and C. J. Conselice. Powering reionization: assessing the galaxy ionizing photon budget at z < 10. *MNRAS*, 451:2030–2049, Aug. 2015. doi: 10.1093/mnras/stv1049.

J. S. Dunlop. Observing the First Galaxies. In T. Wiklind, B. Mobasher, and V. Bromm, editors, *The First Galaxies*, volume 396 of *Astrophysics and Space Science Library*, page 223, 2013. doi: 10.1007/978-3-642-32362-1_5.

J. S. Dunlop, A. B. Rogers, R. J. McLure, R. S. Ellis, B. E. Robertson, A. Koekemoer, P. Dayal, E. Curtis-Lake, V. Wild, S. Charlot, R. A. A. Bowler, M. A. Schenker, M. Ouchi, Y. Ono, M. Cirasuolo, S. R. Furlanetto, D. P. Stark, T. A. Targett, and E. Schneider. The UV continua and inferred stellar populations of galaxies at z âĽČ 7-9 revealed by the Hubble Ultra-Deep Field 2012 campaign. *MNRAS*, 432:3520–3533, July 2013. doi: 10.1093/mnras/stt702.

H. Ebeling, A. C. Edge, and J. P. Henry. MACS: A Quest for the Most Massive Galaxy Clusters in the Universe. *ApJ*, 553:668–676, June 2001. doi: 10.1086/320958.

G. Efstathiou, R. S. Ellis, and B. A. Peterson. Analysis of a complete galaxy redshift survey. II - The field-galaxy luminosity function. *MNRAS*, 232:431–461, May 1988. doi: 10.1093/mnras/232.2.431.

J. Einasto, I. Suhhonenko, G. Hütsi, E. Saar, M. Einasto, L. J. Liivamägi, V. Müller, A. A. Starobinsky, E. Tago, and E. Tempel. Towards understanding the structure of voids in the cosmic web. *A&A*, 534:A128, Oct. 2011. doi: 10.1051/0004-6361/201117248.

R. S. Ellis, M. Colless, T. Broadhurst, J. Heyl, and K. Glazebrook. Autofib Redshift Survey - I. Evolution of the galaxy luminosity function. *MNRAS*, 280:235–251, May 1996. doi: 10.1093/mnras/280.1.235.

R. S. Ellis, R. J. McLure, J. S. Dunlop, B. E. Robertson, Y. Ono, M. A. Schenker, A. Koekemoer, R. A. A. Bowler, M. Ouchi, A. B. Rogers, E. Curtis-Lake, E. Schneider, S. Charlot, D. P. Stark, S. R. Furlanetto, and M. Cirasuolo. The Abundance of Star-forming Galaxies in the Redshift Range 8.5-12: New Results from the 2012 Hubble Ultra Deep Field Campaign. *ApJ*, 763:L7, Jan 2013. doi: 10.1088/2041-8205/763/1/L7.

S. M. Faber, C. N. A. Willmer, C. Wolf, D. C. Koo, B. J. Weiner, J. A. Newman, M. Im, A. L. Coil, C. Conroy, M. C. Cooper, M. Davis, D. P. Finkbeiner, B. F. Gerke, K. Gebhardt, E. J. Groth, P. Guhathakurta, J. Harker, N. Kaiser, S. Kassin, M. Kleinheinrich, N. P. Konidaris, R. G. Kron, L. Lin, G. Luppino, D. S. Madgwick, K. Meisenheimer, K. G. Noeske, A. C. Phillips, V. L. Sarajedini, R. P. Schiavon, L. Simard, A. S. Szalay, N. P. Vogt, and R. Yan. Galaxy Luminosity Functions to z˜1 from DEEP2 and COMBO-17: Implications for Red Galaxy Formation. *ApJ*, 665:265–294, Aug. 2007. doi: 10.1086/519294.

X. Fan, M. A. Strauss, R. H. Becker, R. L. White, J. E. Gunn, G. R. Knapp, G. T. Richards, D. P. Schneider, J. Brinkmann, and M. Fukugita. Constraining the Evolution of the Ionizing Background and the Epoch of Reionization with z˜6 Quasars. II. A Sample of 19 Quasars. *AJ*, 132:117–136, July 2006. doi: 10.1086/504836.

D. J. Farrow, S. Cole, P. Norberg, N. Metcalfe, I. Baldry, J. Bland-Hawthorn, M. J. I. Brown, A. M. Hopkins, C. G. Lacey, J. Liske, J. Loveday, D. P. Palamara, A. S. G. Robotham, and S. Sridhar. Galaxy and mass assembly (GAMA): projected galaxy clustering. *MNRAS*, 454:2120–2145, Dec. 2015. doi: 10.1093/mnras/stv2075.

S. L. Finkelstein, C. Papovich, B. Salmon, K. Finlator, M. Dickinson, H. C. Ferguson, M. Giavalisco, A. M. Koekemoer, N. A. Reddy, R. Bassett, C. J. Conselice, J. S. Dunlop, S. M. Faber, N. A. Grogin, N. P. Hathi, D. D. Kocevski, K. Lai, K.-S.

Lee, R. J. McLure, B. Mobasher, and J. A. Newman. Candels: The Evolution of Galaxy Rest-frame Ultraviolet Colors from z = 8 to 4. *ApJ*, 756:164, Sept. 2012. doi: 10.1088/0004-637X/756/2/164.

S. L. Finkelstein, R. E. Ryan, Jr., C. Papovich, M. Dickinson, M. Song, R. S. Somerville, H. C. Ferguson, B. Salmon, M. Giavalisco, A. M. Koekemoer, M. L. N. Ashby, P. Behroozi, M. Castellano, J. S. Dunlop, S. M. Faber, G. G. Fazio, A. Fontana, N. A. Grogin, N. Hathi, J. Jaacks, D. D. Kocevski, R. Livermore, R. J. McLure, E. Merlin, B. Mobasher, J. A. Newman, M. Rafelski, V. Tilvi, and S. P. Willner. The Evolution of the Galaxy Rest-frame Ultraviolet Luminosity Function over the First Two Billion Years. *ApJ*, 810:71, Sept. 2015. doi: 10.1088/0004-637X/810/1/71.

S. Folkes, S. Ronen, I. Price, O. Lahav, M. Colless, S. Maddox, K. Deeley, K. Glazebrook, J. Bland-Hawthorn, R. Cannon, S. Cole, C. Collins, W. Couch, S. P. Driver, G. Dalton, G. Efstathiou, R. S. Ellis, C. S. Frenk, N. Kaiser, I. Lewis, S. Lumsden, J. Peacock, B. A. Peterson, W. Sutherland, and K. Taylor. The 2dF Galaxy Redshift Survey: spectral types and luminosity functions. *MNRAS*, 308:459–472, Sept. 1999. doi: 10.1046/j.1365-8711.1999.02721.x.

J. W. Fried, B. von Kuhlmann, K. Meisenheimer, H.-W. Rix, C. Wolf, H. H. Hippelein, M. Kümmel, S. Phleps, H. J. Röser, I. Thierring, and C. Maier. The luminosity function of field galaxies and its evolution since z=1. *A&A*, 367:788–800, Mar. 2001. doi: 10.1051/0004-6361:20000466.

C. S. Froning and J. C. Green. The cosmic origins spectrograph: capabilities and prelaunch performance. *Ap&SS*, 320:181–185, Apr. 2009. doi: 10.1007/s10509-008-9758-y.

S. R. Furlanetto, M. Zaldarriaga, and L. Hernquist. The effects of reionization on Lyα galaxy surveys. *MNRAS*, 365:1012–1020, Jan. 2006. doi: 10.1111/j.1365-2966.2005.09785.x.

A. Gabasch, R. Bender, S. Seitz, U. Hopp, R. P. Saglia, G. Feulner, J. Snigula, N. Drory, I. Appenzeller, J. Heidt, D. Mehlert, S. Noll, A. Böhm, K. Jäger, B. Ziegler, and K. J. Fricke. The evolution of the luminosity functions in the FORS Deep Field from low to high redshift. I. The blue bands. *A&A*, 421:41–58, July 2004. doi: 10.1051/0004-6361:20035909.

G. Gamow. Expanding Universe and the Origin of Elements. *Physical Review*, 70: 572–573, Oct. 1946. doi: 10.1103/PhysRev.70.572.2.

L. Gao, N. Yoshida, T. Abel, C. S. Frenk, A. Jenkins, and V. Springel. The first generation of stars in the Λ cold dark matter cosmology. *MNRAS*, 378:449–468, June 2007. doi: 10.1111/j.1365-2966.2007.11814.x.

J. P. Gardner, S. A. Baum, T. M. Brown, C. M. Carollo, J. Christensen, I. Dashevsky, M. E. Dickinson, B. R. Espey, H. C. Ferguson, A. S. Fruchter, A. M. Gonnella, R. A. Gonzalez-Lopezlira, R. N. Hook, M. E. Kaiser, C. L. Martin, K. C. Sahu, S. Savaglio, T. E. Smith, H. I. Teplitz, R. E. Williams, and J. Wilson. The hubble deep field south: STIS imaging. *The Astronomical Journal*, 119(2):486–508, feb 2000. doi: 10.1086/301215. URL `https://doi.org/10.1086%2F301215`.

E. Giallongo, A. Grazian, F. Fiore, A. Fontana, L. Pentericci, E. Vanzella, M. Dickinson, D. Kocevski, M. Castellano, S. Cristiani, H. Ferguson, S. Finkelstein, N. Grogin, N. Hathi, A. M. Koekemoer, J. A. Newman, and M. Salvato. Faint AGNs at z $>$ 4 in the CANDELS GOODS-S field: looking for contributors to the reionization of the Universe. *A&A*, 578:A83, June 2015. doi: 10.1051/0004-6361/201425334.

M. Giavalisco. Lyman-Break Galaxies. *ARA&A*, 40:579–641, 2002. doi: 10.1146/annurev.astro.40.121301.111837.

M. Giavalisco, C. C. Steidel, and F. D. Macchetto. Hubble Space Telescope Imaging of Star-forming Galaxies at Redshifts Z $>$ 3. *ApJ*, 470:189, Oct. 1996. doi: 10.1086/177859.

M. Giavalisco, H. C. Ferguson, A. M. Koekemoer, M. Dickinson, D. M. Alexander, F. E. Bauer, J. Bergeron, C. Biagetti, W. N. Brandt, S. Casertano, C. Cesarsky, E. Chatzichristou, C. Conselice, S. Cristiani, L. Da Costa, T. Dahlen, D. de Mello, P. Eisenhardt, T. Erben, S. M. Fall, C. Fassnacht, R. Fosbury, A. Fruchter, J. P. Gardner, N. Grogin, R. N. Hook, A. E. Hornschemeier, R. Idzi, S. Jogee, C. Kretchmer, V. Laidler, K. S. Lee, M. Livio, R. Lucas, P. Madau, B. Mobasher, L. A. Moustakas, M. Nonino, P. Padovani, C. Papovich, Y. Park, S. Ravindranath, A. Renzini, M. Richardson, A. Riess, P. Rosati, M. Schirmer, E. Schreier, R. S. Somerville, H. Spinrad, D. Stern, M. Stiavelli, L. Strolger, C. M. Urry, B. Vandame, R. Williams, and C. Wolf. The Great Observatories Origins Deep Survey: Initial Results from Optical and Near-Infrared Imaging. *ApJ*, 600:L93–L98, Jan. 2004. doi: 10.1086/379232.

S. Glover. The Formation Of The First Stars In The Universe. *Space Sci. Rev.*, 117:445–508, Apr. 2005. doi: 10.1007/s11214-005-5821-y.

J. González-López, D. A. Riechers, R. Decarli, F. Walter, L. Vallini, R. Neri, F. Bertoldi, A. D. Bolatto, C. L. Carilli, P. Cox, E. da Cunha, A. Ferrara, S. Gallerani, and

L. Infante. Search for [C II] Emission in z = 6.5-11 Star-forming Galaxies. *ApJ*, 784: 99, Apr. 2014. doi: 10.1088/0004-637X/784/2/99.

A. W. Graham and S. P. Driver. A Concise Reference to (Projected) Sérsic $R^{1/n}$ Quantities, Including Concentration, Profile Slopes, Petrosian Indices, and Kron Magnitudes. *PASA*, 22:118–127, 2005. doi: 10.1071/AS05001.

A. Grazian, M. Castellano, A. M. Koekemoer, A. Fontana, L. Pentericci, V. Testa, K. Boutsia, E. Giallongo, M. Giavalisco, and P. Santini. A critical analysis of the UV luminosity function at redshift ˜7 from deep WFC3 data. *A&A*, 532:A33, Aug. 2011. doi: 10.1051/0004-6361/201015754.

A. Grazian, M. Castellano, A. Fontana, L. Pentericci, J. S. Dunlop, R. J. McLure, A. M. Koekemoer, M. E. Dickinson, S. M. Faber, H. C. Ferguson, A. Galametz, M. Giavalisco, N. A. Grogin, N. P. Hathi, D. D. Kocevski, K. Lai, J. A. Newman, and E. Vanzella. The size-luminosity relation at z = 7 in CANDELS and its implication on reionization. *A&A*, 547:A51, Nov. 2012. doi: 10.1051/0004-6361/201219669.

B. Greig and A. Mesinger. The global history of reionization. *MNRAS*, 465:4838–4852, Mar. 2017. doi: 10.1093/mnras/stw3026.

N. A. Grogin, D. D. Kocevski, S. M. Faber, H. C. Ferguson, A. M. Koekemoer, A. G. Riess, V. Acquaviva, D. M. Alexander, O. Almaini, M. L. N. Ashby, M. Barden, E. F. Bell, F. Bournaud, T. M. Brown, K. I. Caputi, S. Casertano, P. Cassata, M. Castellano, P. Challis, R.-R. Chary, E. Cheung, M. Cirasuolo, C. J. Conselice, A. Roshan Cooray, D. J. Croton, E. Daddi, T. Dahlen, R. Davé, D. F. de Mello, A. Dekel, M. Dickinson, T. Dolch, J. L. Donley, J. S. Dunlop, A. A. Dutton, D. Elbaz, G. G. Fazio, A. V. Filippenko, S. L. Finkelstein, A. Fontana, J. P. Gardner, P. M. Garnavich, E. Gawiser, M. Giavalisco, A. Grazian, Y. Guo, N. P. Hathi, B. Häussler, P. F. Hopkins, J.-S. Huang, K.-H. Huang, S. W. Jha, J. S. Kartaltepe, R. P. Kirshner, D. C. Koo, K. Lai, K.-S. Lee, W. Li, J. M. Lotz, R. A. Lucas, P. Madau, P. J. McCarthy, E. J. McGrath, D. H. McIntosh, R. J. McLure, B. Mobasher, L. A. Moustakas, M. Mozena, K. Nandra, J. A. Newman, S.-M. Niemi, K. G. Noeske, C. J. Papovich, L. Pentericci, A. Pope, J. R. Primack, A. Rajan, S. Ravindranath, N. A. Reddy, A. Renzini, H.-W. Rix, A. R. Robaina, S. A. Rodney, D. J. Rosario, P. Rosati, S. Salimbeni, C. Scarlata, B. Siana, L. Simard, J. Smidt, R. S. Somerville, H. Spinrad, A. N. Straughn, L.-G. Strolger, O. Telford, H. I. Teplitz, J. R. Trump, A. van der Wel, C. Villforth, R. H. Wechsler, B. J. Weiner, T. Wiklind, V. Wild, G. Wilson, S. Wuyts, H.-J. Yan, and M. S. Yun. CANDELS: The Cosmic Assembly Near-infrared Deep Extragalactic Legacy Survey. *The Astrophysical Journal Supplement Series*, 197:35, Dec. 2011. doi: 10.1088/0067-0049/197/2/35.

J. E. Gunn and B. A. Peterson. On the Density of Neutral Hydrogen in Intergalactic Space. *ApJ*, 142:1633–1641, Nov. 1965. doi: 10.1086/148444.

H. Hildebrandt, J. Pielorz, T. Erben, P. Schneider, T. Eifler, P. Simon, and J. P. Dietrich. GaBoDS: the Garching-Bonn deep survey. VIII. Lyman-break galaxies in the ESO deep public survey. *A&A*, 462:865–873, Feb. 2007. doi: 10.1051/0004-6361:20065880.

H. Hildebrandt, M. Viola, C. Heymans, S. Joudaki, K. Kuijken, C. Blake, T. Erben, B. Joachimi, D. Klaes, L. Miller, C. B. Morrison, R. Nakajima, G. Verdoes Kleijn, A. Amon, A. Choi, G. Covone, J. T. A. de Jong, A. Dvornik, I. Fenech Conti, A. Grado, J. Harnois-Déraps, R. Herbonnet, H. Hoekstra, F. Köhlinger, J. McFarland, A. Mead, J. Merten, N. Napolitano, J. A. Peacock, M. Radovich, P. Schneider, P. Simon, E. A. Valentijn, J. L. van den Busch, E. van Uitert, and L. Van Waerbeke. KiDS-450: cosmological parameter constraints from tomographic weak gravitational lensing. *MNRAS*, 465:1454–1498, Feb. 2017. doi: 10.1093/mnras/stw2805.

G. Hinshaw, D. Larson, E. Komatsu, D. N. Spergel, C. L. Bennett, J. Dunkley, M. R. Nolta, M. Halpern, R. S. Hill, N. Odegard, L. Page, K. M. Smith, J. L. Weiland, B. Gold, N. Jarosik, A. Kogut, M. Limon, S. S. Meyer, G. S. Tucker, E. Wollack, and E. L. Wright. Nine-year Wilkinson Microwave Anisotropy Probe (WMAP) Observations: Cosmological Parameter Results. *ApJS*, 208:19, Oct. 2013. doi: 10.1088/0067-0049/208/2/19.

M. Hirschmann, T. Naab, R. S. Somerville, A. Burkert, and L. Oser. Galaxy formation in semi-analytic models and cosmological hydrodynamic zoom simulations. *MNRAS*, 419:3200–3222, Feb. 2012. doi: 10.1111/j.1365-2966.2011.19961.x.

D. W. Hogg. Distance measures in cosmology. *ArXiv Astrophysics e-prints*, May 1999.

B. W. Holwerda, M. Trenti, W. Clarkson, K. Sahu, L. Bradley, M. Stiavelli, N. Pirzkal, G. De Marchi, M. Andersen, R. Bouwens, and R. Ryan. Milky Way Red Dwarfs in the BoRG Survey; Galactic Scale-height and the Distribution of Dwarf Stars in WFC3 Imaging. *ApJ*, 788:77, June 2014. doi: 10.1088/0004-637X/788/1/77.

B. W. Holwerda, R. Bouwens, P. Oesch, R. Smit, G. Illingworth, and I. Labbe. The Sizes of Candidate zĬČ9-10 Galaxies: Confirmation of the Bright CANDELS Sample and Relation with Luminosity and Mass. *ApJ*, 808:6, July 2015. doi: 10.1088/0004-637X/808/1/6.

J. D. Hunter. Matplotlib: A 2d graphics environment. *Computing In Science & Engineering*, 9(3):90–95, 2007. doi: 10.1109/MCSE.2007.55.

O. Ilbert, L. Tresse, E. Zucca, S. Bardelli, S. Arnouts, G. Zamorani, L. Pozzetti, D. Bottini, B. Garilli, V. Le Brun, O. Le Fèvre, D. Maccagni, J.-P. Picat, R. Scaramella, M. Scodeggio, G. Vettolani, A. Zanichelli, C. Adami, M. Arnaboldi, M. Bolzonella, A. Cappi, S. Charlot, T. Contini, S. Foucaud, P. Franzetti, I. Gavignaud, L. Guzzo, A. Iovino, H. J. McCracken, B. Marano, C. Marinoni, G. Mathez, A. Mazure, B. Meneux, R. Merighi, S. Paltani, R. Pello, A. Pollo, M. Radovich, M. Bondi, A. Bongiorno, G. Busarello, P. Ciliegi, F. Lamareille, Y. Mellier, P. Merluzzi, V. Ripepi, and D. Rizzo. The VIMOS-VLT deep survey. Evolution of the galaxy luminosity function up to z = 2 in first epoch data. *A&A*, 439:863–876, Sept. 2005. doi: 10.1051/0004-6361:20041961.

O. Ilbert, S. Lauger, L. Tresse, V. Buat, S. Arnouts, O. Le Fèvre, D. Burgarella, E. Zucca, S. Bardelli, G. Zamorani, D. Bottini, B. Garilli, V. Le Brun, D. Maccagni, J. P. Picat, R. Scaramella, M. Scodeggio, G. Vettolani, A. Zanichelli, C. Adami, M. Arnaboldi, M. Bolzonella, A. Cappi, S. Charlot, T. Contini, S. Foucaud, P. Franzetti, I. Gavignaud, L. Guzzo, A. Iovino, H. J. McCracken, B. Marano, C. Marinoni, G. Mathez, A. Mazure, B. Meneux, R. Merighi, S. Paltani, R. Pello, A. Pollo, L. Pozzetti, M. Radovich, M. Bondi, A. Bongiorno, G. Busarello, P. Ciliegi, Y. Mellier, P. Merluzzi, V. Ripepi, and D. Rizzo. The VIMOS-VLT Deep Survey. Galaxy luminosity function per morphological type up to z = 1.2. *A&A*, 453:809–815, July 2006. doi: 10.1051/0004-6361:20053632.

G. D. Illingworth, D. Magee, P. A. Oesch, R. J. Bouwens, I. Labbé, M. Stiavelli, P. G. van Dokkum, M. Franx, M. Trenti, C. M. Carollo, and V. Gonzalez. The HST eXtreme Deep Field (XDF): Combining All ACS and WFC3/IR Data on the HUDF Region into the Deepest Field Ever. *The Astrophysical Journal Supplement Series*, 209:6, Nov. 2013. doi: 10.1088/0067-0049/209/1/6.

K. Imai, H. Matsuhara, S. Oyabu, T. Wada, T. Takagi, N. Fujishiro, H. Hanami, and C. P. Pearson. J- and Ks-Band Galaxy Counts and Color Distributions in the AKARI North Ecliptic Pole Field. *AJ*, 133:2418–2428, May 2007. doi: 10.1086/513513.

M. Ishigaki, R. Kawamata, M. Ouchi, M. Oguri, K. Shimasaku, and Y. Ono. Full-data Results of Hubble Frontier Fields: UV Luminosity Functions at z $\sim$ 6âŤĂ10 and a Consistent Picture of Cosmic Reionization. *ApJ*, 854:73, Feb. 2018. doi: 10.3847/1538-4357/aaa544.

I. Iwata, K. Ohta, N. Tamura, M. Akiyama, K. Aoki, M. Ando, G. Kiuchi, and M. Sawicki. Differential evolution of the UV luminosity function of Lyman break galaxies from z ˜ 5 to 3. *MNRAS*, 376:1557–1576, Apr. 2007. doi: 10.1111/j.1365-2966.2007.11557.x.

J. C. Jackson. The analysis of quasar samples. *MNRAS*, 166:281–296, Feb. 1974. doi: 10.1093/mnras/166.2.281.

L. Jiang, E. Egami, N. Kashikawa, G. Walth, Y. Matsuda, K. Shimasaku, T. Nagao, K. Ota, and M. Ouchi. Keck Spectroscopy of Lyman-break Galaxies and Its Implications for the UV-continuum and Lyα Luminosity Functions at z $>$ 6. *ApJ*, 743:65, Dec. 2011. doi: 10.1088/0004-637X/743/1/65.

L. Jiang, Y. Shen, F. Bian, Z.-Y. Zheng, J. Wu, G. A. Oyarzún, G. A. Blanc, X. Fan, L. C. Ho, L. Infante, R. Wang, X.-B. Wu, M. Mateo, I. Bailey, John I., J. D. Crane, E. W. Olszewski, S. Shectman, I. Thompson, and M. G. Walker. A Magellan M2FS Spectroscopic Survey of Galaxies at 5.5 < z < 6.8: Program Overview and a Sample of the Brightest Lyα Emitters. *ApJ*, 846:134, Sept. 2017. doi: 10.3847/1538-4357/aa8561.

J. L. Johnson, T. H. Greif, and V. Bromm. Occurrence of metal-free galaxies in the early Universe. *MNRAS*, 388:26–38, July 2008. doi: 10.1111/j.1365-2966.2008.13381.x.

R. Johnston. Shedding light on the galaxy luminosity function. *A&A Rev.*, 19:41, Aug. 2011. doi: 10.1007/s00159-011-0041-9.

E. Jones, T. Oliphant, P. Peterson, et al. SciPy: Open source scientific tools for Python, 2001. URL `http://www.scipy.org/`. [Online; accessed <today>].

G. Jungman, M. Kamionkowski, and K. Griest. Supersymmetric dark matter. *Phys. Rep.*, 267:195–373, Mar. 1996. doi: 10.1016/0370-1573(95)00058-5.

N. Kashikawa, K. Shimasaku, M. A. Malkan, M. Doi, Y. Matsuda, M. Ouchi, Y. Taniguchi, C. Ly, T. Nagao, M. Iye, K. Motohara, T. Murayama, K. Murozono, K. Nariai, K. Ohta, S. Okamura, T. Sasaki, Y. Shioya, and M. Umemura. The End of the Reionization Epoch Probed by Lyα Emitters at z = 6.5 in the Subaru Deep Field. *ApJ*, 648:7–22, Sept. 2006. doi: 10.1086/504966.

J. Kennicutt, Robert C. Star Formation in Galaxies Along the Hubble Sequence. *Annual Review of Astronomy and Astrophysics*, 36:189–232, Jan. 1998. doi: 10.1146/annurev.astro.36.1.189.

T. Kiang. The galaxian luminosity function. *MNRAS*, 122:263, 1961. doi: 10.1093/mnras/122.3.263.

T.-S. Kim, E. M. Hu, L. L. Cowie, and A. Songaila. The Redshift Evolution of the Ly alpha Forest. *AJ*, 114:1–13, July 1997. doi: 10.1086/118446.

T. S. Kim, S. Cristiani, and S. D'Odorico. The Lyalpha forest at 1.5 < z < 4. *A&A*, 373:757–781, July 2001. doi: 10.1051/0004-6361:20010650.

R. P. Kirshner, J. Oemler, A., and P. L. Schechter. A study of field galaxies. II. The luminosity function and space distribution of galaxies. *AJ*, 84:951–959, July 1979. doi: 10.1086/112498.

H. A. Kobulnicky and L. J. Kewley. Metallicities of 0.3<z<1.0 Galaxies in the GOODS-North Field. *ApJ*, 617:240–261, Dec. 2004. doi: 10.1086/425299.

A. M. Koekemoer, A. S. Fruchter, R. N. Hook, and W. Hack. MultiDrizzle: An Integrated Pyraf Script for Registering, Cleaning and Combining Images. In S. Arribas, A. Koekemoer, and B. Whitmore, editors, *HST Calibration Workshop : Hubble after the Installation of the ACS and the NICMOS Cooling System*, page 337, 2003.

A. M. Koekemoer, S. M. Faber, H. C. Ferguson, N. A. Grogin, D. D. Kocevski, D. C. Koo, K. Lai, J. M. Lotz, R. A. Lucas, E. J. McGrath, S. Ogaz, A. Rajan, A. G. Riess, S. A. Rodney, L. Strolger, S. Casertano, M. Castellano, T. Dahlen, M. Dickinson, T. Dolch, A. Fontana, M. Giavalisco, A. Grazian, Y. Guo, N. P. Hathi, K.-H. Huang, A. van der Wel, H.-J. Yan, V. Acquaviva, D. M. Alexander, O. Almaini, M. L. N. Ashby, M. Barden, E. F. Bell, F. Bournaud, T. M. Brown, K. I. Caputi, P. Cassata, P. J. Challis, R.-R. Chary, E. Cheung, M. Cirasuolo, C. J. Conselice, A. Roshan Cooray, D. J. Croton, E. Daddi, R. Davé, D. F. de Mello, L. de Ravel, A. Dekel, J. L. Donley, J. S. Dunlop, A. A. Dutton, D. Elbaz, G. G. Fazio, A. V. Filippenko, S. L. Finkelstein, C. Frazer, J. P. Gardner, P. M. Garnavich, E. Gawiser, R. Gruetzbauch, W. G. Hartley, B. Häussler, J. Herrington, P. F. Hopkins, J.-S. Huang, S. W. Jha, A. Johnson, J. S. Kartaltepe, A. A. Khostovan, R. P. Kirshner, C. Lani, K.-S. Lee, W. Li, P. Madau, P. J. McCarthy, D. H. McIntosh, R. J. McLure, C. McPartland, B. Mobasher, H. Moreira, A. Mortlock, L. A. Moustakas, M. Mozena, K. Nandra, J. A. Newman, J. L. Nielsen, S. Niemi, K. G. Noeske, C. J. Papovich, L. Pentericci, A. Pope, J. R. Primack, S. Ravindranath, N. A. Reddy, A. Renzini, H.-W. Rix, A. R. Robaina, D. J. Rosario, P. Rosati, S. Salimbeni, C. Scarlata, B. Siana, L. Simard, J. Smidt, D. Snyder, R. S. Somerville, H. Spinrad, A. N. Straughn, O. Telford, H. I. Teplitz, J. R. Trump, C. Vargas, C. Villforth, C. R. Wagner, P. Wandro, R. H. Wechsler, B. J. Weiner, T. Wiklind, V. Wild, G. Wilson, S. Wuyts, and M. S. Yun. CANDELS: The Cosmic Assembly Near-infrared Deep Extragalactic Legacy Survey - The Hubble Space Telescope Observations, Imaging Data Products, and Mosaics. *ApJS*, 197:36, Dec. 2011. doi: 10.1088/0067-0049/197/2/36.

A. M. Koekemoer, R. S. Ellis, R. J. McLure, J. S. Dunlop, B. E. Robertson, Y. Ono, M. A. Schenker, M. Ouchi, R. A. A. Bowler, A. B. Rogers, E. Curtis-Lake, E. Schnei-

der, S. Charlot, D. P. Stark, S. R. Furlanetto, M. Cirasuolo, V. Wild, and T. Targett. The 2012 Hubble Ultra Deep Field (UDF12): Observational Overview. *The Astrophysical Journal Supplement Series*, 209:3, Nov 2013. doi: 10.1088/0067-0049/209/1/3.

X. Kong, E. Daddi, N. Arimoto, A. Renzini, T. Broadhurst, A. Cimatti, C. Ikuta, K. Ohta, L. da Costa, L. F. Olsen, M. Onodera, and N. Tamura. A Wide Area Survey for High-Redshift Massive Galaxies. I. Number Counts and Clustering of BzKs and EROs. *ApJ*, 638:72–87, Feb. 2006. doi: 10.1086/498698.

M. Kuhlen and C.-A. Faucher-Giguère. Concordance models of reionization: implications for faint galaxies and escape fraction evolution. *MNRAS*, 423:862–876, June 2012. doi: 10.1111/j.1365-2966.2012.20924.x.

C. Leitherer. Ultraviolet Spectra of Local Galaxies and their Link with the High-z Population. In G. Giobbi, A. Tornambe, G. Raimondo, M. Limongi, L. A. Antonelli, N. Menci, and E. Brocato, editors, *American Institute of Physics Conference Series*, volume 1111 of *American Institute of Physics Conference Series*, pages 175–182, May 2009. doi: 10.1063/1.3141539.

C. Leitherer, D. Schaerer, J. D. Goldader, R. M. G. Delgado, C. Robert, D. F. Kune, D. F. de Mello, D. Devost, and T. M. Heckman. Starburst99: Synthesis Models for Galaxies with Active Star Formation. *The Astrophysical Journal Supplement Series*, 123:3–40, July 1999. doi: 10.1086/313233.

S. J. Lilly, L. Tresse, F. Hammer, D. Crampton, and O. Le Fevre. The Canada-France Redshift Survey. VI. Evolution of the Galaxy Luminosity Function to Z approximately 1. *ApJ*, 455:108, Dec. 1995. doi: 10.1086/176560.

S. J. Lilly, O. Le Fevre, F. Hammer, and D. Crampton. The Canada-France Redshift Survey: The Luminosity Density and Star Formation History of the Universe to Z approximately 1. *ApJ*, 460:L1, Mar. 1996. doi: 10.1086/309975.

H. Lin, R. P. Kirshner, S. A. Shectman, S. D. Landy, A. Oemler, D. L. Tucker, and P. L. Schechter. The Luminosity Function of Galaxies in the Las Campanas Redshift Survey. *ApJ*, 464:60, June 1996. doi: 10.1086/177300.

H. Lin, H. K. C. Yee, R. G. Carlberg, S. L. Morris, M. Sawicki, D. R. Patton, G. Wirth, and C. W. Shepherd. The CNOC2 Field Galaxy Luminosity Function. I. A Description of Luminosity Function Evolution. *ApJ*, 518:533–561, June 1999. doi: 10.1086/307297.

A. D. Linde. A new inflationary universe scenario: A possible solution of the horizon, flatness, homogeneity, isotropy and primordial monopole problems. *Physics Letters B*, 108:389–393, Feb. 1982. doi: 10.1016/0370-2693(82)91219-9.

A. D. Linde. Chaotic inflation. *Physics Letters B*, 129:177–181, Sept. 1983. doi: 10.1016/0370-2693(83)90837-7.

C. Liu, S. J. Mutch, P. W. Angel, A. R. Duffy, P. M. Geil, G. B. Poole, A. Mesinger, and J. S. B. Wyithe. Dark-ages reionization and galaxy formation simulation - IV. UV luminosity functions of high-redshift galaxies. *MNRAS*, 462:235–249, Oct. 2016. doi: 10.1093/mnras/stw1015.

C. Liu, S. J. Mutch, G. B. Poole, P. W. Angel, A. R. Duffy, P. M. Geil, A. Mesinger, and J. S. B. Wyithe. Dark-ages reionization and galaxy-formation simulation - VII. The sizes of high-redshift galaxies. *MNRAS*, 465:3134–3142, Mar. 2017. doi: 10.1093/mnras/stw2912.

R. C. Livermore, S. L. Finkelstein, and J. M. Lotz. Directly Observing the Galaxies Likely Responsible for Reionization. *ApJ*, 835:113, Feb. 2017. doi: 10.3847/1538-4357/835/2/113.

R. C. Livermore, M. Trenti, L. D. Bradley, S. R. Bernard, B. W. Holwerda, C. A. Mason, and T. Treu. HST followup observations of two bright z 8 candidate galaxies from the BoRG pure-parallel survey. *ArXiv e-prints*, art. arXiv:1805.05038, May 2018.

A. Loeb and R. Barkana. The Reionization of the Universe by the First Stars and Quasars. *ARA&A*, 39:19–66, 2001. doi: 10.1146/annurev.astro.39.1.19.

S. Lorenzoni, A. J. Bunker, S. M. Wilkins, J. Caruana, E. R. Stanway, and M. J. Jarvis. Constraining the bright-end of the UV luminosity function for z ≈ 7-9 galaxies: results from CANDELS/GOODS-South. *MNRAS*, 429:150–158, Feb. 2013. doi: 10.1093/mnras/sts325.

J. M. Lotz, A. Koekemoer, D. Coe, N. Grogin, P. Capak, J. Mack, J. Anderson, R. Avila, E. A. Barker, D. Borncamp, G. Brammer, M. Durbin, H. Gunning, B. Hilbert, H. Jenkner, H. Khandrika, Z. Levay, R. A. Lucas, J. MacKenty, S. Ogaz, B. Porterfield, N. Reid, M. Robberto, P. Royle, L. J. Smith, L. J. Storrie-Lombardi, B. Sunnquist, J. Surace, D. C. Taylor, R. Williams, J. Bullock, M. Dickinson, S. Finkelstein, P. Natarajan, J. Richard, B. Robertson, J. Tumlinson, A. Zitrin, K. Flanagan, K. Sembach, B. T. Soifer, and M. Mountain. The Frontier Fields: Survey Design and Initial Results. *ApJ*, 837:97, Mar. 2017a. doi: 10.3847/1538-4357/837/1/97.

J. M. Lotz, A. Koekemoer, D. Coe, N. Grogin, P. Capak, J. Mack, J. Anderson, R. Avila, E. A. Barker, D. Borncamp, G. Brammer, M. Durbin, H. Gunning, B. Hilbert, H. Jenkner, H. Khandrika, Z. Levay, R. A. Lucas, J. MacKenty, S. Ogaz, B. Porterfield, N. Reid, M. Robberto, P. Royle, L. J. Smith, L. J. Storrie-Lombardi, B. Sunnquist, J. Surace, D. C. Taylor, R. Williams, J. Bullock, M. Dickinson, S. Finkelstein, P. Natarajan, J. Richard, B. Robertson, J. Tumlinson, A. Zitrin, K. Flanagan, K. Sembach, B. T. Soifer, and M. Mountain. The Frontier Fields: Survey Design and Initial Results. *ApJ*, 837:97, Mar. 2017b. doi: 10.3847/1538-4357/837/1/97.

J. Loveday. Evolution of the galaxy luminosity function at z $<$ 0.3. *MNRAS*, 347: 601–606, Jan. 2004. doi: 10.1111/j.1365-2966.2004.07230.x.

J. Loveday, B. A. Peterson, G. Efstathiou, and S. J. Maddox. The Stromlo-APM Redshift Survey. I - The luminosity function and space density of galaxies. *ApJ*, 390: 338–344, May 1992. doi: 10.1086/171284.

D. Lynden-Bell. A method of allowing for known observational selection in small samples applied to 3CR quasars. *MNRAS*, 155:95, 1971. doi: 10.1093/mnras/155.1.95.

P. Madau and M. Dickinson. Cosmic Star-Formation History. *ARA&A*, 52:415–486, Aug. 2014. doi: 10.1146/annurev-astro-081811-125615.

P. Madau, H. C. Ferguson, M. E. Dickinson, M. Giavalisco, C. C. Steidel, and A. Fruchter. High-redshift galaxies in the Hubble Deep Field: colour selection and star formation history to z˜4. *MNRAS*, 283:1388–1404, Dec. 1996. doi: 10.1093/mnras/283.4.1388.

P. Madau, L. Pozzetti, and M. Dickinson. The Star Formation History of Field Galaxies. *ApJ*, 498:106–116, May 1998. doi: 10.1086/305523.

P. Madau, F. Haardt, and M. J. Rees. Radiative Transfer in a Clumpy Universe. III. The Nature of Cosmological Ionizing Sources. *ApJ*, 514:648–659, Apr. 1999. doi: 10.1086/306975.

U. Maio, S. Khochfar, J. L. Johnson, and B. Ciardi. The interplay between chemical and mechanical feedback from the first generation of stars. *MNRAS*, 414:1145–1157, June 2011. doi: 10.1111/j.1365-2966.2011.18455.x.

S. Malhotra and J. E. Rhoads. Luminosity Functions of Lyα Emitters at Redshifts z=6.5 and z=5.7: Evidence against Reionization at z<=6.5. *ApJ*, 617:L5–L8, Dec. 2004. doi: 10.1086/427182.

R. O. Marzke, M. J. Geller, J. P. Huchra, and H. G. Corwin, Jr. The luminosity function for different morphological types in the CfA Redshift Survey. *AJ*, 108:437–445, Aug. 1994a. doi: 10.1086/117081.

R. O. Marzke, J. P. Huchra, and M. J. Geller. The luminosity function of the CfA Redshift Survey. *ApJ*, 428:43–50, June 1994b. doi: 10.1086/174218.

C. A. Mason, M. Trenti, and T. Treu. The Galaxy UV Luminosity Function before the Epoch of Reionization. *ApJ*, 813:21, Nov. 2015. doi: 10.1088/0004-637X/813/1/21.

J. C. Mather, E. S. Cheng, J. Eplee, R. E., R. B. Isaacman, S. S. Meyer, R. A. Shafer, R. Weiss, E. L. Wright, C. L. Bennett, N. W. Boggess, E. Dwek, S. Gulkis, M. G. Hauser, M. Janssen, T. Kelsall, P. M. Lubin, J. Moseley, S. H., T. L. Murdock, R. F. Silverberg, G. F. Smoot, and D. T. Wilkinson. A Preliminary Measurement of the Cosmic Microwave Background Spectrum by the Cosmic Background Explorer (COBE) Satellite. *ApJ*, 354:L37, May 1990. doi: 10.1086/185717.

H. J. McCracken, P. Capak, M. Salvato, H. Aussel, D. Thompson, E. Daddi, D. B. Sanders, J.-P. Kneib, C. J. Willott, C. Mancini, A. Renzini, R. Cook, O. Le Fèvre, O. Ilbert, J. Kartaltepe, A. M. Koekemoer, Y. Mellier, T. Murayama, N. Z. Scoville, Y. Shioya, and Y. Tanaguchi. The COSMOS-WIRCam Near-Infrared Imaging Survey. I. BzK-Selected Passive and Star-Forming Galaxy Candidates at z gsim 1.4. *ApJ*, 708: 202–217, Jan. 2010. doi: 10.1088/0004-637X/708/1/202.

D. J. McLeod, R. J. McLure, and J. S. Dunlop. The z = 9-10 galaxy population in the Hubble Frontier Fields and CLASH surveys: the z = 9 luminosity function and further evidence for a smooth decline in ultraviolet luminosity density at $z \geq 8$. *MNRAS*, 459: 3812–3824, July 2016. doi: 10.1093/mnras/stw904.

R. J. McLure, M. Cirasuolo, J. S. Dunlop, S. Foucaud, and O. Almaini. The luminosity function, halo masses and stellar masses of luminous Lyman-break galaxies at redshifts $5 < z < 6$. *MNRAS*, 395:2196–2209, June 2009. doi: 10.1111/j.1365-2966.2009.14677.x.

R. J. McLure, J. S. Dunlop, R. A. A. Bowler, E. Curtis- Lake, M. Schenker, R. S. Ellis, B. E. Robertson, A. M. Koekemoer, A. B. Rogers, Y. Ono, M. Ouchi, S. Charlot, V. Wild, D. P. Stark, S. R. Furlanetto, M. Cirasuolo, and T. A. Targett. A new multifield determination of the galaxy luminosity function at z = 7-9 incorporating the 2012 Hubble Ultra-Deep Field imaging. *MNRAS*, 432:2696–2716, July 2013. doi: 10.1093/mnras/stt627.

M. McQuinn and M. White. On estimating Lyα forest correlations between multiple sightlines. *MNRAS*, 415:2257–2269, Aug. 2011. doi: 10.1111/j.1365-2966.2011.18855.x.

M. Meneghetti, E. Rasia, J. Vega, J. Merten, M. Postman, G. Yepes, F. Sembolini, M. Donahue, S. Ettori, K. Umetsu, I. Balestra, M. Bartelmann, N. Benítez, A. Biviano, R. Bouwens, L. Bradley, T. Broadhurst, D. Coe, N. Czakon, M. De Petris, H. Ford, C. Giocoli, S. Gottlöber, C. Grillo, L. Infante, S. Jouvel, D. Kelson, A. Koekemoer, O. Lahav, D. Lemze, E. Medezinski, P. Melchior, A. Mercurio, A. Molino, L. Moscardini, A. Monna, J. Moustakas, L. A. Moustakas, M. Nonino, J. Rhodes, P. Rosati, J. Sayers, S. Seitz, W. Zheng, and A. Zitrin. The MUSIC of CLASH: Predictions on the Concentration-Mass Relation. *ApJ*, 797:34, Dec. 2014. doi: 10.1088/0004-637X/797/1/34.

M. Meneghetti, P. Natarajan, D. Coe, E. Contini, G. De Lucia, C. Giocoli, A. Acebron, S. Borgani, M. Bradac, J. M. Diego, A. Hoag, M. Ishigaki, T. L. Johnson, E. Jullo, R. Kawamata, D. Lam, M. Limousin, J. Liesenborgs, M. Oguri, K. Sebesta, K. Sharon, L. L. R. Williams, and A. Zitrin. The Frontier Fields lens modelling comparison project. *MNRAS*, 472:3177–3216, Dec. 2017. doi: 10.1093/mnras/stx2064.

A. Mesinger and S. R. Furlanetto. Lyα emitters during the early stages of reionization. *MNRAS*, 386:1990–2002, June 2008. doi: 10.1111/j.1365-2966.2008.13039.x.

G. R. Meurer, T. M. Heckman, C. Leitherer, A. Kinney, C. Robert, and D. R. Garnett. Starbursts and Star Clusters in the Ultraviolet. *AJ*, 110:2665, Dec. 1995. doi: 10.1086/117721.

J. Miralda-Escudé. Reionization of the Intergalactic Medium and the Damping Wing of the Gunn-Peterson Trough. *ApJ*, 501:15–22, July 1998. doi: 10.1086/305799.

S. Mitra, T. R. Choudhury, and A. Ferrara. Cosmic reionization after Planck. *MNRAS*, 454:L76–L80, Nov. 2015. doi: 10.1093/mnrasl/slv134.

S. Miyazaki, Y. Komiyama, M. Sekiguchi, S. Okamura, M. Doi, H. Furusawa, M. Hamabe, K. Imi, M. Kimura, F. Nakata, N. Okada, M. Ouchi, K. Shimasaku, M. Yagi, and N. Yasuda. Subaru Prime Focus Camera – Suprime-Cam. *Publications of the Astronomical Society of Japan*, 54:833–853, Dec. 2002. doi: 10.1093/pasj/54.6.833.

H. J. Mo, X. Yang, F. C. van den Bosch, and Y. P. Jing. The dependence of the galaxy luminosity function on large-scale environment. *MNRAS*, 349:205–212, Mar. 2004. doi: 10.1111/j.1365-2966.2004.07485.x.

P. Morrissey, T. Conrow, T. A. Barlow, T. Small, M. Seibert, T. K. Wyder, T. Budavári, S. Arnouts, P. G. Friedman, K. Forster, D. C. Martin, S. G. Neff, D. Schiminovich, L. Bianchi, J. Donas, T. M. Heckman, Y.-W. Lee, B. F. Madore, B. Milliard, R. M. Rich, A. S. Szalay, B. Y. Welsh, and S. K. Yi. The Calibration and Data Products of GALEX. *ApJS*, 173:682–697, Dec. 2007. doi: 10.1086/520512.

S. J. Mutch, P. M. Geil, G. B. Poole, P. W. Angel, A. R. Duffy, A. Mesinger, and J. S. B. Wyithe. Dark-ages reionization and galaxy formation simulation - III. Modelling galaxy formation and the epoch of reionization. *MNRAS*, 462:250–276, Oct. 2016. doi: 10.1093/mnras/stw1506.

S. Naoz, S. Noter, and R. Barkana. The first stars in the Universe. *MNRAS*, 373: L98–L102, Nov. 2006. doi: 10.1111/j.1745-3933.2006.00251.x.

E. Neistein, S. Khochfar, C. Dalla Vecchia, and J. Schaye. Hydrodynamical simulations and semi-analytic models of galaxy formation: two sides of the same coin. *MNRAS*, 421:3579–3593, Apr. 2012. doi: 10.1111/j.1365-2966.2012.20584.x.

K. Nomoto, N. Tominaga, H. Umeda, C. Kobayashi, and K. Maeda. Nucleosynthesis yields of core-collapse supernovae and hypernovae, and galactic chemical evolution. *Nucl. Phys. A*, 777:424–458, Oct. 2006. doi: 10.1016/j.nuclphysa.2006.05.008.

R. P. Norris. Dawes Review 5: Australian Aboriginal Astronomy and Navigation. *Publications of the Astronomical Society of Australia*, 33:e039, Aug. 2016. doi: 10.1017/pasa.2016.25.

P. A. Oesch, M. Stiavelli, C. M. Carollo, L. E. Bergeron, A. M. Koekemoer, R. A. Lucas, C. M. Pavlovsky, M. Trenti, S. J. Lilly, S. V. W. Beckwith, T. Dahlen, H. C. Ferguson, J. P. Gardner, C. Lacey, B. Mobasher, N. Panagia, and H. W. Rix. The UDF05 Follow-up of the Hubble Ultra Deep Field. I. The Faint-End Slope of the Lyman Break Galaxy Population at z ˜5. *ApJ*, 671:1212–1226, Dec 2007. doi: 10.1086/522423.

P. A. Oesch, C. M. Carollo, M. Stiavelli, M. Trenti, L. E. Bergeron, A. M. Koekemoer, R. A. Lucas, C. M. Pavlovsky, S. V. W. Beckwith, T. Dahlen, H. C. Ferguson, J. P. Gardner, S. J. Lilly, B. Mobasher, and N. Panagia. The UDF05 Follow-Up of the Hubble Ultra Deep Field. II. Constraints on Reionization from Z-Dropout Galaxies. *ApJ*, 690:1350–1357, Jan. 2009. doi: 10.1088/0004-637X/690/2/1350.

P. A. Oesch, R. J. Bouwens, C. M. Carollo, G. D. Illingworth, D. Magee, M. Trenti, M. Stiavelli, M. Franx, I. Labbé, and P. G. van Dokkum. The Evolution of the Ultraviolet Luminosity Function from z ˜ 0.75 to z ˜ 2.5 Using HST ERS WFC3/UVIS Observations. *ApJ*, 725:L150–L155, Dec. 2010. doi: 10.1088/2041-8205/725/2/L150.

P. A. Oesch, R. J. Bouwens, G. D. Illingworth, I. Labbé, M. Franx, P. G. van Dokkum, M. Trenti, M. Stiavelli, V. Gonzalez, and D. Magee. Probing the Dawn of Galaxies at z 9-12: New Constraints from HUDF12/XDF and CANDELS data. *ApJ*, 773:75, Aug. 2013. doi: 10.1088/0004-637X/773/1/75.

P. A. Oesch, R. J. Bouwens, G. D. Illingworth, I. Labbé, R. Smit, M. Franx, P. G. van Dokkum, I. Momcheva, M. L. N. Ashby, G. G. Fazio, J.-S. Huang, S. P. Willner, V. Gonzalez, D. Magee, M. Trenti, G. B. Brammer, R. E. Skelton, and L. R. Spitler. The Most Luminous z ˜ 9-10 Galaxy Candidates Yet Found: The Luminosity Function, Cosmic Star-formation Rate, and the First Mass Density Estimate at 500 Myr. *ApJ*, 786:108, May 2014. doi: 10.1088/0004-637X/786/2/108.

P. A. Oesch, G. Brammer, P. G. van Dokkum, G. D. Illingworth, R. J. Bouwens, I. Labbé, M. Franx, I. Momcheva, M. L. N. Ashby, G. G. Fazio, V. Gonzalez, B. Holden, D. Magee, R. E. Skelton, R. Smit, L. R. Spitler, M. Trenti, and S. P. Willner. A Remarkably Luminous Galaxy at z=11.1 Measured with Hubble Space Telescope Grism Spectroscopy. *ApJ*, 819:129, Mar. 2016. doi: 10.3847/0004-637X/819/2/129.

P. A. Oesch, R. J. Bouwens, G. D. Illingworth, I. Labbé, and M. Stefanon. The Dearth of z $\sim$ 10 Galaxies in All HST Legacy Fields—The Rapid Evolution of the Galaxy Population in the First 500 Myr. *ApJ*, 855:105, Mar. 2018. doi: 10.3847/1538-4357/aab03f.

J. B. Oke and J. E. Gunn. Secondary standard stars for absolute spectrophotometry. *ApJ*, 266:713–717, Mar. 1983. doi: 10.1086/160817.

T. Oliphant. NumPy: A guide to NumPy. USA: Trelgol Publishing, 2006. URL `http://www.numpy.org/`. [Online; accessed <today>].

Y. Ono, M. Ouchi, Y. Harikane, J. Toshikawa, M. Rauch, S. Yuma, M. Sawicki, T. Shibuya, K. Shimasaku, M. Oguri, C. Willott, M. Akhlaghi, M. Akiyama, J. Coupon, N. Kashikawa, Y. Komiyama, A. Konno, L. Lin, Y. Matsuoka, S. Miyazaki, T. Nagao, K. Nakajima, J. Silverman, M. Tanaka, Y. Taniguchi, and S.-Y. Wang. Great Optically Luminous Dropout Research Using Subaru HSC (GOLDRUSH). I. UV Luminosity Functions at $z \sim 4-7$ Derived with the Half-Million Dropouts on the 100 deg^2 Sky. *ArXiv e-prints*, Apr. 2017.

B. W. O'Shea, J. H. Wise, H. Xu, and M. L. Norman. Probing the Ultraviolet Luminosity Function of the Earliest Galaxies with the Renaissance Simulations. *ApJ*, 807: L12, July 2015. doi: 10.1088/2041-8205/807/1/L12.

M. Ouchi, K. Shimasaku, H. Furusawa, M. Miyazaki, M. Doi, M. Hamabe, T. Hayashino, M. Kimura, K. Kodaira, Y. Komiyama, Y. Matsuda, S. Miyazaki, F. Nakata, S. Okamura, M. Sekiguchi, Y. Shioya, H. Tamura, Y. Taniguchi, M. Yagi, and N. Yasuda. Subaru Deep Survey. II. Luminosity Functions and Clustering Properties of Lyα Emitters at z=4.86 in the Subaru Deep Field. *ApJ*, 582:60–68, Jan. 2003. doi: 10.1086/344476.

M. Ouchi, K. Shimasaku, S. Okamura, H. Furusawa, N. Kashikawa, K. Ota, M. Doi, M. Hamabe, M. Kimura, Y. Komiyama, M. Miyazaki, S. Miyazaki, F. Nakata, M. Sekiguchi, M. Yagi, and N. Yasuda. Subaru Deep Survey. V. A Census of Lyman Break Galaxies at z˜=4 and 5 in the Subaru Deep Fields: Photometric Properties. *ApJ*, 611:660–684, Aug. 2004. doi: 10.1086/422207.

M. Ouchi, B. Mobasher, K. Shimasaku, H. C. Ferguson, S. M. Fall, Y. Ono, N. Kashikawa, T. Morokuma, K. Nakajima, S. Okamura, M. Dickinson, M. Giavalisco, and K. Ohta. Large Area Survey for z = 7 Galaxies in SDF and GOODS-N: Implications for Galaxy Formation and Cosmic Reionization. *ApJ*, 706:1136–1151, Dec. 2009. doi: 10.1088/0004-637X/706/2/1136.

M. Ouchi, K. Shimasaku, H. Furusawa, T. Saito, M. Yoshida, M. Akiyama, Y. Ono, T. Yamada, K. Ota, N. Kashikawa, M. Iye, T. Kodama, S. Okamura, C. Simpson, and M. Yoshida. Statistics of 207 Lyα Emitters at a Redshift Near 7: Constraints on Reionization and Galaxy Formation Models. *ApJ*, 723:869–894, Nov. 2010. doi: 10.1088/0004-637X/723/1/869.

R. Paterno-Mahler, K. Sharon, D. Coe, G. Mahler, C. Cerny, T. L. Johnson, T. Schrabback, F. Andrade-Santos, R. J. Avila, M. Bradač, L. D. Bradley, D. Carrasco, N. G. Czakon, W. A. Dawson, B. L. Frye, A. T. Hoag, K.-H. Huang, C. Jones, D. Lam, R. Livermore, L. Lovisari, R. Mainali, P. A. Oesch, S. Ogaz, M. Past, A. Peterson, R. E. Ryan, B. Salmon, I. Sendra-Server, D. P. Stark, K. Umetsu, B. Vulcani, and A. Zitrin. RELICS: A Strong Lens Model for SPT-CLJ0615âŤĂ5746, a z = 0.972 Cluster. *ApJ*, 863:154, Aug. 2018. doi: 10.3847/1538-4357/aad239.

P. J. Peebles and B. Ratra. The cosmological constant and dark energy. *Reviews of Modern Physics*, 75:559–606, Apr. 2003. doi: 10.1103/RevModPhys.75.559.

P. J. E. Peebles. Statistical Analysis of Catalogs of Extragalactic Objects. I. Theory. *ApJ*, 185:413–440, Oct. 1973. doi: 10.1086/152431.

L. Pentericci, A. Fontana, E. Vanzella, M. Castellano, A. Grazian, M. Dijkstra, K. Boutsia, S. Cristiani, M. Dickinson, E. Giallongo, M. Giavalisco, R. Maiolino, A. Moorwood, D. Paris, and P. Santini. Spectroscopic Confirmation of z ˜7 Lyman Break

Galaxies: Probing the Earliest Galaxies and the Epoch of Reionization. *ApJ*, 743: 132, Dec. 2011. doi: 10.1088/0004-637X/743/2/132.

A. A. Penzias and R. W. Wilson. A Measurement of Excess Antenna Temperature at 4080 Mc/s. *ApJ*, 142:419–421, July 1965. doi: 10.1086/148307.

P. G. Pérez-González, J. Gallego, J. Zamorano, A. Alonso-Herrero, A. Gil de Paz, and A. Aragón-Salamanca. Luminosity and Stellar Mass Functions of Local Star-forming Galaxies. *ApJ*, 587:L27–L30, Apr. 2003. doi: 10.1086/375123.

Planck Collaboration, P. A. R. Ade, N. Aghanim, M. Arnaud, M. Ashdown, J. Aumont, C. Baccigalupi, A. J. Banday, R. B. Barreiro, J. G. Bartlett, and et al. Planck 2015 results. XIII. Cosmological parameters. *A&A*, 594:A13, Sept. 2016. doi: 10.1051/0004-6361/201525830.

Planck Collaboration, N. Aghanim, Y. Akrami, M. Ashdown, J. Aumont, C. Baccigalupi, M. Ballardini, A. J. Banday, R. B. Barreiro, N. Bartolo, S. Basak, R. Battye, K. Benabed, J. P. Bernard, M. Bersanelli, P. Bielewicz, J. J. Bock, J. R. Bond, J. Borrill, F. R. Bouchet, F. Boulanger, M. Bucher, C. Burigana, R. C. Butler, E. Calabrese, J. F. Cardoso, J. Carron, A. Challinor, H. C. Chiang, J. Chluba, L. P. L. Colombo, C. Combet, D. Contreras, B. P. Crill, F. Cuttaia, P. de Bernardis, G. de Zotti, J. Delabrouille, J. M. Delouis, E. Di Valentino, J. M. Diego, O. Doré, M. Douspis, A. Ducout, X. Dupac, S. Dusini, G. Efstathiou, F. Elsner, T. A. Enßlin, H. K. Eriksen, Y. Fantaye, M. Farhang, J. Fergusson, R. Fernandez-Cobos, F. Finelli, F. Forastieri, M. Frailis, E. Franceschi, A. Frolov, S. Galeotta, S. Galli, K. Ganga, R. T. Génova-Santos, M. Gerbino, T. Ghosh, J. González-Nuevo, K. M. Górski, S. Gratton, A. Gruppuso, J. E. Gudmundsson, J. Hamann, W. Handley, D. Herranz, E. Hivon, Z. Huang, A. H. Jaffe, W. C. Jones, A. Karakci, E. Keihänen, R. Keskitalo, K. Kiiveri, J. Kim, T. S. Kisner, L. Knox, N. Krachmalnicoff, M. Kunz, H. Kurki-Suonio, G. Lagache, J. M. Lamarre, A. Lasenby, M. Lattanzi, C. R. Lawrence, M. Le Jeune, P. Lemos, J. Lesgourgues, F. Levrier, A. Lewis, M. Liguori, P. B. Lilje, M. Lilley, V. Lindholm, M. López-Caniego, P. M. Lubin, Y. Z. Ma, J. F. Macías-Pérez, G. Maggio, D. Maino, N. Mandolesi, A. Mangilli, A. Marcos-Caballero, M. Maris, P. G. Martin, M. Martinelli, E. Martínez- González, S. Matarrese, N. Mauri, J. D. McEwen, P. R. Meinhold, A. Melchiorri, A. Mennella, M. Migliaccio, M. Millea, S. Mitra, M. A. Miville-Deschênes, D. Molinari, L. Montier, G. Morgante, A. Moss, P. Natoli, H. U. Nørgaard-Nielsen, L. Pagano, D. Paoletti, B. Partridge, G. Patanchon, H. V. Peiris, F. Perrotta, V. Pettorino, F. Piacentini, L. Polastri, G. Polenta, J. L. Puget, J. P. Rachen, M. Reinecke, M. Remazeilles, A. Renzi, G. Rocha, C. Rosset, G. Roudier, J. A. Rubiño-Martín, B. Ruiz-Granados, L. Salvati, M. Sandri, M. Save-

lainen, D. Scott, E. P. S. Shellard, C. Sirignano, G. Sirri, L. D. Spencer, R. Sunyaev, A. S. Suur-Uski, J. A. Tauber, D. Tavagnacco, M. Tenti, L. Toffolatti, M. Tomasi, T. Trombetti, L. Valenziano, J. Valiviita, B. Van Tent, L. Vibert, P. Vielva, F. Villa, N. Vittorio, B. D. Wandelt, I. K. Wehus, M. White, S. D. M. White, A. Zacchei, and A. Zonca. Planck 2018 results. VI. Cosmological parameters. *ArXiv e-prints*, art. arXiv:1807.06209, July 2018.

M. Postman, D. Coe, N. Benítez, L. Bradley, T. Broadhurst, M. Donahue, H. Ford, O. Graur, G. Graves, S. Jouvel, A. Koekemoer, D. Lemze, E. Medezinski, A. Molino, L. Moustakas, S. Ogaz, A. Riess, S. Rodney, P. Rosati, K. Umetsu, W. Zheng, A. Zitrin, M. Bartelmann, R. Bouwens, N. Czakon, S. Golwala, O. Host, L. Infante, S. Jha, Y. Jimenez-Teja, D. Kelson, O. Lahav, R. Lazkoz, D. Maoz, C. McCully, P. Melchior, M. Meneghetti, J. Merten, J. Moustakas, M. Nonino, B. Patel, E. Regös, J. Sayers, S. Seitz, and A. Van der Wel. The Cluster Lensing and Supernova Survey with Hubble: An Overview. *ApJS*, 199:25, Apr. 2012. doi: 10.1088/0067-0049/199/2/25.

A. M. Price-Whelan, B. M. Sipőcz, H. M. Günther, P. L. Lim, S. M. Crawford, S. Conseil, D. L. Shupe, M. W. Craig, N. Dencheva, A. Ginsburg, J. T. VanderPlas, L. D. Bradley, D. Pérez-Suárez, M. de Val-Borro, P. Paper Contributors, T. L. Aldcroft, K. L. Cruz, T. P. Robitaille, E. J. Tollerud, A. Coordination Committee, C. Ardelean, T. Babej, Y. P. Bach, M. Bachetti, A. V. Bakanov, S. P. Bamford, G. Barentsen, P. Barmby, A. Baumbach, K. L. Berry, F. Biscani, M. Boquien, K. A. Bostroem, L. G. Bouma, G. B. Brammer, E. M. Bray, H. Breytenbach, H. Buddelmeijer, D. J. Burke, G. Calderone, J. L. Cano Rodríguez, M. Cara, J. V. M. Cardoso, S. Cheedella, Y. Copin, L. Corrales, D. Crichton, D. D'Avella, C. Deil, É. Depagne, J. P. Dietrich, A. Donath, M. Droettboom, N. Earl, T. Erben, S. Fabbro, L. A. Ferreira, T. Finethy, R. T. Fox, L. H. Garrison, S. L. J. Gibbons, D. A. Goldstein, R. Gommers, J. P. Greco, P. Greenfield, A. M. Groener, F. Grollier, A. Hagen, P. Hirst, D. Homeier, A. J. Horton, G. Hosseinzadeh, L. Hu, J. S. Hunkeler, Ž. Ivezić, A. Jain, T. Jenness, G. Kanarek, S. Kendrew, N. S. Kern, W. E. Kerzendorf, A. Khvalko, J. King, D. Kirkby, A. M. Kulkarni, A. Kumar, A. Lee, D. Lenz, S. P. Littlefair, Z. Ma, D. M. Macleod, M. Mastropietro, C. McCully, S. Montagnac, B. M. Morris, M. Mueller, S. J. Mumford, D. Muna, N. A. Murphy, S. Nelson, G. H. Nguyen, J. P. Ninan, M. Nöthe, S. Ogaz, S. Oh, J. K. Parejko, N. Parley, S. Pascual, R. Patil, A. A. Patil, A. L. Plunkett, J. X. Prochaska, T. Rastogi, V. Reddy Janga, J. Sabater, P. Sakurikar, M. Seifert, L. E. Sherbert, H. Sherwood-Taylor, A. Y. Shih, J. Sick, M. T. Silbiger, S. Singanamalla, L. P. Singer, P. H. Sladen, K. A. Sooley, S. Sornarajah, O. Streicher, P. Teuben, S. W. Thomas, G. R. Tremblay, J. E. H. Turner, V. Ter-

rón, M. H. van Kerkwijk, A. de la Vega, L. L. Watkins, B. A. Weaver, J. B. Whitmore, J. Woillez, V. Zabalza, and A. Contributors. The Astropy Project: Building an Open-science Project and Status of the v2.0 Core Package. *AJ*, 156:123, Sept. 2018. doi: 10.3847/1538-3881/aabc4f.

J. R. Pritchard, A. Loeb, and J. S. B. Wyithe. Constraining reionization using 21-cm observations in combination with CMB and Lyα forest data. *MNRAS*, 408:57–70, Oct. 2010. doi: 10.1111/j.1365-2966.2010.17150.x.

C. Pryke, N. W. Halverson, E. M. Leitch, J. Kovac, J. E. Carlstrom, W. L. Holzapfel, and M. Dragovan. Cosmological Parameter Extraction from the First Season of Observations with the Degree Angular Scale Interferometer. *ApJ*, 568:46–51, Mar. 2002. doi: 10.1086/338880.

R. Riediger, P. Petitjean, and J. P. Mucket. Evolution of the Lymanalpha forest from high to low redshift. *A&A*, 329:30–38, Jan. 1998.

A. G. Riess, A. V. Filippenko, P. Challis, A. Clocchiatti, A. Diercks, P. M. Garnavich, R. L. Gilliland, C. J. Hogan, S. Jha, R. P. Kirshner, B. Leibundgut, M. M. Phillips, D. Reiss, B. P. Schmidt, R. A. Schommer, R. C. Smith, J. Spyromilio, C. Stubbs, N. B. Suntzeff, and J. Tonry. Observational Evidence from Supernovae for an Accelerating Universe and a Cosmological Constant. *AJ*, 116:1009–1038, Sept. 1998. doi: 10.1086/300499.

A. G. Riess, L. M. Macri, S. L. Hoffmann, D. Scolnic, S. Casertano, A. V. Filippenko, B. E. Tucker, M. J. Reid, D. O. Jones, J. M. Silverman, R. Chornock, P. Challis, W. Yuan, P. J. Brown, and R. J. Foley. A 2.4% Determination of the Local Value of the Hubble Constant. *ApJ*, 826:56, July 2016. doi: 10.3847/0004-637X/826/1/56.

G. W. Roberts-Borsani, R. J. Bouwens, P. A. Oesch, I. Labbe, R. Smit, G. D. Illingworth, P. van Dokkum, B. Holden, V. Gonzalez, M. Stefanon, B. Holwerda, and S. Wilkins. z$\gtrsim$ 7 GALAXIES WITH REDSPITZER/IRAC [3.6]–[4.5] COLORS IN THE FULL CANDELS DATA SET: THE BRIGHTEST-KNOWN GALAXIES ATz$\sim$ 7–9 AND a PROBABLE SPECTROSCOPIC CONFIRMATION ATz= 7.48. *The Astrophysical Journal*, 823(2):143, jun 2016. doi: 10.3847/0004-637x/823/2/143. URL `https://doi.org/10.3847%2F0004-637x%2F823%2F2%2F143`.

B. E. Robertson, R. S. Ellis, J. S. Dunlop, R. J. McLure, and D. P. Stark. Early star-forming galaxies and the reionization of the Universe. *Nature*, 468:49–55, Nov. 2010. doi: 10.1038/nature09527.

B. E. Robertson, S. R. Furlanetto, E. Schneider, S. Charlot, R. S. Ellis, D. P. Stark, R. J. McLure, J. S. Dunlop, A. Koekemoer, M. A. Schenker, M. Ouchi, Y. Ono,

E. Curtis-Lake, A. B. Rogers, R. A. A. Bowler, and M. Cirasuolo. New Constraints on Cosmic Reionization from the 2012 Hubble Ultra Deep Field Campaign. *ApJ*, 768: 71, May 2013. doi: 10.1088/0004-637X/768/1/71.

B. E. Robertson, R. S. Ellis, S. R. Furlanetto, and J. S. Dunlop. Cosmic Reionization and Early Star-forming Galaxies: A Joint Analysis of New Constraints from Planck and the Hubble Space Telescope. *ApJ*, 802:L19, Apr. 2015. doi: 10.1088/2041-8205/802/2/L19.

A. B. Rogers, R. J. McLure, and J. S. Dunlop. The unbiased measurement of ultraviolet spectral slopes in low- luminosity galaxies at z $\approx$ 7. *MNRAS*, 429:2456–2468, Mar. 2013. doi: 10.1093/mnras/sts515.

A. B. Rogers, R. J. McLure, J. S. Dunlop, R. A. A. Bowler, E. F. Curtis-Lake, P. Dayal, S. M. Faber, H. C. Ferguson, S. L. Finkelstein, N. A. Grogin, N. P. Hathi, D. Kocevski, A. M. Koekemoer, and P. Kurczynski. The colour distribution of galaxies at redshift five. *MNRAS*, 440:3714–3725, June 2014. doi: 10.1093/mnras/stu558.

M. Rowan-Robinson, S. Oliver, L. Wang, D. Farrah, D. L. Clements, C. Gruppioni, L. Marchetti, D. Rigopoulou, and M. Vaccari. The star formation rate density from z = 1 to 6. *MNRAS*, 461:1100–1111, Sep 2016. doi: 10.1093/mnras/stw1169.

V. C. Rubin, J. Ford, W. K., and N. Thonnard. Rotational properties of 21 SC galaxies with a large range of luminosities and radii, from NGC 4605 (R=4kpc) to UGC 2885 (R=122kpc). *ApJ*, 238:471–487, June 1980. doi: 10.1086/158003.

B. Salmon, C. Papovich, S. L. Finkelstein, V. Tilvi, K. Finlator, P. Behroozi, T. Dahlen, R. Davé, A. Dekel, M. Dickinson, H. C. Ferguson, M. Giavalisco, J. Long, Y. Lu, B. Mobasher, N. Reddy, R. S. Somerville, and R. H. Wechsler. The Relation between Star Formation Rate and Stellar Mass for Galaxies at 3.5 <= z <= 6.5 in CANDELS. *ApJ*, 799:183, Feb. 2015. doi: 10.1088/0004-637X/799/2/183.

B. Salmon, D. Coe, L. Bradley, R. Bouwens, M. Bradac, K.-H. Huang, P. Oesch, D. Stark, K. Sharon, M. Trenti, R. J. Avila, S. Ogaz, F. Andrade- Santos, D. Carrasco, C. Cerny, W. Dawson, B. L. Frye, A. Hoag, T. L. Johnson, C. Jones, D. Lam, L. Lovisari, R. Mainali, M. Past, R. Paterno-Mahler, A. Peterson, A. Riess, S. A. Rodney, R. Ryan, I. Sendra-Server, L. Strolger, K. Umetsu, B. Vulcani, and A. Zitrin. The Reionization Lensing Cluster Survey (RELICS) and the Brightest High-z Galaxies. *ArXiv e-prints*, art. arXiv:1710.08930, Oct. 2017.

B. Salmon, D. Coe, L. Bradley, M. Bradač, K.-H. Huang, V. Strait, P. Oesch, R. Paterno-Mahler, A. Zitrin, A. Acebron, N. Cibirka, S. Kikuchihara, M. Oguri,

G. B. Brammer, K. Sharon, M. Trenti, R. J. Avila, S. Ogaz, F. Andrade-Santos, D. Carrasco, C. Cerny, W. Dawson, B. L. Frye, A. Hoag, C. Jones, R. Mainali, M. Ouchi, S. A. Rodney, D. Stark, and K. Umetsu. A Candidate $z \sim 10$ Galaxy Strongly Lensed into a Spatially Resolved Arc. *ArXiv e-prints*, art. arXiv:1801.03103, Jan. 2018.

A. Sandage, G. A. Tammann, and A. Yahil. The velocity field of bright nearby galaxies. I - The variation of mean absolute magnitude with redshift for galaxies in a magnitude-limited sample. *ApJ*, 232:352–364, Sept. 1979. doi: 10.1086/157295.

M. Sawicki and D. Thompson. Keck Deep Fields. II. The Ultraviolet Galaxy Luminosity Function at z ˜ 4, 3, and 2. *ApJ*, 642:653–672, May 2006. doi: 10.1086/500999.

D. Schaerer. On the properties of massive Population III stars and metal-free stellar populations. *A&A*, 382:28–42, Jan. 2002. doi: 10.1051/0004-6361:20011619.

P. Schechter. An analytic expression for the luminosity function for galaxies. *ApJ*, 203: 297–306, Jan. 1976. doi: 10.1086/154079.

K. B. Schmidt, T. Treu, M. Trenti, L. D. Bradley, B. C. Kelly, P. A. Oesch, B. W. Holwerda, J. M. Shull, and M. Stiavelli. The Luminosity Function at z ˜ 8 from 97 Y-band Dropouts: Inferences about Reionization. *ApJ*, 786:57, May 2014. doi: 10.1088/0004-637X/786/1/57.

M. Schmidt. Space Distribution and Luminosity Functions of Quasi-Stellar Radio Sources. *ApJ*, 151:393, Feb. 1968. doi: 10.1086/149446.

P. Schneider. *Extragalactic Astronomy and Cosmology: An Introduction*. 2015. doi: 10.1007/978-3-642-54083-7.

J. L. Sérsic. *Atlas de galaxias australes*. 1968.

S. L. Shapiro. The Density of Matter in the Form of Galaxies. *AJ*, 76:291, May 1971. doi: 10.1086/111122.

A. E. Shapley, C. C. Steidel, M. Pettini, and K. L. Adelberger. Rest-Frame Ultraviolet Spectra of z˜3 Lyman Break Galaxies. *ApJ*, 588:65–89, May 2003. doi: 10.1086/373922.

T. Shibuya, M. Ouchi, and Y. Harikane. Morphologies of ÌČ190,000 Galaxies at z = 0-10 Revealed with HST Legacy Data. I. Size Evolution. *The Astrophysical Journal Supplement Series*, 219:15, Aug. 2015. doi: 10.1088/0067-0049/219/2/15.

J. M. Shull. Where do Galaxies End? *ApJ*, 784:142, Apr. 2014. doi: 10.1088/0004-637X/784/2/142.

J. M. Shull, A. Harness, M. Trenti, and B. D. Smith. Critical Star Formation Rates for Reionization: Full Reionization Occurs at Redshift z ≈ 7. *ApJ*, 747:100, Mar. 2012. doi: 10.1088/0004-637X/747/2/100.

M. Sirianni, M. J. Jee, N. Benítez, J. P. Blakeslee, A. R. Martel, G. Meurer, M. Clampin, G. De Marchi, H. C. Ford, R. Gilliland, G. F. Hartig, G. D. Illingworth, J. Mack, and W. J. McCann. The Photometric Performance and Calibration of the Hubble Space Telescope Advanced Camera for Surveys. *Publications of the Astronomical Society of the Pacific*, 117:1049–1112, Oct. 2005. doi: 10.1086/444553.

R. A. Skibba, M. S. M. Smith, A. L. Coil, J. Moustakas, J. Aird, M. R. Blanton, A. D. Bray, R. J. Cool, D. J. Eisenstein, A. J. Mendez, K. C. Wong, and G. Zhu. PRIMUS: Galaxy Clustering as a Function of Luminosity and Color at 0.2 < z < 1. *ApJ*, 784:128, Apr. 2014. doi: 10.1088/0004-637X/784/2/128.

R. Smit, R. J. Bouwens, M. Franx, G. D. Illingworth, I. Labbé, P. A. Oesch, and P. G. van Dokkum. The Star Formation Rate Function for Redshift z ~4-7 Galaxies: Evidence for a Uniform Buildup of Star-forming Galaxies during the First 3 Gyr of Cosmic Time. *ApJ*, 756:14, Sep 2012. doi: 10.1088/0004-637X/756/1/14.

G. F. Smoot, C. L. Bennett, A. Kogut, E. L. Wright, J. Aymon, N. W. Boggess, E. S. Cheng, G. de Amici, S. Gulkis, M. G. Hauser, G. Hinshaw, P. D. Jackson, M. Janssen, E. Kaita, T. Kelsall, P. Keegstra, C. Lineweaver, K. Loewenstein, P. Lubin, J. Mather, S. S. Meyer, S. H. Moseley, T. Murdock, L. Rokke, R. F. Silverberg, L. Tenorio, R. Weiss, and D. T. Wilkinson. Structure in the COBE Differential Microwave Radiometer First-Year Maps. *ApJ*, 396:L1, Sept. 1992. doi: 10.1086/186504.

D. Sobral, J. Matthee, B. Darvish, D. Schaerer, B. Mobasher, H. J. A. Röttgering, S. Santos, and S. Hemmati. Evidence for PopIII-like Stellar Populations in the Most Luminous Lyman-α Emitters at the Epoch of Reionization: Spectroscopic Confirmation. *ApJ*, 808:139, Aug. 2015. doi: 10.1088/0004-637X/808/2/139.

R. S. Somerville and R. Davé. Physical models of galaxy formation in a cosmological framework. *Annual Review of Astronomy and Astrophysics*, 53(1):51–113, 2015. doi: 10.1146/annurev-astro-082812-140951. URL `https://doi.org/10.1146/annurev-astro-082812-140951`.

D. N. Spergel, L. Verde, H. V. Peiris, E. Komatsu, M. R. Nolta, C. L. Bennett, M. Halpern, G. Hinshaw, N. Jarosik, A. Kogut, M. Limon, S. S. Meyer, L. Page, G. S. Tucker, J. L. Weiland, E. Wollack, and E. L. Wright. First-Year Wilkinson Microwave Anisotropy Probe (WMAP) Observations: Determination of Cosmological Parameters. *ApJS*, 148:175–194, Sept. 2003. doi: 10.1086/377226.

E. R. Stanway, A. J. Bunker, and R. G. McMahon. Lyman break galaxies and the star formation rate of the Universe at z˜6. *MNRAS*, 342:439–445, June 2003. doi: 10.1046/j.1365-8711.2003.06546.x.

E. R. Stanway, R. G. McMahon, and A. J. Bunker. Near-infrared properties of i-drop galaxies in the Hubble Ultra Deep Field. *MNRAS*, 359:1184–1192, May 2005. doi: 10.1111/j.1365-2966.2005.08977.x.

E. R. Stanway, M. N. Bremer, and M. D. Lehnert. On contamination and completeness in $z \geq 5$ Lyman-break galaxy surveys. *MNRAS*, 385:493–510, Mar. 2008. doi: 10.1111/j.1365-2966.2008.12853.x.

D. P. Stark. Galaxies in the First Billion Years After the Big Bang. *ARA&A*, 54: 761–803, Sept. 2016. doi: 10.1146/annurev-astro-081915-023417.

D. P. Stark, R. S. Ellis, A. Bunker, K. Bundy, T. Targett, A. Benson, and M. Lacy. The Evolutionary History of Lyman Break Galaxies Between Redshift 4 and 6: Observing Successive Generations of Massive Galaxies in Formation. *ApJ*, 697:1493–1511, June 2009. doi: 10.1088/0004-637X/697/2/1493.

D. P. Stark, R. S. Ellis, K. Chiu, M. Ouchi, and A. Bunker. Keck spectroscopy of faint 3 < z < 7 Lyman break galaxies - I. New constraints on cosmic reionization from the luminosity and redshift-dependent fraction of Lyman α emission. *MNRAS*, 408: 1628–1648, Nov. 2010. doi: 10.1111/j.1365-2966.2010.17227.x.

D. P. Stark, G. Walth, S. Charlot, B. Clément, A. Feltre, J. Gutkin, J. Richard, R. Mainali, B. Robertson, B. Siana, M. Tang, and M. Schenker. Spectroscopic detection of C IV λ1548 in a galaxy at z = 7.045: implications for the ionizing spectra of reionization-era galaxies. *MNRAS*, 454:1393–1403, Dec. 2015. doi: 10.1093/mnras/stv1907.

A. A. Starobinsky. A new type of isotropic cosmological models without singularity. *Physics Letters B*, 91:99–102, Mar. 1980. doi: 10.1016/0370-2693(80)90670-X.

C. C. Steidel and D. Hamilton. Deep imaging of high redshift QSO fields below the Lyman limit. II - Number counts and colors of field galaxies. *AJ*, 105:2017–2030, June 1993. doi: 10.1086/116579.

C. C. Steidel, K. L. Adelberger, M. Giavalisco, M. Dickinson, and M. Pettini. Lyman-Break Galaxies at z>˜4 and the Evolution of the Ultraviolet Luminosity Density at High Redshift. *ApJ*, 519:1–17, July 1999. doi: 10.1086/307363.

C. C. Steidel, K. L. Adelberger, A. E. Shapley, M. Pettini, M. Dickinson, and M. Giavalisco. Lyα Imaging of a Proto-Cluster Region at <z>=3.09. *ApJ*, 532:170–182, Mar. 2000. doi: 10.1086/308568.

M. Stiavelli and M. Trenti. The Clustering Properties of the First Galaxies. *ApJ*, 716: L190–L194, June 2010. doi: 10.1088/2041-8205/716/2/L190.

R. A. Sunyaev and Y. B. Zeldovich. Formation of Clusters of Galaxies; Protocluster Fragmentation and Intergalactic Gas Heating. *A&A*, 20:189, Aug. 1972.

T. T. Takeuchi, V. Buat, and D. Burgarella. The evolution of the ultraviolet and infrared luminosity densities in the universe at $0 < z < 1$. *A&A*, 440:L17–L20, Sept. 2005. doi: 10.1051/0004-6361:200500158.

M. Tegmark, J. Silk, M. J. Rees, A. Blanchard, T. Abel, and F. Palla. How Small Were the First Cosmological Objects? *ApJ*, 474:1, Jan. 1997. doi: 10.1086/303434.

E. Tempel, E. Saar, L. J. Liivamägi, A. Tamm, J. Einasto, M. Einasto, and V. Müller. Galaxy morphology, luminosity, and environment in the SDSS DR7. *A&A*, 529:A53, May 2011. doi: 10.1051/0004-6361/201016196.

A. T. Tokunaga and W. D. Vacca. "The Mauna Kea Observatories Near-Infrared Filter Set. III. Isophotal Wavelengths and Absolute Calibration" (<A href="/abs/2005PASP.117..421T">PASP, 117, 421 [2005]</A>). *Publications of the Astronomical Society of the Pacific*, 117:1459–1459, Dec. 2005. doi: 10.1086/499029.

M. Trenti and M. Stiavelli. Cosmic Variance and Its Effect on the Luminosity Function Determination in Deep High-z Surveys. *ApJ*, 676:767-780, Apr. 2008. doi: 10.1086/528674.

M. Trenti and M. Stiavelli. Formation Rates of Population III Stars and Chemical Enrichment of Halos during the Reionization Era. *ApJ*, 694:879–892, Apr. 2009. doi: 10.1088/0004-637X/694/2/879.

M. Trenti, L. D. Bradley, M. Stiavelli, P. Oesch, T. Treu, R. J. Bouwens, J. M. Shull, J. W. MacKenty, C. M. Carollo, and G. D. Illingworth. The Brightest of Reionizing Galaxies Survey: Design and Preliminary Results. *ApJ*, 727:L39, Feb. 2011. doi: 10.1088/2041-8205/727/2/L39.

M. Trenti, L. D. Bradley, M. Stiavelli, J. M. Shull, P. Oesch, R. J. Bouwens, J. A. Muñoz, E. Romano-Diaz, T. Treu, I. Shlosman, and C. M. Carollo. Overdensities of Y-dropout Galaxies from the Brightest-of-Reionizing Galaxies Survey: A Candidate Protocluster at Redshift $z \approx 8$. *ApJ*, 746:55, Feb. 2012. doi: 10.1088/0004-637X/746/1/55.

T. Treu, M. Trenti, M. Stiavelli, M. W. Auger, and L. D. Bradley. Inferences on the Distribution of Lyα Emission of z 7 and z 8 Galaxies. *ApJ*, 747:27, Mar. 2012. doi: 10.1088/0004-637X/747/1/27.

T. Treu, K. B. Schmidt, M. Trenti, L. D. Bradley, and M. Stiavelli. The Changing Lyα Optical Depth in the Range $6 < z < 9$ from the MOSFIRE Spectroscopy of Y-dropouts. *ApJ*, 775:L29, Sept. 2013. doi: 10.1088/2041-8205/775/1/L29.

E. L. Turner. Statistics of the Hubble diagram. II - The form of the luminosity function and density variations with application to quasars. *ApJ*, 231:645–652, Aug. 1979. doi: 10.1086/157227.

S. van den Bergh. The Luminosity Function of Galaxies. With 2 Figures in the Text. *ZAp*, 53:219, 1961.

E. Vanzella, M. Giavalisco, M. Dickinson, S. Cristiani, M. Nonino, H. Kuntschner, P. Popesso, P. Rosati, A. Renzini, D. Stern, C. Cesarsky, H. C. Ferguson, and R. A. E. Fosbury. Spectroscopic Observations of Lyman Break Galaxies at Redshifts ˜4, 5, and 6 in the Goods-South Field. *ApJ*, 695:1163–1182, Apr. 2009. doi: 10.1088/0004-637X/695/2/1163.

B. Vulcani, M. Trenti, V. Calvi, R. Bouwens, P. Oesch, M. Stiavelli, and M. Franx. Characterization and Modeling of Contamination for Lyman Break Galaxy Samples at High Redshift. *ApJ*, 836:239, Feb. 2017. doi: 10.3847/1538-4357/aa5caf.

J. V. Wall and C. R. Jenkins. *Detection and surveys*, page 182âĂŞ229. Cambridge Observing Handbooks for Research Astronomers. Cambridge University Press, 2 edition, 2012. doi: 10.1017/CBO9781139031998.012.

D. Watson, L. Christensen, K. K. Knudsen, J. Richard, A. Gallazzi, and M. J. Michałowski. A dusty, normal galaxy in the epoch of reionization. *Nature*, 519: 327–330, Mar. 2015. doi: 10.1038/nature14164.

S. M. Wilkins, R. J. Bouwens, P. A. Oesch, I. Labbé, M. Sargent, J. Caruana, J. Wardlow, and S. Clay. Quantifying the UV-continuum slopes of galaxies to z ÌČ 10 using deep Hubble+Spitzer/IRAC observations. *MNRAS*, 455:659–667, Jan. 2016a. doi: 10.1093/mnras/stv2263.

S. M. Wilkins, Y. Feng, T. Di-Matteo, R. Croft, E. R. Stanway, A. Bunker, D. Waters, and C. Lovell. The photometric properties of galaxies in the early Universe. *MNRAS*, 460:3170–3178, Aug. 2016b. doi: 10.1093/mnras/stw1154.

S. M. Wilkins, Y. Feng, T. Di Matteo, R. Croft, C. C. Lovell, and D. Waters. The properties of the first galaxies in the BlueTides simulation. *MNRAS*, 469:2517–2530, Aug 2017. doi: 10.1093/mnras/stx841.

R. E. Williams, B. Blacker, M. Dickinson, W. V. D. Dixon, H. C. Ferguson, A. S. Fruchter, M. Giavalisco, R. L. Gilliland, I. Heyer, R. Katsanis, Z. Levay, R. A. Lucas, D. B. McElroy, L. Petro, M. Postman, H.-M. Adorf, and R. Hook. The Hubble Deep Field: Observations, Data Reduction, and Galaxy Photometry. *AJ*, 112:1335, Oct. 1996. doi: 10.1086/118105.

C. N. A. Willmer. Estimating galaxy luminosity functions. *AJ*, 114:898–912, Sept. 1997. doi: 10.1086/118522.

C. J. Willott, P. Delorme, C. Reylé, L. Albert, J. Bergeron, D. Crampton, X. Delfosse, T. Forveille, J. B. Hutchings, R. J. McLure, A. Omont, and D. Schade. The Canada-France High-z Quasar Survey: Nine New Quasars and the Luminosity Function at Redshift 6. *AJ*, 139:906–918, Mar. 2010. doi: 10.1088/0004-6256/139/3/906.

C. J. Willott, R. J. McLure, P. Hibon, R. Bielby, H. J. McCracken, J.-P. Kneib, O. Ilbert, D. G. Bonfield, V. A. Bruce, and M. J. Jarvis. An Exponential Decline at the Bright End of the z = 6 Galaxy Luminosity Function. *AJ*, 145:4, Jan. 2013. doi: 10.1088/0004-6256/145/1/4.

R. A. Windhorst, S. H. Cohen, N. P. Hathi, P. J. McCarthy, R. E. Ryan, Jr., H. Yan, I. K. Baldry, S. P. Driver, J. A. Frogel, D. T. Hill, L. S. Kelvin, A. M. Koekemoer, M. Mechtley, R. W. O'Connell, A. S. G. Robotham, M. J. Rutkowski, M. Seibert, A. N. Straughn, R. J. Tuffs, B. Balick, H. E. Bond, H. Bushouse, D. Calzetti, M. Crockett, M. J. Disney, M. A. Dopita, D. N. B. Hall, J. A. Holtzman, S. Kaviraj, R. A. Kimble, J. W. MacKenty, M. Mutchler, F. Paresce, A. Saha, J. I. Silk, J. T. Trauger, A. R. Walker, B. C. Whitmore, and E. T. Young. The Hubble Space Telescope Wide Field Camera 3 Early Release Science Data: Panchromatic Faint Object Counts for 0.2-2 μm Wavelength. *ApJS*, 193:27, Apr. 2011. doi: 10.1088/0067-0049/193/2/27.

J. H. Wise and T. Abel. Resolving the Formation of Protogalaxies. III. Feedback from the First Stars. *ApJ*, 685:40–56, Sept. 2008. doi: 10.1086/590417.

J. H. Wise, V. G. Demchenko, M. T. Halicek, M. L. Norman, M. J. Turk, T. Abel, and B. D. Smith. The birth of a galaxy - III. Propelling reionization with the faintest galaxies. *MNRAS*, 442:2560–2579, Aug. 2014. doi: 10.1093/mnras/stu979.

C. Wolf, K. Meisenheimer, H.-W. Rix, A. Borch, S. Dye, and M. Kleinheinrich. The COMBO-17 survey: Evolution of the galaxy luminosity function from 25 000 galaxies with 0.2< z <1.2. *A&A*, 401:73–98, Apr. 2003. doi: 10.1051/0004-6361:20021513.

B. E. Woodgate, R. A. Kimble, C. W. Bowers, S. Kraemer, M. E. Kaiser, A. C. Danks, J. F. Grady, J. J. Loiacono, M. Brumfield, L. Feinberg, T. R. Gull, S. R. Heap, S. P. Maran, D. Lindler, D. Hood, W. Meyer, C. Vanhouten, V. Argabright, S. Franka, R. Bybee, D. Dorn, M. Bottema, R. Woodruff, D. Michika, J. Sullivan, J. Hetlinger, C. Ludtke, R. Stocker, A. Delamere, D. Rose, I. Becker, H. Garner, J. G. Timothy, M. Blouke, C. L. Joseph, G. Hartig, R. F. Green, E. B. Jenkins, J. L. Linsky, J. B. Hutchings, H. W. Moos, A. Boggess, F. Roesler, and D. Weistrop. The Space Telescope Imaging Spectrograph Design. *Publications of the Astronomical Society of the Pacific*, 110:1183–1204, Oct. 1998. doi: 10.1086/316243.

L. Xia, X. Zhou, Y. Yang, J. Ma, and Z. Jiang. Evolution of the Galaxy Luminosity Function for Redshift and Density Environment at $0.03 < z < 0.5$. *ApJ*, 652:249–256, Nov. 2006. doi: 10.1086/507698.

H. Yajima, J.-H. Choi, and K. Nagamine. Effect of radiative transfer on damped Lyα and Lyman limit systems in cosmological SPH simulations. *MNRAS*, 427:2889–2904, Dec. 2012. doi: 10.1111/j.1365-2966.2012.22131.x.

H. Yan and R. A. Windhorst. The Major Sources of the Cosmic Reionizing Background at z =6. *ApJ*, 600:L1–L5, Jan. 2004. doi: 10.1086/381573.

H. Yan, S. L. Finkelstein, K.-H. Huang, R. E. Ryan, H. C. Ferguson, A. M. Koekemoer, N. A. Grogin, M. Dickinson, J. A. Newman, R. S. Somerville, R. Davé, S. M. Faber, C. Papovich, Y. Guo, M. Giavalisco, K.-s. Lee, N. Reddy, A. R. Cooray, B. D. Siana, N. P. Hathi, G. G. Fazio, M. Ashby, B. J. Weiner, R. A. Lucas, A. Dekel, L. Pentericci, C. J. Conselice, D. D. Kocevski, and K. Lai. Luminous and High Stellar Mass Candidate Galaxies at z $\approx$ 8 Discovered in the Cosmic Assembly Near-Infrared Deep Extragalactic Legacy Survey. *ApJ*, 761:177, Dec. 2012. doi: 10.1088/0004-637X/761/2/177.

D. G. York, J. Adelman, J. E. Anderson, Jr., S. F. Anderson, J. Annis, N. A. Bahcall, J. A. Bakken, R. Barkhouser, S. Bastian, E. Berman, W. N. Boroski, S. Bracker, C. Briegel, J. W. Briggs, J. Brinkmann, R. Brunner, S. Burles, L. Carey, M. A. Carr, F. J. Castander, B. Chen, P. L. Colestock, A. J. Connolly, J. H. Crocker, I. Csabai, P. C. Czarapata, J. E. Davis, M. Doi, T. Dombeck, D. Eisenstein, N. Ellman, B. R. Elms, M. L. Evans, X. Fan, G. R. Federwitz, L. Fiscelli, S. Friedman, J. A. Frieman, M. Fukugita, B. Gillespie, J. E. Gunn, V. K. Gurbani, E. de Haas,

M. Haldeman, F. H. Harris, J. Hayes, T. M. Heckman, G. S. Hennessy, R. B. Hindsley, S. Holm, D. J. Holmgren, C.-h. Huang, C. Hull, D. Husby, S.-I. Ichikawa, T. Ichikawa, Ž. Ivezić, S. Kent, R. S. J. Kim, E. Kinney, M. Klaene, A. N. Kleinman, S. Kleinman, G. R. Knapp, J. Korienek, R. G. Kron, P. Z. Kunszt, D. Q. Lamb, B. Lee, R. F. Leger, S. Limmongkol, C. Lindenmeyer, D. C. Long, C. Loomis, J. Loveday, R. Lucinio, R. H. Lupton, B. MacKinnon, E. J. Mannery, P. M. Mantsch, B. Margon, P. McGehee, T. A. McKay, A. Meiksin, A. Merelli, D. G. Monet, J. A. Munn, V. K. Narayanan, T. Nash, E. Neilsen, R. Neswold, H. J. Newberg, R. C. Nichol, T. Nicinski, M. Nonino, N. Okada, S. Okamura, J. P. Ostriker, R. Owen, A. G. Pauls, J. Peoples, R. L. Peterson, D. Petravick, J. R. Pier, A. Pope, R. Pordes, A. Prosapio, R. Rechenmacher, T. R. Quinn, G. T. Richards, M. W. Richmond, C. H. Rivetta, C. M. Rockosi, K. Ruthmansdorfer, D. Sandford, D. J. Schlegel, D. P. Schneider, M. Sekiguchi, G. Sergey, K. Shimasaku, W. A. Siegmund, S. Smee, J. A. Smith, S. Snedden, R. Stone, C. Stoughton, M. A. Strauss, C. Stubbs, M. SubbaRao, A. S. Szalay, I. Szapudi, G. P. Szokoly, A. R. Thakar, C. Tremonti, D. L. Tucker, A. Uomoto, D. Vanden Berk, M. S. Vogeley, P. Waddell, S.-i. Wang, M. Watanabe, D. H. Weinberg, B. Yanny, N. Yasuda, and SDSS Collaboration. The Sloan Digital Sky Survey: Technical Summary. *AJ*, 120:1579–1587, Sept. 2000. doi: 10.1086/301513.

J. T. Yu and P. J. E. Peebles. Superclusters of Galaxies? *ApJ*, 158:103, Oct. 1969. doi: 10.1086/150175.

L. Y. A. Yung, R. S. Somerville, S. L. Finkelstein, G. Popping, and R. Davé. Semi-analytic forecasts for JWST - I. UV luminosity functions at z = 4-10. *MNRAS*, 483: 2983–3006, Mar 2019. doi: 10.1093/mnras/sty3241.

A. Zitrin, W. Zheng, T. Broadhurst, J. Moustakas, D. Lam, X. Shu, X. Huang, J. M. Diego, H. Ford, J. Lim, F. E. Bauer, L. Infante, D. D. Kelson, and A. Molino. A Geometrically Supported z $\sim$ 10 Candidate Multiply Imaged by the Hubble Frontier Fields Cluster A2744. *ApJ*, 793:L12, Sept. 2014. doi: 10.1088/2041-8205/793/1/L12.

A. Zitrin, A. Fabris, J. Merten, P. Melchior, M. Meneghetti, A. Koekemoer, D. Coe, M. Maturi, M. Bartelmann, M. Postman, K. Umetsu, G. Seidel, I. Sendra, T. Broadhurst, I. Balestra, A. Biviano, C. Grillo, A. Mercurio, M. Nonino, P. Rosati, L. Bradley, M. Carrasco, M. Donahue, H. Ford, B. L. Frye, and J. Moustakas. Hubble Space Telescope Combined Strong and Weak Lensing Analysis of the CLASH Sample: Mass and Magnification Models and Systematic Uncertainties. *ApJ*, 801:44, Mar. 2015. doi: 10.1088/0004-637X/801/1/44.

E. Zucca, G. Zamorani, G. Vettolani, A. Cappi, R. Merighi, M. Mignoli, G. M. Stirpe, H. MacGillivray, C. Collins, C. Balkowski, V. Cayatte, S. Maurogordato, D. Proust,

G. Chincarini, L. Guzzo, D. Maccagni, R. Scaramella, A. Blanchard, and M. Ramella. The ESO Slice Project (ESP) galaxy redshift survey. II. The luminosity function and mean galaxy density. *A&A*, 326:477–488, Oct. 1997.

F. Zwicky. Die Rotverschiebung von extragalaktischen Nebeln. *Helvetica Physica Acta*, 6:110–127, Jan. 1933.